Multiscale analysis of CNT and GnP-reinforced composites using FEM/XFEM

Dimitrios Savvas

School of Civil Engineering
Institute of Structural Analysis & Antiseismic Research
National Technical University of Athens

A thesis submitted for the degree of

Doctor of Philosophy

November, 2014

Supervisor:
Prof. M. Papadrakakis

APPROVAL

PhD THESIS EXAMINATION COMMITTEE:

Prof. Manolis Papadrakakis
(Supervisor and Principal Advisor of the Committee)
National Technical University of Athens
School of Civil Engineering

Assoc. Prof. Ioannis Raftoyiannis
(Member Advisor of the Committee)
National Technical University of Athens
School of Civil Engineering

Ass. Prof. Vissarion Papadopoulos
(Member Advisor of the Committee)
National Technical University of Athens
School of Civil Engineering

Prof. Efstathios Theotokoglou
(Member of the Examination Committee)
National Technical University of Athens
School of Applied Mathematical and Physical Science

Prof. Evangelia Kontou
(Member of the Examination Committee)
National Technical University of Athens
School of Applied Mathematical and Physical Science

Prof. Konstantinos Spiliopoulos
(Member of the Examination Committee)
National Technical University of Athens
School of Civil Engineering

Ass. Prof. George Stefanou
(Member of the Examination Committee)
Aristotle University of Thessaloniki
Department of Civil Engineering

Δέν ελπίζω τίποτα
Δέ φοβούμαι τίποτα
Είμαι λέφτερος

”I hope for nothing. I fear nothing. I am free”

Nikos Kazantzakis

Acknowledgements

This PhD thesis was carried out at the Institute of Structural Analysis and Antiseismic Research of the National Technical University of Athens from July 2010 to October 2014. The research work was mainly funded by the European Community FP7 Collaborative Project "M-RECT-Multiscale reinforcement of semicrystalline thermoplastic sheets and honeycombs", (FP7-NMP-2009-2.5-1) and the European Research Council Advanced Grant "MASTER-Mastering the computational challenges in numerical modeling and optimum design of CNT reinforced composites", (ERC-2011-ADG-20110209). The work presented in Chapter 5 was implemented within the framework of the research project "MICROLINK: Linking micromechanics-based properties with the stochastic finite element method: a challenge for multiscale modeling of heterogeneous materials and structures" - Action "Supporting Postdoctoral Researchers" of the Operational Program "Education and Lifelong Learning" (Action's Beneficiary: General Secretariat for Research and Technology), and was co-financed by the European Social Fund (ESF) and the Greek State. Also, the financial support from the Research Funding Department of the National Technical University of Athens is greatly acknowledged.

First and foremost, I would like to express my heartfelt gratitude to my supervisor Prof. Manolis Papadrakakis for providing me the opportunity to work on the state of the art topics in computational mechanics, which are related to this PhD thesis. His passion in developing innovative numerical methods and tools for large scale engineering problems of multidisciplinary character has stimulated my research interest on multiscale analysis of nano-reinforced composites. I am deeply grateful for his support, guidance and advice on professional, as well as personal level.

I would like to express my sincere appreciation to my advisory committee member, Ass. Prof. Vissarion Papadopoulos for his collaborative research work. His constructive criticism and his ability to seek solutions to complex computational problems contributed a lot to the success of this research study related mainly to

CNT-reinforced composites. I wish also to extend my deepest appreciation to my committee member, Ass. Prof. George Stefanou for his invaluable contribution on the research work related to GnP-reinforced composites. I am very grateful to him for giving me the opportunity to work on his research project and I would like to thank him for his confidence and trust on me.

Following, I would like to thank my advisory committee member, Assoc. Prof. Ioannis Raftoyiannis and the other members of my examination committee, Prof. Efstathios Theotokoglou, Prof. Evangelia Kontou and Prof. Konstantinos Spiliopoulos for their encouragement, insightful comments and hard questions. Special thanks to Prof. Evangelia Kontou for providing the experimental master curves of PEEK presented in Chapter 3.

Furthermore, I would like to thank all my PhD colleagues who worked in the research team of Prof. Manolis Papadrakakis, with whom I have shared the same agonies and the same visions during our PhD studies. Their presence was very important in creating an inspired work environment.

Finally, no words can express my love to my parents, Nikiforo and Christina. This thesis is dedicated to them.

Dimitrios Savvas
Athens, November 2014

Abstract

The subject of the current thesis is the multiscale analysis of nanocomposites reinforced by carbon nanotubes (CNTs) and graphene nanoplatelets (GnPs), using the conventional and extended finite element method (FEM/XFEM). Specifically, various modeling techniques are hierarchically applied, through different length scales from atomistic to nano, then to micro and finally to macro-scale, in order to study the mechanical and damping properties of the nano-reinforced polymer composites. Simulations of representative volume elements (RVEs) of nanocomposites are performed, where various stochastic parameters have been considered in order to account for the real microstructure geometry of the heterogeneous media.

In the context of carbon nanotube-reinforced composites (CNT-RCs), the effect of interfacial shear strength (ISS) on the mechanical and damping properties of the material is investigated. The atomic lattice of CNTs is modeled using the molecular structural mechanics (MSM) approach and is reduced to an equivalent beam element (EBE). This beam is used as the basic building block for the construction of full length CNTs, which are then embedded in the polymer matrix. Elastic, as well as plastic, material properties are assigned to the EBEs for modeling their linear or nonlinear behavior, while the Maxwell-Wiechert material model is used for modeling viscoelasticity of the polymer. The interfacial load transfer mechanism between the lateral surface of the CNT and the surrounding matrix is taken into account with a nonlinear bond-slip friction-type model. Finite element (FE) models of RVEs are constructed comprised of two independent meshes: a structured with solid elements for the matrix and a series of embedded EBEs for the full length CNTs. Straight, as well as wavy CNTs, are considered. In the case of wavy CNTs, random CNT geometries are generated using the spectral representation method with evolutionary power spectra (EPS), which are derived from processing scanning electron microscope (SEM) images. Stochastic average properties are derived through Monte Carlo (MC) simulation. The mechanical and damping properties of CNT-RCs are assessed on the basis of sensitivity analyses with respect to various weight fractions (wf) and ISS values. Numerical results are presented, showing the significant effect of the ISS, as well as the influence of CNT waviness, on the damping behavior of CNT-RCs. Then, the multiscale modeling proceeds to macro-scale through the implementation of a nonlinear homogenization method. In the context of sequential homogenization, a novel viscoplastic constitutive model is introduced, which accounts for anisotropic stiffness and energy dissipation of the composite due to CNT reinforcement and slip. Sensitivity analysis is again performed with respect to various wf and ISS values where the mechanical and damping properties of the homogeneous models are assessed and compared with direct calculations on detailed fine scale heterogeneous models.

The other class of materials studied in the current thesis is the graphene nanoplatelet-reinforced composites (GnP-RCs). Effective elastic properties are calculated from GnP-RC RVEs through a computational homogenization method, which accounts for arbitrarily shaped platelet inclusions. The homogenization combines the extended finite element method (XFEM) for the microstructural analysis with Monte Carlo simulation (MCS). The implementation of XFEM is particularly suitable for this type of problems since there is no need to generate a new finite element mesh at each MCS. The inclusions are randomly distributed and oriented within the medium while their shape is implicitly modeled by the iso-zero of an analytically defined random level set function, which also serves as the enrichment function in the framework of XFEM. Hill's energy condition is satisfied by the proposed homogenization method, which involves the generation of a large number of random RVE realizations. The microstructure geometries of these RVEs include specific volume fraction (vf) of inclusions with various stochastic parameters (e.g. number, shape, spatial distribution and orientation). The influence of the inclusion shape on the effective properties of the random media is highlighted. It is shown that the statistical characteristics of the effective properties can be significantly affected by the shape of the inclusions, especially in the case of large volume fraction and stiffness ratio.

Contents

Abstract in Greek

Περίληψη

Το θέμα της παρούσας διδακτορικής διατριβής είναι η προσομοίωση υπό πολλαπλές κλίμακες νανοσύνθετων υλικών και η ανάλυση αυτών, με χρήση τόσο της συμβατικής μεθόδου ανάλυσης με τα πεπερασμένα στοιχεία όσο και της εξελιγμένης μεθόδου ανάλυσης με τα εμπλουτισμένα πεπερασμένα στοιχεία. Συγκεκριμένα, οι κατηγορίες των νανοσύνθετων υλικών που μελετώνται αφορούν μήτρες από θερμοπλαστικά πολυμερή ενισχυμένες είτε με νανοσωλήνες άνθρακα (CNTs), είτε με νανοσωματίδια γραφενίου (GnPs). Για την προσομοίωση των ετερογενών αυτών υλικών εφαρμόζονται ιεραρχικά, από την ατομική στη νάνο, έπειτα στη μίκρο, μέχρι τελικά στη μάκρο κλίμακα, διαφορετικές τεχνικές προσομοίωσης. Σκοπός είναι να αναπτυχθεί ένα κατάλληλο υπολογιστικό εργαλείο ικανό για την ακριβή και γρήγορη πρόβλεψη των μηχανικών ιδιοτήτων των συγκεκριμένων νανοσύνθετων υλικών. Στο πλαίσιο αυτό, η μηχανική συμπεριφορά αντιπροσωπευτικών στοιχείων όγκου του υλικού, που επηρεάζεται από φαινόμενα μικροδομής, προσομοιώνεται από κατάλληλα καταστατικά μοντέλα, οι ενεργές παράμετροι των οποίων προκύπτουν μέσω μιας υπολογιστικής διαδικασίας ομογενοποίησης. Συγκεκριμένα, το αντιπροσωπευτικό στοιχείο όγκου του ενισχυμένου με νανοσωλήνες σύνθετου υλικού προσομοιώνεται στις διάφορες κλίμακες με χρήση των εξής μεθοδολογιών: α) στην ατομική κλίμακα με τη μέθοδο της δομικής μοριακής μηχανικής προσομοιώνεται το ατομικό πλέγμα των χημικών δεσμών άνθρακα-άνθρακα των νανοσωλήνων με ένα χωρικό πλαίσιο αποτελούμενο από ενεργειακά ισοδύναμες δοκούς, β)

στη νάνο κλίμακα με χρήση της μεθόδου των πεπερασμένων στοιχείων το χωρικό πλαίσιο αντικαθίσταται από ένα ισοδύναμο στοιχείο δοκού, γ) με χρήση της τεχνικής του εγκιβωτισμένου στοιχείου, εν σειρά συνδεδεμένα ισοδύναμα στοιχεία δοκού που προσομοιώνουν την γεωμετρία των νανοσωλήνων στην μίκρο κλίμακα εγκιβωτίζονται εντός των τρισδιάστατων στερεών στοιχείων που προσομοιώνουν την μήτρα του σύνθετου υλικού και δ) στη μάκρο κλίμακα η συμπεριφορά της μικροδομής προσομοιώνεται από ένα πρωτότυπο ιξωδοπλαστικό καταστατικό μοντέλο. Το μοντέλο αυτό λαμβάνει υπόψιν του την ολίσθηση των νανοσωλήνων άνθρακα στην διεπιφάνεια τους με το πολυμερές, όταν μια κρίσιμη τιμή της διεπιφανειακής διατμητικής αντοχής του υλικού ξεπεραστεί. Τα αριθμητικά αποτελέσματα που παρουσιάζονται, καταδεικνύουν την επίδραση της κατά βάρους περιεκτικότητας σε νανοσωλήνες άνθρακα, της τυχαίας γεωμετρίας αυτών, καθώς και της διεπιφανειακής διατμητικής αντοχής στις τελικές μηχανικές ιδιότητες και στην ικανότητα απόσβεσης ενέργειας του σύνθετου υλικού. Από την άλλη, το αντιπροσωπευτικό στοιχείο όγκου του νανοσύνθετου υλικού που περιέχει νανοσωματίδια γραφενίου, προσομοιώνεται με χρήση της μεθόδου των εξελιγμένων πεπερασμένων στοιχείων. Οι στοχαστικές παράμετροι που διερευνώνται στο πλαίσιο των υλικών αυτών σχετίζονται με την τυχαία γεωμετρία των νανοσωματιδίων, την θέση τους και τον προσανατολισμό τους μέσα στην μήτρα. Οι ενεργές ελαστικές παράμετροι που χαρακτηρίζουν την μηχανική συμπεριφορά των συγκεκριμένων σύνθετων υλικών προκύπτουν μέσω ομογενοποίησης, με χρήση Monte Carlo προσομοιώσεων. Τα αριθμητικά αποτελέσματα που παρουσιάζονται αφορούν αντιπροσωπευτικά στοιχεία όγκου του σύνθετου υλικού με διαφορετική κατ΄ όγκο περιεκτικότητά σε νανοσωματίδια, καθώς και διαφορετικούς λόγους των μέτρων ελαστικότητας των υλικών της μικροδομής.

Extended abstract in Greek

Εκτενής Περίληψη

«Ανάλυση πολλαπλών κλιμάκων νανοσύνθετων υλικών με χρήση συμβατικών και εξελιγμένων πεπερασμένων στοιχείων»

1. Εισαγωγή

1.1 Σκοπός της εργασίας

Το θέμα της παρούσας διδακτορικής διατριβής είναι η προσομοίωση υπό πολλαπλές κλίμακες νανοσύνθετων υλικών και η ανάλυση αυτών, με χρήση τόσο της συμβατικής μεθόδου ανάλυσης με τα πεπερασμένα στοιχεία όσο και της εξελιγμένης μεθόδου ανάλυσης με τα εμπλουτισμένα πεπερασμένα στοιχεία. Συγκεκριμένα, οι κατηγορίες των νανοσύνθετων υλικών που μελετώνται αφορούν μήτρες από θερμοπλαστικά πολυμερή ενισχυμένες είτε με νανοσωλήνες άνθρακα (CNTs), είτε με νανοσωματίδια γραφενίου (GnPs). Για την προσομοίωση των ετερογενών αυτών υλικών εφαρμόζονται διάφορες τεχνικές προσομοίωσης. Ξεκινώντας από την ατομική κλίμακα όπου προσομοιώνονται οι χημικοί δεσμοί του άνθρακα και προχωρώντας ιεραρχικά μέχρι και την μάκρο κλίμακα, είναι δυνατόν να προσομοιωθεί μέσω κατάλληλης διαδικασίας ομογενοποίησης η μηχανική συμπεριφορά ολόκληρων κατασκευών από νανοσύνθετα υλικά. Για τον σκοπό αυτό, στην παρούσα εργασία αναπτύσσονται κατάλληλα καταστατικά μοντέλα που λαμβάνουν υπόψιν τους φαινόμενα μικροδομής. Οι ενεργές παράμετροι των μακροσκοπικών αυτών μοντέλων προκύπτουν από την ανάλυση αντιπροσωπευτικών στοιχείων όγκου (RVEs) των νανοσύνθετων υλικών. Διάφορες στοχαστικές παράμετροι λαμβάνονται υπόψιν κατά την κατασκευή των RVEs όπως η τυχαία γεωμετρία των CNTs και GnPs, ο αριθμός τους, η θέση και ο προσανατολισμός τους. Μετά την στατιστική επεξεργασία των αποτελεσμάτων που προκύπτουν από την ανάλυση Monte Carlo σε ένα μεγάλο αριθμό RVEs τυχαίας μικροδομής, εξάγονται τα στοχαστικά χαρακτηριστικά των ενεργών παραμέτρων του υλικού που ανατίθενται στο μακροσκοπικό μοντέλο του σύνθετου ύλικου.

Η προσομοίωση υπό πολλαπλές κλίμακες συνθέτων υλικών ενισχυμένων με νανοσωλήνες άνθρακα (CNT-RCs) ξεκινά από την ατομική κλίμακα και προχωρά προς την νάνο κλίμακα μέσω της αντικατάστασης της μοριακής δομής του νανοσωλήνα άνθρακα από ένα χωρικό πλαίσιο αποτελούμενο από κατάλληλα συνδεδεμένα στοιχεία δοκού. Οι ιδιότητες των στοιχείων δοκού αντιστοιχούν στις ιδιότητες και την συμπεριφορά του ομοιοπολικού δεσμού μεταξύ των ατόμων άνθρακα (C-C). Για την εξαγωγή των ιδιοτήτων της δοκού εφαρμόζονται οι αρχές της δομικής μοριακής μηχανικής (MSM). Η μέθοδος αυτή προϋποθέτει την ισοδυναμία των ενεργειών παραμόρφωσης ενός μοριακού συστήματος, δηλαδη την εξίσωση της ενεργεακής έκφρασης που προκύπτει εφαρμόζοντας τις αρχές της μοριακής μηχανικής με την ενεργειακή έκφραση που προκύπτει εφαρμόζοντας τις αρχές της δομικής μηχανικής. Η μετάβαση από την ατομική κλίμακα στην νάνο κλίμακα και από εκεί στην μίκρο κλίμακα γίνεται με βάση τις αρχές της μηχανικής του συνεχούς μέσου. Συγκεκριμένα, το χωρικό πλαίσιο που αντιπροσωπεύει το μοριακό πλέγμα του νανοσωλήνα υποβάλλεται σε αξονικό εφελκυσμό, κάμψη και στρέψη με στόχο η απόκριση της νανοδομής του CNT να αντικατασταθεί με ένα ισοδύναμο, ως προς την μηχανική συμπεριφορά, στοιχείο δοκού (EBE). Για την κατασκευή μεγάλου μήκους νανοσωλήνων στην μίκρο κλίμακα χρησιμοποιούνται εν σειρά συνδεδεμένα ισοδύναμα στοιχεία δοκών, EBEs. Με τον τρόπο αυτό μπορούν να κατασκευαστούν ευθύγραμμοι αλλά και τυχαίας κυματοειδούς μορφής νανοσωλήνες, η γεωμετρία των όποιων προκύπτει με την εφαρμογή μιας καινοτόμας στοχαστικής διαδικασίας. Συγκεκριμένα, τα τυχαία σχήματα των CNTs προσομοιώνονται σαν ένα μη ομογενές στοχαστικό πεδίο, χρησιμοποιώντας την μέθοδο της φασματικής απεικόνισης σε συνδυασμό με ένα εξελικτικό φάσμα ενέργειας (EPS). Μέσω της επεξεργασίας ενός αντιπροσωπευτικού αριθμού εικόνων ηλεκτρονικού μικροσκοπίου σάρωσης των CNTs προκύπτουν οι στατιστικές ιδιότητες του εξελικτικού φάσματος ενέργειας.

Ένα αξιοσημείωτο χαρακτηριστικό της προτεινόμενης διαδικασίας προσομοίωσης είναι ότι η αλληλεπίδραση που παρατηρείται στην διεπιφάνεια των CNTs και της περιβάλλουσας μήτρας λαμβάνεται υπόψιν τόσο από το μικρομοντέλο όσο και από το τελικό ομογενές καταστατικό μοντέλο του σύνθετου υλικού. Όσον αφορά στο μικρομοντέλο η διεπιφανειακή αυτή αλληλεπίδραση υλοποιείται μέσω ενός μοντέλου τριβής, που βασίζεται σε ένα νόμο ολίσθησης-προσκόλλησης. Ο νόμος αυτός ενσωματώνεται στον κώδικα των πεπερασμένων στοιχείων και συνεπώς οδηγεί στην διαμόρφωση ενός συστήματος μη γραμμικών εξισώσεων, οι οποίες λύνονται με χρήση του μη γραμμικού αλγορίθμου των Newton-Raphson. Όσον αφορά στο ομογενές μάκρομοντέλο η εσωτερική ολίσθηση των νανοσωλήνων μέσα στην μήτρα λαμβάνεται υπόψιν μέσω της υλοποίησης ενός κατάλληλου πλαστικού μοντέλου με κινηματικό νόμο κράτυνσης και ανισοτροπική επιφάνεια διαρροής.

Ένα άλλο σημαντικό ζήτημα που αντιμετωπίζεται στην παρούσα διατριβή είναι η ακριβής πρόβλεψη της ιξωδοελαστικής συμπεριφοράς του θερμοπλαστικού υλικού της μήτρας του νανοσύνθετου υλικού. Συγκεκριμένα το πολυμερές υλικό που χρησιμοποιείται στην εργασία είναι η πολυαιθερική κετόνη poly-ether-ether-ketone ή PEEK, ένα κρυσταλλικό θερμοπλαστικό υλικό με αξιοσημείωτες μηχανικές ιδιότητες. Για την ακριβή πρόβλεψη της ιξωδοελαστικής συμπεριφοράς πολυμερών, όπως το PEEK, που παρουσιάζουν πολλαπλούς χρόνους χαλάρωσης απαιτούνται εξελιγμένα καταστατικά ιξωδοελαστικά μοντέλα. Για τον λόγο αυτό στην παρούσα εργασία χρησιμοποιείται το μοντέλο των Maxwell-Wiechert, που αποτελείται από μια σειρά παράλληλα συνδεδεμένων αποσβεστήρων και ελατηρίων. Για την βαθμονόμηση του συγκεκριμένου μοντέλου διεξάγονται πειράματα δυναμικής μηχανικής ανάλυσης (DMA) από τα οποία προκύπτουν οι σταθερές των ελατηρίων και οι χρόνοι χαλάρωσης που αντιστοιχούν στους αποσβεστήρες. Στην συνέχεια διεξάγονται αριθμητικές προσομοιώσεις δοκιμίων από PEEK σε κόπωση, τα αποτελέσματα των οποίων συγκρίνονται με αντίστοιχα πειραματικά για την επιβεβαίωση της ορθής βαθμονόμησης του ιξωδοελαστικού μοντέλου.

Για την ανάλυση των CNT-RC RVEs χρησιμοποιείται η μέθοδος των πεπερασμένων στοιχείων (FEM). Συγκεκριμένα, η μήτρα διακριτοποιείται με τρισδιάστατα στοιχεία συνεχούς μέσου ενώ τα CNTs με στοιχεία δοκού. Επιπλέον, με χρήση της τεχνικής του εγκιβωτισμένου στοιχείου αποφεύγονται πολύπλοκα δίκτυα πεπερασμένων στοιχείων. Με την μέθοδο αυτή το μητρώο στιβαρότητας του εγκιβωτισμένου στοιχείου δοκού ενσωματώνεται στο μητρώο στιβαρότητας του στερεού στοιχείου που το περιέχει. Συνεπώς, η διαδικασία αυτή επιτρέπει την διακριτοποίηση του σύνθετου υλικού από δύο ανεξάρτητα πλέγματα, ένα για την μήτρα και ένα άλλο για τους νανοσωλήνες. Το πλεονέκτημα της διαδικασία αυτής είναι η μείωση του υπολογιστικού κόστους καθώς επιταχύνεται η προεπεξεργασία (post-processing) του μοντέλου, η μόρφωση του συνολικού μητρώου στιβαρότητας και η επίλυση του συστήματος των εξισώσεων που προκύπτουν. Στην παρούσα διατριβή διερευνάται η επίδραση της διεπιφανειακής τάσης αντοχής (ISS) στις μηχανικές ιδιότητες και στην ικανότητα απόσβεσης ταλαντώσεων του CNT-RC υλικού, μέσω προσομοιώσεων σε RVEs με διαφορετικό περιεχόμενο κατά βάρος (wf) σε CNTs. Τα αριθμητικά αποτελέσματα που παρουσιάζονται στην εργασία επιβεβαιώνουν τον σημαντικό ρόλο της διαδικασίας του «functionalization» και του «straightening» των CNTs πριν την ανάμειξή τους με το πολυμερές, ώστε τελικά το παραγόμενο νανοσύνθετο υλικό να παρουσιάζει βέλτιστες μηχανικές ιδιότητες.

Η μακροσκοπική συμπεριφορά των CNT-RCs μπορεί να προβλεφθεί με αρκετά καλή ακρίβεια μέσω ενός πρωτότυπου καταστατικού μοντέλου που προτείνεται στην παρούσα διατριβή. Στα πλαίσια της ανάλυσης πολλαπλών κλιμάκων, το μοντέλο αυτό χρησιμοποιείται για την μετάβαση από την μικροκλίμακα στην μάκροκλίμακα και είναι ικανό για την πρόβλεψη της ιξωδοπλαστικής συμπεριφοράς του σύνθετου υλικού, η οποία προέρχεται από την ιξωδοελαστική συμπεριφορά της μήτρας, την ελαστική ενίσχυση που προσφέρουν τα CNTs καθώς και την απόσβεση της ενέργειας παραμόρφωσης λόγω του μηχανισμού της ολίσθησης των CNTs μέσα στην μήτρα. Το καταστατικό αυτό μοντέλο, που συνδυάζει το ιξωδοελαστικό μοντέλο των Maxwell-Wiechert με το ανισοτροπικό μοντέλο πλαστικότητας του Hill, μπορεί να προβλέψει την ανισοτροπική ενίσχυση και ολίσθηση που προκαλεί η τυχαία κατανομή των CNTs εντός της ιξωδοελαστικής μήτρας του σύνθετου υλικού. Οι ενεργές παράμετροι του καταστατικού μοντέλου που αφορούν στα ιξωδοελαστικά χαρακτηριστικά, την αρχική επιφάνεια διαρροής και τον κινηματικό νόμο κράτυνσης προκύπτουν μέσω μιας αριθμητικής διαδικασίας βαθμονόμησης που περιλαμβάνει αναλύσεις μοντέλων RVEs στην μικροκλίμακα. Τα αριθμητικά αποτελέσματα που παρουσιάζονται καταδεικνύουν την αποτελεσματικότητα της προτεινόμενης ιεραρχικής προσομοίωσης πολλαπλών κλιμάκων για την πρόβλεψη της δομικής συμπεριφοράς κατασκευών από πολυμερή υλικά ενισχυμένα με νανοσωλήνες άνθρακα. Η προτεινόμενη αυτή μέθοδος αποτελεί ένα ισχυρό υπολογιστικό εργαλείο με το οποίο μεγάλης κλίμακας κατασκευές από CNT-RC μπορούν να αναλυθούν με ακρίβεια και ταχύτητα. Το πλεονέκτημα της είναι το γεγονός ότι, φαινόμενα μικροκλίμακας λαμβάνονται υπόψιν από το ομογενές μοντέλο μέσω κατάλληλων καταστατικών νόμων υλικού.

Η άλλη κατηγορία νανοσύνθετου υλικού που μελετάται στην παρούσα εργασία είναι πολυμερή ενισχυμένα με νανοσωματίδια γραφενίου (GnPs). Στα σύνθετα αυτά υλικά που είναι γνωστά ως GnP-RCs τα νανοσωματίδια αποτελούνται από στοιβαγμένα φύλλα γραφενίου που συνδέονται μεταξύ τους με ασθενείς δυνάμεις van der Waals. Για την προσομοίωση της μικροδομής των GnP-RCs χρησιμοποιούνται τα εξελιγμένα πεπερασμένα στοιχεία (XFEM), ενώ για τον προσδιορισμό των ενεργών παραμέτρων του μακρομοντέλου εκτελείται ένας μεγάλος αριθμός από Monte Carlo (MC) προσομοιώσεις. Επομένως, η διαδικασία της ομογενοποίησης στα GnP-RCs βασίζεται στον συνδυασμό της μεθόδου XFEM με MC προσομοιώσεις. Η πρωτοτυπία της παρούσας εργασίας είναι ότι μελετάει την επίδραση του τυχαίου σχήματος των GnPs στις ενεργές παραμέτρους του ομογενούς σύνθετου υλικού. Αναλυτικότερα, το τυχαίο σχήμα των νανοσωματιδίων προσομοιώνεται μέσω μια αναλυτικά ορισμένης τυχαίας συνάρτησης (level set function), η οποία στο πλαίσιο της μεθόδου XFEM χρησιμοποιείται και ως συνάρτηση εμπλουτισμού του τασικού πεδίου των στοιχείων. Από τα αριθμητικά αποτελέσματα που παρουσιάζονται καταδεικνύεται η σημαντική επίδραση του σχήματος των εγκλεισμάτων στο τελικό σύνθετο υλικό, γεγονός που δεν λαμβάνονταν υπόψιν μέχρι τώρα κατά την διαδικασία παραγωγής του υλικού. Το σύνηθες ήταν να απλοποιείται η μορφή των εγκλεισμάτων και να αντικαθίσταται από ιδανικά σχήματα όπως σφαίρες και ελλείψεις. Η απλοποιημένη αυτή προσέγγιση όπως αποδεικνύεται στην παρούσα εργασία οδηγεί σε σημαντικό σφάλμα κατά τον προσδιορισμό των μηχανικών ιδιοτήτων του τελικού σύνθετου υλικού.

1.2 Στόχοι της εργασίας

Ο κύριος στόχος της παρούσας διδακτορικής διατριβής είναι να συνδυάσει διαφορετικές τεχνικές προσομοίωσης υπό πολλαπλές κλίμακες και να αναπτύξει νέα καταστατικά μοντέλα ικανά να προσομοιώσουν την μηχανική συμπεριφορά νανοσύνθετων υλικών με ακρίβεια και ταχύτητα. Συγκεκριμένα, το αποτέλεσμα της εργασίας είναι η ανάπτυξη ενός ισχυρού υπολογιστικού εργαλείου που μπορεί να εφαρμοστεί για την προσομοίωση της συμπεριφοράς των δύο κυριότερων κατηγοριών νανοσύνθετων υλικών: πολυμερή ενισχυμένα με νανοσωλήνες άνθρακα (CNT-RCs) και πολυμερή ενισχυμένα με νανοσωματίδια γραφενίου (GnP-RCs). Ειδικότερα οι επιμέρους στόχοι της εργασίας συνοψίζονται στα εξής:

1. Εφαρμογή της μεθόδου δομικής μοριακής μηχανικής (MSM) για την προσομοίωση της ατομικής δομής νανοσωλήνων άνθρακα ως χωρικό πλαίσιο.

2. Υπολογισμός της γραμμικής/μη γραμμικής συμπεριφοράς ισοδύναμου στοιχείου δοκού (EBE) για την αντικατάσταση του χωρικού πλαισίου του νανοσωλήνα.

3. Εφαρμογή μιας νέας στοχαστικής διαδικασίας που βασίζεται στην επεξεργασία εικόνων ηλεκτρονικού μικροσκοπίου σάρωσης (SEM) για την προσομοίωση νανοσωλήνων τυχαίας κυματοειδούς μορφής.

4. Ανάπτυξη και ενσωμάτωση μοντέλου ολίσθησης (bond-slip model) σε κώδικα πεπερασμένων στοιχείων για την προσομοίωση της ολίσθησης των νανοσωλήνων εντός της μήτρας του CNT-RC υλικού.

5. Εφαρμογή της τεχνικής του ενσωματωμένου στοιχείου (embedded element technique) για την διακριτοποίηση αντιπροσωπευτικών στοιχείων όγκου (RVEs) του CNT-RC υλικού και την παραγωγή πλεγμάτων πεπερασμένων στοιχείων απλής γεωμετρίας.

6. Υλοποίηση του ιξωδοελαστικού καταστατικού μοντέλου των Maxwell-Wiechert για την προσομοίωση της ιξωδοελαστικής συμπεριφοράς του θερμοπλαστικού υλικού της μήτρας.

7. Διερεύνηση της επίδρασης στις μηχανικές ιδιότητες και στην ικανότητα απόσβεσης ενέργειας του CNT-RC υλικού των εξής παραμέτρων: α) κατά βάρος περιεκτικότητα σε νανοσωλήνες άνθρακα (wf%), β) διατμητική αντοχή στην διεπιφάνεια μεταξύ νανοσωλήνα και πολυμερούς (ISS) και γ) τυχαία κυματοειδή γεωμετρία των νανοσωλήνων άνθρακα (CNT waviness).

8. Ανάπτυξη και υλοποίηση ιξωδοπλαστικού καταστατικού μοντέλου για την προσομοίωση της ομογενούς μηχανικής συμπεριφοράς του CNT-RC υλικού λαμβάνοντας υπόψιν φαινόμενα μικροδομής: α) ανισοτροπική ενίσχυση, β) ιξωδοελαστική συμπεριφορά της μήτρας και γ) ανισοτροπική απόσβεση ενέργειας λόγω ολίσθησης των νανοσωλήνων.
9. Εφαρμογή της μεθόδου των εξελιγμένων πεπερασμένων στοιχείων (XFEM) για την προσομοίωση της μικροδομής αντιπροσωπευτικών στοιχείων όγκου του GnP-RC υλικού.
10. Ανάπτυξη αριθμητικής διαδικασίας ομογενοποίησης της μηχανικής συμπεριφοράς του GnP-RC υλικού, με εφαρμογή μεγάλου αριθμού Monte Carlo προσομοιώσεων σε αντιπροσωπευτικά στοιχεία όγκου που περιέχουν νανοσωματίδια τυχαίας γεωμετρίας.
11. Διερεύνηση της επίδρασης στις ομογενείς ελαστικές ιδιότητες του GnP-RC υλικού των εξής παραμέτρων: α) τυχαίο σχήμα των νανοσωματιδίων β) περιεκτικότητα κατά όγκο σε νανοσωματίδια (vf%) και γ) διαφορετικός λόγος μέτρου ελαστικότητας των συστατικών υλικών του σύνθετου (stiff and compliant inclusions).

2. Νανοσωλήνες άνθρακα

2.1 Δομή νανοσωλήνων άνθρακα

Ένας μονότοιχος νανοσωλήνας άνθρακα (SWCNT) προσομοιάζεται με μια σωληνοειδή κατασκευή που προκύπτει από την περιέλαση ενός φύλλου γραφενίου. Οι πολύτοιχοι νανοσωλήνες άνθρακα (MWCNTs) αποτελούνται από ομόκεντρους SW-CNTs διαφορετικής ακτίνας. Η ατομική δομή του νανοσωλήνα προσδιορίζεται από ένα χαρακτηριστικό διάνυσμα $\vec{C_h}$ (chiral vector), το οποίο μαζί με την γωνία θ (chiral angle) καθορίζει την διεύθυνση δίπλωσης του φύλλου γραφενίου. Όπως φαίνεται στο σχήμα 1, ένας νανοσωλήνας με chirality (n, m) προκύπτει κόβοντας το φύλλο γραφενίου κατα μήκος των διακεκομμένων γραμμών και διπλώνοντάς το κατα την διεύθυνση του χαρακτηριστικού διανύσματος. Το διάνυσμα αυτό ορίζεται ως εξής:

$$\vec{C_h} = n\ \vec{\alpha_1} + m\ \vec{\alpha_2} \tag{1}$$

και η γωνία θ του χαρακτηριστικού διανύσματος δίνεται από την εξίσωση

$$\theta = \mathrm{atan}\left(\frac{\sqrt{3}\ m}{2n + m}\right) \tag{2}$$

όπου $\vec{\alpha_1}$ και $\vec{\alpha_2}$ είναι τα διανύσματα βάσης που φαίνονται στο σχήμα 1 ενώ (n, m) είναι οι παράμετροι που χαρακτηρίζουν το chirality του νανοσωλήνα.

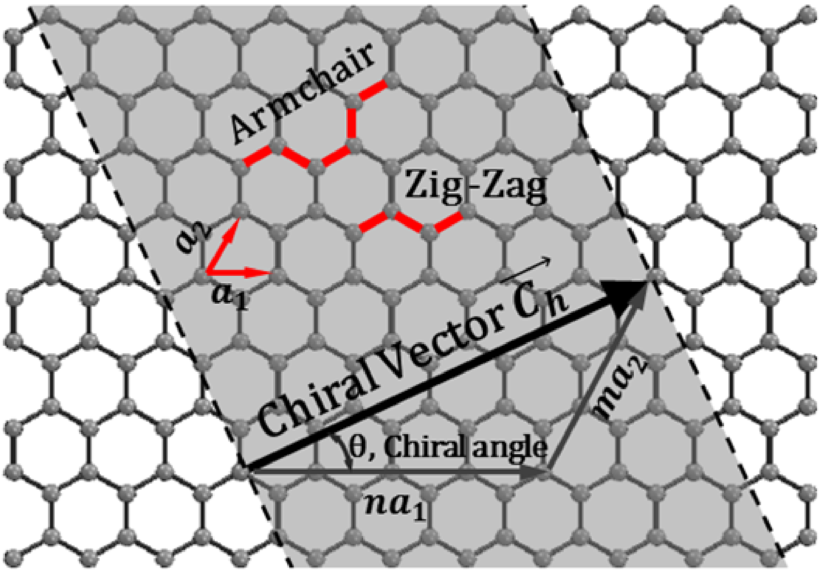

Σχήμα 1: Ατομικό πλέγμα φύλλου γραφενίου: Προσδιορισμός του chiral vector $\vec{C_h}$ από τα διανύσματα βάσης $\vec{\alpha_1}$ και $\vec{\alpha_2}$

Ανάλογα με τις τιμές του ζεύγους (n, m) οι νανοσωλήνες είναι και διαφορετικού τύπου. Συνεπώς, για $n = m$ ο νανοσωλήνας χαρακτηρίζεται ως «armchair» και η γωνία θ είναι 30° ενώ για $n \neq 0$, $m = 0$ ο νανοσωλήνας χαρακτηρίζεται ως «zig-zag» και η γωνία θ είναι 0°. Για οποιοδήποτε άλλο συνδυασμό τιμών των παραμέτρων n και m η γωνία $\theta \in (0°, 30°)$ και ο νανοσωλήνας χαρακτηρίζεται ως «chiral». Στο σχήμα 2 παρουσιάζονται οι τρείς διαφορετικοί τύποι νανοσωλήνων.

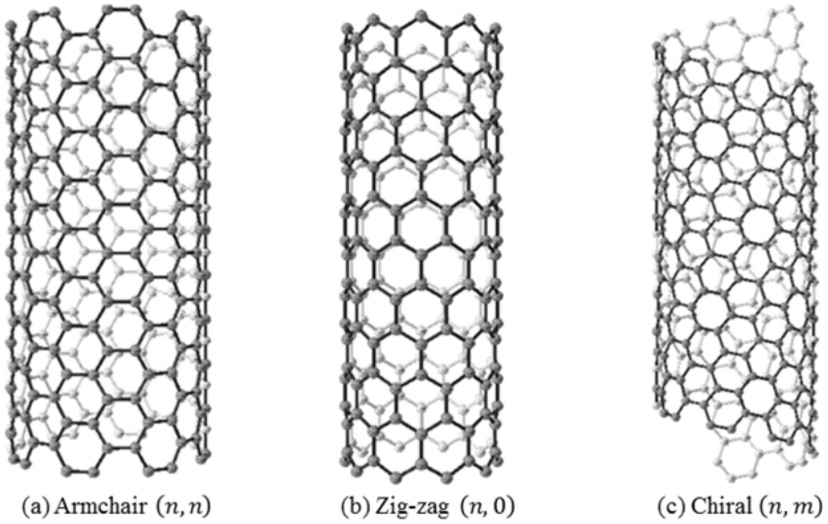

Σχήμα 2: Ατομική δομή νανοσωλήνα τύπου: a) armchair, b) zig-zag και c) chiral

2.2 Προσομοίωση νανοσωλήνων άνθρακα

Για την προσομοίωση των νανοσωλήνων άνθρακα τρείς είναι οι κύριες τεχνικές που χρησιμοποιούνται: α) η μοριακή προσομοίωση β) η προσομοίωση συνεχούς μέσου και γ) η υβριδική μέθοδος που βασίζεται στον συνδυασμό αυτών. Στην παρούσα εργασία εφαρμόζεται η μέθοδος της δομικής μοριακής μηχανικής η οποία εμπίπτει στην τρίτη κατηγορία και χρησιμοποιείται ευρύτερα λόγω της ικανότητάς της να προσομοιώνει μεγάλης κλίμακας μοντέλα με ακρίβεια και ταχύτητα.

2.2.1 Δομική μοριακή μηχανική

Η μέθοδος της δομικής μοριακής μηχανικής βασίζεται στην αντικατάσταση των αλληλεπιδράσεων του χημικού ομοιοπολικού δεσμού άνθρακα-άνθρακα (C-C) με ένα ισοδύναμο δομικό στοιχείο, συγκεκριμένα με μια ενεργειακά ισοδύναμη δοκό. Στο σχήμα 3 εικονίζονται οι ενδοατομικές αλληλεπιδράσεις των δεσμών οι οποίες συνεισφέρουν στην συνολική δυναμική ενέργεια του μοριακού συστήματος:

$$U = \sum U_r + \sum U_\theta + \sum U_\phi + \sum U_\omega + \sum U_{vdW} \tag{3}$$

$U_r, U_\theta, U_\phi, U_\omega$ και U_{vdW} είναι η ενέργεια εξ' αιτίας του εφελκυσμού του δεσμού, της μεταβολής της γωνίας κάμψης, της μεταβολής της δίεδρης γωνίας στρέψης, της εκτός επιπέδου στρέψης και των δυνάμεων van der Waals αντίστοιχα. Για την έκφραση των ενεργειών αυτών έχουν προταθεί διάφορα δυναμικά όπως για παράδειγμα το δυναμικό του Morse, των Tersoff-Brenner, Lenard-Jones κ.α. Στην παρούσα μελέτη γίνεται η υπόθεση των μικρών παραμορφώσεων του νανοσωλήνα και συνεπώς οι αλληλεπιδράσεις των ατόμων άνθρακα θεωρούνται γραμμικές, επιτρέποντας την έκφραση των ενεργειακών όρων μέσω αρμονικών συναρτήσεων της μορφής:

$$U_r = \frac{1}{2}k_r\left(r - r_0\right)^2 = \frac{1}{2}k_r\left(\Delta r\right)^2, \tag{4}$$

$$U_\theta = \frac{1}{2}k_\theta\left(\theta - \theta_0\right)^2 = \frac{1}{2}k_\theta\left(\Delta\theta\right)^2, \tag{5}$$

$$U_\tau = U_\phi + U_\omega = \frac{1}{2}k_\tau\left(\Delta\phi\right)^2 \tag{6}$$

όπου k_r , k_θ και k_τ είναι οι σταθερές των δυνάμεων αντίστασης που αντιστοιχούν στις παραμορφώσεις των δεσμών λόγω μεταβολής της αξονικής απόστασης Δr, της γωνίας κάμψης $\Delta\theta$ και της γωνίας στρέψης $\Delta\phi$.

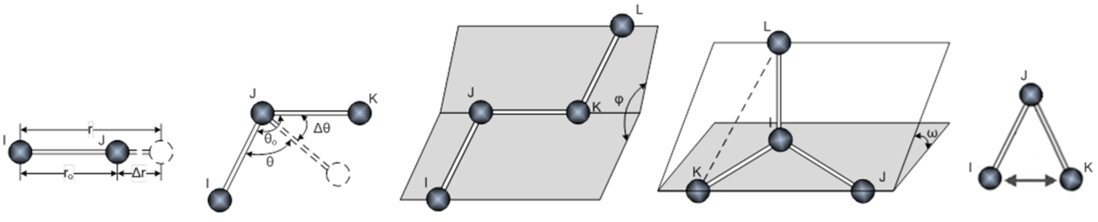

(a) (b) (c) (d) (e)

Σχήμα 3: Ενδοατομικές αλληλεπιδράσεις: a) εφελκυσμός, b) κάμψη, c) δίεδρη στρέψη, d) εκτός επιπέδου στρέψη και e) van der Waals

Με βάση τις αρχές της δομικής μηχανικής οι παραμορφώσεις των δεσμών αντιστοιχούν στην παραμόρφωση μιας συνεχής δοκού αρχικού μήκους L που υποβάλλεται σε αξονική φόρτιση N, καθαρή κάμψη M και καθαρή στρέψη T, μεταβάλοντας αντίστοιχα το αξονικό μήκος της κατά ΔL, την γωνία κάμψης των άκρων της κατά α και την στρεπτική γωνία της κατά $\Delta\beta$ (σχήμα 4). Η ενέργεια παραμόρφωσης της δοκού που αντιστοιχεί σε κάθε φόρτιση δίνεται από τις εξισώσεις:

$$U_A = \frac{1}{2}\int_0^L \frac{N^2}{EA} dL = \frac{1}{2}\frac{N^2 L}{EA} = \frac{1}{2}\frac{EA}{L}(\Delta L)^2, \tag{7}$$

$$U_M = \frac{1}{2}\int_0^L \frac{M^2}{EI} dL = \frac{1}{2}\frac{M^2 L}{EI} = \frac{1}{2}\frac{EI}{L}(2\alpha)^2, \tag{8}$$

$$U_T = \frac{1}{2}\int_0^L \frac{T^2}{GJ} dL = \frac{1}{2}\frac{T^2 L}{GJ} = \frac{1}{2}\frac{GJ}{L}(\Delta\beta)^2 \tag{9}$$

Συνδυάζοντας τις ενεργειακές εκφράσεις που προκύπτουν από την δομική μηχανική (Εξ.4-6) με αυτές που προκύπτουν από την μοριακή μηχανική (Εξ.7-9), μπορούν να υπολογιστούν η αξονική, καμπτική και στρεπτική ακαμψία της δοκού με βάση γνωστές δυνάμεις αντίστασης ως εξής:

$$EA = k_r L,\ EI = k_\theta L,\ GJ = k_\tau L \tag{10}$$

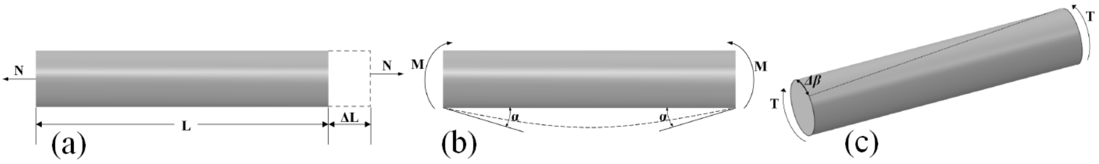

Σχήμα 4: Παραμορφώσεις δοκού σε: a) εφελκυσμό, b) κάμψη και c) στρέψη

2.2.2 Ισοδύναμο στοιχείο δοκού

Για την μείωση του υπολογιστικού φόρτου κατά την επίλυση του νανοσωλήνα που προσομοιώθηκε με την μέθοδο MSM, το χωρικό πλαίσιο που σχηματίζουν οι δοκοί που αναπαριστούν τους χημικούς δεσμούς, αντικαθίσταται εκ νέου από ένα ισοδύναμο στοιχείο δοκού (EBE). Για τον καθορισμό των σταθερών ακαμψίας του EBE το χωρικό πλαίσιο υποβάλλεται σε μια σειρά φορτίσεων που περιλαμβάνει αξονικό εφελκυσμό, καθαρή κάμψη και στρέψη. Στο σχήμα 5 διακρίνονται τα φορτία και οι συνοριακές συνθήκες που εφαρμόζονται στο χωρικό πλαίσιο του CNT σε κάθε μία από τις περιπτώσεις φόρτισης. Για την εξαγωγή των ακαμψιών του EBE χρησιμοποιούνται οι εξισώσεις:

$$(EA)_{eq} = \frac{F_x L_0}{u_x},\ (EI)_{eq} = \frac{F_y}{3u_y} L_0^3,\ (GJ)_{eq} = \frac{T}{\phi} L_0 \tag{11}$$

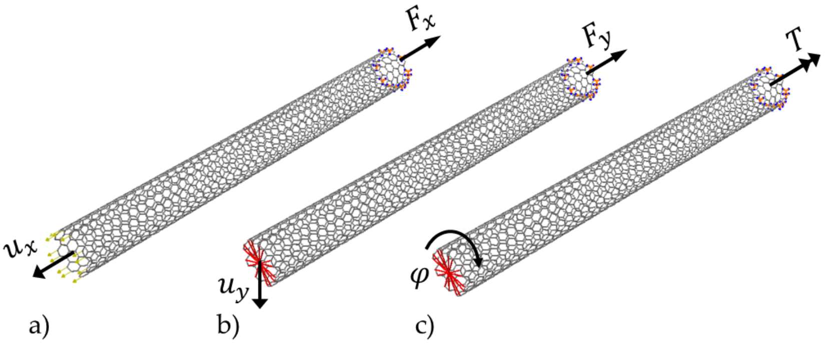

Σχήμα 5: Φορτία και συνοριακές συνθήκες στο χωρικό πλαίσιο του CNT σε: a) εφελκυσμό, b) κάμψη και c) στρέψη

Επιλέγοντας ένα συγκεκριμένο σχήμα για την διατομή της ισοδύναμης δοκού υπολογίζονται οι χαρακτηριστικές παράμετροί της όπως το εμβαδόν διατομής A_{eq}, η καμπτική ροπή I_{eq} και η πολική ροπή αδράνειας J_{eq}. Στην συνέχεια από τις Εξ. (11) υπολογίζονται το μέτρο ελαστικότητας E και το μέτρο διάτμησης G του ΕΒΕ. Στα σχήματα 6a και 6b αναπαριστάνονται οι τιμές του μέτρου ελαστικότητας και του μέτρου διάτμησης αντίστοιχα σε σχέση με την διάμετρο νανοσωλήνων τύπου «armchair» και «zig-zag» σωληνωτής διατομής. Ο λόγος μήκος/διάμετρος των νανοσωλήνων είναι σε όλες τις περιπτώσεις περίπου δέκα.

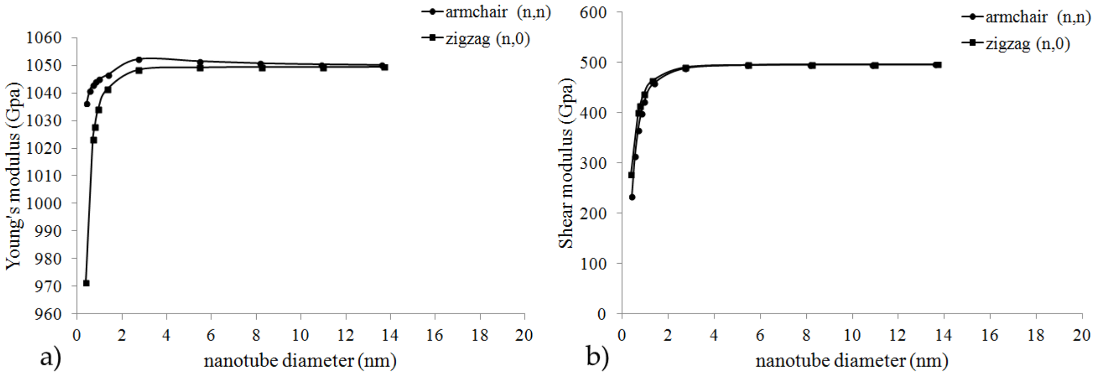

Σχήμα 6: Μεταβολή μέτρου a) ελαστικότητας και b) διάτμησης νανοσωλήνων τύπου «armchair» και «zig-zag» σωληνωτής διατομής ως προς την διάμετρο τους

3. Θερμοπλαστική μήτρα

Τα θερμοπλαστικά υλικά χρησιμοποιούνται ευρέως στην κατασκευή σύνθετων υλικών ως μήτρες λόγω των εξαιρετικών μηχανικών ιδιοτήτων τους και της εύκολης κατεργασία τους. Ένα άλλο σημαντικό πλεονέκτημά της χρήσης τους είναι η γρήγορη απόσβεση ενέργειας σε ταλαντώσεις. Στην παρούσα εργασία χρησιμοποιείται η πολυαιθερική κετόνη «poly-ether-ether-ketone» ή «PEEK». Το συγκεκριμένο υλικό όπως και τα περισσότερα πολυμερή παρουσιάζουν ιξωδοελαστική συμπεριφορά, δηλαδή η απόκρισή τους εξαρτάται από την χρονική διάρκεια της φόρτισης, τον ρυθμό της παραμόρφωσης και την ένταση του μεγέθους της παραμόρφωσης. Για την προσομοίωση της ιξωδοελαστικής συμπεριφοράς εφαρμόζονται τα βασικά μοντέλα ελατηρίων και αποσβεστήρων σε κατάλληλους συνδυασμούς.

Συγκεκριμένα, για την προσομοίωση του PEEK χρησιμοποιήθηκε το ιξωδοελαστικό μοντέλο των Maxwell-Wiechert το οποίο μπορεί να προβλέψει πολλαπλούς χρόνους χαλάρωσης για το υλικό. Στο σχήμα 7 παρουσιάζεται η μονοδιάστατη αναπαράσταση του συγκεκριμένου μοντέλου. Πρόκειται για N παράλληλα συνδεδεμένα επιμέρους στοιχεία Maxwell (ελατήριο E_i σε εν σειρά σύνδεση με αποσβεστήρα n_i) και σε παράλληλη σύνδεση με ελατήριο E_∞. Το συγκεκριμένο μοντέλο σε πείραμα χαλάρωσης, όπου μια σταθερή παραμόρφωση $\hat{\varepsilon}(0)$ επιβάλλεται για μακρό χρονικό διάστημα στο δοκίμιο υλικού, προβλέπει την εξής χρονική συνάρτηση της τάσης:

$$\hat{\sigma}(t) = E_\infty \hat{\varepsilon}(0) + \sum_{j=1}^{N} E_j e^{-\frac{t}{\tau_j}} \hat{\varepsilon}(0) \tag{12}$$

όπου τ_j είναι ο χρόνος χαλάρωσης που αντιστοιχεί στο j^{th} Maxwell στοιχείο του μοντέλου. Η χαρακτηριστική εξίσωση που δίνει το μέτρο χαλάρωσης του υλικού εκφράζεται από την παρακάτω χρονική συνάρτηση:

$$\hat{\Gamma}(t) = E_\infty + \sum_{j=1}^{N} E_j e^{-\frac{t}{\tau_j}} \tag{13}$$

από την Εξ. (13) προκύπτουν το βραχύχρονο και το μακρόχρονο μέτρο χαλάρωσης αντίστοιχα ως εξής:

$$\hat{\Gamma}_0 = \lim_{t \to 0} \hat{\Gamma}(t) = E_\infty + \sum_{j=1}^{N} E_j, \tag{14}$$

$$\hat{\Gamma}_\infty = \lim_{t \to \infty} \hat{\Gamma}(t) = E_\infty \tag{15}$$

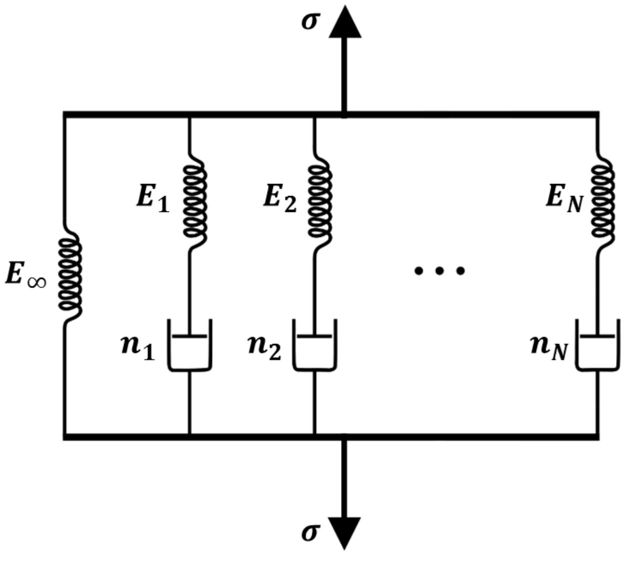

Σχήμα 7: Ιξωδοελαστικό μοντέλο Maxwell-Wiechert

3.1 Βαθμονόμηση μοντέλου Maxwell-Wiechert

Για την βαθμονόμηση ενός ιξωδοελαστικού υλικού που προσομοιώνεται από το καταστατικό μοντέλο των Maxwell-Wiechert χρησιμοποιούνται πειραματικά αποτελέσματα που προκύπτουν από δυναμικές μηχανικές μετρήσεις (DMA). Στα πειράματα αυτά το υλικό υποβάλλεται σε εναλλασσόμενη αρμονική παραμόρφωση εντός ενός ευρύ φάσματος συχνοτήτων ω. Με κατάλληλες μετρήσεις εξάγονται σε κάθε συχνότητα τα δυναμικά μέτρα αποθήκευσης $\bar{\Gamma}'$ και απωλειών $\bar{\Gamma}''$. Αντίστοιχα, τα δυναμικά μέτρα που υπολογίζονται αριθμητικά από το καταστατικό μοντέλο δίνονται από τις εξισώσεις:

$$\Gamma' = E\frac{\omega^2\tau^2}{1+\omega^2\tau^2}, \tag{16}$$

$$\Gamma'' = E\frac{\omega\tau}{1+\omega^2\tau^2} \tag{17}$$

Μέσω της ελαχιστοποίησης της παρακάτω συνάρτησης σφάλματος προκύπτουν οι παράμετροι του ιξωδοελαστικού μοντέλου E_j, n_j

$$R^2 = \sum_{i=1}^{M} \frac{1}{\hat{\Gamma}^2_\infty} \left[\left(\Gamma' - \bar{\Gamma}'\right)_i^2 + \left(\Gamma'' - \bar{\Gamma}''\right)_i^2 \right] \tag{18}$$

M είναι ο αριθμός των πειραματικών μετρήσεων υπό διαφορετικές συχνότητες ω. Στα σχήματα 8 και 9 παρουσιάζονται οι πειραματικές και οι αριθμητικές καμπύλες των δυναμικών μέτρων αποθήκευσης και απωλειών αντίστοιχα που αφορούν το PEEK. Οι τιμές τους δίνονται για ένα ευρύ φάσμα συχνοτήτων ω. Από την σύγκριση των πειραματικών και αριθμητικών καμπυλών διαπιστώνεται ότι το μοντέλο των Maxwell-Wiechert προβλέπει με ακρίβεια την ιξωδοελαστική συμπεριφορά του PEEK σε κάθε περίπτωση συχνότητας φόρτισης.

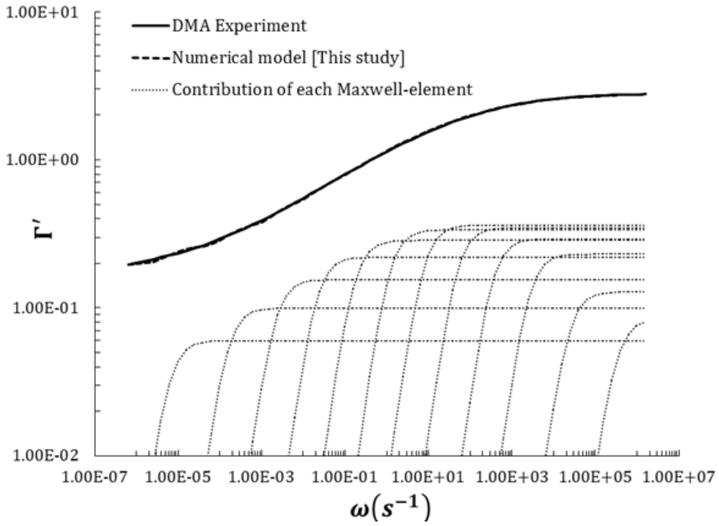

Σχήμα 8: Δυναμικό μέτρο αποθήκευσης: πειραματική vs αριθμητική καμπύλη

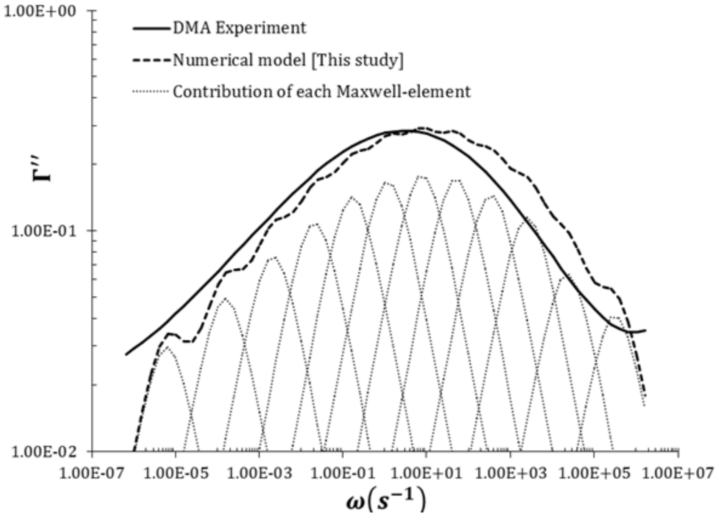

Σχήμα 9: Δυναμικό μέτρο απωλειών: πειραματική vs αριθμητική καμπύλη

4. Σύνθετα υλικά ενισχυμένα με νανοσωλήνες άνθρακα

Οι νανοσωλήνες άνθρακα, λόγω των εξαιρετικών μηχανικών ιδιοτήτων τους, του μεγάλου λόγου μήκους προς διάμετρο και την χαμηλή πυκνότητά τους, αποτελούν ιδανικά στοιχεία για την ενίσχυση πολυμερών, συμβάλλοντας έτσι στην κατασκευή προηγμένων νανοσύνθετων υλικών. Στην ατομική κλίμακα η αλληλεπίδραση του μοριακού πλέγματος των CNTs με τις μοριακές αλυσίδες του πολυμερούς γίνεται μέσω ασθενών δυνάμεων van der Waals. Κατά την φόρτιση του σύνθετου υλικού οι δεσμοί αυτοί λύονται σχεδόν ακαριαία με αποτέλεσμα να παρατηρείται σχετική ολίσθηση στην διεπιφάνεια μεταξύ των CNTs και της θερμοπλαστικής μήτρας. Λόγω του γεγονότος αυτού, η ποιότητα της ενίσχυσης που προσφέρουν τα CNTs και η αναμενόμενη βελτίωση των μηχανικών ιδιοτήτων του σύνθετου υλικού δεν είναι ικανοποιητική. Το πρόβλημα διορθώνεται εφαρμόζοντας ειδικές τεχνικές ενεργοποίησης (functionalization) των ατόμων άνθρακα στην πλευρική επιφάνεια των CNTs, ώστε να σχηματίσουν ισχυρούς χημικούς δεσμούς με τις μοριακές αλυσίδες του πολυμερούς. Ως αποτέλεσμα, η διεπιφανειακή διατμητική αντοχή (ISS) αυξάνεται, με συνέπεια τα CNTs να παραμένουν συνδεδεμένα με την μήτρα ακόμη και σε μεγάλες δυνάμεις φόρτισης του σύνθετου υλικού, προσφέροντας έτσι βέλτιστη ακαμψία.

Στην παρούσα εργασία μελετάται η επίδραση του ISS στις μηχανικές ιδιότητες και στην αποσβενόμενη ενέργεια ταλάντωσης του σύνθετου υλικού με χρήση προσομοιώσεων υπό πολλαπλές κλίμακες. Συγκεκριμένα, η υπολογιστική διαδικασία περιλαμβάνει προσομοιώσεις στην ατομική κλίμακα όπου ο δεσμός άνθρακα-άνθρακα προσομοιώνεται ως στοιχείο δοκού, στην νάνο κλίμακα όπου το μοριακό πλέγμα του νανοσωλήνα άνθρακα προσομοιώνεται ως χωρικό πλαίσιο και στην μίκρο κλίμακα όπου για την προσομοίωση του RVE του σύνθετου υλικού χρησιμοποιούνται τρισδιάστατα στερεά στοιχεία για την μήτρα και εν σειρά συνδεδεμένα ισοδύναμα στοιχεία δοκών για τους νανοσωλήνες. Η ανάλυση υπό πολλαπλές κλίμακες συνεχίζεται έως και την μακρο κλίμακα, όπου μέσω της εφαρμογής μιας πρωτότυπης υπολογιστικής διαδικασίας ομογενοποίησης και την βαθμονόμηση ενός νέου ιξωδοπλαστικού καταστατικού μοντέλου είναι δυνατή η πρόβλεψη της συμπεριφοράς του μικρομοντέλου. Στο σχήμα 10 παρουσιάζεται γραφικά η προσομοίωση του σύνθετου υλικού στις διάφορες κλίμακες.

4.1 Προσομοίωση του CNT-RC RVE

Η μικροδομή του αντιπροσωπευτικού στοιχείου όγκου του νανοσύνθετου υλικού προσομοιώνεται με χρήση της κλασικής μεθόδου των πεπερασμένων στοιχείων.

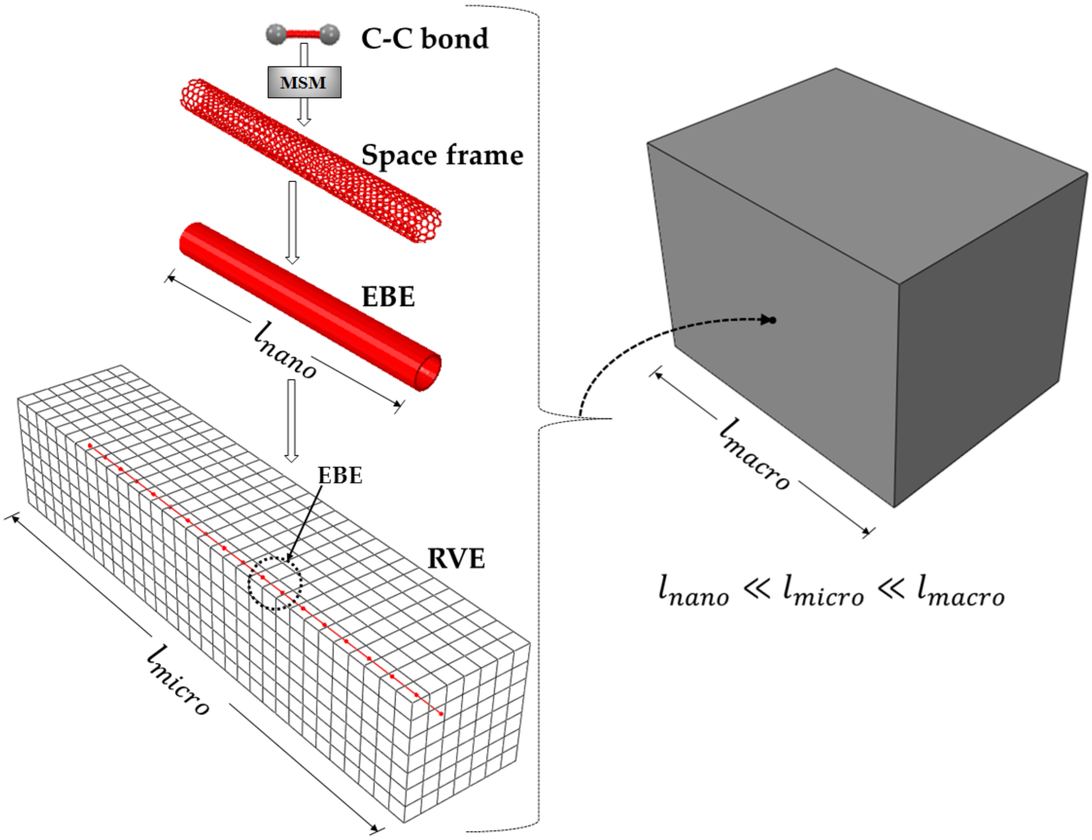

Σχήμα 10: Προσομοίωση υπό πολλαπλές κλίμακες των CNT-RCs

Συγκεκριμένα, για την διακριτοποίηση της θερμοπλαστικής μήτρας χρησιμοποιούνται τρισδιάστατα στερεά στοιχεία στα οποία ανατίθεται το ιξωδοελαστικό καταστατικό μοντέλο των Maxwell-Wiechert που αναλύθηκε στην ενότητα 3. Η γεωμετρία των CNTs αναπαρίσταται με εν σειρά συνδεδεμένα στοιχεία δοκού EBEs (ενότητα 2.2.2), τα οποία εγκιβωτίζονται εντός των στερεών στοιχείων της μήτρας. Το πλεονέκτημα της τεχνικής αυτής είναι ότι οδηγεί σε δομημένα πλέγματα πεπερασμένων στοιχείων, μειώνοντας έτσι τον υπολογιστικό φόρτο κατά την επίλυση των μικρομοντέλων. Η ολίσθηση των CNTs εντός της μήτρας λαμβάνεται υπόψιν από την υπολογιστική διαδικασία μέσω της ενσωμάτωσης κατάλληλου μοντέλου τριβής στον κώδικα πεπερασμένων στοιχείων. Συγκεκριμένα, οι εξισώσεις του μοντέλου μπορούν να αναπτυχθούν για ένα αντιπροσωπευτικό στοιχείο όγκου που περιέχει έναν ευθύγραμμο νανοσωλήνα διακριτοποιημένο από τρεις ισοδύναμες δοκούς όπως φαίνεται στο σχήμα 11. Η εξίσωση ισορροπίας για το κεντρικό στοιχείο δοκού γράφεται ως εξής:

$$|\sigma_{Ri} - \sigma_{Li}|\, A_i = \tau_i \pi \left(D_i + t_i\right) l_i \tag{19}$$

όπου A_i είναι η επιφάνεια της διατομής της κοίλης δοκού η εξωτερική διάμετρος της οποιάς είναι $D_i + t_i$ και το μήκος της l_i. Οι κομβικές αξονικές τάσεις σ_{Ri} και σ_{Li} αντίστοιχα προκύπτουν ύστερα από μια διαδικασία εξομάλυνσης. Επιλύοντας την Εξ. (19) ως προς την διεπιφανειακή διατμητική τάση τ_i και συγκρίνοντας την τιμή αυτή με την κρίσιμη διεπιφανειακή διατμητική αντοχή ISS, το μοντέλο ολίσθησης αναπτύσσεται ως εξής:

$$\tau_i = \frac{A_i}{\pi(D_i + t_i)l_i}\,|\sigma_{Ri} - \sigma_{Li}| \begin{cases} < ISS, & \text{στερεά σύνδεση} \\ \geq ISS, & \text{ολίσθηση} \end{cases} \tag{20}$$

Εάν μία ισοδύναμη δοκό που αντιπροσωπεύει ένα τμήμα από το συνολικό μήκος του νανοσωλήνα είναι σε κατάσταση ολίσθησης, τότε ο διεπιφανειακός της δεσμός με την περιβάλλουσα μήτρα έχει σπάσει και συνεπώς η συγκεκριμένη δοκός δεν συνεισφέρει στην μετάδοση φορτίων από την μήτρα. Η κατάσταση ολίσθησης μιας δοκού προσομοιώνεται μειώνοντας την αξονική της στιβαρότητά σε μια ελάχιστη τιμή. Σημειώνεται ότι, η καμπτική και στρεπτική στιβαρότητα της δοκού δεν επηρεάζονται, με αποτέλεσμα η δοκός να παραλαμβάνει καμπτικά και στρεπτικά φορτία μέσω της μήτρας.

4.2 Μη γραμμική διαδικασία ομογενοποίησης

Για την πρόβλεψη της συμπεριφοράς του CN-RC RVE προτείνεται ένα ιξωδοπλαστικό καταστατικό μοντέλο που μπορεί να χρησιμοποιηθεί στην μάκρο κλίμακα, λαμβάνοντας συγχρόνως υπόψιν του φαινόμενα μικρότερης κλίμακας. Η μονοδιάστατη αναπαράσταση του ιξωδοπλαστικού αυτού μοντέλου δίνεται στο σχήμα 12. Συγκεκριμένα, το μοντέλο αποτελεί συνδυασμό του ιξωδοελαστικού μοντέλου των Maxwell-Wiechert, που χρησιμοποιείται για την προσομοίωση της ιξωδοελαστικής συμπεριφοράς της μήτρας του σύνθετου υλικού και του ανισοτροπικού πλαστικού μοντέλου του Hill, που χρησιμοποιείται για την προσομοίωση τόσο της ανισοτροπικής

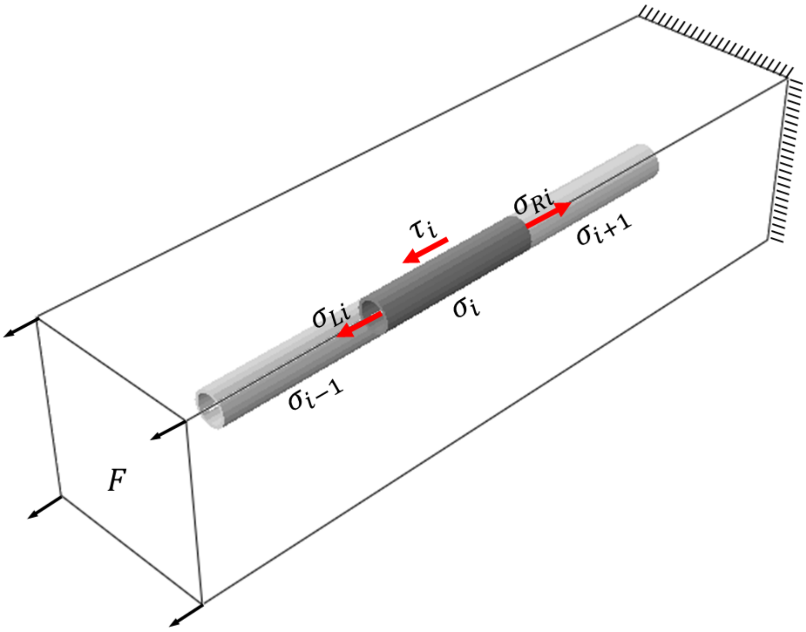

Σχημα 11: Εφελκυσμός RVE με ευθύγραμμο CNT, τάσεις στο κεντρικό ΕΒΕ

ενίσχυσης που προσφέρουν τα CNTs όσο και της αποσβενόμενης ενέργειας λόγω όλίσθησης αυτών μέσα στην μήτρα. Για την βαθμονόμηση του προτεινόμενου μοντέλου απαιτείται ο προσδιορισμός των ιξωδοελαστικών και πλαστικών παραμέτρων του. Όσον αφορά τα ιξωδοελαστικά χαρακτηριστικά του μοντέλου ο προσδιορισμός τους γίνεται μέσω της διαδικασίας που περιγράφηκε στην ενότητα 3.1 για την μήτρα, ενώ για τον προσδιορισμό των ενεργών πλαστικών παραμέτρων ακολουθείται μια μη γραμμική διαδικασία ομογενοποίησης. Οι πλαστικές παράμετροι που ζητούνται να καθοριστούν είναι η αρχική τάση διαρροής και τα κινηματικά χαρακτηριστικά κράτυνσης του υλικού. Τα χαρακτηριστικά αυτά σχετίζονται με την κρίσιμη διεπιφανειακή διατμητική τάση και την αποσβενόμενη ενέργεια λόγω ολίσθησης των νανοσωλήνων.

Η ομογενοποίηση που ακολουθείται θα πρέπει να ικανοποιεί την ενεργειακή συνθήκη του Hill η οποία ορίζεται από την εξίσωση:

$$\boldsymbol{\Sigma} : \boldsymbol{E} = \frac{1}{|V|} \int_{\Omega} \boldsymbol{\sigma} : \boldsymbol{\varepsilon} \, \mathrm{d}\boldsymbol{Y} \tag{21}$$

όπου $\boldsymbol{\Sigma}$, $\boldsymbol{E}$ είναι οι μακροσκοπικοί τανυστές τάσης και παραμόρφωσης αντίστοιχα

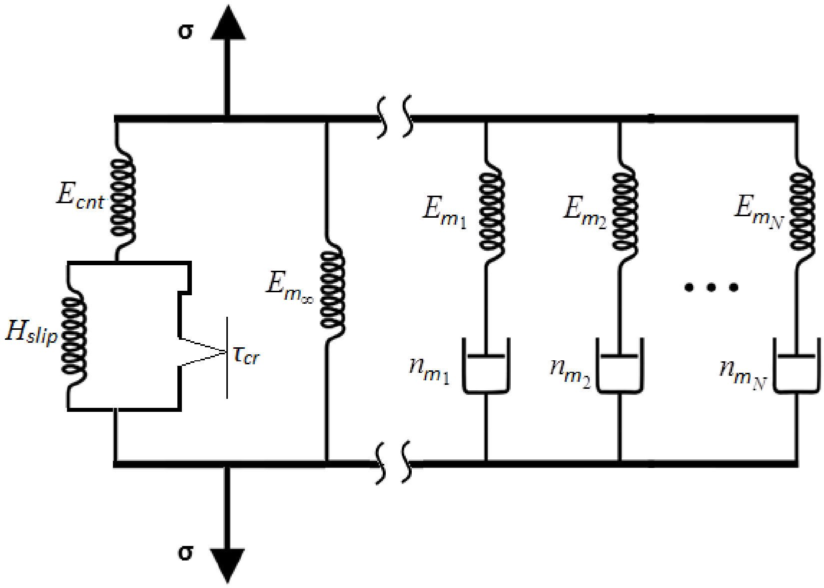

Σχήμα 12: Ιξωδοπλαστικό καταστατικό μοντέλο για το CNT-RC

ενώ $\boldsymbol{\sigma}$, $\boldsymbol{\varepsilon}$ είναι οι αντίστοιχοι τανυστές στην μίκρο κλίμακα. Οποιοδήποτε μακροσκοπικό μέγεθος $\boldsymbol{\Psi}$ μπορεί να εκφραστεί ως ένα ογκικό ολοκλήρωμα του αντίστοιχου μεγέθους στην μίκρο κλίμακα πάνω στον όγκο R του μοντέλου RVE ως εξής:

$$\boldsymbol{\Psi} = \langle \psi \rangle (\boldsymbol{X}) = \frac{1}{V} \int_R \psi(\boldsymbol{X}, \boldsymbol{Y}) \, \mathrm{d}\boldsymbol{Y} \quad \text{όπου} \quad V = \int_R \mathrm{d}\boldsymbol{Y} \tag{22}$$

$\boldsymbol{X}$ είναι το μακροσκοπικό διάνυσμα θέσης ενώ $\boldsymbol{Y}$ είναι το διάνυσμα θέσης που αντιστοιχεί στο αντιπροσωπευτικό στοιχείο όγκου στην μίκρο κλίμακα. Για την περίπτωση που το CNT-RC RVE περιέχει ευθύγραμμους νανοσωλήνες προσανατολισμένους προς μία κατεύθυνση ο μακροσκοπικός τανυστής τάσεων συνδέεται με τον τανυστή παραμορφώσεων μέσω ενός ορθοτροπικού ελαστικού μητρώου ως εξής:

$$\begin{bmatrix} \Sigma_{11} \\ \Sigma_{22} \\ \Sigma_{33} \\ \Sigma_{12} \\ \Sigma_{13} \\ \Sigma_{23} \end{bmatrix} = \begin{bmatrix} \mathbb{C}_{1111} & \mathbb{C}_{1122} & \mathbb{C}_{1133} & 0 & 0 & 0 \\ & \mathbb{C}_{2222} & \mathbb{C}_{2233} & 0 & 0 & 0 \\ & & \mathbb{C}_{3333} & 0 & 0 & 0 \\ & & & \mathbb{C}_{1212} & 0 & 0 \\ & sym. & & & \mathbb{C}_{1313} & 0 \\ & & & & & \mathbb{C}_{2323} \end{bmatrix} \begin{bmatrix} E_{11} \\ E_{22} \\ E_{33} \\ E_{12} \\ E_{13} \\ E_{23} \end{bmatrix} \tag{23}$$

Οι κύριοι άξονες κατεύθυνσης που ορίζονται πάνω στο CNT-RC RVE παριστάνονται στο σχήμα 13. Για τον προσδιορισμό των παραμέτρων του ομογενούς μητρώου $\mathbb{C}$ επιβάλλονται στο μικρομοντέλο τέσσερις ανεξάρτητες φορτίσεις υπό μορφή οριακών συνθηκών Dirichlet. Συγκεκριμένα προδιαγεγραμμένοι τανυστές παραμόρφωσης επιβάλλονται στο RVE με την μορφή μετατοπίσεων ως εξής:

$$\boldsymbol{u}_q = \mathbb{D}_{\boldsymbol{q}}\boldsymbol{E} \text{ για } \boldsymbol{E} = \left\{ \begin{bmatrix} E_{11} \\ 0 \\ 0 \\ 0 \\ 0 \\ 0 \end{bmatrix}, \begin{bmatrix} 0 \\ E_{22} \\ 0 \\ 0 \\ 0 \\ 0 \end{bmatrix}, \begin{bmatrix} 0 \\ 0 \\ E_{33} \\ 0 \\ 0 \\ 0 \end{bmatrix}, \begin{bmatrix} 0 \\ 0 \\ 0 \\ E_{12} \\ E_{13} \\ E_{23} \end{bmatrix} \right\} \tag{24}$$

όπου $\mathbb{D}_{\boldsymbol{q}}$ είναι ένα γεωμετρικό μητρώο που περιέχει τις συντεταγμένες των συνοριακών κόμβων q του μικρομοντέλου. Από την επίλυση της μικροδομής ο μακροσκοπικός τανυστής τάσης υπολογίζεται για κάθε περίπτωση φόρτισης ως εξής:

$$\boldsymbol{\Sigma} = \frac{1}{|V|}\sum_{q=1}^{n_q} \mathbb{D}_{\boldsymbol{q}}\boldsymbol{f}_{\boldsymbol{q}} \tag{25}$$

όπου $\boldsymbol{f}_{\boldsymbol{q}}$ είναι οι δυνάμεις αντίδρασεις που υπολογίζονται στους συνοριακούς κόμβους q του μοντέλου του RVE, n_q ο συνολικός αριθμός των συνοριακών κόμβων και V ο όγκος του RVE. Επιβάλλοντας για παράδειγμα τον πρώτο μακροσκοπικό τανυστή παραμόρφωσης στο μικρομοντέλο μπορούν να υπολογιστούν οι όροι $\mathbb{C}_{1111} = \Sigma_{11}/E_{11}$, $\mathbb{C}_{2211} = \Sigma_{22}/E_{11}$ και $\mathbb{C}_{3311} = \Sigma_{33}/E_{11}$. Επομένως, με την επιβολή και των υπολοίπων ανεξάρτητων φορτίσεων καθορίζεται πλήρως το ελαστικό καταστατικό μητρώο $\mathbb{C}$ του μακρομοντέλου. Όταν η διεπιφανειακή διατμητική τάση που αναπτύσσεται στην διεπιφάνεια νανοσωλήνων/μήτρας ξεπεράσει την κρίσιμη διεπιφανειακή διατμητική αντοχή τότε ξεκινά η ολίσθηση των νανοσωλήνων. Το φαινόμενο αυτό λαμβάνεται υπόψιν από το μακρομοντέλο μέσω των πλαστικών παραμέτρων οι οποίες θα πρέπει να προσδιοριστούν. Για την περίπτωση αξονικού εφελκυσμού στο RVE του σχήματος 13, η αρχική ισοδύναμη τάση διαρροής υπολογίζεται από την επίλυση του μικρομοντέλου την στιγμή ακριβώς που συμβαίνει η αρχική ολίσθηση του νανοσωλήνα:

$$\overline{\Sigma}_y = \sqrt{\frac{3}{2}\Sigma_{ij}^d \Sigma_{ij}^d} \tag{26}$$

όπου Σ_{ij}^d είναι οι αποκλίνουσες τάσεις του μακροσκοπικού τανυστή τάσεων $\boldsymbol{\Sigma}$. Για τον προσδιορισμό της καμπύλης κινηματικής κράτυνσης του υλικού σε κάθε προσαυξητικό βήμα επίλυσης του μικρομοντέλου υπολογίζεται το ζεύγος ισοδύναμης τάσης διαρροής και ισοδύναμης πλαστικής παραμόρφωσης, $\left(\overline{\Sigma}, \overline{E}^p\right)$.

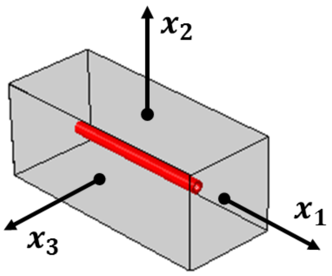

Σχήμα 13: Σύστημα κύριων κατευθύνσεων στο RVE του CNT-RC

4.3 Αριθμητικά αποτελέσματα

Η αποτελεσματικότητα του προτεινόμενου ιξωδοπλαστικού καταστατικού μοντέλου επιβεβαιώνεται μέσω της σύγκρισης των καμπυλών τάσης-παραμόρφωσης που προκύπτουν από την προσομοίωση ανακυκλιζόμενης φόρτισης στο μακροσκοπικό και στο μικροσκοπικό μοντέλο του σύνθετου υλικού αντίστοιχα. Συγκεκριμένα, αναλύονται με την μέθοδο των πεπερασμένων στοιχείων RVEs από CNT-RC με περιεκτικότητα κατά βάρος σε CNTs (wf) 0.5, 1 και 2% και με διεπιφανειακή διατμητική αντοχή (ISS) 40, 80 και 160 MPa. Στα μικροσκοπικά αυτά μοντέλα εφαρμόζεται ο μακροσκοπικός τανυστής παραμόρφωσης $\boldsymbol{E} = [E_{11} \;\; 0 \;\; 0 \;\; 0 \;\; 0 \;\; 0]^T$ όπου $E_{11} = E_0 \sin(2\pi\nu t)$. Στο σχήμα 14 φαίνεται η γεωμετρία και η διακριτοποίηση με τα πεπερασμένα στοιχεία του μικρομοντέλου των RVEs. Από την ανάλυση και με βάση την διαδικασία ομογενοποίησης που περιγράφηκε στην ενότητα 4.2 προσδιορίζονται οι ενεργές παράμετροι του ιξωδοπλαστικού μακροσκοπικού μοντέλου. Στην συνέχεια το μακροσκοπικό μοντέλο υποβάλλεται στην ίδια μορφή φόρτισης όπως και το μικρομοντέλο. Μετά την ανάλυση του εξάγονται τα αριθμητικά αποτελέσματα, που συγκρίνονται με εκείνα που προέκυψαν προηγουμένως από την ανάλυση του μικροσκοπικού μοντέλου. Στα σχήματα 15-17 παρουσιάζονται οι καμπύλες τάσης-παραμόρφωσης για κάθε περίπτωση wf και ISS. Σημειώνεται ότι, τα αποτελέσματα αυτά αφορούν ανακυκλιζόμενη φόρτιση σε πολύ υψηλή συχνότητα ($\nu \to \infty$), όπου η θερμοπλαστική μήτρα (PEEK) συμπεριφέρεται ελαστικά με βάση το στιγμιαίο μέτρο ελαστικότητας. Στο σχήμα 18 παρουσιάζονται τα ίδια αποτελέσματα όπως στο σχήμα 17 μόνο που τώρα η συχνότητα φόρτισης είναι ν=1 Hz και συνεπώς η μήτρα συμπεριφέρεται ιξωδοελαστικά.

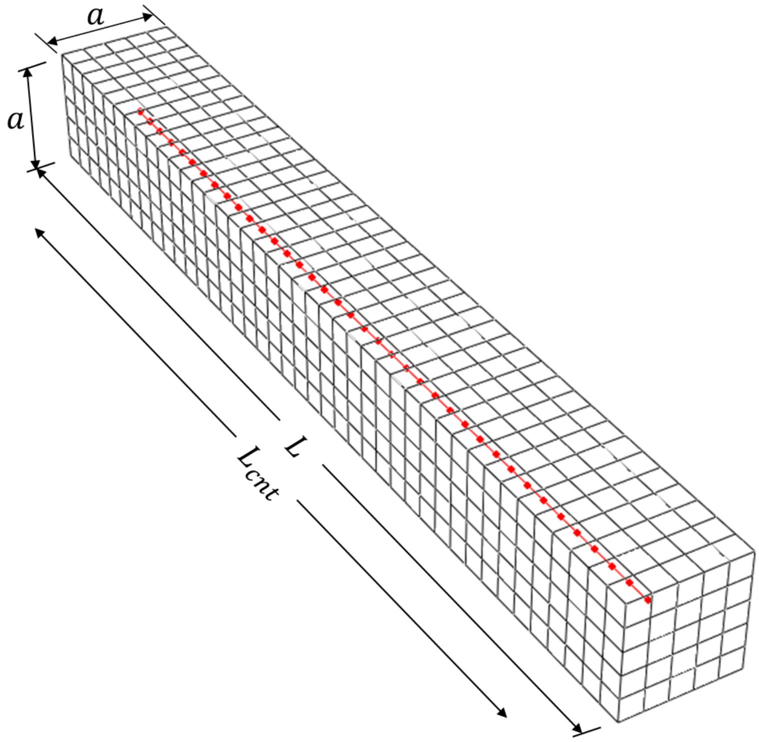

Σχήμα 14: Γεωμετρία και διακριτοποίηση με πεπερασμένα στοιχεία του CNT-RC RVE

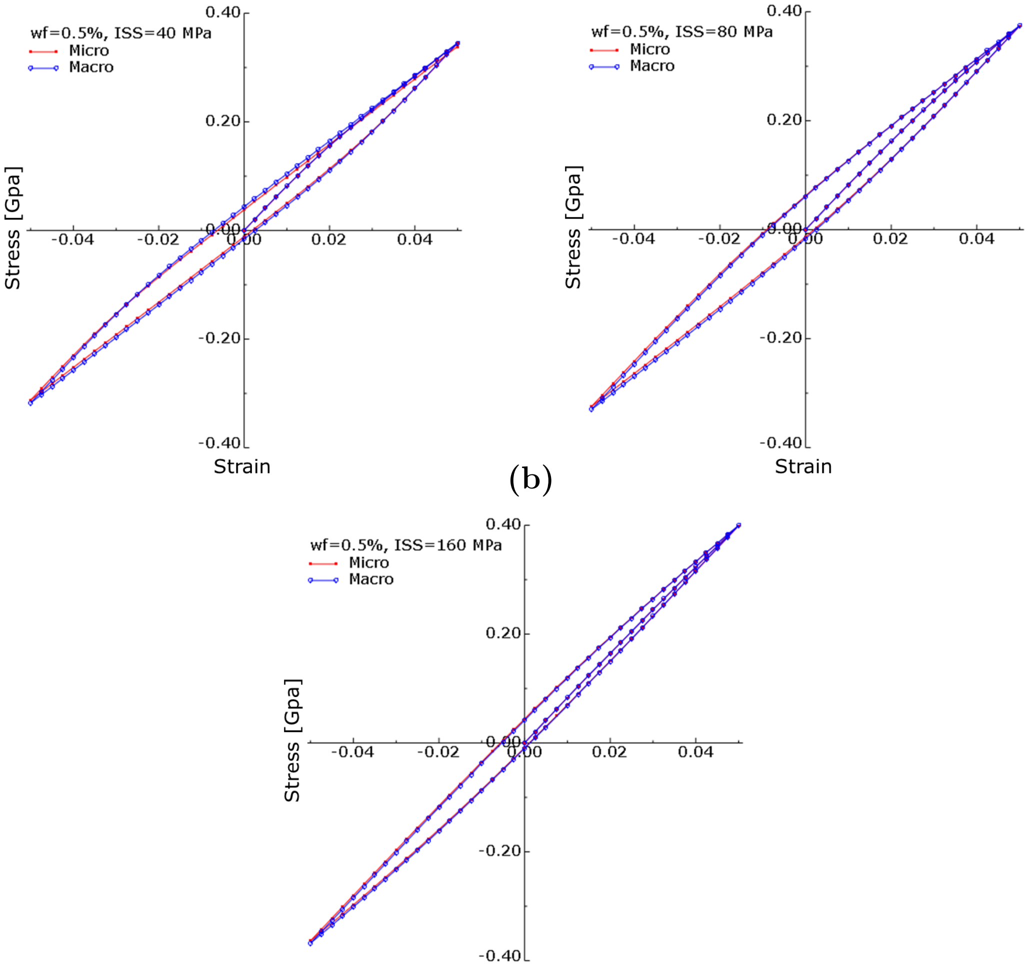

(a) **(b)** **(c)**

Σχήμα 15: Σύγκριση καμπυλών τάσης-παραμόρφωσης σε ανακύκλιση με συχνότητα $\nu \rightarrow \infty$ μεταξύ μικροσκοπικού και μακροσκοπικού μοντέλου για wf=0.5% και (a) ISS=40 MPa, (b) ISS=80 MPa, (c) ISS=160 MPa.

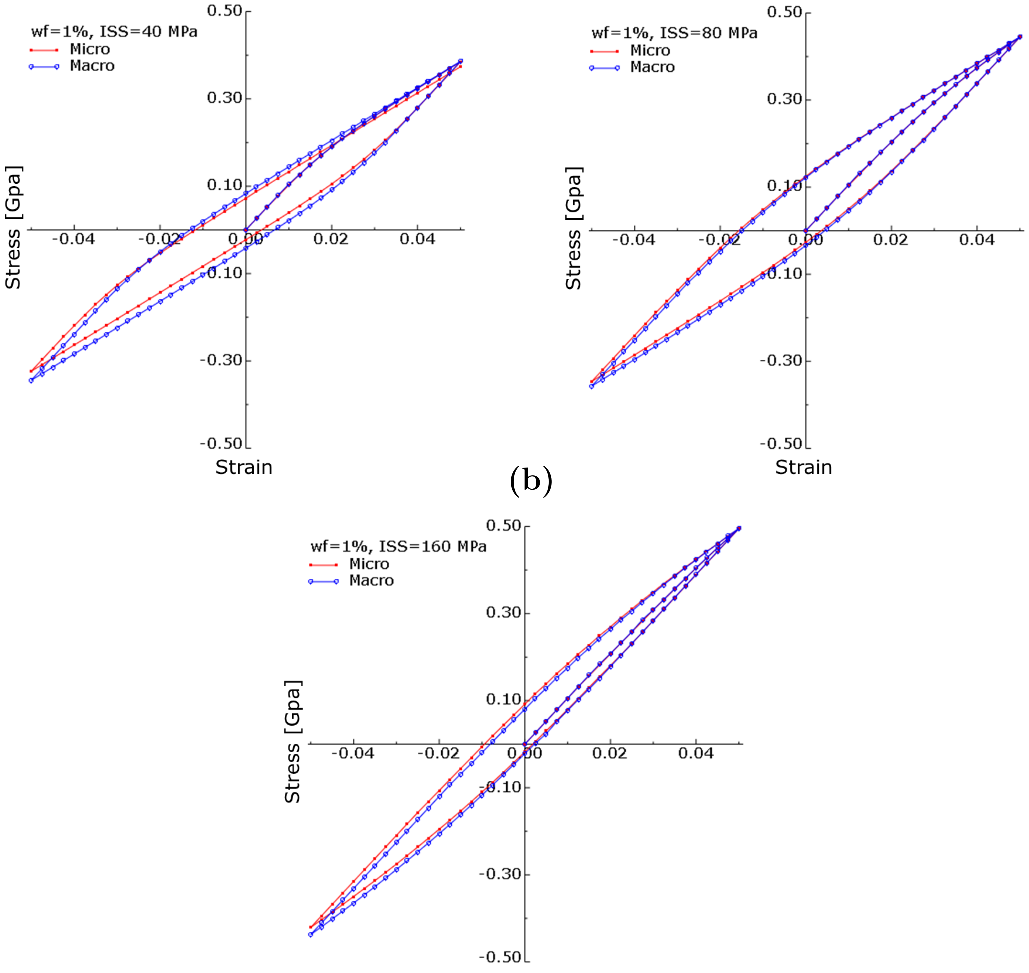

(a) **(b)** **(c)**

Σχήμα 16: Σύγκριση καμπυλών τάσης-παραμόρφωσης σε ανακύκλιση με συχνότητα $\nu \rightarrow \infty$ μεταξύ μικροσκοπικού και μακροσκοπικού μοντέλου για wf=1% και (a) ISS=40 MPa, (b) ISS=80 MPa, (c) ISS=160 MPa.

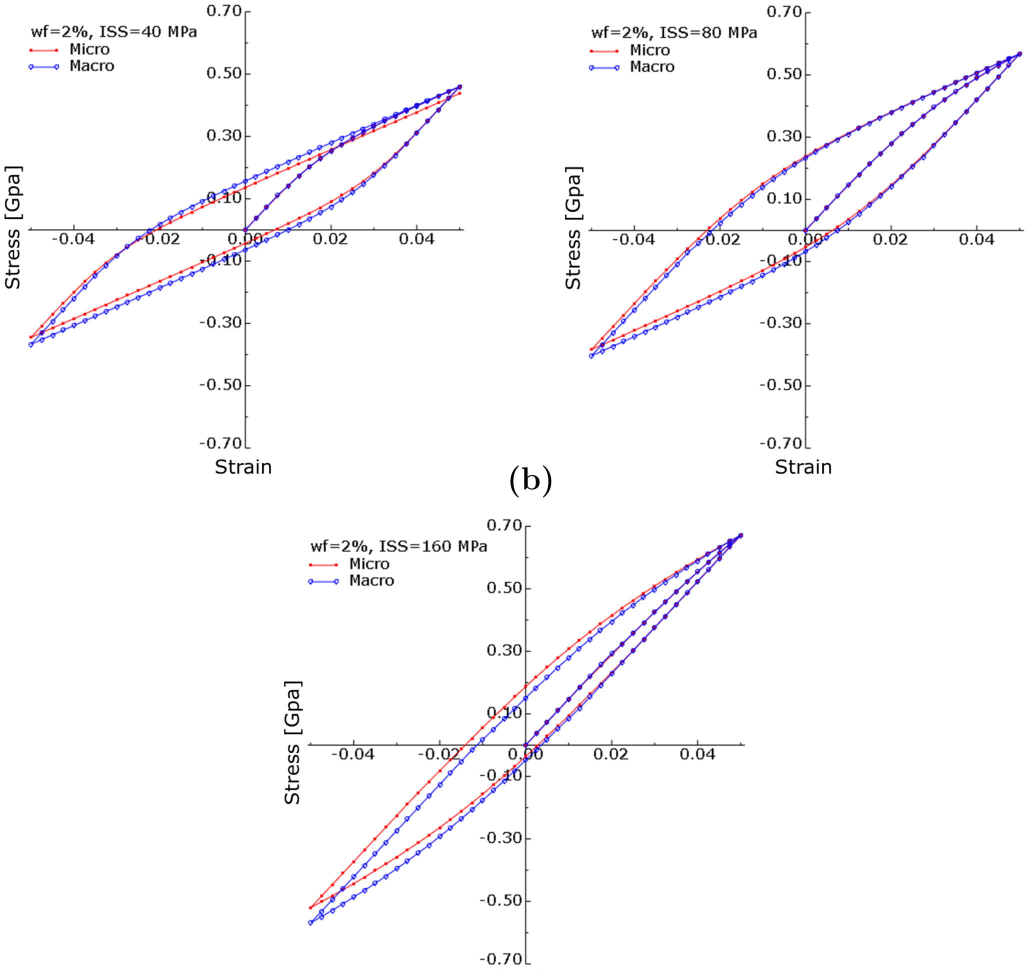

(a) **(b)** **(c)**

Σχήμα 17: Σύγκριση καμπυλών τάσης-παραμόρφωσης σε ανακύκλιση με συχνότητα $\nu \rightarrow \infty$ μεταξύ μικροσκοπικού και μακροσκοπικού μοντέλου για wf=2% και (a) ISS=40 MPa, (b) ISS=80 MPa, (c) ISS=160 MPa.

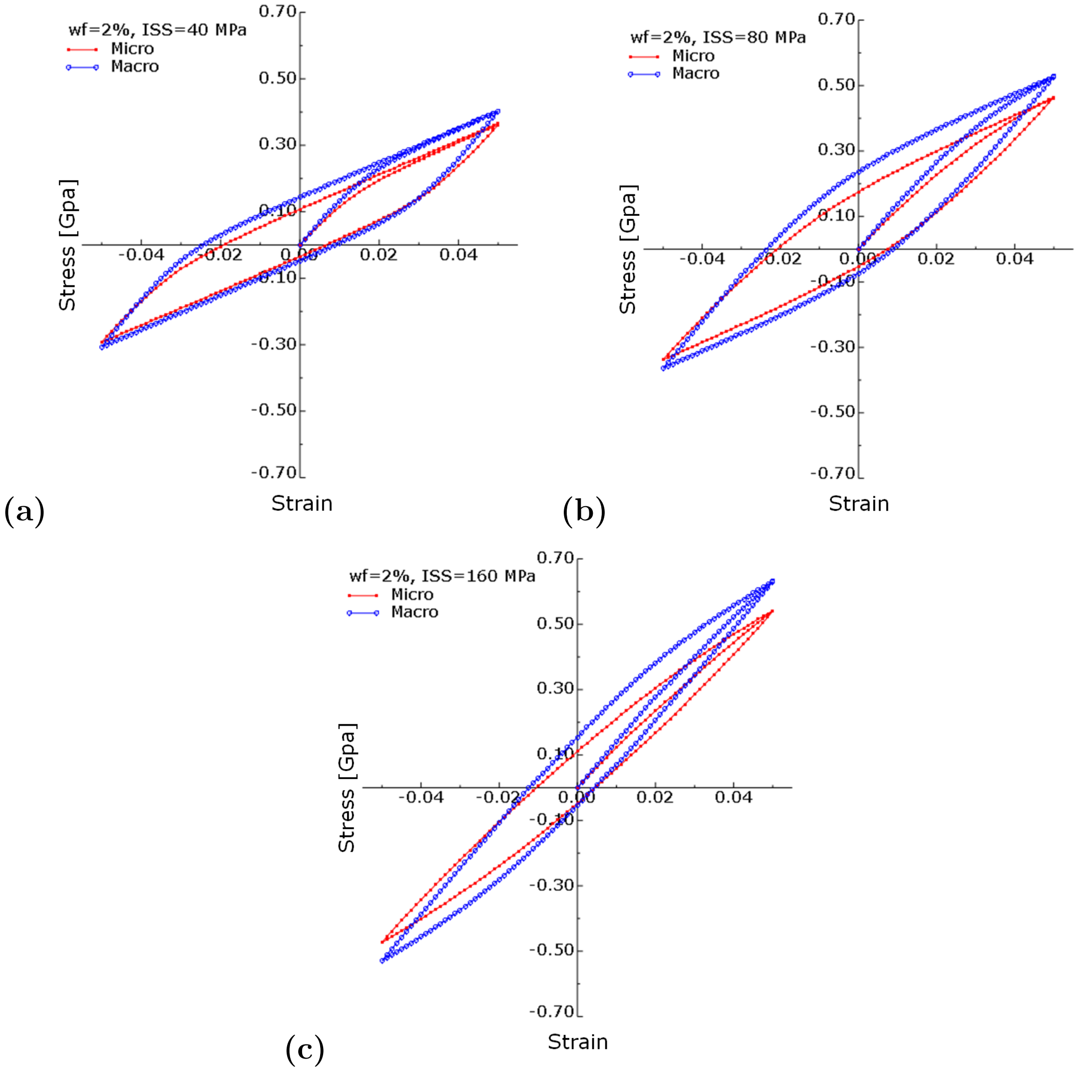

Σχήμα 18: Σύγκριση καμπυλών τάσης -παραμόρφωσης σε ανακύκλιση με συχνότητα ν=1 Hz μεταξύ μικροσκοπικού και μακροσκοπικού μοντέλου για wf=2% και (a) ISS=40 MPa, (b) ISS=80 MPa, (c) ISS=160 MPa.

5. Σύνθετα υλικά ενισχυμένα με νανοσωματίδια γραφενίου

Τα νανοσωματίδια γραφενίου (GnPs) αποτελούνται από φύλλα γραφενίου διατεταγμένα τό ένα πάνω από το άλλο, συνδεδεμένα μεταξύ τους με δεσμούς van der Waals. Το πάχος των σωματιδίων αυτών κυμαίνεται μεταξύ 1-15 nm ενώ το πλάτος τους κυμαίνεται μεταξύ 1-100 μm. Συνεπώς, μπορούν να θεωρηθούν ως δισδιάστατα σωματίδια η γεωμετρία των οποίων φαίνεται στις εικόνες ηλεκτρονικού μικροσκοπίου σάρωσης του σχήματος 19.

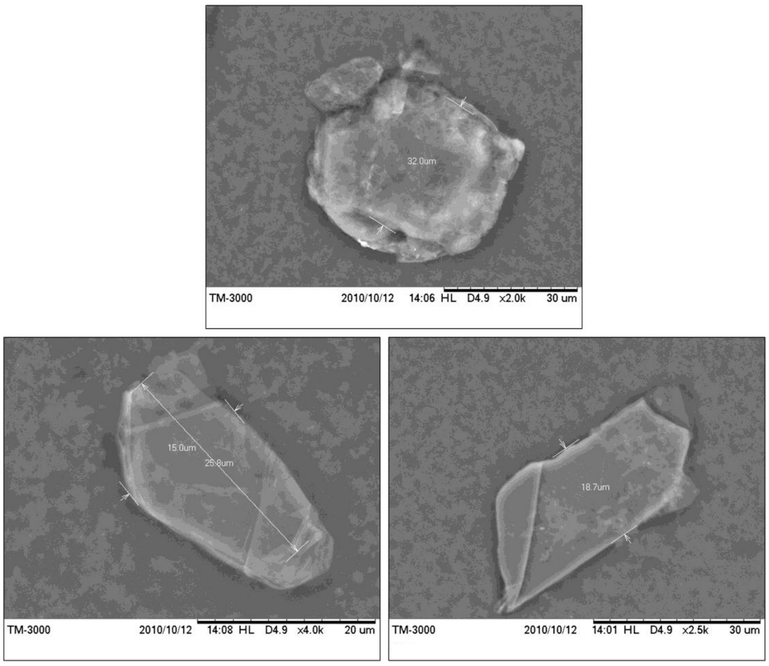

Σχήμα 19: Εικόνες GnPs από ηλεκτρονικό μικροσκόπιο σάρωσης.

Όπως οι νανοσωλήνες άνθρακα έτσι και τα νανοσωματίδια γραφενίου επιδεικνύουν εξαιρετικές μηχανικές και φυσικές ιδιότητες. Συγκεκριμένα, τα GnPs έχουν αξονικό μέτρο ελαστικότητας περίπου 1 TPa, ενώ η εφελκυστική αντοχή τους είναι της τάξης των 10-20 GPa. Η γεωμετρία των GnPs λόγω της ύπαρξης ελεύθερων ατόμων άνθρακα στα άκρα του μοριακού πλέγματος των φύλλων γραφενίου, ευνοεί την δημιουργία χημικών δεσμών με τις μοριακές αλυσίδες του πολυμερούς. Συνεπώς, η τεχνική ενεργοποίησης (functionalization) των ατόμων άνθρακα, που εφαρμόζεται στην επιφάνεια του μοριακού πλέγματος των CNTs, δεν είναι απαραίτητη στην περίπτωση των GnPs. Το πλεονέκτημα αυτό σε συνδυασμό με το μεγάλο λόγο επιφάνειας προς όγκο, καθιστούν τα GnPs ισχυρούς ανταγωνιστές έναντι των CNTs για την ενίσχυση πολυμερών και την δημιουργία προηγμένων νανοσύνθετων υλικών.

Στην παρούσα εργασία αναπτύσσεται μια πρωτότυπη υπολογιστική διαδικασία ομογενοποίησης της μηχανικής συμπεριφοράς RVEs από GnP-RC που λαμβάνει υπόψιν της την τυχαία γεωμετρία των νανοσωματιδίων. Η διαδικασία βασίζεται στην επίλυση των μικρομοντέλων με χρήση της μεθόδου των εξελιγμένων πεπερασμένων στοιχείων (XFEM), σε συνδυασμό με την στοχαστική τους ανάλυση με χρήση προσομοιώσεων Monte Carlo. Η εργασία τονίζει ιδιαίτερα την επίδραση του σχήματος των GnPs στις ενεργές ελαστικές παραμέτρους του σύνθετου υλικού. Το τυχαίο σχήμα των GnPs προσομοιώνεται στα πλαίσια της XFEM με χρήση μιας αναλυτικά ορισμένης συνάρτησης level-set, η οποία περιγράφει το σχήμα ενός «τραχύ» κύκλου (rough circle). Στο πλαίσιο της μεθόδου Monte Carlo προσομοιώνεται ένας μεγάλος αριθμός από RVEs με συγκεκριμένη κατ΄ όγκο περιεκτικότητα τυχαία κατανεμημένών GnPs. Η διαδικασία ομογενοποίησης που ακολουθείται ικανοποιεί την ενεργειακή συνθήκη του Hill.

5.1 Μέθοδος εξελιγμένων πεπερασμένων στοιχείων

Η μέθοδος των εξελιγμένων πεπερασμένων στοιχείων χρησιμοποιείται για την ανάλυση φορέων που περιέχουν ισχυρές ή ασθενείς ασυνέχειες. Για παράδειγμα φορείς με ρωγμές παρουσιάζουν ασυνέχεια στο πεδίο των μετατοπίσεων ενώ φορείς από ετερογενή υλικά παρουσιάζουν ασυνέχεια στο πεδίο τάσεων-παραμορφώσεων. Τα GnP-RC υλικά που εξετάζουμε στην παρούσα εργασία ανήκουν στην κατηγορία των ετερογενών υλικών με ασυνεχή πρώτη παράγωγο των μετατοπίσεων. Το πεδίο συνεπώς των μετατοπίσεων που προβλέπουν τα εξελιγμένα πεπερασμένα στοιχεία περιλαμβάνει κάποιους επιπλέον όρους ικανούς να περιγράψουν την ασυνέχεια αυτήν εξ΄ αιτίας της παρουσίας των GnPs εντός της πολυμερικής μήτρας. Συγκεκριμένα, το πεδίο των μετατοπίσεων δίνεται από την εξίσωση:

$$u^h(\mathbf{x}) = \sum_{i \in I} N_i(\mathbf{x})\, u_i + \sum_{j \in J} N_j(\mathbf{x}) \left(\sum_{k=1}^{n_0} \psi_k(\mathbf{x})\, \alpha_{jk} \right) \tag{27}$$

όπου I είναι το σύνολο των κόμβων του μοντέλου πεπερασμένων στοιχείων που κατέχουν τους κλασικούς βαθμούς ελευθερίας u, ενώ J είναι το σύνολο των κόμβων που εμπλουτίζονται με τους επιπλέον πλασματικούς βαθμούς ελευθερίας α, μέσω των οποίων περιγράφεται η ασυνέχεια υλικού. Οι πλασματικοί αυτοί βαθμοί ελευθερίας προστίθενται στην εξίσωση των μετατοπίσεων ως όροι γινομένων μεταξύ των συναρτήσεων σχήματος κάθε κόμβου N και της συνάρτησης ψ_k που περιγράφει το σχήμα του k^{th} νανοσωματιδίου. Το σχήμα κάθε νανοσωματιδίου περιγράφεται μέσω των τιμών της συνάρτησης level-set ϕ πάνω στους κόμβους του πλέγματος των πεπερασμένων στοιχείων και της παρεμβολής αυτής σε κάθε σημείο $\mathbf{x}$ μέσω της εξίσωσης:

$$\psi_k\left(\mathbf{x}\right) = \sum_{i \in I} N_i\left(\mathbf{x}\right)\left|\phi_i^k\right| - \left|\sum_{i \in I} N_i\left(\mathbf{x}\right)\phi_i^k\right| \tag{28}$$

όπου ϕ η συνάρτηση του «rough circle»:

$$\phi\left(\mathbf{x}, \theta\right) = \left\|\mathbf{x} - \mathbf{c}\right\| - R\left(\alpha\left(\mathbf{x}\right), \theta\right) \tag{29}$$

και R η τυχαία ακτίνα του κύκλου που αντιστοιχεί σε κάθε θέση $\mathbf{x}$ πάνω στην συνοριακή καμπύλη Γ_{incl} (σχήμα 20)

$$\begin{aligned} R\left(\alpha, \theta\right) = 0.2 + 0.03Y_1(\theta) + 0.015\{Y_2(\theta)cos(k_1\alpha) + \\ Y_3(\theta)sin(k_1\alpha) + Y_4(\theta)cos(k_2\alpha) + Y_5(\theta)sin(k_2\alpha)\} \end{aligned} \tag{30}$$

οι ανεξάρτητες τυχαίες μεταβλητές $Y_i(\theta)$ ακολουθούν την ίδια ομοιόμορφη κατανομή στο $U\left(-\sqrt{3}, \sqrt{3}\right)$. Στο σχήμα 21 εικονίζονται οι ισοϋψείς καμπύλες που προκύπτουν από την εξίσωση (29) για τιμές $k_1 = 0$ και $k_2 = 3$ στην εξίσωση (30). Η συνοριακή καμπύλη Γ_{incl} που δίνει το τυχαίο σχήμα του νανοσωματιδίου προκύπτει από την ισοϋψής με τιμή μηδέν.

5.2 Κατασκευή RVEs τυχαίας μικροδομής

Για την γέννηση της τυχαίας μικροδομής των GnP-RC RVEs χρησιμοποιείται ο αλγόριθμος που περιγράφεται στόν πίνακα 1. Κάθε RVE έχει διαστάσεις $X_1 \times X_2$ και

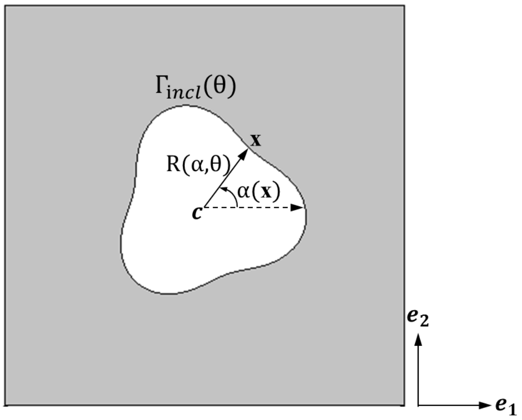

Σχήμα 20: Σχηματική αναπαράσταση της συνάρτησης του «rough circle»

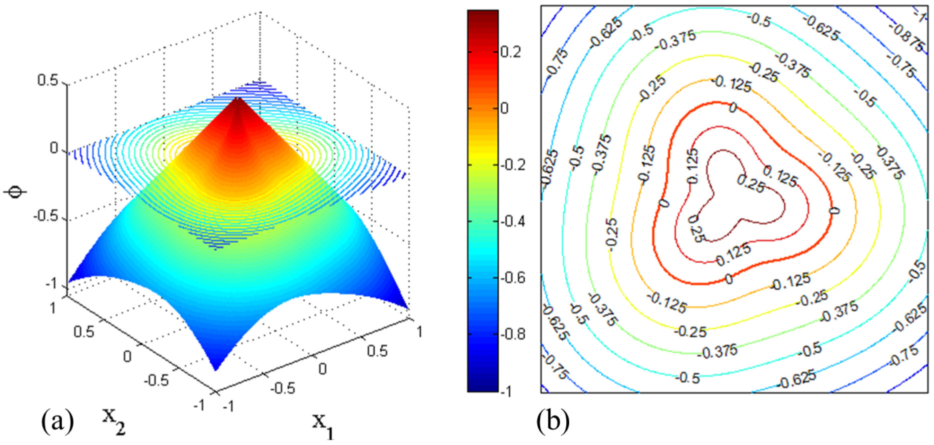

Σχήμα 21: a) Προσημασμένη συνάρτηση level set και b) ισοϋψείς καμπύλες για $k_1 = 0$, $k_2 = 3$

περιέχει n_{incl} αριθμό νανοσωματιδίων σε συγκεκριμένη κατ΄ όγκο αναλογία (%vf). Το τυχαίο σχήμα των νανοσωματιδίων προκύπτει από την εφαρμογή των εξισώσεων (29)-(30) όπου οι παράμετροι k_1 και k_2 είναι σταθερές, ενώ οι στοχαστικές μεταβλητές $Y_i(\theta)$ επιλέγονται με χρήση της ομοιόμορφης συνάρτησης πυκνότητας πιθανότητας f_{Y_i}. Στο σχήμα 22 εικονίζονται τα διαφορετικά σχήματα των GnP νανοσωματιδίων που μελετόνται στην παρούσα εργασία. Η συνοριακή καμπύλη Γ_{incl} που περιγράφει το τυχαίο σχήμα των νανοσωματιδίων διακριτοποιείται από n_p σημεία, η θέση των οποίων καθορίζεται από το παρακάτω διάνυσμα συντεταγμένων:

$$\Gamma_{incl}(\theta) : \{\mathbf{x} = \mathbf{c} + R\left(\alpha,\theta\right)\left(cos\alpha \cdot \mathbf{e_1} + sin\alpha \cdot \mathbf{e_2}\right)\} \tag{31}$$

$\mathbf{e_1}$, $\mathbf{e_2}$ είναι τα μοναδιαία καρτεσιανά διανύσματα. Η θέση του κέντρου κάθε σωματιδίου καθώς και ο προσανατολισμός τους προκύπτουν από τις συναρτήσεις πυκνότητας πιθανότητας f_c και f_β αντίστοιχα. Μετά την δημιουργία n_{incl} πλήθους νανοσωματιδίων και πριν αυτά κατανεμηθούν μέσα στην μήτρα, θα πρέπει να γίνει κατάλληλη προσαρμογή του μεγέθους τους (scalling), ώστε να προκύπτει πάντα η επιθυμητή τιμή της κατ΄ όγκο αναλογίας τους στο RVE. Για την μείωση της πιθανότητας κατά την κατανομή τους τα νανοσωματίδια να πέσουν το ένα πάνω στο άλλο, γίνεται πρώτα η ταξινόμησή τους κατά φθίνουσα σειρά μεγέθους και στην συνέχεια επιχειρείται η τοποθέτησή τους μέσα στην μήτρα. Ο έλεγχος για επικάλυψη διεξάγεται με χρήση ενός αλγορίθμου δοκιμής-λάθους, έτσι ώστε κάθε σωματίδιο που βρεθεί να επικαλύπτει τα ήδη υπάρχοντα να επανατοποθετείται συνεχώς μέχρι να βρεθεί η κατάλληλη θέση του στην μήτρα. Στο σχήμα 23 φαίνεται η τοποθέτηση $n_{incl} = 1, 5, 10, 20$ νανοσωματιδίων μέσα σε RVEs με 30% vf.

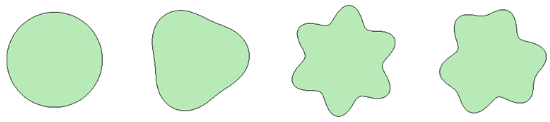
(a) (b) (c) (d)

Σχήμα 22: Σχήμα GnP νανοσωματιδίων για a) ($k_1 = 0$, $k_2 = 0$), b) ($k_1 = 0$, $k_2 = 3$), c) ($k_1 = 0$, $k_2 = 6$) και d) ($k_1 = 3$, $k_2 = 6$)

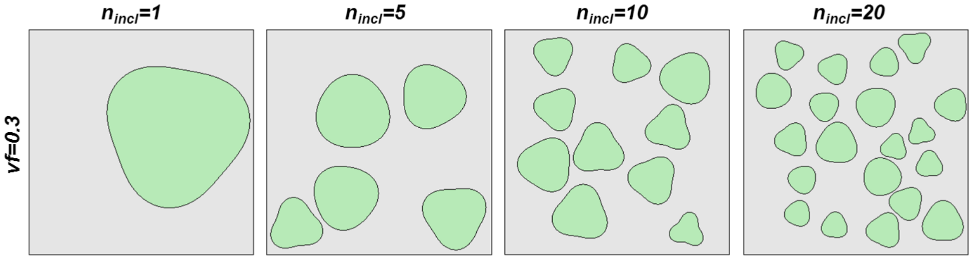

Σχήμα 23: Τοποθέτηση νανοσωματιδίων ($k_1 = 0$, $k_2 = 3$) σε RVEs με vf=30%

Πίνακας 1: Αλγόριθμος γέννησης της τυχαίας μικροδομής των GnP-RC RVEs

- ΔΕΔΟΜΕΝΑ
    - X_1, X_2: Μέγεθος του RVE
    - vf: Περιεκτικότητα κατ΄ όγκο σε νανοσωματίδια
    - n_{incl}: Συνολικός αριθμός νανοσωματιδίων στο RVE
    - f_{Y_i}: Συνάρτηση πυκνότητας πιθανότητας που ακολουθούν οι τυχαίες μεταβλητές $Y_i(\theta)$
    - f_c, f_β: Συναρτήσεις πυκνότητας πιθανότητας που ακολουθεί η θέση του κέντρου και η γωνία προσανατολισμού του νανοσωματιδίου
    - k_1, k_2: Σταθερές παράμετροι που καθορίζουν την διακύμανση της συνοριακής καμπύλης του «rough circle»
- ΔΗΜΙΟΥΡΓΙΑ / ΠΡΟΣΑΡΜΟΓΗ ΜΕΓΕΘΟΥΣ / ΤΑΞΙΝΟΜΗΣΗ ΝΑΝΟΣΩΜΑΤΙΔΙΩΝ
    - Δημιουργία n_{incl} πλήθους τυχαίων σωματιδίων
    - Αριθμητικός υπολογισμός με τον κανόνα του τραπεζίου της συνολικής επιφάνειας των παραγόμενων σωματιδίων
      $$\hat{A}_{incl} = \sum_{k=1}^{n_{incl}} \left\{ \sum_{n=1}^{n_p} \left[\left(x_{1,n+1}^k - x_{1,n}^k\right) \cdot \left(\frac{x_{2,n}^k + x_{2,n+1}^k}{2} \right) \right] \right\}$$
      $n = 1, ..., n_p$: αριθμός σημείων διακριτοποίησης της συνοριακής καμπύλης του «rough circle», $\left(x_{1,n}^k, x_{2,n}^k\right) \in \Gamma_{incl}^k(\theta)$
    - Προσαρμογή του μεγέθους της ακτίνας του «rough circle»: $R_n = \hat{R}_n \sqrt{\mathrm{vf} \frac{X_1 X_2}{\hat{A}_{incl}}}$
    - Ταξινόμηση των νανοσωματιδίων σε φθίνουσα σειρά ανάλογα με το μέγεθος της επιφάνειάς τους
- ΧΩΡΙΚΗ ΚΑΤΑΝΟΜΗ ΝΑΝΟΣΩΜΑΤΙΔΙΩΝ ΣΤΟ RVE
    - Βρόγχος επανάληψης από $k = 1$ μέχρι n_{incl}
        - Εξαγωγή τυχαίων μεταβλητών θέσης $\left(x_1^k, x_2^k\right)$ και γωνίας προσανατολισμού β^k που ακολουθούν ομοιόμορφη κατανομή στο διάστημα $[0, X_1]$, $[0, X_2]$ και $[0, 2\pi]$ αντίστοιχα
        - Έλεγχος επικάλυψης του k^{th} σωματιδίου με τα ήδη τοποθετημένα $k-1$ σωματίδια
            - Εάν ΑΛΗΘΗΣ, επανατοποθέτηση του k^{th} σωματίδιο επιλέγοντας νέες μεταβλητές θέσης και γωνίας προσανατολισμού
            - Εάν ΨΕΥΔΗΣ, επιτυχής τοποθέτηση

5.3 Ομογενοποίηση

Η διαδικασία της ομογενοποίησης βασίζεται στο ενεργειακό θεώρημα του Hill. Το θεώρημα αυτό αξιώνει ότι η ενέργεια παραμόρφωσης του ομογενούς μακροσκοπικού μοντέλου είναι ίση κατά μέσο όρο με την αντίστοιχη ενέργεια που προκύπτει από την παραμόρφωση της μικροδομής. Η ενεργειακή αυτή σχέση εκφράζεται ως εξής:

$$\boldsymbol{\Sigma} : \boldsymbol{E} = \frac{1}{|V|} \int_{\Omega} \boldsymbol{\sigma} : \boldsymbol{\varepsilon} \, \mathrm{d}\boldsymbol{Y} \tag{32}$$

όπου $\boldsymbol{\Sigma}$, $\boldsymbol{E}$ οι μακροσκοπικοί τανυστές τάσης και παραμόρφωσης ενώ $\boldsymbol{\sigma}$, $\boldsymbol{\varepsilon}$ οι αντίστοιχοι τανυστές στην θέση $\boldsymbol{Y}$ της μικροδομής. Οι μακροσκοπικές ποσότητες υπολογίζονται ως το ολοκλήρωμα της αντίστοιχης μικροσκοπικής ποσότητας πάνω στον όγκο Ω της μικροδομής. Η διαδικασία της ομογενοποίησης που εφαρμόστηκε στην ενότητα 4.2 για τα CNT-RC RVEs εφαρμόζεται με παρόμοιο τρόπο και για τα GnP-RC RVEs. Συγκεκριμένα, ένας γνωστός μακροσκοπικός τανυστής παραμόρφωσης επιβάλλεται ως συνοριακές συνθήκες Dirichlet στο μικρομοντέλο του RVE το οποίο διακριτοποιείται με τα εξελιγμένα πεπερασμένα στοιχεία. Από την επίλυσή του XFEM προβλήματος προκύπτουν οι δυνάμεις αντίδρασεις στους συνοριακούς κόμβους του μοντέλου, μέσω των οποίων υπολογίζεται υπό μορφή μέσου όρου ο μακροσκοπικός τανυστής τάσης που αντιστοιχεί στην δεδομένη παραμόρφωση. Θεωρώντας ότι το τελικό σύνθετο υλικό έχει ισοτροπική ελαστική συμπεριφορά η σχέση τάσεων-παραμορφώσεων μπορεί να εκφραστεί ως εξής:

$$\begin{bmatrix} \Sigma_{11} \\ \Sigma_{22} \\ \Sigma_{12} \end{bmatrix} = \begin{bmatrix} C_{eff} & D_{eff} & 0 \\ D_{eff} & C_{eff} & 0 \\ 0 & 0 & G_{eff} \end{bmatrix} \begin{bmatrix} E_{11} \\ E_{22} \\ E_{12} \end{bmatrix} \tag{33}$$

$$\text{όπου } C_{eff} = \begin{cases} \dfrac{E_{eff}}{1-\nu_{eff}^2} & \text{επίπεδη ένταση} \\ \dfrac{(1-\nu_{eff})\,E_{eff}}{(1+\nu_{eff})\,(1-2\nu_{eff})} & \text{επίπεδη παραμόρφωση} \end{cases}, \tag{34}$$

$$D_{eff} = \begin{cases} \dfrac{\nu_{eff}E_{eff}}{1-\nu_{eff}^2} & \text{επίπεδη ένταση} \\ \dfrac{\nu_{eff}E_{eff}}{(1+\nu_{eff})\,(1-2\nu_{eff})} & \text{επίπεδη παραμόρφωση} \end{cases}, \tag{35}$$

$$\text{και } G_{eff} = \frac{E_{eff}}{2\left(1+\nu_{eff}\right)} \tag{36}$$

Για τον υπολογισμό του ενεργού μέτρου ελαστικότητας και του ενεργού λόγου Poisson από τις εξισώσεις (34) και (35) αντίστοιχα, αρκεί η επίλυση του μικρομοντέλου στο οποίο εφαρμόζεται ο μακροσκοπικός τανυστής παραμόρφωσης $\boldsymbol{E} = [1 \ \ 0 \ \ 0]^T$. Μέσω της διαδικασίας της ομογενοποίησης υπολογίζεται ο μακροσκοπικός τανυστής τάσης $\boldsymbol{\Sigma}$. Επομένως, είναι δυνατός ο προσδιορισμός των τιμών των ενεργών όρων του ομογενούς μητρώου $C_{eff} = \Sigma_{11}/E_{11}$ και $D_{eff} = \Sigma_{22}/E_{11}$. Από τις τιμές αυτές μπορούν τώρα να υπολογιστούν τα E_{eff} και ν_{eff} σε κάθε πραγματοποίηση της Monte Carlo προσομοίωσης.

5.4 Αριθμητικά αποτελέσματα

Στην ενότητα αυτή προσδιορίζεται η συνάρτηση κατανομής πιθανότητας του ενεργού μέτρου ελαστικότητας και λόγου Poisson που προέκυψαν από την ανάλυση 1000 προσομοιώσεων Monte Carlo. Τα XFEM μοντέλα των RVEs που αναλύθηκαν περιέχουν τυχαία σχήματα νανοσωματιδίων σε ορισμένη κατ΄ όγκο περιεκτικότητα. Συγκεκριμένα, μελετήθηκαν τέσσερα διαφορετικά σχήματα νανοσωματιδίων, τα οποία προέκυψαν μεταβάλλοντας τις τιμές των σταθερών παραμέτρων k_1 και k_2 στην εξίσωση (30), $(k_1 = 0, k_2 = 0)$, $(k_1 = 0, k_2 = 3)$, $(k_1 = 0, k_2 = 6)$ και $(k_1 = 3, k_2 = 6)$ και τρεις διαφορετικές κατ΄ όγκο αναλογίες vf=20, 30 και 40%. Το υλικό τόσο της μήτρας όσο και των νανοσωματιδίων θεωρείται γραμμικό ελαστικό. Συγκεκριμένα, ο λόγος των μέτρων ελαστικότητας των νανοσωματιδίων προς την μήτρα (E_{incl}/E_m) είναι 1000 ενώ οι λόγοι Poisson είναι $\nu_{incl} = \nu_m = 0.3$. Σημειώνεται ότι η προτεινόμενη μέθοδος δοκιμάστηκε σε διαφορετικούς λόγους E_{incl}/E_m καθώς και σε διαφορετικές τιμές των λόγων Poisson. Το μέγεθος των RVEs είναι 10×10 mm. Στο σχήμα 24 εικονίζονται τα ιστογράμματα του E_{eff} που προέκυψαν από τις προσομοιώσεις Monte Carlo για κάθε περίπτωση σχήματος των νανοσωματιδίων και περιεκτικότητας κατ΄ όγκο. Αντίστοιχα, τα ιστογράμματα του ν_{eff} εικονίζονται στο σχήμα 25. Τα σχήματα 26 και 27 εικονίζουν τις καμπύλες της μέσης τιμής και του συντελεστή διακύμανσης σε σχέση με τον αριθμό των αναλύσεων για τις περιπτώσεις των νανοσωματιδίων με $(k_1 = 0, k_2 = 0)$ και $(k_1 = 0, k_2 = 6)$. Ο πίνακας 2 περιέχει συγκεντρωτικά τις μέσες τιμές του E_{eff} για όλες τις περιπτώσεις σχημάτων και κατ΄

όγκο περιεκτικότητας. Από την σύγκριση των τιμών προκύπτει ότι η μεγαλύτερη αύξηση (16.13%) του ενεργού μέτρου ελαστικότητας του σύνθετου υλικού προκύπτει για τα σχήματα ($k_1 = 0, k_2 = 6$) σε σχέση με τα ($k_1 = 0, k_2 = 0$) για vf=40%. Το αποτέλεσμα αυτό επιβεβαιώνει την σημαντική επίδραση που έχει το σχήμα των νανοσωματιδίων στις τελικές ενεργές παραμέτρους του σύνθετου υλικού. Όπως αποδεικνύεται η εφαρμογή απλοποιήσεων στην γεωμετρία των νανοσωματιδίων και η αντικατάστασή τους με ιδεατά σχήματα κύκλων ή ελλείψεων οδηγούν σε σφάλματα της τάξης του 20% στον υπολογισμό των μηχανικών ιδιοτήτων του νανοσύνθετου υλικού.

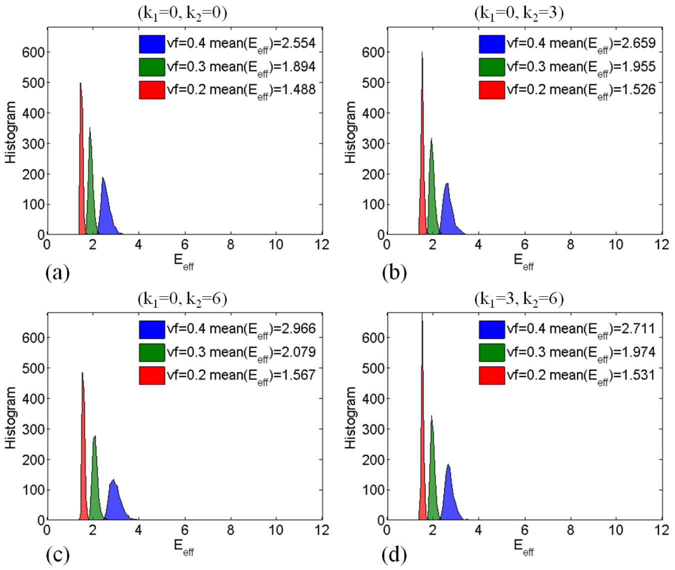

(a)
(b)
(c)
(d)

Σχήμα 24: Ιστογράμματα του E_{eff} : a) ($k_1 = 0, k_2 = 0$), b) ($k_1 = 0, k_2 = 3$), c) ($k_1 = 0, k_2 = 6$) και d) ($k_1 = 3, k_2 = 6$) για vf=[0.2, 0.3, 0.4]

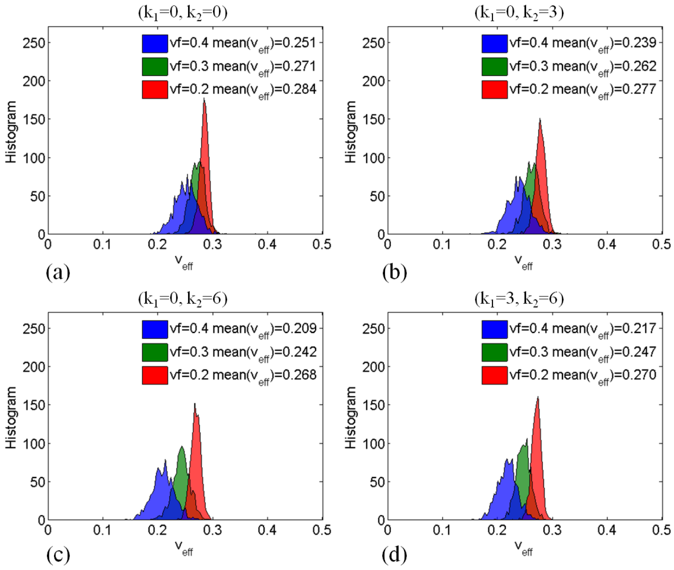

Σχήμα 25: Ιστογράμματα του ν_{eff} : a) $(k_1 = 0, k_2 = 0)$, b) $(k_1 = 0, k_2 = 3)$, c) $(k_1 = 0, k_2 = 6)$ και d) $(k_1 = 3, k_2 = 6)$ για vf=[0.2, 0.3, 0.4]

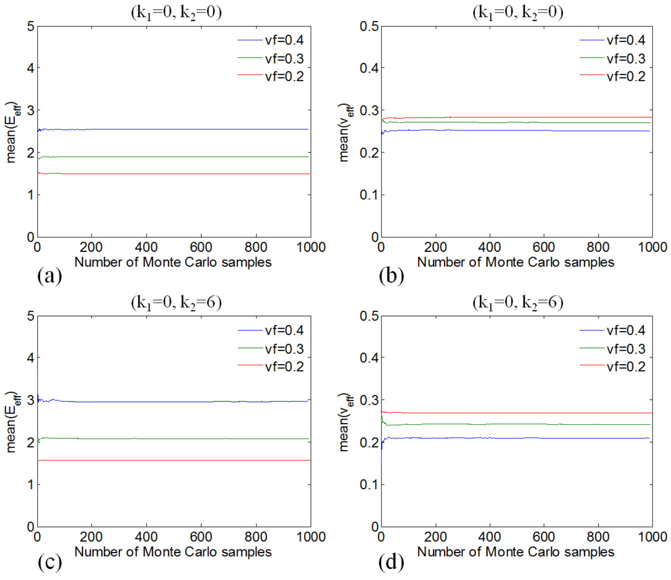

Σχήμα 26: Μέσες τιμές: a-b) mean(E_{eff}), mean(ν_{eff}) για $(k_1 = 0, k_2 = 0)$ και c-d) mean(E_{eff}), mean(ν_{eff}) για $(k_1 = 0, k_2 = 6)$, σε vf=[0.2, 0.3, 0.4]

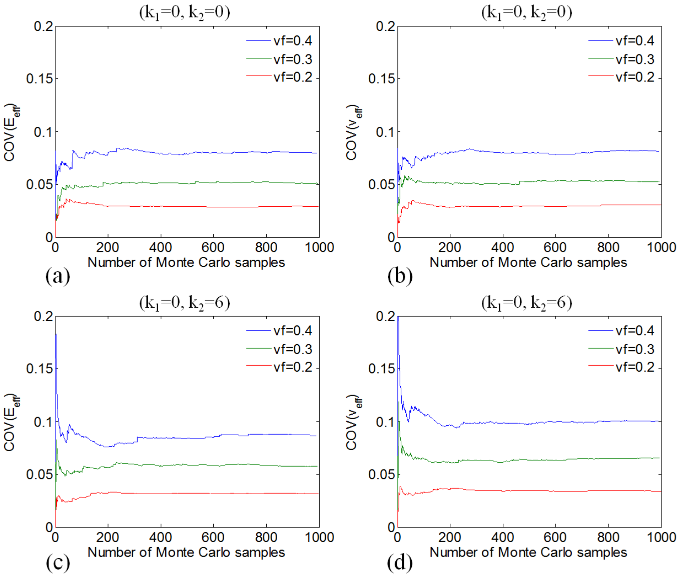

Σχήμα 27: Συντελεστής διακύμανσης: a-b) COV(E_{eff}), COV(ν_{eff}) για ($k_1 = 0, k_2 = 0$) και c-d) COV(E_{eff}), COV(ν_{eff}) για ($k_1 = 0, k_2 = 6$), σε vf=[0.2, 0.3, 0.4]

vf	$(0,0)-(0,3)$	$(0,0)-(0,6)$	$(0,3)-(0,6)$	$(0,0)-(3,6)$
0.2	2.55	5.31	2.69	2.89
0.3	3.22	9.77	6.34	4.22
0.4	4.11	16.13	11.55	6.15

Πίνακας 2: Σύγκριση (% αύξηση) των μέσων τιμών του E_{eff} μεταξύ GnP-RC RVEs με διαφορετικά σχήματα νανοσωματιδίων (k_1, k_2)

List of Figures

List of Tables

Nomenclature

List of Abbreviations

C-C	Carbon-Carbon
CM	Continuum Mechanics
CNT	Carbon Nanotube
CNT-RC	Carbon Nanotube Reinforced Composite
COV	Coefficient of Variation
DFT	Density Functional Theory
DMA	Dynamic Mechanical Analysis
dofs	degrees of freedom
EBE	Equivalent Beam Element
EC	Equivalent-Continuum
EPS	Evolutionary Power Spectra
FE	Finite Element
FEM	Finite Element Method
GnP	Graphene nanoPlatelet
GnP-RC	Graphene nanoPlatelet Reinforced Composite
i.i.d.	independent identically distributed
ISS	Interfacial Shear Strength
LD	Local Density
MC	Monte Carlo
MCS	Monte Carlo Simulation
MD	Molecular Dynamics
MM	Micromechanics
MSM	Molecular Structural Mechanics
MWCNT	Multi Walled Carbon Nanotube

PDF	Probability Density Function
PEEK	Poly-Ether-Ether-Ketone
QC	Quasi-Continuum
QC	Quasi-Continuum
QM	Quantum Mechanics
RVE	Representative Volume Element
SEM	Scanning Electron Microscope
SmXFEM	Smoothed eXtended Finite Element Method
SWCNT	Single Walled Carbon Nanotube
TBMD	Tight Binding Molecular Dynamics
vdW	van der Waals
vf	volume fraction
wf	weight fraction
WLF	Williams Landel and Ferry equation
X-SFEM	eXtended-Stochastic Finite Element Method
XFE	eXtended Finite Element
XFEM	eXtended Finite Element Method

Chapter 1

Introduction

"Nanotechnology is the understanding and control of matter at dimensions between approximately 1 and 100 nanometers, where unique phenomena enable novel applications. Encompassing nanoscale science, engineering, and technology, nanotechnology involves imaging, measuring, modeling, and manipulating matter at this length scale. A nanometer is one-billionth of a meter. A sheet of paper is about 10^5 nanometers thick; a single gold atom is about a third of a nanometer in diameter. Dimensions between approximately 1 and 100 nanometers are known as the nanoscale. Unusual physical, chemical, and biological properties can emerge in materials at the nanoscale. These properties may differ in important ways from the properties of bulk materials and single atoms or molecules", (*Description of Nanotechnology as established by National Nanotechnology Initiative*, `http://nano.gov`).

1.1 Nanocomposites

In the large field of nanotechnology, polymer matrix based nanocomposites have become a prominent area of current research and development. The expansion of length scales from meters, micrometers to nanometers introduced tremendous opportunities for innovative approaches in the processing, characterization, and analysis/modeling of this new generation of composite materials. As scientists and engineers seek to make practical materials and devices from nanostructures, understanding material behavior across length scales from the atomistic to macroscopic levels is required. Unlike the conventional top-down material development approaches, nanocomposite fabrication techniques utilize a bottom-up approach starting from atoms and molecules. The most common fabrication strategies for nanocomposites include: solution processing, melt spinning, melt processing and in situ polymerization. Details about these methods along with other strategies and new trends in nanocomposites are reviewed in many literature papers [94, 15, 10, 46].

A polymer nanocomposite is a multiphase solid material, which consists of a polymer matrix and a weight fraction (wf) of dispersed nanofillers acting as reinforcements to the bulk material. These nanofillers may be of different shape (e.g. spheroids, fibers, platelets), but at least one of their dimensions is less than 100 nm. The most studied nanofillers are the carbon nanotubes (CNTs) and the graphene nanoplatelets (GnPs). The unique combination of their mechanical and physical properties, make them ideal candidates for reinforcement in composite materials, shifting scientific interest from microscale composites to nanocomposites. There are a number of advantages associated with dispersing nanofillers in polymeric materials. While some credit can be attributed to the intrinsic properties of the fillers, most of these advantages stem from the extreme reduction in filler size combined with the large enhancement in the specific surface area and interfacial area they present to the matrix phase. In addition, whereas traditional composites use over 40 wf% of the reinforcing phase, a small weight fraction of nanofillers into polymeric matrices could lead to dramatic changes in their mechanical [40, 111], thermal [26, 72, 108], electrical [26], and damping [87, 75] properties with added functionalities.

Polymers and polymer matrix based composites are being utilized in an increasing number of industrial applications including transportation, automotive, aerospace, defence, sporting goods, energy and infrastructure sectors. This is due to their high durability, high strength, light weight, design and process flexibility. The advantages obtained from nanoscale polymer reinforcement and the subsequent supreme mechanical and physical properties of nanocomposites can lead to myriad of new application possibilities. Particularly, both CNT-reinforced composites (CNT-RCs) and GnP-reinforced composites (GnP-RCs) offer substantial opportunities in advanced emerging technologies related to electrical/electronics/optoelectronics, photovoltaic cells, biomedical applications, flame resistance structures, UV screens, sensors, LEDs and to many others future commodities [92, 33, 18, 1].

Undoubtedly, nano-reinforced composites offer new and exciting possibilities in the already exhausted field of microscale composite science. Their utilization in a wide range of applications exhibits a promising future for various industries. However, there are still major challenges that scientists have to overcome in order to fully exploit the multifunctional capabilities of these multiphase materials. The full potential of employing nanofillers as reinforcement is severely limited due to the existing processing techniques of nanocomposites. There are two critical interrelated issues that must be addressed during the fabrication process of nanocomposites, namely: filler dispersion and functionalization. In addition, distinct size dependence of the material properties is observed at such a small scale. This is attributed to an intrinsic morphological characteristic of the nanofillers; that is their large surface area to volume ratio. Especially in CNT-reinforced composites, despite the desired increase in their stress transfer capability, the large surface/volume ratio of CNTs leads to strong attractive intermolecular van der Waals (vdW) forces causing an excessive agglomeration of the nanofillers. This tendency of the nanofillers to agglomerate degrade the properties of the nanocomposites as it leads to nonuniform dispersion and weak bonding of interfaces. Many studies on new fabrication technologies in nanocomposites have been recently published, which aim to cope with such unresolved processing issues caused by the nanoscale size of fillers [69, 49, 59].

1.2 Modeling techniques for nanocomposites

Nanocomposite technology development requires optimization of processes and fabrication techniques for producing enhanced materials with outstanding mechanical and physical properties. Some critical issues that have to be regarded during the production process of the nanocomposites are related to alignment, dispersion, aspect ratio, orientation, and load transfer of the nanofillers. Since experimentation at nanoscale is still an evolving field, the best way to quantify the effects of such parameters is through computational modeling techniques. To date, a vast number of numerical models for the characterization of nanocomposites have been developed, primarily because of the different modeling techniques that can be adopted. Due to the multiscale nature of nanocomposite materials various computational modeling methods can be implemented, from atomistic based methods such as quantum mechanics, (QM) and molecular dynamics (MD), to micromechanics (MM) and to continuum mechanics (CM).

Atomistic methods are used to simulate the physical movements of atoms and molecules at nanoscale. In this context, MD has been extensively used to model nanostructured materials. This method uses realistic many-body inter-atomic potential functions (force fields) to calculate the total energy of a system of particles. When the total potential energy and the force fields of a molecular system are obtained, then the realistic behavior of atoms and their properties can be calculated. Although the atomistic methods can provide with accurate predictions of the properties of the nanocomposites, however their usage is limited to small system sizes. This drawback originates from the fact that the classical equations of motion for each atom have to be integrated stepwise in time. These time steps can range from 1 to 10 femtoseconds, and the corresponding simulation times can range from several picoseconds to nanoseconds, depending on the system being investigated. Due to the huge number of degrees of freedom involved in atomistic simulations, these approaches are generally too computationally intensive that can not even be handled by the state-of-the-art parallel supercomputers. Atomistic based models have been mainly applied in investigations related to the interfacial bonding mechanisms between CNTs and a variety of polymer systems. Many molecular studies have been devoted to interfacial shear strength (ISS) calculations on CNT/polymer interfaces and to investigations of functionalization effect on nanocomposite material properties [51, 22, 27, 113].

Continuum mechanics approaches have also been applied in order to study nanoscale materials. In the framework of continuum modeling of nanocomposites, the underlying atomic structure of matter is neglected and replaced with a continuous and homogeneous material representation. Therefore, continuum approaches tend to be a more efficient modeling technique for simulating larger-scale systems or longer time spans than the atomistic based approaches. However, traditional continuum based models cannot accurately describe the influence of the nanofillers upon the mechanical properties, bond formation/breakage, and their interactions in composite systems, because they lack the appropriate constitutive relations that govern material behavior at the finer scales. Particularly, traditional continuum mechanical concepts applied at nanoscale do not maintain their validity and thus gross oversimplifications can arise when a purely continuum model is used. For instance, the continuum shell model adopted by many researchers for studying the material properties of CNTs neglects the chirality and curvature effects and thus leads to inaccurate numerical predictions [100, 67]. Such scale-up issues can be addressed by coupling atomistic models with established micromechanical techniques, where the mechanical behavior of nanocomposite materials can still be described on a macroscopic level. In this case, the problem is often formulated at the atomistic scale using the concept of a representative volume element (RVE), where an homogenization method based on micromechanics is applied to in order to define effective material properties for the homogenized medium [64, 13, 62, 74, 76].

The observed macroscale behavior of the nanostructured materials is governed by processes that occur on many different length and time scales. Since these processes are often dependent on each other, it is therefore necessary to model this class of materials using a variety of length scales. Thus, implementation of multiscale modeling techniques is prerequisite in order to capture the underlying governing physics of nanomaterials. Multiscale models can be also used to simulate multiscale phenomena in nanocomposites such as mechanical deformation and failure. Most multiscale modeling techniques adopt either atomistic based or coupled continuum approaches to treat this class of problems. In atomistic based multiscale models the different scales are integrated into a unified approach where continuum mechanics is employed to describe position of atoms, their interactions, and the governing interatomic potentials. These interatomic potentials, which are introduced in these hybrid models through deformation measures, used to capture the underlying atomistic structure of the different phases considered. Thus, the influence of the nanophase is taken into account via appropriate atomistic constitutive formulations. Consequently, these measures are fundamentally different from those in the classical continuum theory. The advantage of using atomistic based continuum techniques over discrete modeling ones lies in their ability to avoid large number of degrees of freedom, while at the same time allowing for the description of the nonlinear constitutive behavior of the constituents. One particular approach of this class of methods is the Quasi-Continuum (QC) method which has been widely used to simulate the mechanical response of polycrystalline materials [58].

In the coupled continuum approach the multiscale modeling employs quantum or molecular mechanics (eg. tight binding or MD method) for atomic scale and finite element method (FEM) for continuum scale. This class of multiscale methods can be further subdivided into sequential and concurrent coupling methods. Sequential methods, sometimes referred to as hierarchical methods, pass information (displacements or forces) from the finer scale as boundary conditions to the coarser one. This approach assumes that the problem considered can be easily separated into processes that are governed by different length and time scales. Thus a complete separation of scales exists, allowing to the coarse-scale physics to be completely determined in the fine scale. In this multiscale procedure the micro to macro relations need to be established. The macroscopic behavior of the continuum model provides the fine-scale model with appropriate boundary conditions which in turn through an homogenization procedure provides the macroscopic effective properties of the continuum. Appropriate constitutive models assigned to the continuum model are often derived from the knowledge of the corresponding local properties and the phase arrangement in the finer scale [82, 106, 76].

Concurrent methods, on the other hand, are better suited in representing scales with a heavy dependence on each other because of the continuous transfer of information between the different scales. This method performs the entire multiscale analysis simultaneously and thus data are continually fed from one length scale to the other in a dynamic process. In that way, all the complexity of the local microstructure is present during the analysis of the structural component without summarizing it in some overall constitutive framework. This method can handle nonlinearities arising from localization phenomena taking place at finer scales (e.g. cracks, shear bands). During the analysis of such localized problems, in each time increment, the macroscopic material point ”asks” for the mechanical response of the microstructured model. This multiscale analysis is accomplished through the implementation of a localization-homogenization process [57, 43]. Despite the capabilities of concurrent methods in modeling multiscale phenomena there are serious unresolved issues that can lead to erroneous nonphysical effects. These issues are mainly related to modeling problems especially in the transition zones between the different scales [19, 101].

1.3 Scope-novelty of the Thesis

The scope of the thesis is to study the mechanical and damping properties of the nano-reinforced polymer based composites through multiscale modeling techniques. Specifically, two types of nanoscale reinforcement elements are examined: carbon nanotubes (CNTs) and graphene nanoplatelets (GnPs). These carbon based nanostructured materials are used to reinforce bulk matrices made by poly-ether-ether-ketone (PEEK), a thermoplastic polymer with supreme mechanical and physical properties. The novelty of the thesis lies in the efficient utilization and excellent synergy of the different modeling techniques, which are applied hierarchically through various spatial scales, from atomistic to micro and finally to macro scale.

In the context of multiscale modeling of CNT-reinforced composites (CNT-RCs), an atomistic based multiscale approach, which couple molecular mechanics to structural mechanics known as molecular structural mechanics (MSM) approach, is adopted for modeling CNTs. In this approach the carbon-carbon (C-C) atomic interactions in the lattice structure of CNTs are simulated by equivalent continuum elements. The transition from atomic to nano scale is performed in the context of continuum mechanics, where the response of the space frame structure of a CNT is projected onto an equivalent beam element (EBE). This continuum element is able to capture phenomena taking place at the finer scale. Then, the multiscale modeling proceeds to the micro scale, where long CNTs built by connected EBEs are embedded into the polymer matrix to form RVEs. For the generation of random wavy CNT structures a novel stochastic procedure is introduced. Specifically the randomness of the CNT geometry is derived from a nonhomogeneous stochastic field using the spectral representation method in conjunction with evolutionary power spectra (EPS). The statistical properties of the EPS are derived from processing a number of CNTs with random geometries obtained from scanning electron microscope (SEM) images. Monte Carlo (MC) simulation is used in order to evaluate the effect of stochastic wavy geometry of CNTs into the mechanical and damping properties of CNT-RC RVEs.

A remarkable characteristic of the proposed multiscale modeling procedure is that the CNT/polymer interfacial adhesion behavior is incorporated in the CNT-RC model through the implementation of a bond-slip law for EBEs. This law, which is related to the developed interfacial shear stresses on the CNT/polymer interface, affects the constitutive behavior of EBEs. Another important issue handled by the proposed modeling procedure is the prediction of multiple relaxation times for PEEK viscoelastic material. For this purpose, the Maxwell-Wiechert constitutive model is assigned to the composite matrix. Effective material parameters for PEEK are derived after the conduction of suitable calibration tests on the Maxwell-Wiechert model. The finite element method is used to analyze the RVE models of the microstructured nanocomposites. To avoid complicated mesh discretization of the CNT-RC RVEs the embedded element technique is applied. By this procedure the stiffness contributions of the EBEs which represent the CNT reinforcements are comprised to the stiffness matrix of the parent solid elements used to simulate the composite matrix. The effect of ISS on the mechanical and damping properties of CNT-RCs is investigated through simulations on RVE models with various weight fraction of CNTs. The numerical results of this study confirm the major role of functionalization and straightening of nanotubes in producing enhanced CNT-reinforced composite materials, and set the ISS limit for which optimum properties can be obtained.

In the framework of sequential multiscale modeling, a novel constitutive model which can capture the macroscopic behavior of the CNT-reinforced composites is proposed. This model can efficiently simulate the resulting viscoplastic behavior of the nanocomposite, which attributed to the material characteristics of its constituent phases and the stick-slip mechanism on the interphase region. The anisotropic stiffness reinforcement of the bulk polymer, and the anisotropic adhesive behavior at the CNT/polymer interface caused by the randomly dispersed CNTs inside the matrix can be also predicted. This is accomplished by the proposed homogenization method through a novel constitutive model which combines

---

Hill's anisotropic plasticity with Maxwell-Wiechert viscoelasticity models. The calibration procedure followed for the definition of the effective material parameters of the proposed viscoplastic model is also introduced. This procedure is based on numerical analyses of microstructured RVE models. The presented numerical results show the efficiency of the proposed sequential multiscale modeling technique in simulating the structural response of CNT-reinforced composites. The proposed multiscale method constitutes a novel numerical tool for the simulation of large scale structures made by CNT-reinforced polymers. The advantage of its usage lies in the fact that finer scale phenomena are considered in a continuum manner so that analyses can be performed within reasonable computational time and accuracy.

The other class of nanocomposite materials studied in the thesis is GnP-reinforced composites (GnP-RCs). In the context of modeling GnP-RC materials, different techniques are adopted which aim to homogenize the behavior of such multiphase materials. In this study simulations are based on the extended finite element method (XFEM) which is combined with Monte Carlo simulation so as effective material parameters of GnP-RC material can be derived from random RVE models. The originality of this study is that it investigates the effect of random shape graphene inclusions on the effective mechanical properties of the nanocomposite material. Modeling of random shaped inclusions is performed via an analytically defined random level set function, which also serves as the enrichment function in the framework of XFEM. Stochastic dispersion and orientation of GnPs are also considered. The numerical results show an obvious influence of these stochastic parameters on the derived material properties of the composite. Particularly, the study highlights the surface effects in nanocomposites, such as the change in surface to volume ratio of the arbitrarily shaped inclusions, which have a significant impact on the overall effective properties of the composite material. These effects are often neglected during the fabrication process of nanocomposites. Therefore, for the numerical characterization of the nanocomposite materials, geometry idealizations of the nanofillers, often used by many researchers, may lead to inaccurate stiffness calculations.

1.4 Objectives

The main objective of this research is to utilize different multiscale modeling techniques and develop new models in order to simulate nanocomposite materials within reasonable computational time and accuracy. A novel numerical tool which can predict the mechanical properties of CNT and GnP-reinforced composites is the outcome of this PhD thesis. Specific research objectives are summarized in the following statements:

1. To apply the MSM approach in order to model the atomic lattice of CNTs as a space frame structure.
2. To project the response of the space frame model onto a linear or nonlinear EBE in order to construct full length CNTs in micro scale.
3. To implement a stochastic procedure for the construction of random wavy CNT geometries exploiting SEM images.
4. To develop a bond-slip model and incorporate it into the FEM code in order to simulate CNT slippage at the CNT/polymer interface.
5. To apply the embedded element technique in order to construct simple finite element (FE) meshes for the CNT-RC RVE models.
6. To implement the Maxwell-Wiechert constitutive model in order to simulate viscoelasticity of PEEK matrix.
7. To study the effect of: a) wf content of CNTs in the composite, b) ISS developed at CNT/polymer interface, and c) random CNT waviness in the mechanical and damping properties of CNT-RC materials.
8. To develop and implement a novel viscoplastic model in order to simulate the homogeneous mechanical behavior of CNT-RC material which can capture microstructural phenomena: a) anisotropic stiffness, b) viscoelasticity of polymer matrix and c) anisotropic energy dissipation due to slip of CNTs.
9. To apply the extended finite element method (XFEM) in order to model the microstructure of the GnP-RC material.

10. To develop a computational homogenization method for GnP-RC material exploiting the excellent synergy of XFEM with Monte Carlo simulation.

11. To study the effect of: a) random inclusion shape, b) vf content of inclusions in the composite and c) stiffness ratio of material constituents in the effective elastic properties of GnP-RC material.

1.5 Thesis Structure

The thesis is organized into six chapters. Chapter 1 is an introduction to nanotechnology and specifically to polymer matrix based nanocomposite science. An overview of the exceptional mechanical and physical properties of nanocomposites, along with their promising applications and the major fabrication challenges are presented. Different modeling techniques, appropriate for each scale from atomistic to continuum level, are illustrated, while the significance of adopting multiscale models in simulating such multiphase materials is highlighted. The scope of the thesis and the introduced novelties are outlined along with the main research objectives.

The structure of CNTs relative to their different chirality types are explained in Chapter 2 where also the exceptional mechanical properties of CNTs are reported. In addition different modeling techniques for CNTs are discussed with emphasis to the atomistic based continuum multiscale method of MSM which is the computational approach followed in this research. Numerical results from parametric studies conducted on MSM CNT models are presented, where the axial, bending and torsional stiffness of CNTs are plotted against various nanotube diameters and different CNT chiralities.

In Chapter 3 the thermoplastic polymers which can be used during the nanocomposite fabrication process as matrices are discussed. Their distinct mechanical properties along with their vast area of applications are listed. Special reference to the viscoelastic behavior of this class of polymers is accomplished along with suitable constitutive models which can capture such a time dependent behavior. Specifically the Maxwell-Wiechert viscoelasticity model is explained and its calibration from both relaxation and dynamic mechanical analysis (DMA) tests is performed for the case of PEEK polymer.

Chapter 4 is devoted to CNT-reinforced composites. It demonstrates all the multiscale modeling steps required for the construction of RVE FE models of CNT-RCs. Initially the computational procedure to pass from the nanoscale space frame model of CNT to its microscale model, which is build by connected EBEs, is presented. The stochastic modeling technique which is used to simulate random wavy CNT geometries by exploiting real SEM images of specimens made by CNT-RCs is also exhibited. Next the embedded element technique is formulated which serves to keep simple structured FE meshes of the RVE models which are analyzed using FEM. Also the implementation of a bond-slip model for capturing the stick-slip interfacial mechanisms at the CNT/polymer interface and its incorporation to the FE analysis code is described. Simulation of cycling loading on microstructured RVE models provide with numerical results showing the effect of ISS on stiffness and damping behavior of CNT-RCs. Further, a nonlinear homogenization method is developed capable to predict the macrocontinuum constitutive response of CNT-RCs. The homogenization is performed through utilization of a constitutive model which combines Hill's anisotropic plasticity model and the Maxwell-Wiechert viscoelasticity model. In that way anisotropic stiffness and slippage of the randomly dispersed CNT reinforcements along with the viscoelastic nature of the polymer matrix can be efficiently captured. Calibration of the proposed model is performed through numerical analyses of microstructured RVE models for different ISS values. Numerical results are provided confirming the efficiency of the homogenized model in predicting the microscale behavior of the composite.

Chapter 5 is referred to GnP-reinforced composites. First the morphology of GnPs is discussed and their supreme mechanical properties are reported. The work done in this chapter aims to study the influence of random shaped GnP inclusions on the effective properties of this class of nanocomposites. In order to achieve this target the proposed homogenization method utilizes the excellent synergy of XFEM and MC simulations. The theoretical formulation of XFEM problem for multiphase media is initially explained. Then an analytically defined random level set function is introduced in order to describe the random shaped nanoplatelets. This function also serves as the enrichment function used in the displacement approximation scheme of the extended finite elements. Different enrichment strategies are applied and their accuracy is tested by conducting various convergence tests in which the extended finite element size is plotted against the energy and displacement norms. An algorithm to generate random RVE models of GnP-RCs with specific weight fraction is illustrated. This code accounts for random dispersion, orientation and geometry of inclusions. In addition the proposed computational homogenization approach by which effective material parameters are calculated, is displayed along with the chosen solution strategy. Numerical results are presented showing an obvious inclusion shape influence on the mechanical properties of GnP-RCs. Finally, Chapter 6 contains the conclusions of the thesis and some recommendations for future work.

Chapter 2

Carbon nanotubes

Since their discovery in 1991 by Iijima [34], CNTs have received significant interest among nanocomposite scientists due to their extraordinary mechanical and physical properties. The density of the CNTs is about $1.3 - 1.8$ g/cm^3, which is just one-half of the density of aluminum. Their elastic modulus is in the range of 1 TPa which is comparable to that of diamond, while their reported tensile strength is in the range of 150 GPa which is much higher than that of high-strength steel (2 GPa). In addition, CNTs exhibit elastic strains up to 5% and fracture strains up to 20% and thus they can sustain larger tensile and bending deformations, when used as reinforcements in polymers, compared to that of carbon fibers. These exceptional mechanical properties along with their supreme electrical and thermal capabilities have established CNTs as ideal reinforcement elements for nanocomposite materials.

In this chapter a detailed description of the CNT geometry is presented. Specifically, the formation of the CNT lattice structure from a hexagonal network of covalently bonded carbon atoms is explained. Indeed, it is the properties of the C-C covalent bonds which are responsible for the supreme mechanical properties of the CNTs. Different modeling techniques applied to CNTs are discussed, from atomistic, to continuum and to hybrid multiscale models. Especially, the basic principles of molecular structural mechanics (MSM) approach are presented, as this method is preferred over others in modeling nanotubes because of its simplicity and effectiveness. The MSM method is implemented into parametric studies of CNTs, where the provided numerical results confirm the dependence of elastic moduli on the chirality type and diameter of CNTs. Finally a finite element model based on the modified Morse interatomic potential is developed, which accounts for the nonlinear interactions of the atoms in the C-C bonds. Validation of this nonlinear space frame model of the CNT is performed by comparing the obtained stress-strain curves with corresponding others, obtained from both theoretical and experimental literature studies.

2.1 Structure of CNTs

CNTs are regarded as a new allotrope of carbon. They are long, slender fullerene structures with aspect ratio greater than 1000. They can be produced by an array of techniques, such as arc discharge, laser ablation and chemical vapor deposition [93]. Their lattice structure resembles a thin, hollow cylinder constructed by hexagonal networks of covalently bonded carbon atoms. The ends of the nanotubes might be cupped by fullerene hemispherical structures. They can be formed either as single-walled (SWCNTs) or as multi-walled (MWCNTs) depending on the number of graphene layers. Specifically, a SWCNT can be imaginary generated by rolling up a graphene sheet into a seamless tube with a constant radius. MWCNTs are essentially nested SWCNTs. The concentric CNT shells have an interlayer spacing of approximately 0.34 nm, that is close to the typical atomic spacing of graphite, and they are stacked together with weak van der Waals forces acting between their carbon atoms.

The diameter of a SWCNT is uniquely defined by the roll-up vector $\vec{C_h}$, which is named chiral vector, because it characterizes the helicity of the nanotube. This property is specified in terms of a pair of integers (n, m), which constitute the multiples of the magnitude of the basis vectors $\vec{\alpha_1}$, $\vec{\alpha_2}$, which are defined on the haxagonal network of the graphene lattice (see Fig. 2.1). The chiral vector is defined as a linear combination of these basis vectors:

$$\vec{C_h} = n\ \vec{\alpha_1} + m\ \vec{\alpha_2} \tag{2.1}$$

The relation between chiral indices n and m results in different CNT configurations which can be classified into three categories. For $n = m$ the (n, n) CNT is

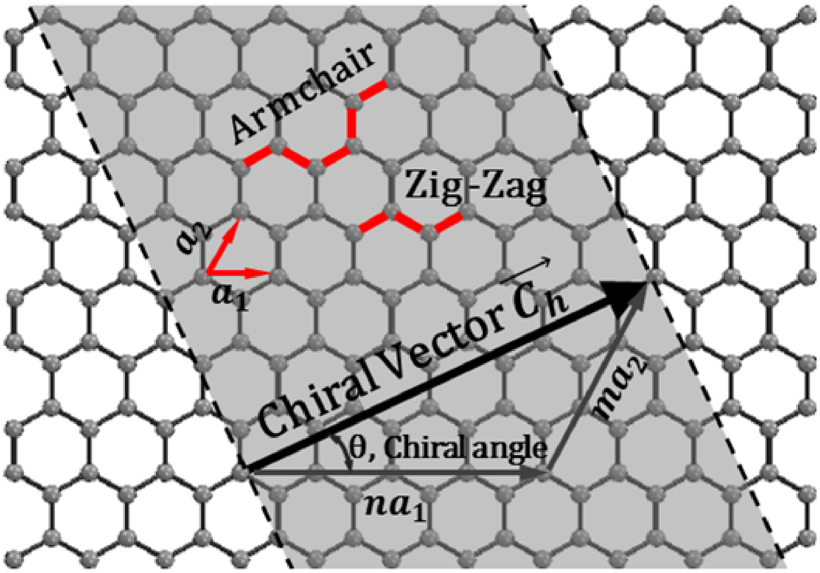

Figure 2.1: Graphene lattice structure and definition of chiral vector $\vec{C}_h$

constructed, which is usually labeled as "armchair", while for $m = 0$ the $(n, 0)$ CNT is constructed, which is usually labeled as "zig-zag". These two CNT types are generaly named "achiral nanotubes". On the other hand, the nanotubes derived from the (n, m) pair of indices, where $n \neq 0$ and $n \neq m$, are labelled as "chiral nanotubes". Figure 2.2 illustrates the lattice structure of each chiral type CNT. The chirality of the tube has significant impact on the transport properties of the CNT, particularly on its electronic properties. For a given (n, m) CNT, if $(2n + m)$ is a multiple of 3, then the nanotube is metallic, otherwise the nanotube is a semiconductor. A (n, m) SWCNT can be constructed by cutting the graphene sheet along the dotted lines (see Fig. 2.1) and rolling it across the chiral vector direction so as the perimeter of the tube to be equal to the length of chiral vector. The angle between the vectors $\vec{C}_h$ and $\vec{\alpha_1}$ which defines the twist of the tube is the helicity angle and can be calculated by:

$$\theta_{\vec{C}_h} = \text{atan}\left(\frac{\sqrt{3}\, m}{2n + m}\right) \tag{2.2}$$

From Eq. (2.2) it is simple to evaluate that $\theta_{\vec{C}_h} = 30°$ for armchair configuration and $\theta_{\vec{C_h}} = 0°$ for zig-zag configuration. For any other chiral nanotube the angle $\theta_{\vec{C_h}} \in (0°, 30°)$. The nanotube diameter is defined as:

$$d_n = |\vec{\alpha_1}| \frac{\sqrt{n^2 + n.m + m^2}}{\pi} \tag{2.3}$$

where $|\vec{\alpha_1}| = |\vec{\alpha_2}|$ is the length of the basis vectors, which equals to $\sqrt{3}\alpha_{CC}$. The length of C-C bonds is $\alpha_{CC} = 0.1421$ nm, which is shorter than that in diamond, indicating the superior strength of CNTs. To roll up a graphene sheet into a SWCNT the following simple rule is followed:

$$[x_n, y_n, z_n] = \left[r_n \cos\left(\frac{x_g}{r_n}\right),\ r_n \sin\left(\frac{x_g}{r_n}\right), y_g \right] \tag{2.4}$$

where x_g and y_g are initially the spatial coordinates on the graphene sheet and x_n, y_n and z_n are the spatial coordinates after the rolling up of the graphene sheet, which results in a nanotube with radious r_n. Fundamental relations governing the geometry of CNTs are reviewed in Dresselhaus et al [20] along with explicit examples.

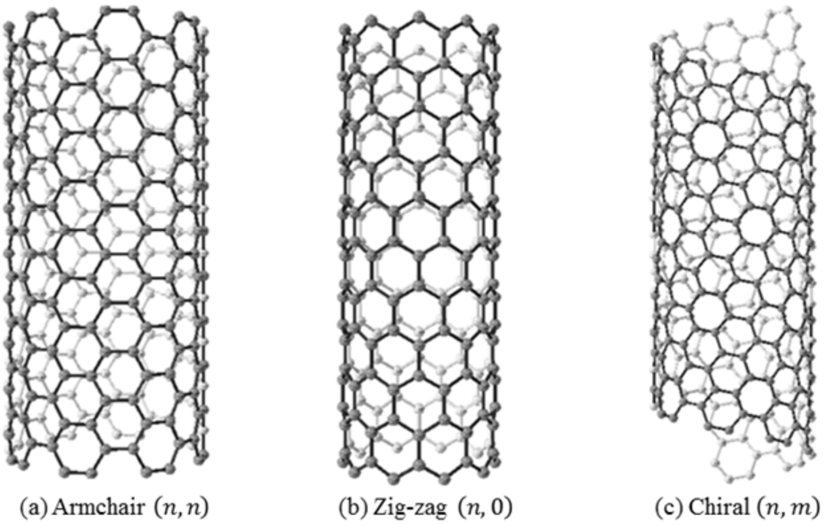

(a) Armchair (n, n) (b) Zig-zag $(n, 0)$ (c) Chiral (n, m)

Figure 2.2: Lattice of: a) Armchair, b) Zig-zag and c) Chiral CNTs

2.2 Modeling techniques for CNTs

Experimental characterization of CNT materials is still remaining a great challenge. This is due to the technological difficulties in handling matter at nano scale and the excessive cost of the required experimental setups. On the other hand, many computational techniques have been introduced as an alternative for the characterization of CNT materials. These can be classified into three main categories: a) atomistic, b) continuum and c) continuum based nanoscale modeling techniques. Different CNT models constructed by employing each of the aforementioned approaches are illustrated in Fig. 2.3.

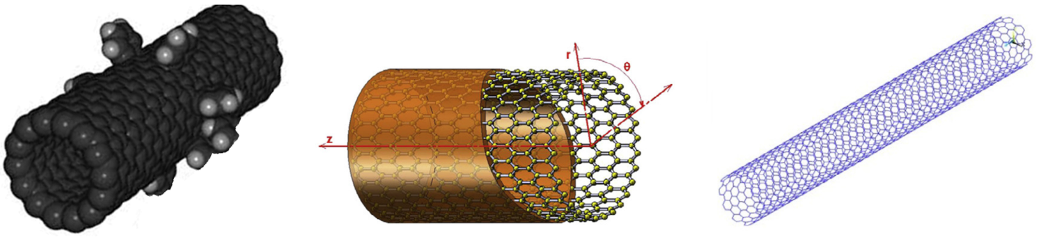

(a) (b) (c)

Figure 2.3: CNT models derived from a) atomistic, b) continuum and c) continuum based nanoscale modeling techniques

In atomistic techniques, the Schrodinger's wave equation, which is the analogue of Newton's second law of motion for quantum mechanics, is solved. From the analysis the time evolution of bond interactions in a system of carbon atoms and thus the physical properties of CNTs can be computed. Specific interactive forces (force field potentials), which are related to the chemical bonding of atoms and the system's energy, have to be prescribed before the analysis. These force fields act as the boundary conditions in the nonlinear differential equation of the atomistic boundary value problem. Three basic categories in the context of atomistic modeling techniques exist, namely the molecular dynamics (MD), Monte Carlo (MC) and *ab initio* method. In both MD and MC methods, the atomic forces are obtained by differentiating the interatomic force field potentials. These can be pair-wise or many-body potentials, such as harmonic, Brenner, Tersof, Tersof-Brener, Morse potential or even non bonded pair potentials, such as

Lennard-Jones potential, which is used for calculating van der Waals forces [48]. Molecular dynamics is a deterministic method while Monte Carlo is a stochastic one. On the other hand *ab initio* is totally different from the other two as it is a potential-free method. Here the forces on atoms are found progressively from electronic structure calculations. Many atomistic numerical studies are reported in literature, such as tight binding molecular dynamics (TBMD), local density (LD), and density functional theory (DFT) approaches [35, 17, 107, 29, 73], all employed in order to predict the elastic moduli and strength of CNTs. Despite their accuracy, atomistic modeling techniques have a limited range of applicability into short time and small size simulations. So, large molecular systems, spanning over the range of a few picoseconds in time and a few nanometers in size, can not be simulated with atomistic techniques, even by the state-of-the-art supercomputers due to excessive computational time and insufficient computer memory resources.

Continuum modeling techniques employ the continuum mechanics theories of rod, trusses, beams, shells, or curved plates in order to study the mechanical properties of CNTs. The basic assumption in these theories is that the lattice structure of CNTs is replaced by a continuum medium which has continuous distribution of mass and stiffness. The validity of the continuum models need to be carefully tested, as they ignore the real discrete structure of CNT lattice. In the context of continuum approaches, both analytical and numerical models have been introduced. Many researchers have employed continuum shell models to study CNTs. Similarities between the MD model and the macroscopic shell model of the CNT was presented by Yakobson et al [105]. They have also shown that mechanical properties of CNTs were strongly dependent on helicity and atomic structure of the tubes. Thus, the effect of curvature and chirality on the mechanical properties of CNTs cannot be captured by an isotropic shell model. Chang [12] used an anisotropic shell model. Unlike common shell models, which assume isotropic elastic properties, this model can predict the chirality induced anisotropic effects on some mechanical behaviors of CNTs by incorporating molecular and continuum mechanics. In general, more complex shell theories, such as Sanders theory, are capable of reproducing the results of MD simulation. However, some parameters, such as wall thickness of CNTs, are not well defined by the continuum models. The applicability and limitations of shell models in predicting the mechanical properties of CNTs have been extensively discussed in many literature papers [100, 67]. Recently, nonlocal continuum theories have been also employed for the CNT material characterization. Specifically, Arash and Wang [2] have pointed out the superiority of nonlocal elasticity models of beams, shells and plates in simulating CNTs, compared to the classical continuum models.

Contrary to continuum modeling of CNTs, where the whole nanostructure is replaced by a continuum medium, continuum based nanoscale modeling provides a rationally acceptable compromise by replacing C-C bonds with continuum elements. In other words, in continuum based nanoscale modeling the C-C atomic interactions are captured using structural members, whose properties are obtained through atomistic modeling. In this context, the quasi-continuum (QC) and the equivalent-continuum (EC) methods have been utilized in modeling CNTs, where continuum mechanics theories are applied at nanoscale. In the quasi-continuum method, introduced by Tadmor et al [90], a relationship is established between the strain energy of a material point on the continuum and the deformation of its crystal lattice. This relation follows the Cauchy-Born rule. On the other hand, in the equivalent-continuum method , introduced by Odegard et al [64], a correlation between computational chemistry and continuum structural mechanics is provided. Here the modeling procedure is performed into two stages. In the first stage, the discrete molecular structure of the material is replaced with an intermediate continuum model consisting of two types of truss elements, one of which captures changes in bond length and the other describes angle variations. It has been shown that this replacement may be accomplished by equating the potential energy of the whole molecular system to the strain energy of the truss elements of the continuum model. In the second stage, the truss-based continuum model is replaced with an equivalent continuous cylinder based once again on energy equivalence. The main shortcomings of this method are the complexity of the model and the excessive computations required for its analysis.

2.2.1 Molecular structural mechanics

Among the EC approaches the molecular structural mechanics (MSM) developed by Li and Chou [50] has attracted great attention because of its simplicity and effectiveness. The energy equivalence in this approach is established in a different way than that in the classical EC method. The potential energy produced by the C-C atomic interactions is equating to the sum of energies produced by the deformations of a beam element, which substitute the C-C chemical bond. Thus, the method results in a space frame model built by connected beam elements, which is equivalent to the atomistic model of the lattice of the CNT material. In principle, this approach provides a linkage between molecular mechanics and continuum structural mechanics by which geometry and material properties of the beam elements are obtained. Figure 2.4 illustrates the lattice structure of a CNT which is modeled by the MSM method, where a pattern of a hexagonal network of beams can be recognized.

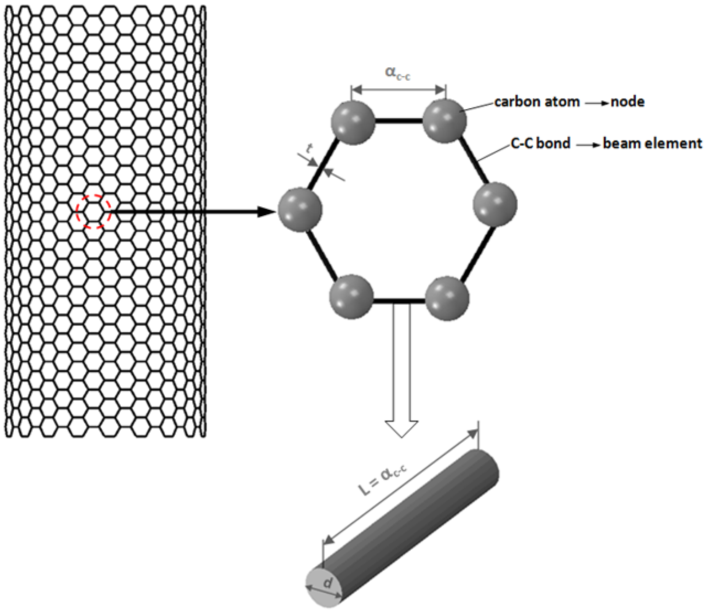

Figure 2.4: Lattice structure of a CNT modeled by MSM method

2.2.1.1 Structural mechanics

In structural mechanics analysis the displacements, strains and stresses of a structure subjected to specific loading conditions are determined. In this context, the stiffness matrix method is widely used to analyze structures of any geometry. It can be applied in linear elastic static problems as well as in problems involving buckling, plasticity and dynamics. Specifically, for linear elastic problems the formulation of the method starts with the elemental equilibrium equation written for an element in the space frame model (see Fig. 2.5) as follows:

$$\mathbf{K}\mathbf{u} = \mathbf{f} \tag{2.5}$$

where

$$\mathbf{u} = [u_{xi}, u_{yi}, u_{zi}, \theta_{xi}, \theta_{yi}, \theta_{zi}, u_{xj}, u_{yj}, u_{zj}, \theta_{xj}, \theta_{yj}, \theta_{zj}]^T \tag{2.6}$$

$$\mathbf{f} = [f_{xi}, f_{yi}, f_{zi}, m_{xi}, m_{yi}, m_{zi}, f_{xj}, f_{yj}, f_{zj}, m_{xj}, m_{yj}, m_{zj}]^T \tag{2.7}$$

are the nodal displacement vector and nodal force vector of the element, respectively. $\mathbf{K}$ is the elemental stiffness matrix, which is formed by the following submatrices:

$$\mathbf{K} = \begin{bmatrix} \mathbf{K_{ii}} & \mathbf{K_{ij}} \\ \mathbf{K_{ij}^T} & \mathbf{K_{jj}} \end{bmatrix} \tag{2.8}$$

where

$$\mathbf{K_{ii}} = \begin{bmatrix} EA/L & 0 & 0 & 0 & 0 & 0 \\ 0 & 12EI_x/L^3 & 0 & 0 & 0 & 6EI_x/L^2 \\ 0 & 0 & 12EI_y/L^3 & 0 & -6EI_y/L^2 & 0 \\ 0 & 0 & 0 & GJ/L & 0 & 0 \\ 0 & 0 & -6EI_y/L^2 & 0 & 4EI_y/L & 0 \\ 0 & 6EI_x/L^2 & 0 & 0 & 0 & 4EI_x/L \end{bmatrix}, \tag{2.9}$$

$$\mathbf{K_{ij}} = \begin{bmatrix} -EA/L & 0 & 0 & 0 & 0 & 0 \\ 0 & -12EI_x/L^3 & 0 & 0 & 0 & 6EI_x/L^2 \\ 0 & 0 & -12EI_y/L^3 & 0 & -6EI_y/L^2 & 0 \\ 0 & 0 & 0 & -GJ/L & 0 & 0 \\ 0 & 0 & 6EI_y/L^2 & 0 & 2EI_y/L & 0 \\ 0 & -6EI_x/L^2 & 0 & 0 & 0 & 2EI_x/L \end{bmatrix}, \tag{2.10}$$

$$\mathbf{K_{jj}} = \begin{bmatrix} EA/L & 0 & 0 & 0 & 0 & 0 \\ 0 & 12EI_x/L^3 & 0 & 0 & 0 & -6EI_x/L^2 \\ 0 & 0 & 12EI_y/L^3 & 0 & 6EI_y/L^2 & 0 \\ 0 & 0 & 0 & GJ/L & 0 & 0 \\ 0 & 0 & 6EI_y/L^2 & 0 & 4EI_y/L & 0 \\ 0 & -6EI_x/L^2 & 0 & 0 & 0 & 4EI_x/L \end{bmatrix} \tag{2.11}$$

Given the length L of a frame element, only the four stiffness parameters need to be determined in order to define the elemental stiffness matrix $\mathbf{K}$. These are the tensile resistance EA, the flexural rigidities EI_x and EI_y and the torsional stiffness GJ. In order to obtain the deformation of a space frame model, the above elemental stiffness equations should be established for every element in the model and then all these equations should be transformed from local coordinates to a global reference system. Finally, a system of linear equations is assembled according to the requirements of nodal equilibrium. By solving this system and taking into account the boundary restraints, the nodal displacements can be obtained.

2.2.1.2 Molecular mechanics for CNTs

In the framework of molecular mechanics, a CNT can be regarded as a molecular system consisting of carbon atoms. The deformation of the CNT under a specific load is governed by the atomic motions which are regulated by a force field. This force field, which is generated by electron-nucleus and nucleus-nucleus interactions, is usually expressed in the form of a steric potential energy. The general expression of this total steric potential energy is a sum of energies due to valence

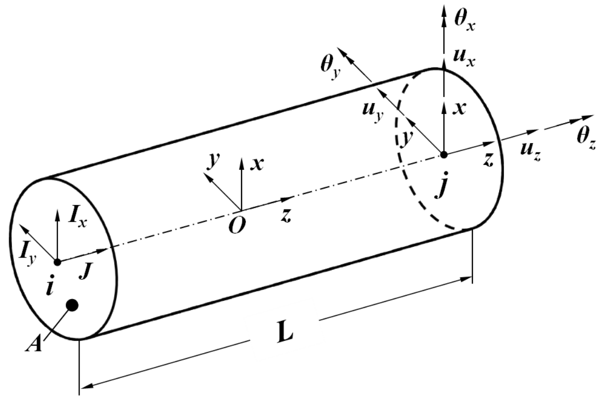

Figure 2.5: Illustration of a beam element of the space frame model.

or bonded and nonbonded interactions as follows:

$$U = \sum U_r + \sum U_\theta + \sum U_\phi + \sum U_\omega + \sum U_{vdW}, \tag{2.12}$$

where $U_r, U_\theta, U_\phi, U_\omega$ and U_{vdW} are the bond-stretching energy, the bond-angle variation energy, the dihedral-angle torsion energy, the inversion (out of plane torsion) energy and the van der Waals interaction energy, respectively. Note that the energy terms due to the electrostatic interactions of the bonds are omitted. The corresponding interatomic interactions are schematically represented in Fig. 2.6.

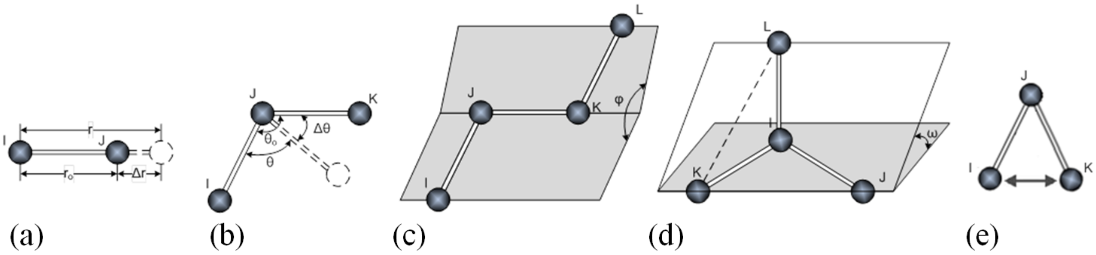

Figure 2.6: Interatomic interactions in molecular mechanics: a) stretching, b) bending, c) dihedral angle torsion, d) out of plane torsion and e) van der Waals.

There are a lot of studies in the field of molecular mechanics proposing different functional forms for the potential energy terms in Eq. (2.12), [8, 71, 16].

These functional forms depend on the particular material and the loading conditions considered, for describing the bond interactions. Both linear and nonlinear potential expressions have been applied. The most widely used are the harmonic, Morse, Tersoff-Brenner and Lenard-Jones potentials. In general, for covalent systems, the main contributions to the total steric energy come from the first four terms. Under the assumption of small deformation, the harmonic approximation is adequate for describing the energy [25]. For sake of simplicity and convenience, we adopt the simplest harmonic forms and merge the energy terms from dihedral angle torsion and the improper torsion into a single equivalent term, i.e.,

$$U_r = \frac{1}{2} k_r \left(r - r_0\right)^2 = \frac{1}{2} k_r \left(\Delta r\right)^2 , \tag{2.13}$$

$$U_\theta = \frac{1}{2} k_\theta \left(\theta - \theta_0\right)^2 = \frac{1}{2} k_\theta \left(\Delta \theta\right)^2 , \tag{2.14}$$

$$U_\tau = U_\phi + U_\omega = \frac{1}{2} k_\tau \left(\Delta \phi\right)^2 , \tag{2.15}$$

where k_r , k_θ and k_τ are the bond stretching, bond angle bending and torsional-resistance force constants respectively, and Δr, $\Delta\theta$ and $\Delta\phi$ represent the bond-stretching, bond-angle and bond-twisting-angle variations, respectively. In principle, the bond-angle variation force constant is the sectional bending rigidity about the major principal axis of the covalent bond for a graphite sheet.

2.2.1.3 Linking molecular mechanics to structural mechanics

As discussed in Section 2.1 the carbon atoms on the CNT lattice are covalently bonded to each other forming hexagon networks on the wall of the tube. These covalent bonds are formed in three-dimensional space exhibiting characteristic bond lengths and bond angles. The total deformation of a CNT subjected to specific external forces is the result of the bond interactions which constrain the displacements of the carbon atoms. A CNT could be simulated as a space frame structure where the covalent bonds are represented by connected beam elements while the carbon atoms act as joints of the connected elements. The stiffness and geometric parameters of an equivalent beam can be determined from the relationship between the potential energy of the covalent bond due to atomic interactions and the strain energy of the equivalent beam as a result of structural deformation. According to structural mechanics, the strain energy of a uniform beam with length L, Young"s modulus E, and circular cross-section A subjected to a pure axial force N (Fig. 2.7a) can be expressed as:

$$U_A = \frac{1}{2}\int_0^L \frac{N^2}{EA} dL = \frac{1}{2}\frac{N^2 L}{EA} = \frac{1}{2}\frac{EA}{L}(\Delta L)^2 \tag{2.16}$$

where ΔL is the axial stretching deformation. The strain energy of a uniform beam subjected to a pure bending moment M (see, Fig. 2.7b) is written as:

$$U_M = \frac{1}{2}\int_0^L \frac{M^2}{EI} dL = \frac{1}{2}\frac{M^2 L}{EI} = \frac{1}{2}\frac{EI}{L}(2\alpha)^2 \tag{2.17}$$

where α denotes the rotational angle at the ends of the beam. Notice that for circular cross section $I_x = I_y = I$. The strain energy of a uniform beam subjected to a pure torsion T (Fig. 2.7c) is denoted as:

$$U_T = \frac{1}{2}\int_0^L \frac{T^2}{GJ} dL = \frac{1}{2}\frac{T^2 L}{GJ} = \frac{1}{2}\frac{GJ}{L}(\Delta\beta)^2 \tag{2.18}$$

where $\Delta\beta$ is the relative rotation between the ends of the beam.

Comparing the molecular Eqs. (2.13)-(2.15) with the corresponding Eqs. (2.16)-(2.18) of structural mechanics it can be deduced that both U_r and U_A represent the stretching energy, both U_θ and U_M indicate the bending energy, and both U_τ and U_T stand for the torsional energy. Accordingly, Δr is reasonably assumed to equal ΔL, $\Delta\theta$ equals 2α, and $\Delta\phi$ equals $\Delta\beta$. Therefore, equating the aforementioned energy expressions the stiffness parameters of the structural beam element are related with known molecular mechanics force field constants as follows:

$$EA = k_r L, \quad EI = k_\theta L, \quad GJ = k_\tau L \tag{2.19}$$

Equation (2.19) establishes the foundation of applying the theory of structural mechanics to the modeling of carbon nanotubes or other similar fullerene structures. As long as the force constants k_r, k_θ and k_τ are known, the sectional stiffness parameters EA, EI and GJ can be readily obtained. Then by following the solution procedure of stiffness matrix method for frame structures, the deformation and related elastic behavior of graphene sheets and nanotubes at the atomistic scale can be simulated.

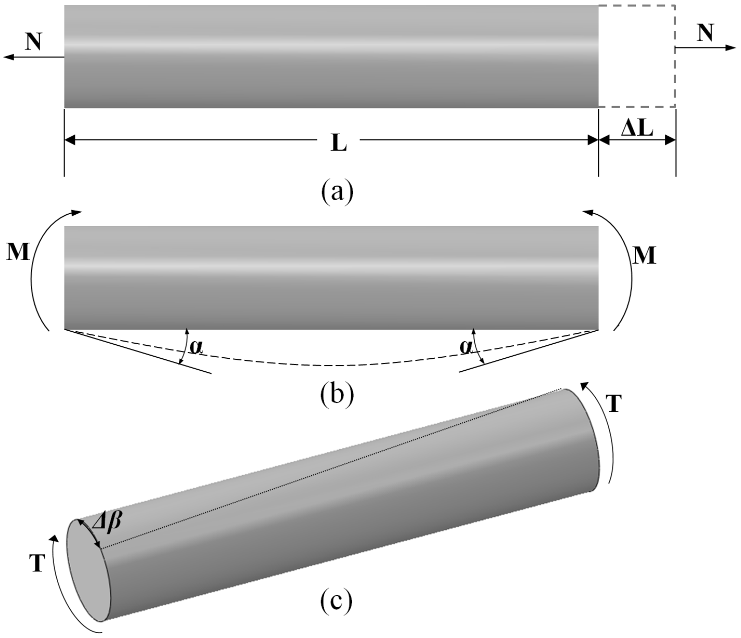

Figure 2.7: Structural deformations of a beam element: a) tension, b) bending and c) torsion.

2.2.1.4 Parametric studies

In this section parametric studies are conducted in order to compute the mechanical properties of both armchair and zig-zag SWCNTs with respect to their diameters. The MSM approach, described previously, is applied where the space frame model is constructed by assuming round beam finite elements. The diameter d, Young's modulus E and shear modulus G of the beams are obtained from Eqs. (2.19) as follows:

$$d = 4\sqrt{\frac{EI}{EA}} = 4\sqrt{\frac{k_\theta}{k_\tau}},\ E = \frac{k_r^2 L}{4\pi k_\theta},\ G = \frac{k_r^2 k_\tau L}{8\pi k_\theta^2} \tag{2.20}$$

The force field constant values $k_r = 938$ kcal·mole^{-1}·$\mathring{A}^{-2}$$= 6.52 \times 10^{-7}$ N·nm^{-1},

$k_\theta = 126$ kcal·mole^{-1}·rad^{-2}$= 8.76\times10^{-10}$ N·nm·rad^{-2} and $k_\tau = 40$ kcal·mole^{-1}·rad^{-2}$=$ 2.78×10^{-10} N·nm·rad^{-2}, defined by Cornell et al [16], are used in the subsequent analyses. Substituting these force field constant values and the characteristic bond length $L = \alpha_{C-C} = 0.1421$ nm into Eqs. (2.20) the values of $d = 0.147$ nm, $E = 5.49$ TPa and $G = 0.871$ TPa of the beam elements are obtained. Then, the space frame model of a CNT is analyzed using FEM and its stiffness properties can be calculated. Specifically, the axial, bending and torsional rigidities of a SWCNT are derived by simulating a space frame model subjected to three independent loading conditions, namely tension, bending and torsion. The boundary and loading conditions for each test case are depicted in Fig. 2.8.

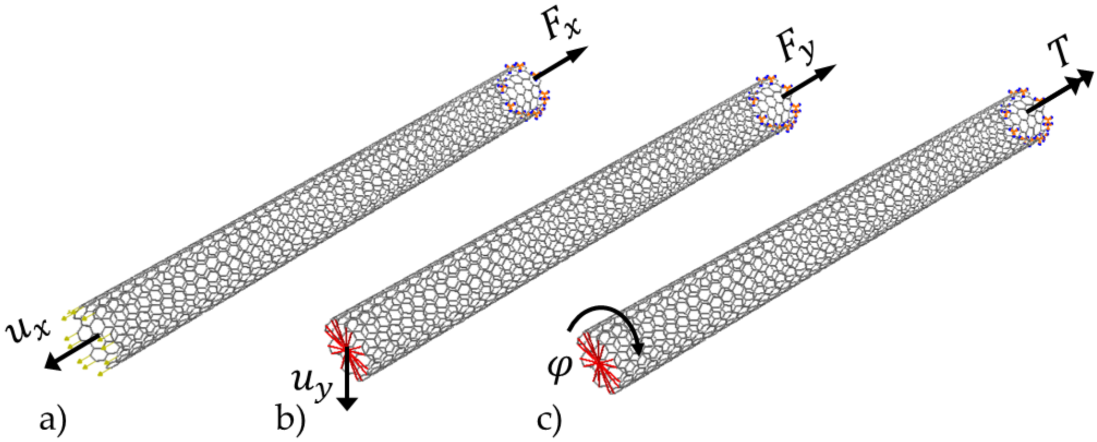

Figure 2.8: FE mesh and boundary conditions of a space frame model in a) tension, b) bending and c) torsion

Specifically, the axial stiffness of a CNT with initial lengh L_0 is calculated by imposing an axial displacement u_x at one end of the space frame model, while its opposite end is kept fixed. The finite element analysis provides with the resulting reaction forces F_x (see Fig. 2.8(a)). Therefore, the equivalent value for the axial stiffness of the CNT can be derived by the equation:

$$(EA)_{eq} = \frac{F_x L_0}{u_x} \tag{2.21}$$

In bending loading case, a transverse displacement u_y is applied at the center point of the one end of the space frame model, where all nodes are kinematically constrained (see Fig. 2.8(b)). The other end, where the resulting reaction forces F_y are calculated, is considered fixed. The equivalent bending stiffness of the CNT is thus computed by:

$$(EI)_{eq} = \frac{F_y}{3u_y} L_0^3 \tag{2.22}$$

Similarly, in torsion case, a torque T is applied at the center point of one end of the model, which is kinematically constrained to the peripheral nodes of this section, as shown in Fig. 2.8(c). The nodes at the other end section of the model are fully constrained. The angle of rotation ϕ of the center point is calculated by means of a FE analysis and the equivalent torsional stiffness of the CNT is calculated as follows:

$$(GJ)_{eq} = \frac{T}{\phi} L_0 \tag{2.23}$$

A number of space frame models for both armchair (n, n) and zigzag $(n, 0)$ chirality type nanotubes with aspect ratio approximately ten have been analyzed. Figure 2.9 illustrates the stiffness values of the CNTs computed from Eqs. (2.21)-(2.23) with regard to their real diameters (Eq. (2.3)). As it can be observed from the figure, the chirality type of the CNT slightly affects its stiffness, which seems to be strongly dependent on the diameter of the CNT. It can be deduced that the stiffness parameters of a nanotube with theoretically infinity diameter correspond to these of a graphene sheet.

2.2.2 Modeling the nonlinear C-C bond behavior

The quadratic potential, which results in harmonic approximations of the molecular energies (Eqs. (2.13)- (2.15)), is adequate for describing small deformations of the CNT lattice in the context of MSM approach. However, when the behavior of CNTs under large strains is to be simulated, the nonlinear behavior of the C-C bonds has to be modeled. For this reason, the empirical interatomic potentials are adopted, which can adequately describe the interatomic interactions even when large deviations from equilibrium occur. There are two types of such potentials, pairwise and many-body. The major difference between them lies in the consid-

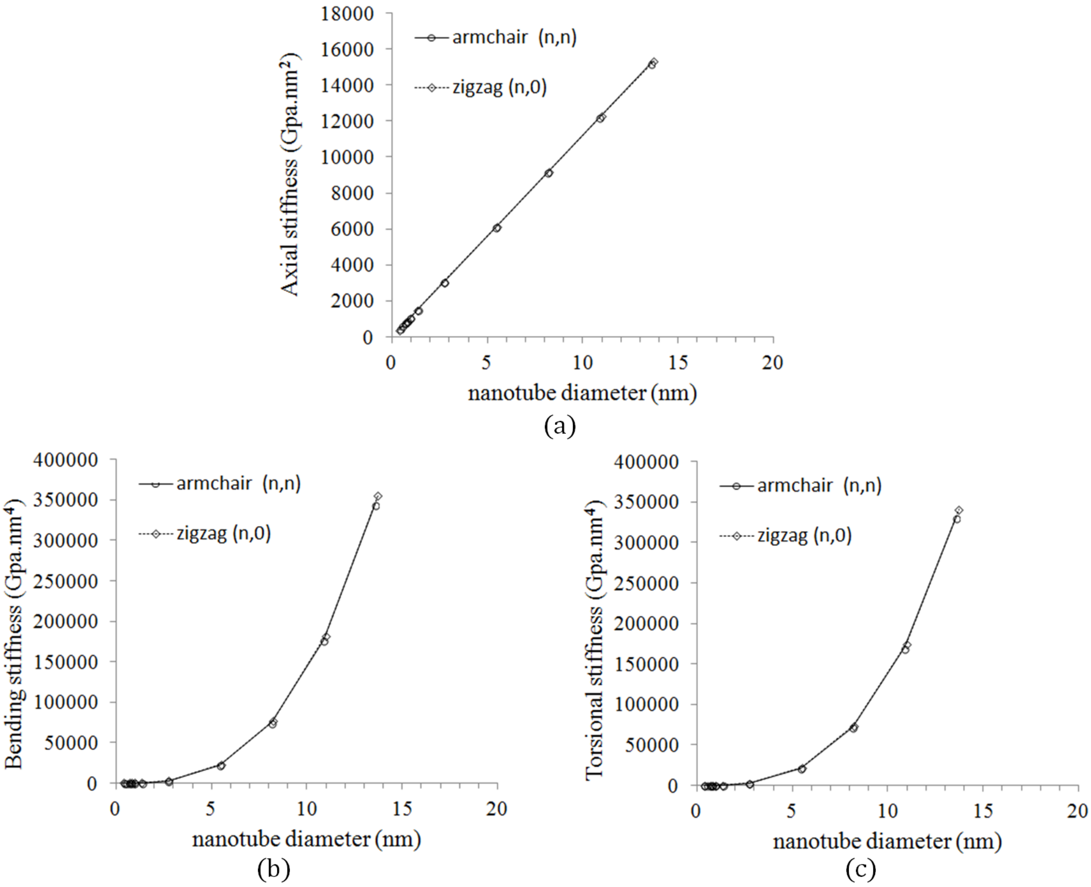

Figure 2.9: Stiffness values in a) axial, b) bending and c) torsion case for armchair and zig-zag nanotubes vs diameter

eration of non-bonded interactions by many-body potentials. In order to restrict the pair potential to nearest neighbors, many-body potentials introduce a cut-off function, which has found to cause strange features in the resulted force-strain curve [5]. On the other hand, the pairwise modified Morse potential has been employed in many studies because of its simplicity over many-body potentials and its adaptability with FEM [103, 89]. According to the modified Morse potential, the total potential energy of the nanotube system is expressed as:

$$U = \sum U_r + \sum U_\theta \tag{2.24}$$

$$U_r = D_e \left[\left(1 - e^{-\beta(r-r_0)}\right)^2 - 1 \right] \tag{2.25}$$

$$U_\theta = \frac{1}{2} k_\theta \left(\theta - \theta_0\right)^2 \left[1 + k_{\text{sextic}} \left(\theta - \theta_0\right)^4\right] \tag{2.26}$$

where U_r , U_θ are the bond energy due to bond stretching and bond angle-bending and r, θ are the current bond length and the current bond angle, respectively. According to Belytschko et al [5] the parameters of the Morse potential are: $r_0 = 1.421 \times 10^{-10}$ m, $D_e = 6.03105 \times 10^{-19}$ N·m, $\beta = 2.625 \times 10^{10}$ m^{-1}, $\theta_0 = 2.094$ rad, $k_\theta = 0.9 \times 10^{-18}$ N·m/rad^2, $k_{\text{sextic}} = 0.754$ rad^{-4}. Belytschko et al [5] have defined these specific parameters so as to enforce equivalence between Morse's potential and Brenner's potential for strains below 10%.

Differentiation of Eq. (2.25) results to the definition of the nonlinear stretching force between the carbon atoms in the C-C bond. This relation is given by the following molecular force-field:

$$F = 2\beta D_e \left(1 - e^{-\beta(r-r_0)}\right) e^{-\beta(r-r_0)} \tag{2.27}$$

Figure 2.10 plots the relationship between the axial force F and the axial strain ε for the C-C bonds. The strain of the bond is defined by $\varepsilon = (r - r_0)/r_0$. As may be seen, the force-strain relation is highly nonlinear at the attraction region especially at large strains. The inflection point (peak force) occurs at 19% strain. The repulsive force ($\varepsilon < 0$) increases rapidly as the bond length shortens from the equilibrium length r_0 with less nonlinearity than the attractive force.

Also differentiation of Eq. (2.26) results to the definition of the bond moment M with respect to the bond angle change $\Delta\theta = \theta - \theta_0$. This relation can be expressed in the form:

$$M = k_\theta \Delta\theta \left(1 + 3k_{\text{sextic}} \Delta\theta^4\right) \tag{2.28}$$

In Fig. 2.11 the bond moment M is plotted against the bond angle change $\Delta\theta$. It can be seen that for small angles (< 0.5 rad) the moments are kept low and linear behavior is observed. The nonlinear bending behavior is obvious for larger angles where significant increase in moment values occurs.

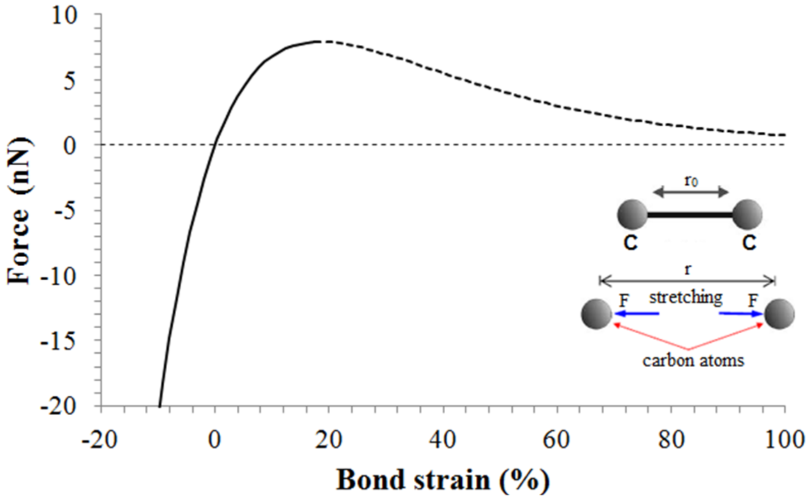

Figure 2.10: Force-strain curve of the modified Morse potential

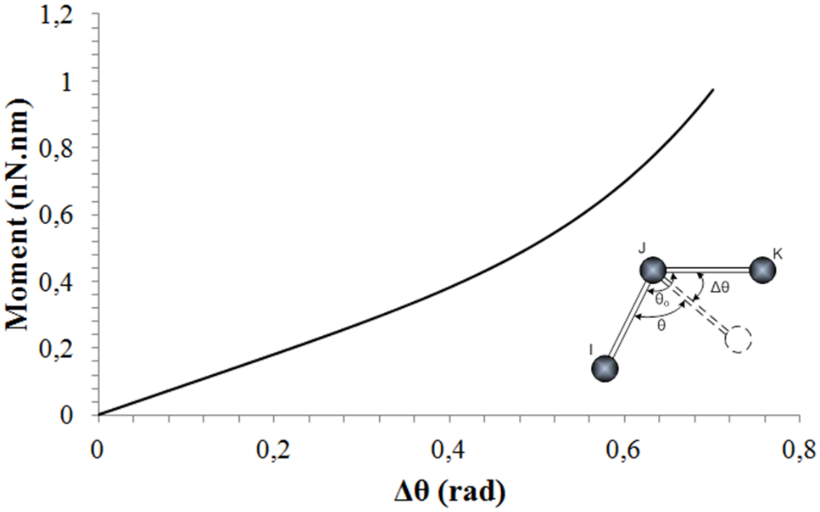

Figure 2.11: Moment-angle change curve of the modified Morse potential

For modeling the C-C nonlinear bond behavior in nanotubes, Bernoulli beam elements, which have been assigned material nonlinearity, are used. Specifically, the von Mises plasticity model is applied, where yielding parameters of beams are defined from the nonlinear force-strain curve of the modified Morse potential (Fig. 2.10). Initially, the stiffness of the beam elements is evaluated from the initial slope of that curve using the element's cross-sectional area A. Then for each load increment the total engineering stresses $\sigma = F/A$ are calculated. Therefore, assuming a very small elastic strain limit ($\simeq 0.2\%$), the yield stress-plastic strain data for the von Mises model are defined. Figure 2.12 presents the yield stress-plastic strain curve derived for beam elements with diameters $d = 0.34$ nm, which are equal to the interlayer spacing of graphite.

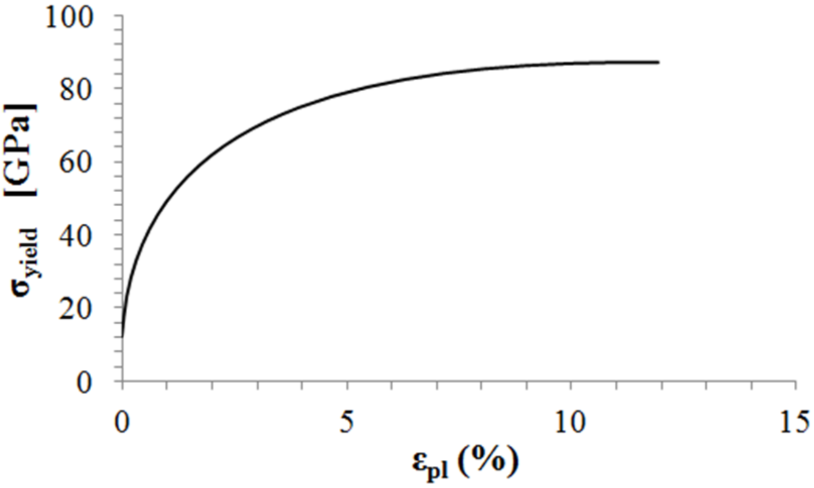

Figure 2.12: Yield stress-plastic strain curve for von Mises model obtained for beams with diameter $d = 0.34$ nm

The validity of the proposed model is tested on a zig-zag $(20, 0)$ CNT space frame model subjected to an incremental tensile loading. In addition a damage model is incorporated in the FE analysis to account for nanotube fracture. This damage model is based on the element deletion technique which is triggered when the total axial strain on a beam reaches the inflection strain of the bonds (19%). Notice that as bond stretching dominates nanotube fracture and the effect of angle-bending potential is very small, only the bond stretching potential is considered in the simulation. Figure 2.13 shows the comparison of the stress-strain curves predicted by the proposed modeling technique with those obtained by the MD simulation of Belytschko et al [5], the progressive fracture model (PFM) of Tserpes et al [96] and the experiments of Yu et al [109]. As it can be observed, the experimental curves show very large dispersion, probably due to insufficient experimental setups at nanoscale. The strain of the nanotube is calculated by

$\varepsilon_n = (L_n - L_{n_0})/L_{n_0}$, where L_n is the current nanotube length and L_{n_0} is the initial length prior to loading ($L_{n_0} = 41.9$ nm). The stress is given by $\sigma_n = F_n/A_n$, where F_n is the total reaction force computing on the fixed end of the nanotube by summing over all the nodal reaction forces lying there. $A_n = \pi d_n t$ is the cross-sectional area of the uniform nanotube, which has a diameter $d_n = 1.57$ nm and a wall thickness $t = 0.34$ nm. The stress-strain curve, obtained by the proposed modeling technique, show a very good correlation with the corresponding curve obtained by the MD simulation of Belytschko et al [5]. This fact implies the efficiency of the proposed continuum base nanoscale model in predicting the nonlinear mechanical behavior of CNTs.

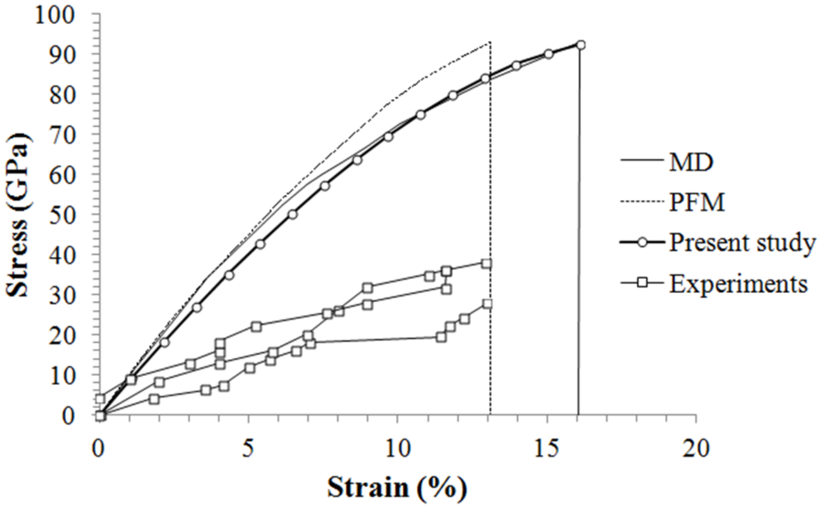

Figure 2.13: Nonlinear stress-strain curve of zig-zag (20,0) CNT predicted in present study, comparison with other theoretical and experimental studies: MD simulation of Belytschko et al [5], PFM of Tserpes et al [96], experiments of Yu et al [109]

Chapter 3

Thermoplastic polymers

Depending on the type of polymer matrix used to fabricate composites, these are classified as being thermosets or thermoplastics. Unlike thermosets which require a crosslinking chemical reaction in order to solidify, thermoplastics do not have crosslinks; hence, they are essentially stronger than thermosets and can be easily reprocessed. In this chapter the main properties and applications of thermoplastic polymers are discussed. Suitable constitutive models, which can simulate the viscoelastic behavior of thermoplastics, are introduced along with the calibration procedure for specific materials.

3.1 Properties and applications

When considering materials for load-bearing applications, designers are increasingly examining the advantages of using thermoplastics materials, instead of traditionally accepted materials and, in particular, metals. Thermoplastics have three main advantages, their low specific gravity, their low energy requirements for manufacture and their low cost of fabrication, particularly by the injection moulding route. In Table 3.1 the main properties of the most common used thermoplastic polymers are recorded. Because of their interesting properties and their relatively ease of production, thermoplastic polymers are widely used in various industrial sectors such as in automotive, aerospace, sporting goods, consumer electronics, and many other fields. Although thermoplastics have higher strength-to-weight ratios than aluminium and steel, their main drawback is their low stiffness-to-weight ratios especially at elevated temperatures. For this reason, reinforcement of thermoplastics is crucial for achieving improved mechanical properties, so that they can be used in a variety of applications.

Polymer	Density (g cm^{-3})	Young's modulus (20^{o}C 100s) (GPa)	Tensile strength (MPa)	Fracture toughness (20^{o}C) (MPa m$^{1/2}$)	Glass temperature T_G (K)	Softening expansion temperature T_s (K)	Thermal conductivity (Wm^{-1} K^{-1})
Polyethylene, PE	0.91-0.94	0.15-0.24	7-17	1-2	270	355	0.35
Polypropylene, PP	0.91	1.2-1.7	50-70	3.5	253	31	0.2
Polystyrene, PS	1.1	3.0-3.3	35-68	2	370	370	0.1-0.15
Polyvinyl, PVC	1.4	2.4-3.0	40-60	2.4	350	370	0.15
Poly-ether-ether-ketone, PEEK	1.3-1.4	2.7-3.5	80-100	-	416	426	-

Table 3.1: Properties of common thermoplastic polymers

3.2 Modeling viscoelasticity

The behavior of a thermoplastic polymer is rather complex due to time, strain rate and temperature dependence. This complex multivariate behavior is described as viscoelastic behavior. Viscoelastic materials are distinguished from materials which are idealized as being purely elastic. They exhibit properties such as relaxation, creep, frequency dependent stiffness and dissipative characteristics as well as strain rate dependent hysteretic behavior. The mathematical models used to simulate viscoelastic materials are formulated as differential equations or convolution integrals. The latter approach is followed by the models presented in this section.

3.2.1 Basic assumptions

Formulation of constitutive models for viscoelastic polymers is based on some fundamental assumptions. Thermorheologically simple materials for which the time-temperature superposition principle is valid, are initially considered (see Schwarzl and Staverman [80]). The thermomechanically coupled process is simplified and the generation of heat is not taken into account, i.e., an isothermal situation is assumed. Furthermore, fatigue damage phenomena usually observed during the first loading cycles of polymers are not taken into account. Linear viscoelastic material models are considered in this theses, for which the Boltzmann superposition principle is applicable.

3.2.2 Elementary mechanical models

Elementary mechanical models that can describe some aspects of viscoelastic behavior of polymers are described in this section. Although these simple models are based on some fundamental assumptions and cannot represent the behavior of real polymers over the complete time history of their use, they are very helpful in gaining physical understanding of the phenomena of creep, relaxation and frequency dependent stiffness. The basic constitutive rheological elements of linear viscoelasticity are the elastic spring called Hooke-element, which represents elastic behavior, and the viscous Newton-element, which represents viscous behavior (Fig. 3.1). The spring constant E stands for the elastic modulus of a bar subjected to uniaxial tension, where the linear relation between the elastic strain ε^e and the elastic stress σ^e is derived as:

$$\sigma^e = E\varepsilon^e \tag{3.1}$$

On the other hand, the Newton-element simulates the behavior of a linear viscous damper, where a linear relation between the viscous strain rate $\dot{\varepsilon}^v$ and the viscous stress σ^v is established through the coefficient of viscosity n:

$$\sigma^v = n\dot{\varepsilon}^v \tag{3.2}$$

The Hooke and the Newton-element can be combined in a variety of arrangements in order to produce any viscoelastic response of a polymer. The simplest viscoelastic model is the Maxwell-element depicted in Fig. 3.1. This consists of a Hooke-element connected in series with a Newton-element. A relation between stress and strain can be obtained for any mechanical model by using equilibrium and kinematic equations for the system and constitutive equations for the

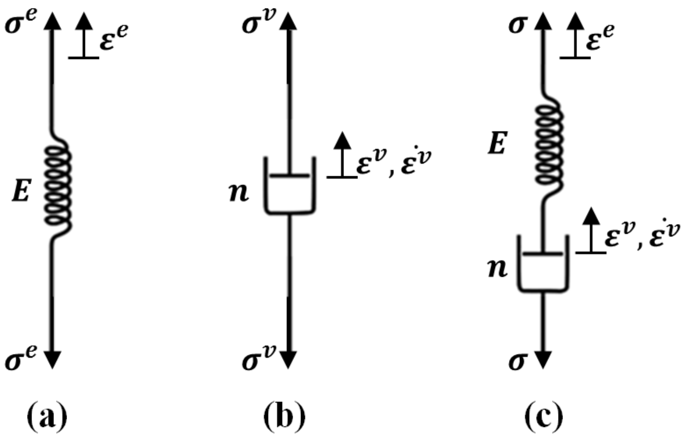

Figure 3.1: Elementary mechanical models: a) Hooke-element, b) Newton-element and c) Maxwell-element

elements. The equilibrium equation for the Maxwell model is as follows:

$$\sigma = \sigma^e = \sigma^v \tag{3.3}$$

where σ is the applied stress, σ^e is the stress in the spring and σ^v is the stress in the damper. The kinematic condition is expressed as:

$$\varepsilon = \varepsilon^e + \varepsilon^v \tag{3.4}$$

where ε is the total strain in the Maxwell-element, ε^e is the strain in the spring and ε^v is the strain in the damper. The constitutive equations are given by Eq. (3.1) and Eq. (3.2) for Hooke and Newton-element respectively. By differentiating the equilibrium and kinematic equations we get:

$$\dot{\sigma} = \dot{\sigma}^e = \dot{\sigma}^v \tag{3.5}$$

and

$$\dot{\varepsilon} = \dot{\varepsilon}^e + \dot{\varepsilon}^v \tag{3.6}$$

Combining Eqs. (3.1), (3.2), (3.5) and (3.6) the fundamental differential equation for Maxwell model is derived in the form:

$$\dot{\varepsilon} = \frac{1}{E}\dot{\sigma} + \frac{1}{n}\sigma \tag{3.7}$$

Equation (3.7) can be written after rearrangement as:

$$\dot{\sigma} + \frac{1}{\tau}\sigma = E\dot{\varepsilon} \tag{3.8}$$

where the relaxation time τ is expressed in terms of the viscosity parameter n and the elastic constant E in the form:

$$\tau = \frac{n}{E} \tag{3.9}$$

Thus, the stress-strain relation of a material which exhibits Maxwellian behavior is given by the solution of the differential equation (3.7) or (3.8) under prescribed loading conditions. For instance, a relaxation test is simulated by applying a constant strain to the Maxwell-element during the total deformation history of the solid:

$$\hat{\varepsilon}(0) = \hat{\varepsilon}(t) = \text{const} \tag{3.10}$$

For this test case the solution of the differential equation (3.8) yields:

$$\sigma_h = ce^{-\frac{t}{\tau}} \;\; \text{and} \;\; \sigma_p = 0 \tag{3.11}$$

where σ_h and σ_p are the homogeneous and the particular solution respectively. By applying the following initial conditions,

$$\text{for} \;\; t = 0, \;\; \hat{\sigma}(0) = E\hat{\varepsilon}(0) \tag{3.12}$$

the constant c in Eq. (3.11) is defined as $c = E\hat{\varepsilon}(0)$. Substituting this to the solution results to the following stress history equation:

$$\hat{\sigma}(t) = E\hat{\varepsilon}(0)e^{-\frac{t}{\tau}} \tag{3.13}$$

where the relaxation function $\hat{\Gamma}$, which characterize the viscoelastic response of the material in time domain, is defined by:

$$\hat{\Gamma}(t) = E e^{-\frac{t}{\tau}} \tag{3.14}$$

Figure 3.2 plots the relaxation behavior of a Maxwell-element in terms of stresses and strains. As shown the relaxation time τ is given by the initial slope of the stress-strain curve. From Eq. (3.13) the stress at a time equal to the relaxation time τ is derived as $\hat{\sigma}(0)/e$. This quantity can be used as a measure of the relaxation time of a polymer subjected to relaxation. Notice that as the time tends to infinity the relaxation stress of the material is fully reduced, $\hat{\sigma}(t \to \infty) = 0$.

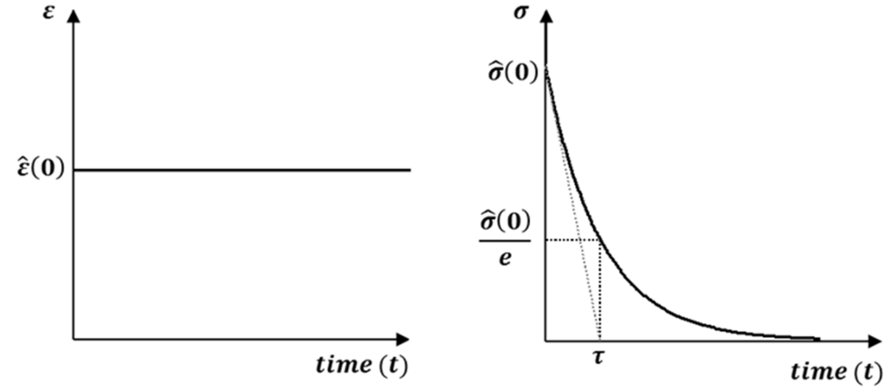

Figure 3.2: Relaxation behavior of a Maxwell-element

3.2.3 The Maxwell-Wiechert model

A real polymer does not relax with a single relaxation time as predicted by the Maxwell model of Section 3.2.2. Usually a distribution of relaxation times exists. Thus, an extension of the Maxwell model is required, so that more accurate predictions of the viscoelastic behavior of polymers can be achieved. Such an advanced viscoelastic model is the Maxwell-Wiechert model, which is formed by a finite number of separated Maxwell-elements connected in parallel with an elastic Hooke-element (see Fig. 3.3). The stress history equation for this model is given by:

$$\hat{\sigma}(t) = E_\infty \hat{\varepsilon}(0) + \sum_{j=1}^{N} E_j e^{-\frac{t}{\tau_j}} \hat{\varepsilon}(0) \tag{3.15}$$

where $\tau_j = n_j/E_j$ is the relaxation time for the j^{th} Maxwell-element, where $j = 1, ..., N$. The response of the N Maxwell-elements and that of the Hooke-element are contributed to the characteristic relaxation function of the model, which is expressed as:

$$\hat{\Gamma}(t) = E_\infty + \sum_{j=1}^{N} E_j e^{-\frac{t}{\tau_j}} \tag{3.16}$$

The instantaneous and the long term relaxation modulus of the model are defined respectively in the form:

$$\hat{\Gamma}_0 = \lim_{t\to 0} \hat{\Gamma}(t) = E_\infty + \sum_{j=1}^{N} E_j \tag{3.17}$$

$$\hat{\Gamma}_\infty = \lim_{t\to \infty} \hat{\Gamma}(t) = E_\infty \tag{3.18}$$

3.2.4 Boltzman superposition principle

The Boltzman superposition principle is one of the simplest but most powerful principles in polymer physics. Considering a creep test where a Maxwellian material is loaded by a constant stress σ_0 for a time period $t \geq t_0$, the strain history is given as:

$$\hat{\varepsilon}(t) = \hat{Y}(t - t_0)\hat{H}(t - t_0)\sigma_0 \tag{3.19}$$

where $\hat{Y}$, $\hat{H}$ are the creep compliance and the Heaviside unit step function, respectively. If an additional stress σ_1 is applied on the material at time $t \geq t_1$, then the equivalent strain response is defined by:

$$\hat{\varepsilon}(t) = \hat{Y}(t - t_0)\hat{H}(t - t_0)\sigma_0 + \hat{Y}(t - t_1)\hat{H}(t - t_1)(\sigma_1 - \sigma_0) \tag{3.20}$$

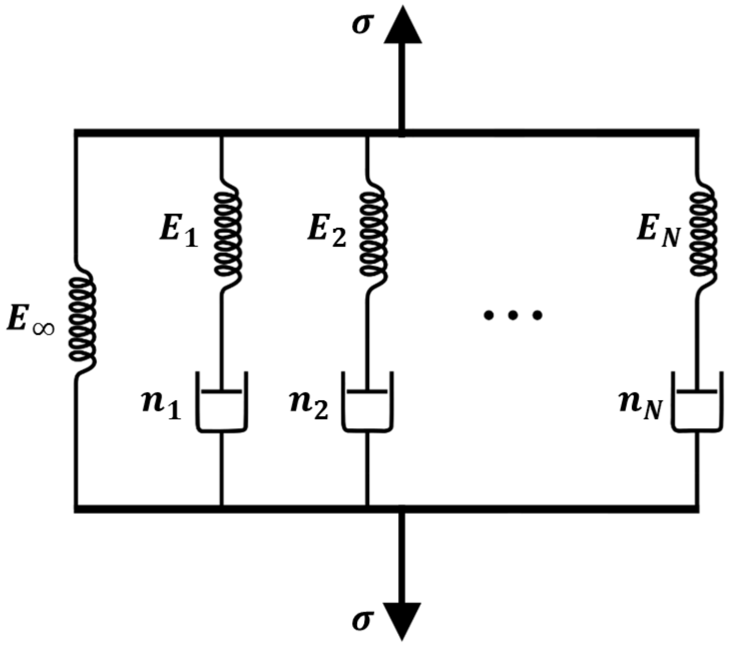

Figure 3.3: Schematic of the Maxwell-Wiechert viscoelastic model.

According to the superposition principle, the strain response of a system at $t \geq t_1$ is a superposition of the response due to the loading σ_0 applied at $t_0 \leq t < t_1$ and the response due to the loading $\Delta\sigma = (\sigma_1 - \sigma_0)$ applied at $t \geq t_1$ (see Fig. 3.4).

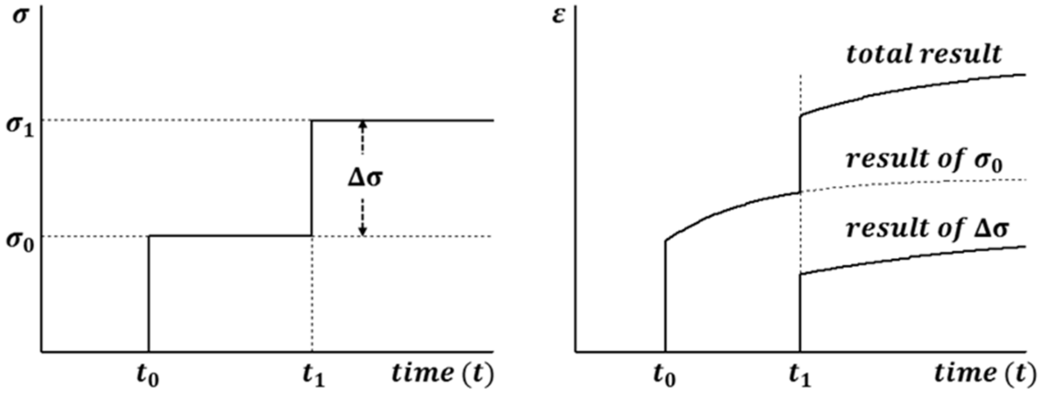

Figure 3.4: Boltzman superposition principle

The Boltzman superposition principle asserts that for a linear viscoelastic material stresses act independently and the resulting strains add linearly. So for a combined load history of the form:

$$\hat{\sigma}(t) = \sum_{i=1}^{M} \hat{H}(t - t_i)\Delta\sigma_i \tag{3.21}$$

the resulting strain is computed directly by superposition of the responses due to the separated loadings $\Delta\sigma_i$ as follows:

$$\hat{\varepsilon}(t) = \sum_{i=1}^{M} \hat{\varepsilon}(t - t_i) = \sum_{i=1}^{M} \hat{Y}(t - t_i)\hat{H}(t - t_i)\Delta\sigma_i \tag{3.22}$$

Assuming infinitesimal loading steps, the total strain is determined by the integral equation:

$$\hat{\varepsilon}(t) = \int_0^t \hat{Y}(t - s)\hat{H}(t - s)\, d\hat{\sigma}(s) \tag{3.23}$$

If the stress history is differentiable with respect to time then the above hereditary integral is reduced to:

$$\hat{\varepsilon}(t) = \int_0^t \hat{Y}(t - s)\frac{\partial\sigma}{\partial s}\, ds \tag{3.24}$$

An equivalent integral representation for the stress history is defined in case of a relaxation test as:

$$\hat{\sigma}(t) = \int_0^t \hat{\Gamma}(t - s)\frac{\partial\varepsilon}{\partial s}\, ds \tag{3.25}$$

where $\hat{\Gamma}(t-s)$ is the relaxation function. Creep and relaxation are merely two different aspects of viscoelasticity. The transition from one property to the other can be done through an integral relationship which is known as convolution integral and is expressed in the form:

$$t = \int_0^t \hat{\Gamma}(s)\, \hat{Y}(t - s)\, ds \tag{3.26}$$

This convolution integral, which is used to transform creep data to relaxation data and vice versa, can be derived using inverse Laplace or Fourier transforms.

3.2.5 Dynamic Mechanical Analysis

In previous sections, the viscoelastic behavior of polymers subjected to creep or relaxation tests was described in time domain. However, viscoelasticity is better understood when is formulated at frequency domain. Thus, viscoelastic properties of polymers are studied by dynamic mechanical analysis (DMA), where a sinusoidal force (or stress σ) is applied to a material and the resulting displacement (or strain ε) is measured. For a perfectly elastic solid, the resulting strain and the applied stress will be perfectly in phase. For a purely viscous fluid, there will be a 90° phase lag of strain with respect to stress. Viscoelastic polymers have the characteristics in between, where some phase lag will occur during DMA tests. Specifically, in the case of an oscillating load, which is expressed by the periodic stress:

$$\sigma = \sigma_0 \cos \omega t \tag{3.27}$$

where σ_0 is the amplitude and ω is the load frequency of the oscillation, the resulting strain oscillates at the same frequency ω but lags behind the stress by the phase shift δ:

$$\varepsilon = \varepsilon_0 \cos(\omega t - \delta) \tag{3.28}$$

To describe an harmonic vibration, it is useful to represent the oscillation by a rotating vector in the complex plane. This complex vector can be expressed in polar form and can be written in terms of trigonometric functions using the Euler relationship:

$$e^{i\omega t} = \cos \omega t + i \sin \omega t \tag{3.29}$$

where i is the imaginary unit which satisfies the equation $i^2 = -1$. Equations (3.27) and (3.28) can be expressed in polar form as:

$$\sigma = \sigma_0 e^{i\omega t} \tag{3.30}$$

$$\varepsilon = \varepsilon_0 e^{i(\omega t - \delta)} \tag{3.31}$$

The phase shift δ, which is often called loss angle, is an important quantity in the viscoelastic material characterization. It is responsible for the observed hysteresis loop in the stress-strain curve of a material under an harmonic vibration. The area filled up by this hysteresis loop is a measure of the dissipated energy of the material per loading cycle.

The frequency based formulation of viscoelasticity is then applied to the Maxwell-element described in Section 3.2.2. Thus, rearranging Eq. (3.8) the differential equation of the Maxwell model is written as:

$$\tau E\dot{\varepsilon} = \tau\dot{\sigma} + \sigma \tag{3.32}$$

Substituting the polar expression of stress and strain to the above equation results to:

$$i\,\omega t E\varepsilon_0 = \sigma_0(1 + i\,\omega\tau)e^{i\delta} \tag{3.33}$$

From Eq. (3.33) the complex relaxation modulus for the Maxwell model can be obtained in the form:

$$\Gamma^* = \frac{\sigma_0}{\varepsilon_0}e^{i\delta} = E\frac{i\,\omega\tau}{1 + i\,\omega\tau} \tag{3.34}$$

The complex modulus Γ^* can be split into a real and an imaginary part as:

$$\Gamma^* = \Gamma' + i\,\Gamma'' = E\frac{\omega^2\tau^2}{1 + \omega^2\tau^2} + i\,E\frac{\omega\tau}{1 + \omega^2\tau^2} \tag{3.35}$$

where the components Γ' and Γ'' are called storage and loss modulus, respectively. These moduli, along with the mechanical loss factor

$$\tan\delta = \frac{\Gamma''}{\Gamma'} = \frac{1}{\omega\tau} \tag{3.36}$$

which is defined as the ratio of imaginary Γ'' and real part Γ', are all functions of frequency ω.

In the case of Maxwell-Wiechert model, where N Maxwell-elements are connected in parallel with an elastic spring E_∞ (see Fig. 3.3), the complex relaxation modulus is defined as:

$$\begin{aligned}\Gamma^* &= \Gamma' + i\,\Gamma'' \\ &= E_\infty + \sum_{j=1}^{N} E_j \frac{i\,\omega\tau_j}{1 + i\,\omega\tau_j} \\ &= E_\infty + \sum_{j=1}^{N} E_j \frac{\omega^2\tau_j^2}{1+\omega^2\tau_j^2} + i\sum_{j=1}^{N} E_j \frac{\omega\tau_j}{1+\omega^2\tau_j^2}\end{aligned} \tag{3.37}$$

Notice that the complex relaxation function (3.37) can be directly derived at frequency domain by applying a Fourier transform of the time-dependent relaxation function (3.16).

3.2.5.1 Master curves of viscoelastic materials

Viscoelastic material characterization requires measurements of elastic moduli over a large range of time or frequency. Notice that time and frequency are equivalent reciprocal quantities. For technical reasons, elastic moduli are determined only within a limited range of time or frequency but within a wide range of temperature. Thus, at a reference temperature T_1, a master curve of a viscoelastic material can be experimentally determined, by shifting the measured values by a factor α_T according to the time-temperature correspondence principle. In this way, the master curve of the material is derived as a continuous graph of its elastic moduli over a wide range of time or frequency. Different master curves are obtained, depending on the reference temperature T_1 for which they are constructed. Figure 3.5 illustrates how the time-temperature correspondence principle for modulus $\hat{M}$ of a material is employed in order to construct its master curve. This principle is described by the following equation:

$$\hat{M}(T_1, t) = \hat{M}\left(T_2, \frac{t}{\alpha_T}\right) \tag{3.38}$$

The values of $\hat{M}$ measured at temperature T_2 are shifted in time or frequency space by a factor α_T, so as from Eq. (3.38) the equivalent values of $\hat{M}$ at temperature T_1 can be calculated. This shifting procedure is repeated for all the experimental values measured at temperatures T_3 and T_4 in Fig. 3.5, so that the master curve of the material at reference temperature T_1 can be constructed. Many expressions of the factor α_T, which shifts the modulus $\hat{M}$ along the time or frequency scale according to the temperature increment, have been introduced in literature. Williams, Landel and Ferry (1955) [102] introduced a quantitative relation for the correspondence principle named after them as WLF equation. The shifting factor α_T in the WLF equation is given explicitly by

$$\log\alpha_T = -\frac{17.4\,(T - T_G)}{51.6 + (T - T_G)} \tag{3.39}$$

which is a function of temperature T. The constants 17.4, 51.6 vary slightly from polymer to polymer and thus the only material parameter required is the glass transition temperature T_G. This parameter serves as the reference temperature for which the master curve of the polymer is constructed and is equivalent to the temperature T_1 in Fig. 3.5.

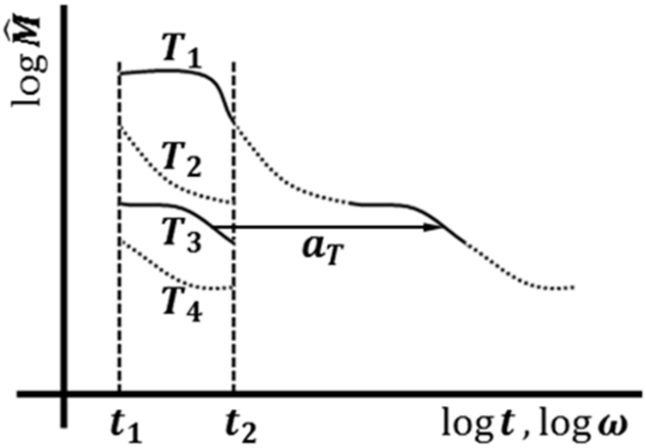

Figure 3.5: Time-temperature correspondence principle

3.2.6 Calibration of Maxwell-Wiechert model for PEEK

The master curves of a material, which are constructed following the experimental procedure of Section 3.2.5.1, are used in viscoelastic material characterization. In the case of a viscoelastic material, which is simulated by the Maxwell-Wiechert model, a nonlinear least-squares algorithm is used in order to define the unknown relaxation times τ_j and the elastic spring constants E_j of Eq. (3.15). The numerical master curves, which are constructed by using the aforementioned defined parameters, are the most accurate ones, which best fit to the experimental master curves. In this section the experimental master curves of PEEK will be used to demonstrate the calibration procedure. The error function which has to be minimized is:

$$R^2 = \sum_{i=1}^{M} \frac{1}{\hat{\Gamma}_{\infty}^2} \left[\left(\Gamma' - \bar{\Gamma}' \right)_i^2 + \left(\Gamma'' - \bar{\Gamma}'' \right)_i^2 \right] \tag{3.40}$$

where Γ' and Γ'' are the numerical predicted storage and loss modulus values of PEEK, while $\bar{\Gamma}'$ and $\bar{\Gamma}''$ are the corresponding experimental data measured at M values of frequency. The master curves of PEEK have been derived from DMA tests which have been conducted by Prof. Evangelia Kontou in the laboratory of mechanics at the School of Applied Mathematics and Physical Sciences of National Technical University of Athens. The results are illustrated in Fig. 3.6 and 3.7, where the values of storage and loss tensile modulus are depicted with respect to frequency ω in logarithmic axes. The numerical master curves, which are also plotted in these figures, seems to be very close to the experimental ones verifying the efficiency of the calibration procedure of PEEK. The instantaneous Young's modulus of the material corresponds to the value of the storage tensile modulus at the highest frequency. From the corresponding master curve this is found to be $E_0 \simeq 2.8$ GPa. The parameters of the Maxwell-Wiechert model for PEEK derived after minimization of the error function (3.40) are recorded in Table 3.2. The nonlinear least-squares fitting algorithm for PEEK results in twelve Maxwell-elements. Each of these elements contribute to the total viscoelastic response of PEEK as shown in Fig. 3.6 and 3.7. Notice that the parameter identification is conducted on the basis of the storage modulus $\bar{\Gamma}'$. This fact leads to some unavoidable discrepancies between the numerical predicted and the experimental values of the loss modulus $\bar{\Gamma}''$.

Using the parameters recorded in Table 3.2 the long term tensile modulus of

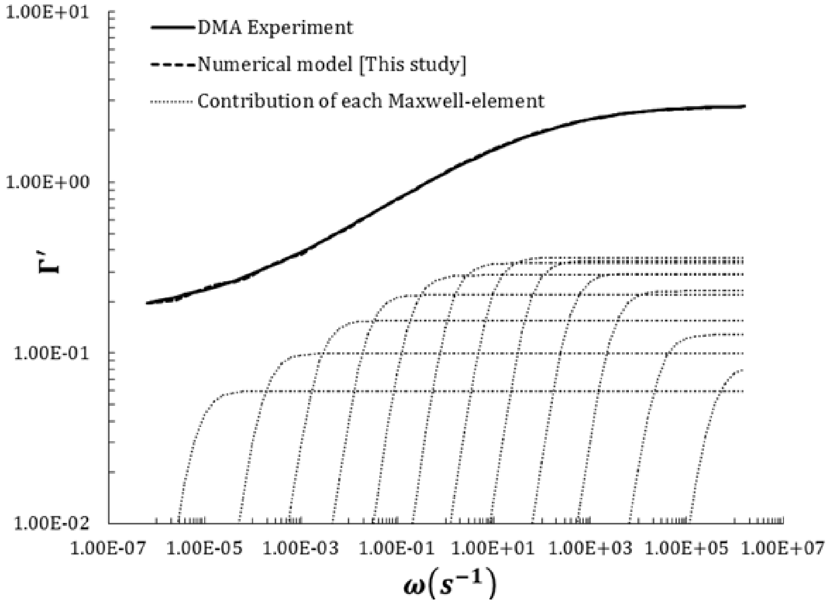

Figure 3.6: Storage modulus: experimental master curve vs mathematical model

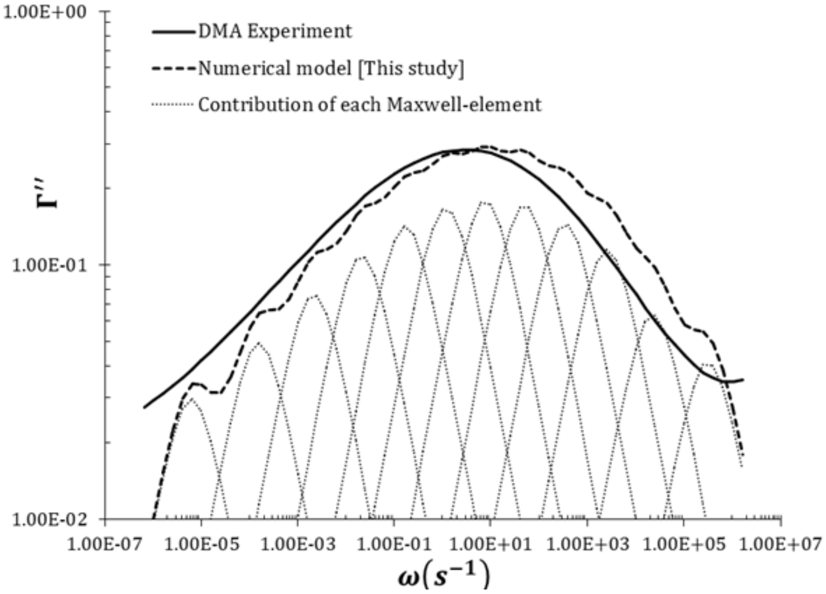

Figure 3.7: Loss Modulus: experimental master curve vs mathematical model

PEEK can be calculated as:

$$E_\infty = E_0 \left(1 - \sum_{j=1}^{N} E_j \right) \tag{3.41}$$

j	E_j [GPa]	τ_j	j	E_j [GPa]	τ_j
1	8.31E-02	1.42E-06	7	3.35E-01	3.77E-01
2	1.28E-01	1.96E-05	8	2.84E-01	2.65E+00
3	2.29E-01	1.74E-04	9	2.19E-01	2.12E+01
4	2.92E-01	1.30E-03	10	1.54E-01	2.09E+02
5	3.47E-01	8.85E-03	11	9.91E-02	2.88E+03
6	3.60E-01	5.78E-02	12	5.97E-02	7.16E+04

Table 3.2: Parameters of Maxwell-Wiechert model for PEEK

Then, from Eq. (3.16) the time dependent relaxation modulus of PEEK can be determined. Creep tests on PEEK specimens are simulated by applying the convolution integral of Eq. (3.26) in order to compute the compliance modulus of the material. Experimental results obtained from creep tests on laminated PEEK specimens have been provided by Victrex (`http://www.victrex.com`). The geometry of the specimens used in these experiments along with the mesh of the FE model used in the numerical analysis are illustrated in Fig. 3.8. Plane stress quadrilateral elements with a global size of 3 mm are used for the discretization of the specimen. Figure 3.9(a) plots the strain history obtained from various creep tests. Each curve corresponds to different constant applied stress magnitudes ranging from 20 to 60 MPa. The numerical curves predicted by the Maxwell-Wiechert model are presented in Fig. 3.9(b) . As it can be observed from these figures, the Maxwell-Wiechert model is also capable of accurate simulation of the creep behavior of PEEK for each stress magnitude. Figure 3.10 plots the tensile isochronous stress-strain curves of PEEK derived after creep tests. Both the experimental and numerical curves have been obtained by applying a constant stress of 50 MPa on the specimen of Fig. 3.8 for a time period ranging from 0.01 to 1000 hours at room temperature. Once again, for these test cases comparison between the measured and predicted results confirm the validity of the Maxwell-Wiechert model in simulating viscoelastic response of PEEK. In Appendix A the viscoelasticity theory is explained in detail where the appropriate viscous equations for both triaxial and reduced states of stress are presented.

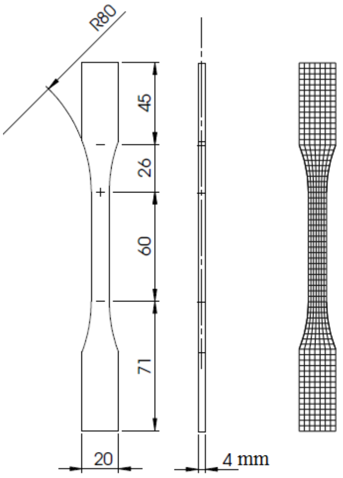

Figure 3.8: Geometry and FE mesh of specimen used in creep tests

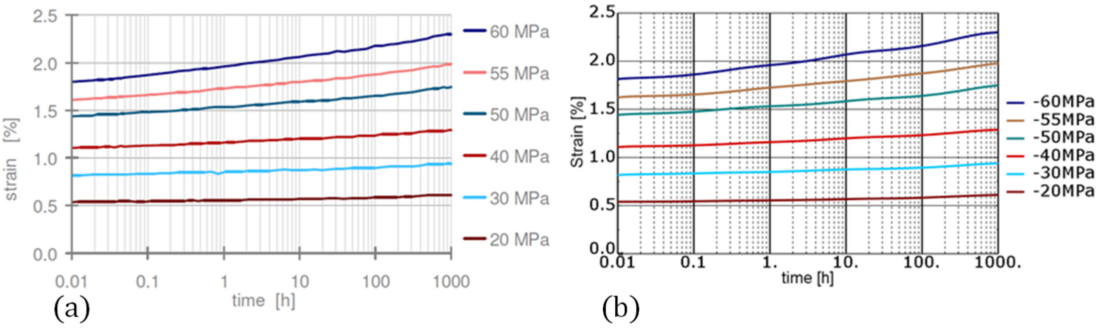

Figure 3.9: Strain history of PEEK obtained from creep tests: a) Experiments and b) Simulations

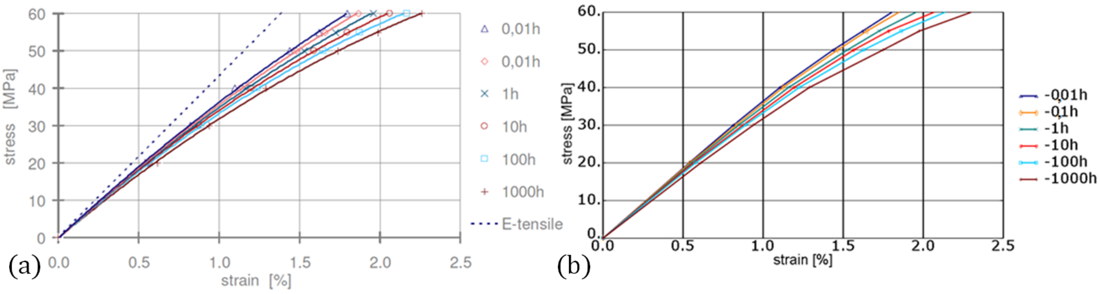

Figure 3.10: Tensile isochronous stress-strain curves of PEEK: a) Experiments and b) Simulations

Chapter 4

Carbon nanotube-reinforced composites

The significant mechanical and physical properties of CNTs described in Chapter 2, as well as their high aspect ratio and low density, make CNTs ideal reinforcements for nanocomposites. Unlike conventional fiber-reinforced composites, CNTs due to their small size, interact with polymer chains through weak van der Waals forces, leading to marginal enhancement of the mechanical properties of the polymer matrices. However, experimental evidence [70, 98, 114] demonstrated that if functionalization techniques are applied on the surface of carbon nanotubes, higher interfacial shear strength (ISS) can be achieved, leading to improved stiffness and damping properties of the CNT-RC materials.

In this chapter, the effect of the ISS on the mechanical and damping properties of CNT-RCs is investigated using a multiscale modeling approach. Furthermore, for the CNT-RC material characterization a nonlinear hierarchical multiscale approach is proposed, considering slippage at CNT/polymer interface. The presented multiscale modeling strategy encompasses various length scales, from nano to micro to macro. A schematic representation of all the multiscale modeling steps followed for the simulation of the CNT-RC material is illustrated in Fig. 4.1.

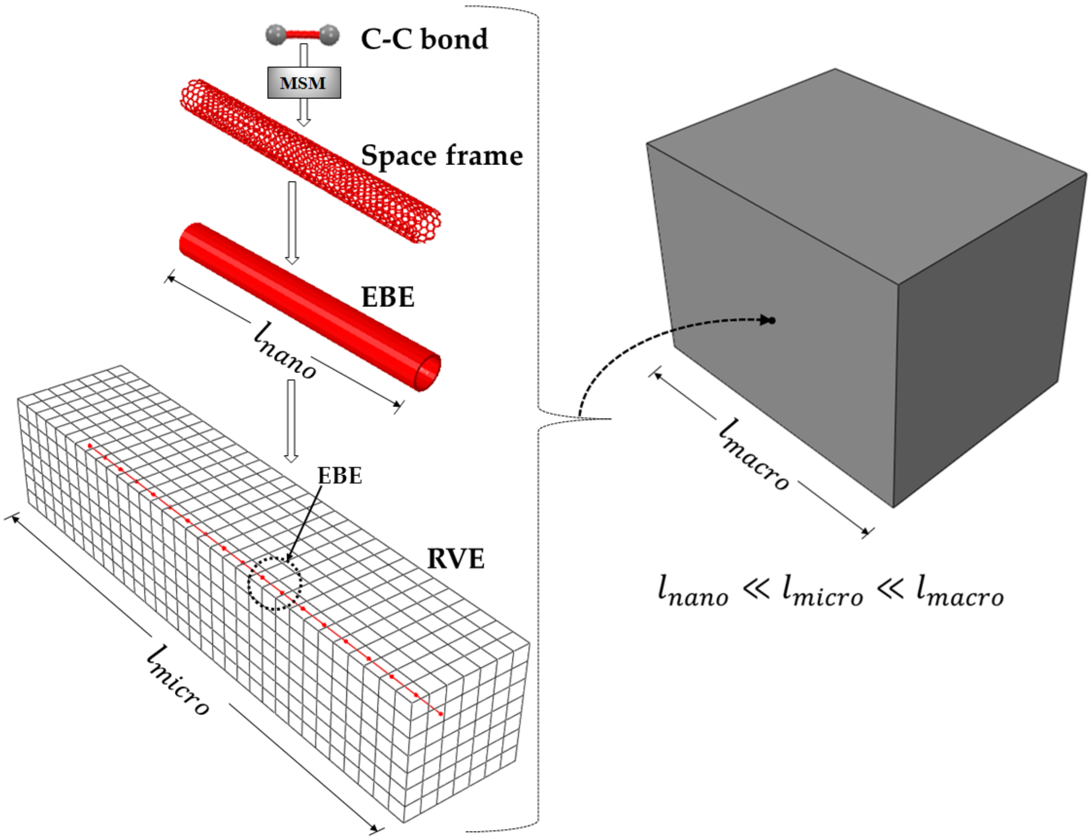

Figure 4.1: Multiscale modeling steps for simulation of CNT-RCs

4.1 Modeling RVEs of CNT-RC

As shown in Section 2.2.1, the atomic lattice of a CNT is modeled by the molecular structural mechanics (MSM) approach as a space frame structure, which is then reduced to an equivalent beam element (EBE). This EBE is used as the basic building block for the construction of full length CNTs embedded in the polymer matrix (Fig. 4.1). Linear material properties are assigned to the EBEs, while the Maxwell-Wiechert model of Section 3.2.3 is assigned to the polymer matrix in order to model its viscoelastic behavior. The interfacial load transfer mechanism between the lateral surface of the carbon nanotube and the surrounding matrix is taken into account with a nonlinear bond-slip interfacial model. Finite element models of representative volume elements (RVEs) are constructed comprised of two independent meshes: a structured with solid elements for the matrix and a series of embedded EBEs for the full length CNTs (see Fig. 4.1). Straight as well as wavy CNTs are considered. In the case of wavy CNTs, random CNT geometries are generated using the spectral representation method with evolutionary power spectra (EPS) which are derived from processing scanning electron microscope (SEM) images. Average mechanical properties of CNT-RC materials are obtained after a stochastic analysis based on the Monte Carlo simulation (MCS). The mechanical and damping properties of the CNT-RCs are assessed on the basis of sensitivity analyses with respect to various weight fractions (wt) and interfacial shear strength (ISS) values. Numerical results are presented, showing the significant effect of the ISS as well as the influence of CNT waviness on the damping behavior of CNT-RCs.

4.1.1 Equivalent beam element for space frame CNT model

Although the MSM approach overcomes the restrictions of the MD method in time and size-scales, the analysis of the space frame model of a full length CNT demands a huge computational effort. For example a CNT of 14 nm in diameter and 1 μm in length corresponds to a numerical problem in the order of 10^7 degrees of freedom. Thus, the analysis of a CNT-RC with only 1 wt% of CNTs is computationally an extremely demanding task. For this reason, the detailed MSM model of the CNT is further reduced to an EBE with equivalent material properties. In order to derive the stiffness properties of the linear EBE, the space frame model of the CNT is subjected to three independent loading conditions, namely tension, bending and torsion (see Section 2.2.1.4).

In order to derive the elastic moduli from the rigidities $(EA)_{eq}$, $(EI)_{eq}$ and $(GJ)_{eq}$ defined from Eqs. (2.21), (2.22) and (2.23) respectively in Section 2.2.1.4, a profile-shaped cross-section of the EBE must be assumed. For instance, if a EBE with a pipe-shaped profile is selected, then its cross-sectional properties are given by

$$A_{eq} = \frac{\pi}{4}\left[(d_{eq}+t)^2 - (d_{eq}-t)^2\right] \tag{4.1}$$

$$I_{eq} = \frac{\pi}{64} 2 \left[(d_{eq} + t)^4 - (d_{eq} - t)^4 \right] \quad \text{and} \quad J_{eq} = 2I_{eq} \tag{4.2}$$

where the equivalent mean diameter d_{eq} of the beam pipe is calculated from the axial and bending rigidities, for arbitrarily selected wall thickness t:

$$d_{eq} = \sqrt{8 \frac{(EI)_{eq}}{(EA)_{eq}} - t^2} \tag{4.3}$$

The Young's moduli of pipe EBEs, which correspond to armchair $(8,8)$ CNTs with various wall thickness values, have been computed using Eqs. (4.1)-(4.3). These values are compared with various results obtained from different methodologies in literature, including MD simulation, tight-binding models, ab initio computations and others [38, 29, 45, 50, 52, 64, 65, 97, 105, 104]. In Table 4.1 calculated Young's moduli corresponding to different wall thickness values are recorded, allowing for a direct comparison between the results obtained applying the method in the present study and the other methods in literature. In addition, the results of the aforementioned comparison are graphically depicted in Fig. 4.2.

Investigators	Method	Wall thickness (nm)	Young's modulus (TPa)	
			Literature	Present study
Yakobson et al [105]	Molecular dynamics	0.066	5.5	5.698
Xin et al [104]	Tight-binding model	0.074	5.1	5.082
Tu and Ou-Yang [97]	Local density approximation model	0.075	4.7	5.015
Kudin et al [45]	Ab initio computations	0.089	3.859	4.226
Pantano et al [65]	Continuum shell modeling	0.075	4.84	5.015
Li and Chou [50]	Structural mechanics: stiffness matrix method	0.34	1.01	1.106
Lu [52]	Molecular dynamics	0.34	0.974	1.106
Hernandez et al [29]	Tight binding molecular dynamics	0.34	1.24	1.106
Jin and Yuan [38]	Molecular dynamics	0.34	1.238	1.106
Odegard et al [64]	Equivalent-continuum modeling	0.69	-	0.545
Present study	MSM	0.147	-	2.558

Table 4.1: Young's moduli of armchair $(8,8)$ CNTs with various wall thickness values computed by different methodologies

The effect of diameter and chirality of the CNTs on the elastic moduli of the resulting EBEs are investigated in this study. Specifically, two types of SWCNTs, namely armchair (n,n) and zigzag $(n,0)$, with diameters ranging from 0.3 to 14 nm are included in the investigation. In all cases, the wall thickness is 0.34

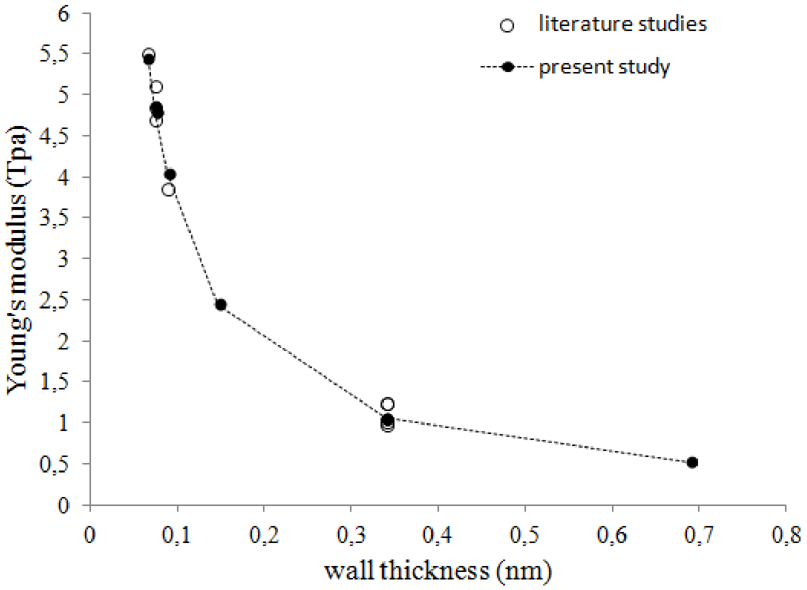

Figure 4.2: Young's modulus vs wall thickness t of a pipe EBE representing armchair $(8,8)$ CNT

nm, which corresponds to the interlayer spacing of graphite. Figure 4.3 plots the Young's moduli of both the armchair and zigzag CNTs with respect to their diameters. A strong effect of diameter can be observed, especially for small values, on the Young's moduli of both chirality types CNTs. By increasing their diameters, their Young's moduli are also increasing, reaching a plateau. This tendency is due to the effect of curvature as Li and Chou [50] have pointed it out in their study. The smaller the diameter of the nanotube is, the higher is its curvature leading to large distortions of the carbon-carbon (C-C) bonds and thus in large elongation of the MSM lattice model. As the diameter of the CNT increases, the effect of curvature diminishes and its Young's modulus approaches that of the graphene sheet (1.1 TPa), where no effect of curvature is present. Figure 4.4 displays the shear moduli of both armchair and zigzag CNTs with respect to their diameters. As it can be observed from this figure, the shear moduli of the CNTs depend strongly on their diameters and weakly on their chirality. This is also verified by Li and Chou [50]. This sensitivity of shear moduli of CNTs on their diameters is due to the effect of curvature. By increasing their diameters, their shear moduli are also increasing for both chirality types, reaching to a plateau value which corresponds to the shear modulus of graphite (0.5 TPa).

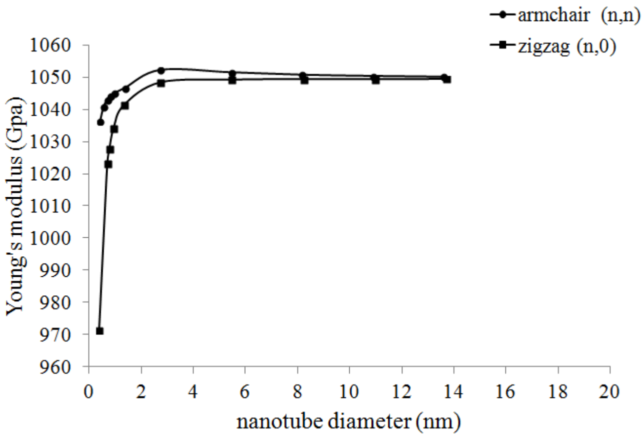

Figure 4.3: Young's modulus vs diameter of armchair and zigzag CNTs

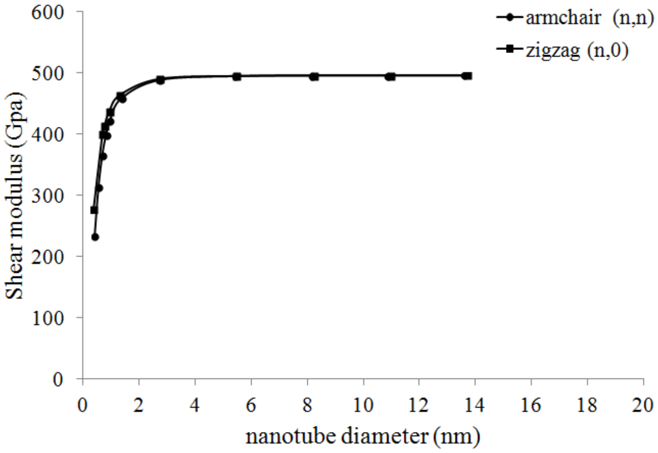

Figure 4.4: Shear modulus vs diameter of armchair and zigzag CNTs

4.1.2 Stochastic modeling of CNT waviness

Random waviness of CNTs is modeled as a non-homogeneous stochastic field using the spectral representation method in conjunction with evolutionary power spectra (EPS). The statistical properties of the EPS are derived from scanning electron microscope (SEM) images of CNT-RCs, by processing the geometry of a number of wavy CNTs (see Fig. 4.5).

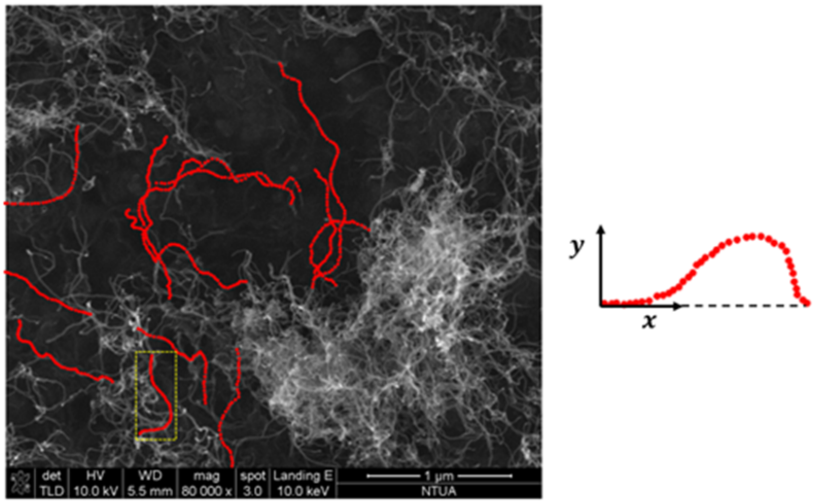

Figure 4.5: SEM image of CNT-RC, processing the geometry of wavy CNTs

4.1.2.1 Method of separation

The EPS depend not only on frequency ω but also on spatial state variables. In case of separable or approximately separable EPS, which is definitely the case of geometric imperfections [78], the corresponding EPS can be expressed as the product of a homogeneous power spectrum $S_h(x)$ and a spatial envelope function $g_h(x)$ as follows:

$$S(\omega, x) = S_h(\omega) \cdot g_h(x) \tag{4.4}$$

Notice that CNT waviness can be regarded as a geometric imperfection of a identical straight tube. Various methodologies have been proposed in the past for estimating EPS from available experimental measurements, i.e., from real samples of stochastic signals. Among them the most widely used are the short-time Fourier transform and the wavelet-based EPS estimation [14, 53, 63, 85]. The basic disadvantage of these approaches is that they cannot achieve simultaneous resolution in space and frequency domains. A novel methodology was proposed in Schillinger and Papadopoulos [78] to obtain estimates of EPS of separable processes. This method is based on simple principles of stochastic process theory and for this reason it is easy to implement as well as computationally efficient, while at the same time proved to be accurate enough with optimum simultaneous resolution in space and frequency [9, 78, 79]. According to this approach an estimate of the first term in Eq. (4.4) can be readily obtained by averaging the periodograms over the ensemble:

$$\bar{S}_h(\omega) = E\left[\frac{1}{2\pi L}\left|\int_0^L f^{(i)}(x)\cdot e^{-i\omega x}dx\right|\right] \tag{4.5}$$

where $f^{(i)}(x)$ is a sample of the stochastic field (in particular the wavy geometry of the i^{th} CNT) and $E[\cdot]$ denotes the mathematical expectation. An estimate of the spatial envelope function can be obtained from the distribution of the mean square over the samples as follows:

$$\bar{g}_h(x) = \frac{E\left[\left|f^{(i)}(x)\right|^2\right]}{2\int_0^\infty \bar{S}_h(\omega)d\omega} \tag{4.6}$$

It can be easily shown that an unbiased estimate of the evolutionary power spectra can be obtained as follows:

$$\bar{S}(\omega, x) = E\left[\left|f^{(i)}(x)\right|^2\right]\frac{\bar{S}_h(\omega)}{2\int_0^\infty \bar{S}_h(\omega)d\omega} \tag{4.7}$$

After the estimation of the EPS by processing the geometry of the wavy CNTs in Fig. 4.5, samples of wavy CNTs can be generated as follows:

$$\hat{f}^{(j)}(x) = \sqrt{2}\sum_{n=0}^{N-1} A_n \cos\left(\omega_n x + \phi_n^{(j)}\right) \tag{4.8}$$

where

$$
\begin{aligned}
&A_n = \sqrt{2\bar{S}(\omega_n, x)\Delta\omega} && n = 0, 1, ..., N-1 \\
&\omega_n = n\Delta\omega && n = 0, 1, ..., N-1 \\
&\Delta\omega = \frac{\omega_{up}}{N} && \\
&A_0 = 0, \quad \bar{S}(\omega_0, x) = 0 &&
\end{aligned}
\tag{4.9}
$$

The parameter ω_{up} refers to an upper limit of the frequency beyond which the autocorrelation function is supposed to be zero. Parameter $\phi_n^{(j)}$ stands for random phase angles with $\phi_n \in U\,[0, 2\pi]$, for each j^{th} realization.

Figure 4.6 presents the EPS estimated from Eq. (4.7), while some realizations of wavy CNTs which have been generated using Eq. (4.8), are plotted in Fig. 4.7. As it can be seen in this figure, a 3D spatial waviness is considered by assuming that the coordinates $z = z(x)$ and $y = y(x)$ of the CNT are independent stochastic fields generated from Eq. (4.8). Discretization of full length wavy CNTs is performed through short straight EBEs.

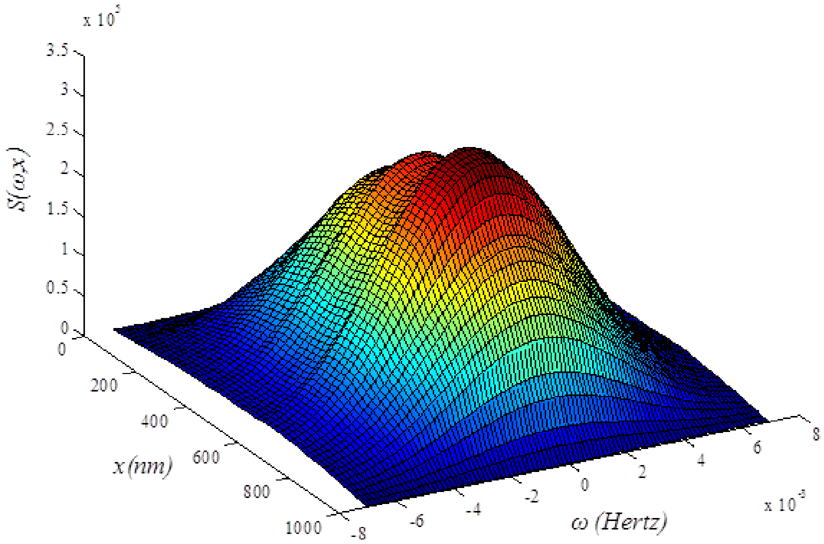

Figure 4.6: EPS for wavy CNTs derived after the method of separation

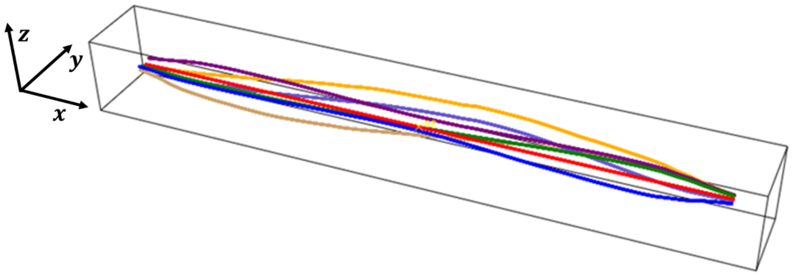

Figure 4.7: Sample of wavy CNT realizations.

4.1.3 Embedded element technique

The embedded element technique is used to specify that an element or group of elements is embedded in "host" elements. This technique has been used in many studies to model rebar reinforcement in concrete [36, 54]. In the context of FE analysis of RVEs of CNT-reinforced composites, the embedded element technique is also applied so as complicated mesh discretizations of the RVE models to be avoided. Initially, this method searches for geometric relationships between nodes of the embedded elements and the host elements. If a node of an embedded element lies within a host element, the translational degrees of freedom (dofs) at the node are eliminated and the node becomes an "embedded node". The translational dofs of the embedded node are constrained to the interpolated values of the corresponding dofs of the host element. Embedded elements are allowed to have rotational dofs, but these rotations are not constrained by the embedding. Figure 4.8 illustrates an EBE element which has both its nodes i and j embedded in a 8-noded solid elemen, which is used to model the polymer matrix. The stiffness matrix of the EBE is calculated in the global coordinate system (XYZ) as follows:

$$K^B = T^T k^b T = T^T \left[\int_{V_e} B^T D B dV_e \right] T \tag{4.10}$$

where k^b is the local stiffness matrix of the beam and T is the transformation matrix which performs the transformation from local to global coordinate system. The matrix D corresponds to the elasticity matrix of the beam while the matrix B

contains the derivatives of the shape functions of the beam element, which relate the strains of the element to its displacements or rotations. The translation dofs of the beam element are constrained to the nodal displacements of the host solid element according to the following restrain:

$$\begin{bmatrix} u_i \\ u_j \\ v_i \\ v_j \\ w_i \\ w_j \end{bmatrix} = \begin{bmatrix} N^M & \varnothing & \varnothing \\ \varnothing & N^M & \varnothing \\ \varnothing & \varnothing & N^M \end{bmatrix} \begin{bmatrix} U^M \\ V^M \\ W^M \end{bmatrix} \tag{4.11}$$

where

$$N^M = \begin{bmatrix} N_1^i \; ... \; N_8^i \\ N_1^j \; ... \; N_8^j \end{bmatrix} \tag{4.12}$$

with N_n^i and N_n^j, $n = 1, ..., 8$ the values of the n^{th} nodal shape function of the solid element, evaluated at its interior points i and j, which are the points where the nodes of the embedded beam element are lying (see Fig. 4.8). The nodal displacements of the host solid element are contained in the vectors:

$$U^M = \begin{bmatrix} U_1 \; ... \; U_8 \end{bmatrix}^T, \;\; V^M = \begin{bmatrix} V_1 \; ... \; V_8 \end{bmatrix}^T, \;\; W^M = \begin{bmatrix} W_1 \; ... \; W_8 \end{bmatrix}^T \tag{4.13}$$

The deformation matrix B of Eq. (4.10), which contains the derivatives of the interpolated local dofs of the beam element, can be expressed in terms of the global dofs of the host element using Eq. (4.11). After some manipulations, an extended stiffness matrix $\bar{K}^B$ of size (30×30) for the beam element is derived. This matrix contains terms that relate the 24 translations $\left[U^M, \, V^M, \, W^M\right]$ of the host element and the 6 rotations $[\theta_{Xi}, \, \theta_{Yi}, \, \theta_{Zi}, \, \theta_{Xj}, \, \theta_{Yj}, \, \theta_{Zj}]$ of the beam element with the external applied unit nodal forces and moments, respectively. Finally, the stiffness matrix of the "super" element, which is assembled by the stiffness matrices of both the embedded and host elements is formulated as:

$$K_{(30\times30)} = \begin{bmatrix} K^M + \bar{K}^B_{TT} & \bar{K}^B_{TR} \\ \bar{K}^B_{RT} & \bar{K}^B_{RR} \end{bmatrix} \tag{4.14}$$

where K^M is the stiffness matrix of the solid element and is of size (24×24); $\bar{K}^B_{TT}$ is the (24×6) submatrix of the extended (30×30) stiffness matrix $\bar{K}^B$ of the beam element related only to its translation dofs; Accordingly, $\bar{K}^B_{RR}$ is the (6×6) submatrix related only to the rotation dofs of the beam element; and $\bar{K}^B_{TR}$ and $\bar{K}^B_{RT}$ are the (24×6) and (6×24) submatrices respectively, which contain the interactions between the translation and rotation dofs of the beam element.

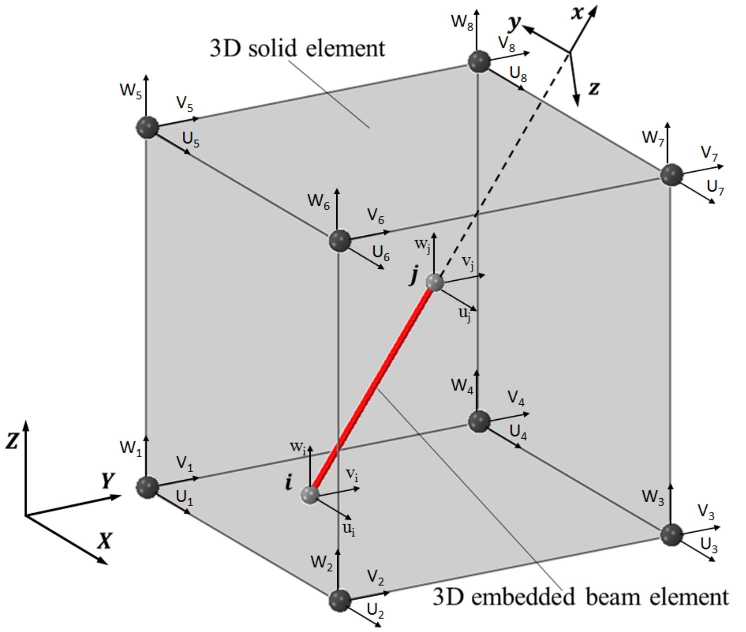

Figure 4.8: Illustration of the embedded beam element into host solid element

4.1.4 Interfacial bond-slip model

The mechanical and damping properties of the CNT-RC material are sensitive to the interfacial characteristics between the CNT and the polymer matrix. Loads are transferred from polymer to CNTs through their interface. Experimental evidence [70, 98, 114] verify that if functionalization techniques are applied on the surface of carbon nanotubes, then higher interfacial shear strength can be achieved. The advanced adhesion characteristics attained by functionalization, combined with the high aspect ratio of CNTs, can lead to composites with enhanced stiffness and damping properties.

Pullout tests [24, 3, 68, 77] on CNT-RCs have revealed a stick-slip behavior of the CNTs inside the polymer matrix. To capture this cohesive behavior, a nonlinear friction-type bond-slip model is incorporated in the mulitscale analysis of the CNT-RCs. The model has been initially incorporated in the finite element analysis software program "ATENA", and has been applied in order to describe cohesion between steel reinforcing bars and concrete (`www.cervenka.cz/products/atena`). Phenomenologically, the nanoscale problem of CNT-RCs is similar to that of any fiber-reinforced composite material, such as reinforced concrete, at the mesoscale. The adopted solution is fairly simple and can provide results with high accuracy at low computation cost. Figure 4.9 depicts a model of a RVE consisted of one straight CNT discretized by three connected EBEs. The EBEs, which have pipe cross-sections, are embedded in the polymer matrix. Solid elements are used for the discretization of the matrix. The equilibrium equation for the central EBE can be written as:

$$\left|\sigma_{Ri} - \sigma_{Li}\right| A_i = \tau_i \pi \left(D_i + t_i\right) l_i \tag{4.15}$$

where A_i is the cross-sectional area of the beam element, $D_i + t_i$ is the outer diameter of its pipe-section profile and l_i is its reference length. A smoothing operation on the nodal axial stresses σ_{Ri} and σ_{Li}, which act on the right and the left end-sections of the beam element, respectively, is performed in the form:

$$\sigma_{Ri} = \frac{\sigma_i l_i + \sigma_{i+1} l_{i+1}}{l_i + l_{i+1}} \tag{4.16}$$

$$\sigma_{Li} = \frac{\sigma_i l_i + \sigma_{i-1} l_{i-1}}{l_i + l_{i-1}} \tag{4.17}$$

Solving Eq. (4.15) for τ_i, the shear stresses acting at the interface between the CNT and the matrix can be calculated. Comparing the computed values to the interfacial shear strength (ISS) obtained by pullout tests, the bond slip friction-type model is expressed by:

$$\tau_i = \frac{A_i}{\pi(D_i + t_i)l_i} \left|\sigma_{Ri} - \sigma_{Li}\right| \begin{cases} < ISS, & \text{fully bonded} \\ \geq ISS, & \text{slip} \end{cases} \tag{4.18}$$

If one EBE, which simulates some portion of the full length CNT, is in slip state, this means that its corresponding interface bond has failed, leading to its inability for further load-transferring. The condition of slip for this beam element is simulated by reducing its axial stiffness to a very small value. Notice that bending and torsion rigidities are not affected at all, allowing the element which is in slip state to resist against bending and torsion.

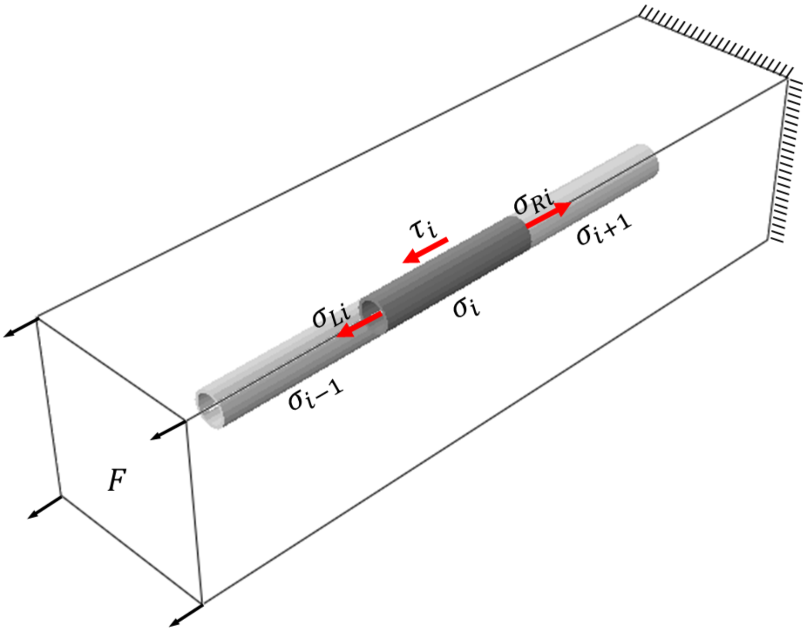

Figure 4.9: Stress states on EBEs in a CNT-RC RVE model in tension

The above procedure is implemented within a full Newton-Raphson incremental-iterative scheme, used for the solution of the nonlinear equations of the problem, as follows:

Step 1: Compute the incremental displacements ${}^{t}\Delta u^{(i)}$ at increment t and iteration i due to the increment ${}^{t}\Delta P$ of the external load vector

$$ {}^{t}\Delta u^{(i)} = \left[{}^{t}K_{T}^{(i)} \right]^{-1} {}^{t}\Delta P \tag{4.19} $$

Step 2: Loop over all beam elements and check each element e for slippage

$$ \text{Slippage} \begin{cases} \text{no} \rightarrow & {}^{t}K_{Te}^{(i)} = {}^{t}K_{Te}^{(i-1)} \\ \text{yes} \rightarrow & {}^{t}K_{Te}^{(i)} = {}^{t}K_{Te}^{(i-1)}, \text{with } (EA)_e \rightarrow 0 \end{cases} \tag{4.20} $$

when slippage occurs, the axial stiffness is reduced to zero resulting in a local modified tangent stiffness matrix ${}^{t}K_{Te}^{(i)}$

Step 3: Correction of internal forces ${}^{t}\Delta F_e^{(i)}$ of element e and update global force vector ${}^{t}F^{(i)}$

$$ {}^{t}\Delta F_e^{(i)} = {}^{t}K_{Te}^{(i)} \Delta u_e^{(i)} \tag{4.21a} $$

$$ {}^{t}F^{(i)} = {}^{t}F^{(i-1)} + \sum_{e=1}^{N} {}^{t}\Delta F_e^{(i)} \tag{4.21b} $$

Step 4: Compute the residuals ${}^{t}r^{(i)}$

$$ {}^{t}r^{(i)} = {}^{t}P - {}^{t}F^{(i)} \begin{cases} \leq tol \ \text{ then } \ t = t+1 \quad \text{go to next increment} \\ > tol \ \text{ then } \ i = i+1 \quad \text{go to } \textbf{Step 1} \end{cases} \tag{4.22} $$

4.1.5 Numerical results on CNT-RC RVEs

4.1.5.1 RVEs with straight CNTs

In this section, numerical results obtained from the FE analysis of the microstructured RVE models of CNT-RC material are presented. The RVE models contain single straight CNTs, placed at the center of the rectangular composite matrix, as shown in Fig. 4.10. The chirality type of the CNTs is armchair $(100, 100)$ with diameter 14 nm, calculated by Eq. (2.3). Following the multiscale modeling procedure of Section 4.1.1, the MSM space frame model of this type of CNTs is first reduced to a linear EBE. A pipe cross-section profile with wall thickness $t = 0.34$ nm is assumed for the EBE. Using the results obtained from the analysis of the MSM model, the equivalent geometrical and material properties of the EBE can be calculated. So, from Eq. (4.3) a mean equivalent diameter of $d_{eq} \simeq 13.453$ nm for the pipe EBE is obtained. From Eqs. (2.21) and (2.23) the values $E \simeq 1.051$ TPa and $G \simeq 0.503$ TPa, for the equivalent Young's and shear modulus respectively, are also obtained. Then, RVEs with different weight fractions of CNTs are constructed by changing only the dimension α of the RVE geometry (see Fig. 4.10). Thus, RVEs with wf=0.1, 0.5, 1 and 2% are constructed for α=130, 59, 42 and 31 nm, respectively, while the length of the rectangular RVE remains constant at L=260 nm. Note that the density of CNTs has been taken equal to 1.8 g·cm^{-3}, while this of PEEK material has been taken equal to 1.4 g·cm^{-3}. The matrix of the RVE in each wf case is discretized with 18081, 3321, 2009 and 1025 solid elements, respectively, while in all wf cases the straight CNT has constant length L_{cnt}=234 nm and is discretized with 37 EBEs. Bernoulli beam elements are used to represent EBEs, which are embedded into the solid elements of the matrix.

Simulations of cyclic axial loading of RVE models are performed for both high and low excitation frequencies. In particular, excitation of composite at very high frequency, practically infinity ($\nu \rightarrow \infty$), invokes the instantaneous elastic response of the polymer matrix. Specifically, in this loading case, PEEK viscoelastic material, which is assigned to the composite matrix, exhibits an instantaneous Young's modulus of $E_m \simeq 2.8$ GPa and a Poisson ratio $\nu_m = 0.4$. On the other hand, excitation of composite at the finite frequency of $\nu = 1$ Hz, invokes the viscoelastic response of PEEK, which is based on the viscoelastic parameters recorded in Table 3.2 of Section 3.2.6. The cyclic loads, which are applied on the models through Dirichlet boundary conditions in sinusoidal form, result in strain amplitudes of ±5%. The effect of interfacial shear strength on both stiffness and damping properties of the CNT-RC material is investigated through parametric studies, where the ISS values are ranging from 5 to 80 MPa. Notice that, the tensile elongation of PEEK at yield point is 5% and its shear strength is 53 MPa (`www.victrex.com`).

Figures 4.11-4.14 plot the stress-strain curves derived from simulations of

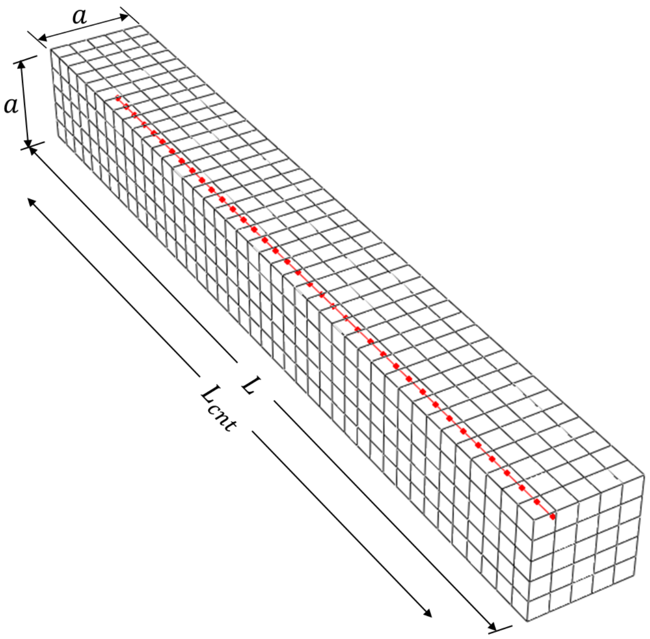

Figure 4.10: Geometry and FE mesh of RVE model with straight and oriented CNT.

cyclic tests on RVE models with ISS=0, 5, 10, 20, 40, 80 and ∞ MPa. Note that ISS=0 corresponds to the neat PEEK model, while ISS=∞ corresponds to the fully bonded model. Each of these figures corresponds to RVE models with specific weight fraction, wf$\simeq$2, 1, 0.5 and 0.1%, respectively. In all these simulations PEEK exhibits instantaneous elastic response as the cyclic loading is performed at excitation frequency $\nu \to \infty$. Thus, the energy dissipation per load cycle is attributed only to CNT slippage and not to the viscoelastic behavior of PEEK. From the figures it can be observed that the stiffness and the energy dissipation of the CNT-RC material are increasing with the increase of the ISS. Also, the total stiffness of the composite approaches that of the fully bonded case and can reach three times the stiffness of the neat PEEK for wf$\simeq$2%. On the other hand, with the addition of only 0.1% of CNTs in the bulk matrix, its mechanical behavior is marginally influenced.

The effective loss factor of the CNT-RC material is computed as the ratio of its dissipated energy per unit volume to its maximum stored energy per unit volume. This parameter, which is used to evaluate damping characteristics of the material, is expressed as:

$$\tan\delta = \frac{D}{\pi \sigma_0 \varepsilon_0} \tag{4.23}$$

where σ_0 and ε_0 are the mean stress and strain amplitudes developed on the RVE models due to their cyclic excitation. D is the area of the hysteresis loop, which is observed in the stress-strain curves of the models, and it corresponds to the dissipated energy per load cycle. In Table 4.2 the loss factor values obtained from the stress-strain curves of Figs. 4.11-4.14 are recorded. These values express the amount of energy dissipation of the CNT-RC material, which for these simulations is only due to the mechanism of slip at the CNT/polymer interface. As previously mentioned, at very high excitation frequencies the mechanical response of PEEK is elastic. Thus, for the case of neat PEEK model (ISS=0) and the fully bonded model (ISS=∞) no dissipating mechanisms exist and therefore no loss factor values are calculated. Figure 4.15 plots the values of Table 4.2, where an increase of the loss factor is observed with respect to the ISS. It can also be observed that, higher wf content of CNTs in the CNT-RC results in larger loss factor values, when ISS is kept constant.

ISS (MPa)	5	10	20	40	80
wf=2%	0.0235	0.0666	0.1184	0.2493	0.2569
wf=1%	0.0153	0.0242	0.0644	0.1277	0.2128
wf=0.5%	0.0090	0.0141	0.0289	0.0742	0.1116
wf=0.1%	0.0020	0.0021	0.0062	0.0158	0.0163

Table 4.2: Loss factor of CNT-RC material in various wf and ISS values when energy dissipation is only due to slip

Figures 4.16-4.19, like Figs. 4.11-4.14, plot the stress-strain curves of the RVE models, but this time simulations of the cyclic tests have been conducted at frequency $\nu = 1$ Hz. In these test cases PEEK exhibits viscoelastic response. Thus, the energy dissipation per load cycle is now attributed to both CNT slippage and viscoelasticity of PEEK. Once again, the energy dissipation of the CNT-RC material is increasing with the increase of the ISS, while its stiffness is approaching

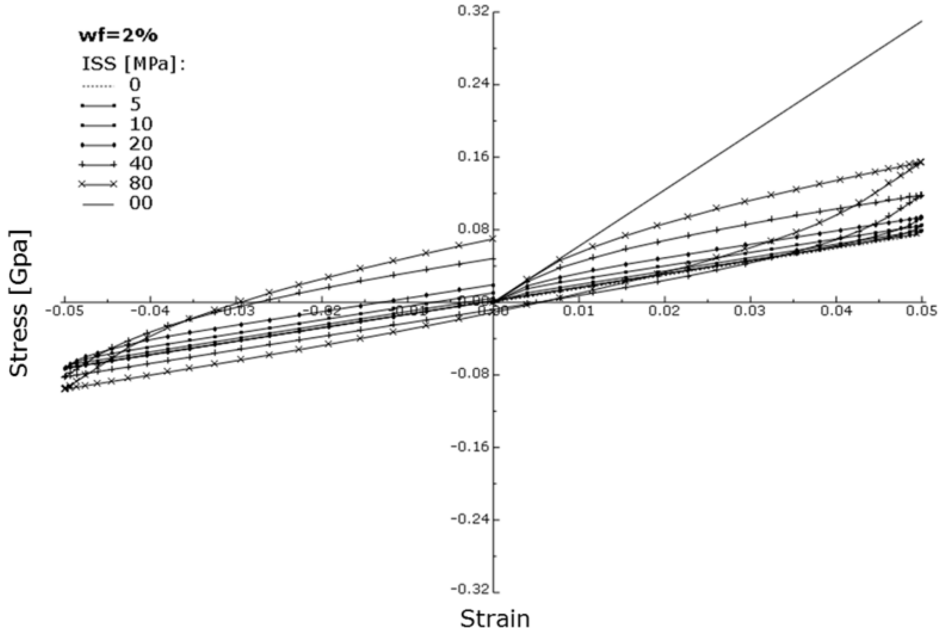

Figure 4.11: Stress-strain curves from cyclic tests at $\nu \to \infty$ of CNT-RC RVEs with wf$\simeq$2% and ISS = 0, 5, 10, 20, 40, 80 and ∞ MPa

that of the fully bonded case. In case of large wf ($\geq$0.5%), the energy dissipation characteristics of the CNT-RC material are more pronounced than that in case of small wf ($\leq$0.1%), where the damping behavior of composite is very similar to that of neat PEEK.

Table 4.3 records the values of the effective loss factor of the CNT-RC material for all the wf and ISS of the RVE models considered. The same results are also plotted in Fig. 4.20 with respect to the ISS, where each curve corresponds to different wf. Note that the presented loss factor values refer to cyclic tests on RVE models at frequency $\nu = 1$ Hz. Thus, in this excitation frequency the loss factor represents the dissipation characteristics of the composite material due to both the CNT slippage and the viscoelastic response of PEEK. The loss factor of the neat PEEK material (ISS = 0) and of the the fully bonded CNT-RC material (ISS = ∞) are also included in the curves. The increase of the energy dissipation of the CNT-RC material due to the increase of its ISS is also visualized in Fig. 4.20. Specifically, the loss factor, which is reaching a peak value for ISS=80 MPa, is more than 200, 250 and 300% of the loss factor of the neat PEEK material for

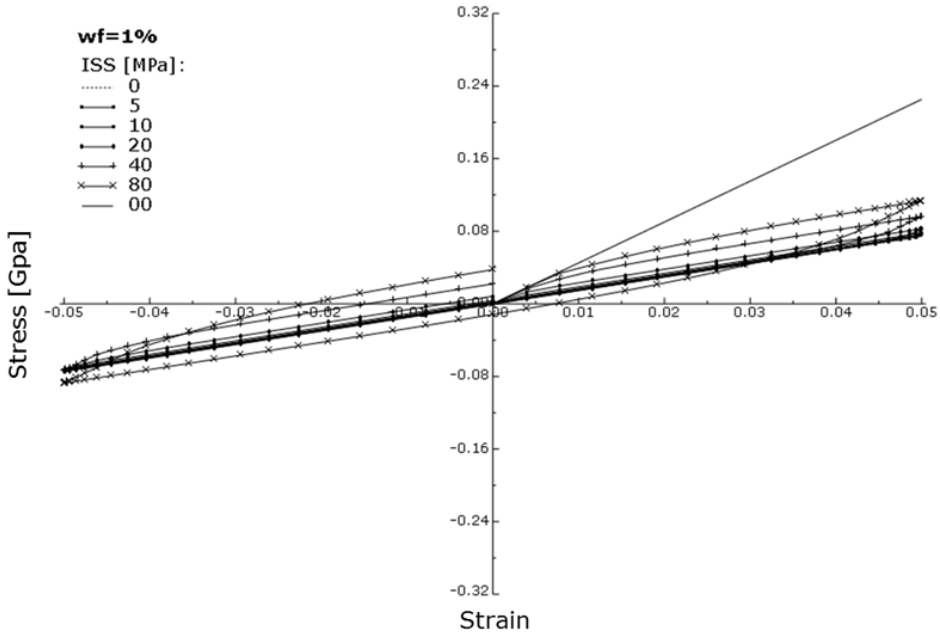

Figure 4.12: Stress-strain curves from cyclic tests at $\nu \to \infty$ of CNT-RC RVEs with wf$\simeq$1% and ISS = 0, 5, 10, 20, 40, 80 and ∞ MPa

wf$\simeq$0.5, 1 and 2%, respectively. This increase, however, is marginal in the case of small wf, lower than 0.1%. In all wf cases, the loss factor is decreasing for ISS>80 MPa, as for such large values of the ISS the fully bonded case is approached. Note also that, shear fracture in matrix could be initiated for ISS>53 MPa, as for this value the shear strength of PEEK is exceeded. The above numerical findings imply that successful functionalization of CNTs could be crucial for producing CNT-RC materials with optimum damping characteristics, especially in the case where ISS values close or slightly higher than the shear strength of the polymer could be achieved from the applied functionalization technique.

From Fig. 4.20 it is concluded that the loss factor of the CNT-RC material depends on its stiffness. Specifically, the stiffness of the material is increasing due to the increase in the wf of CNTs. This increase in stiffness subsequently leads to a decrease in loss factor of the material. The aforementioned observation is more obvious in the case of fully bonded RVE models. However, as wf is increasing the total area of the lateral surface of the CNTs is increasing too. A reduction in the developed interfacial shear stresses under the same external

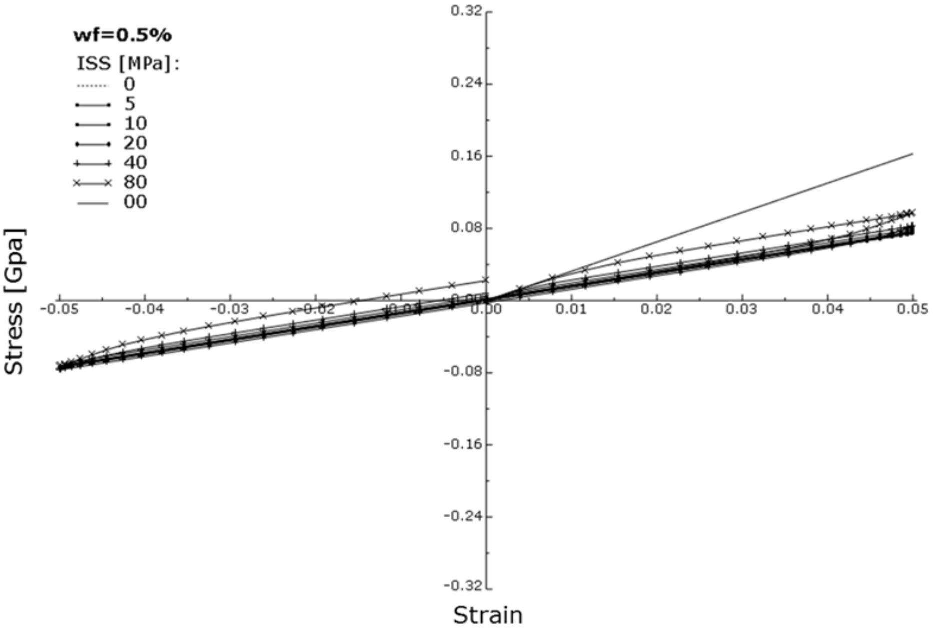

Figure 4.13: Stress-strain curves from cyclic tests at $\nu \rightarrow \infty$ of CNT-RC RVEs with wf$\simeq$0.5% and ISS = 0, 5, 10, 20, 40, 80 and ∞ MPa

loads on the RVE models is thus succeeded. This means that higher external loads can be sustained by the material before its critical ISS value is exceeded and subsequently slip occurs. The delay of CNT slippage in the composite is the reason for the enlargement of the hysteresis loop in the stress-strain curves in Figs. 4.16-4.19. However, for ISS>80 MPa, CNT slippage for strain loading up to ±5% is not initiated, thus the high stiffness of the CNT-RC material is preserved during the whole strain history. In this case, the loss factor of the CNT-RC material is only due to the viscoelastic nature of PEEK and is approximately equal to that of neat PEEK.

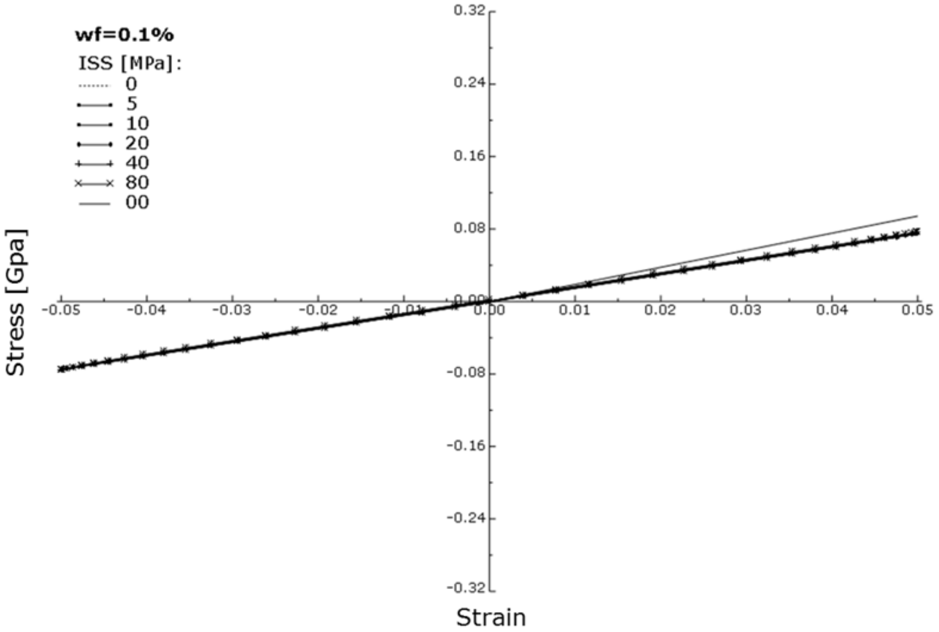

Figure 4.14: Stress-strain curves from cyclic tests at $\nu \to \infty$ of CNT-RC RVEs with wf≃0.1% and ISS = 0, 5, 10, 20, 40, 80 and ∞ MPa

ISS (MPa)	0	5	10	20	40	80	∞
wf=2%	0.1434	0.1757	0.2211	0.2770	0.3744	0.4056	0.1350
wf=1%	0.1434	0.1604	0.2182	0.2266	0.2951	0.3364	0.1340
wf=0.5%	0.1434	0.1534	0.1625	0.1951	0.2262	0.2892	0.1328
wf=0.1%	0.1434	0.1472	0.1473	0.1575	0.1617	0.1780	0.1383

Table 4.3: Loss factor of CNT-RC material in various wf and ISS values when energy dissipation is due to slip and viscocity

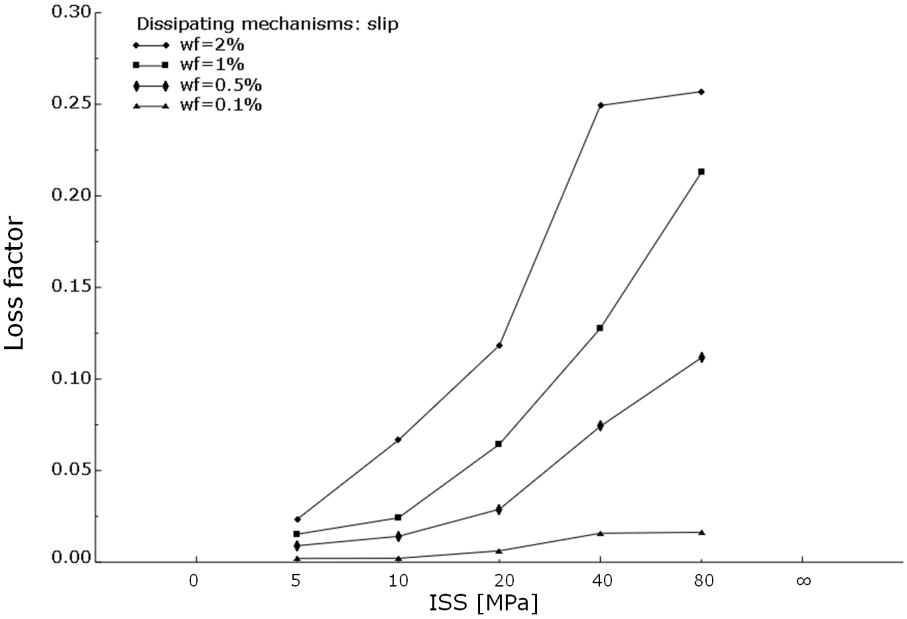

Figure 4.15: Loss factor vs ISS of CNT-RC material derived from cyclic tests of RVE models with wf≃2, 1, 0.5, 0.1% at $\nu \to \infty$

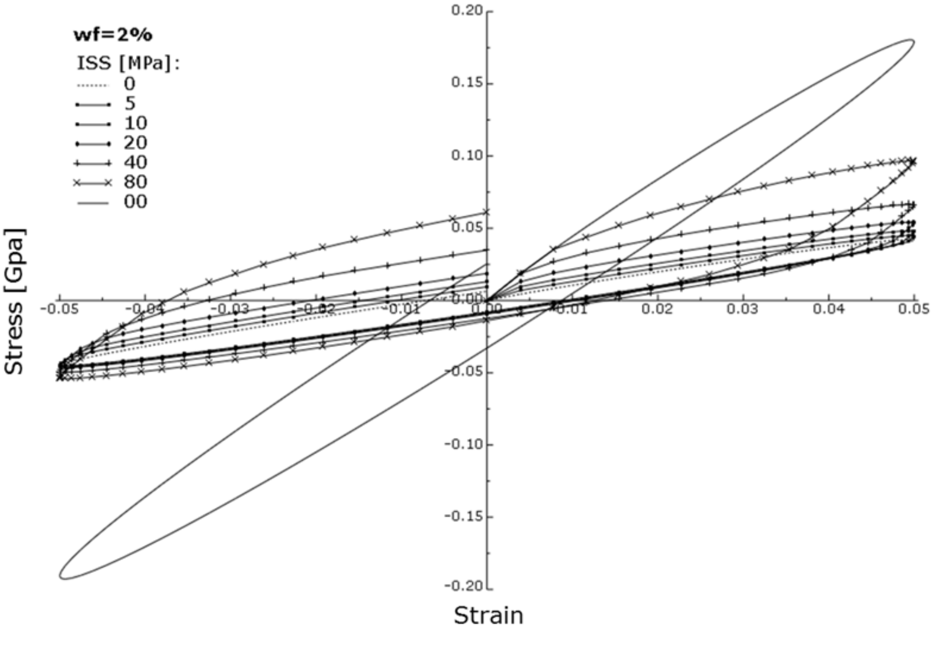

Figure 4.16: Stress-strain curves from cyclic tests at $\nu = 1$ Hz of CNT-RC RVEs with wf≃2% and ISS = 0, 5, 10, 20, 40, 80 and ∞ MPa

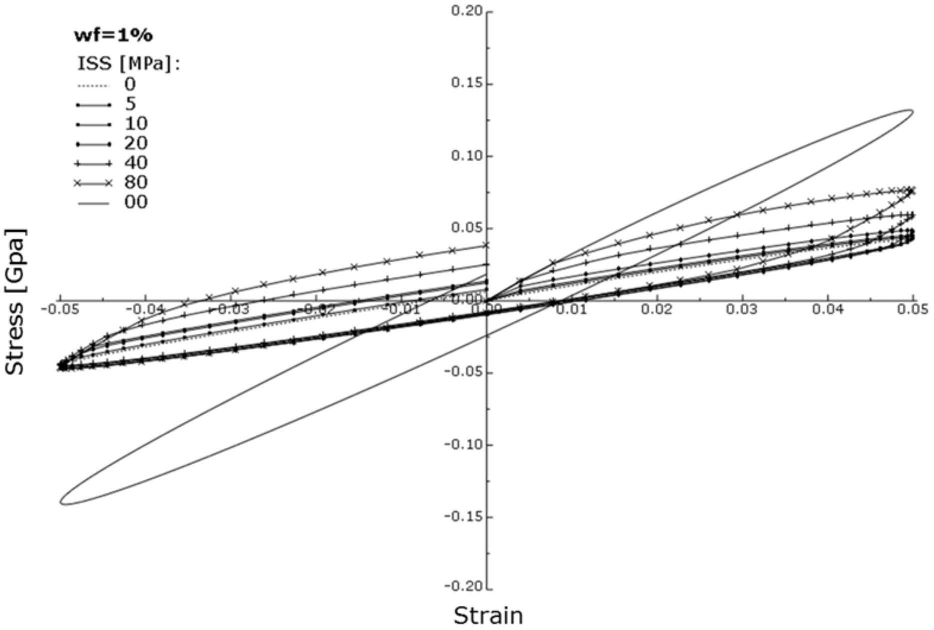

Figure 4.17: Stress-strain curves from cyclic tests at $\nu = 1$ Hz of CNT-RC RVEs with wf$\simeq$1% and ISS = 0, 5, 10, 20, 40, 80 and ∞ MPa

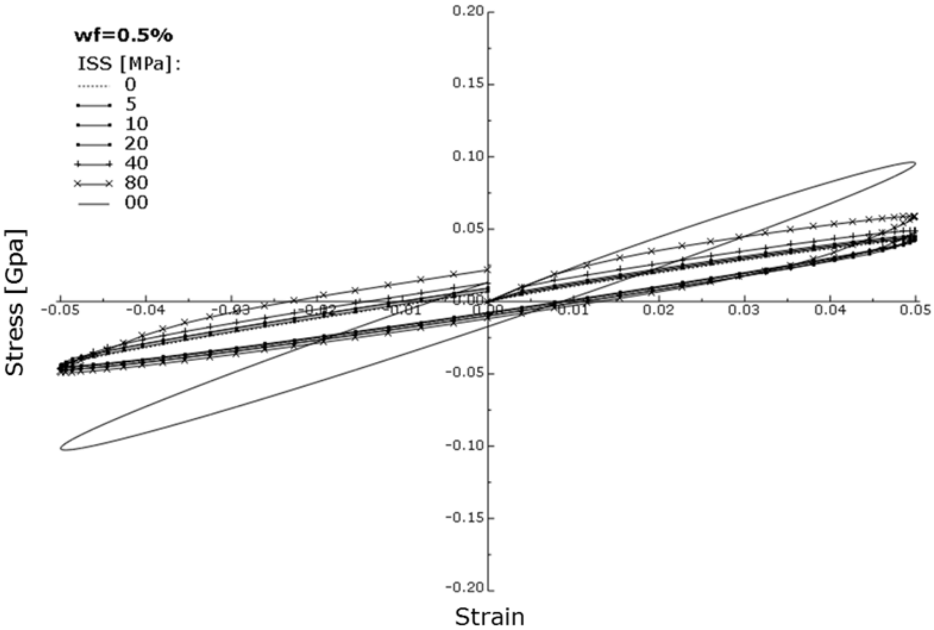

Figure 4.18: Stress-strain curves from cyclic tests at $\nu = 1$ Hz of CNT-RC RVEs with wf$\simeq$0.5% and ISS = 0, 5, 10, 20, 40, 80 and ∞ MPa

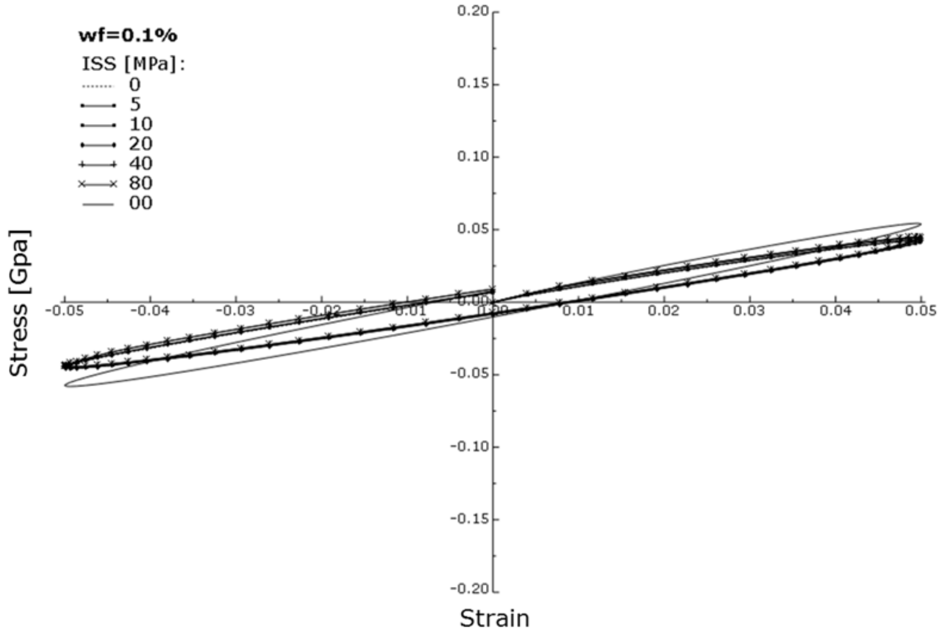

Figure 4.19: Stress-strain curves from cycli tests at $\nu = 1$ Hz of CNT-RC RVEs with wf$\simeq$0.1% and ISS = 0, 5, 10, 20, 40, 80 and ∞ MPa

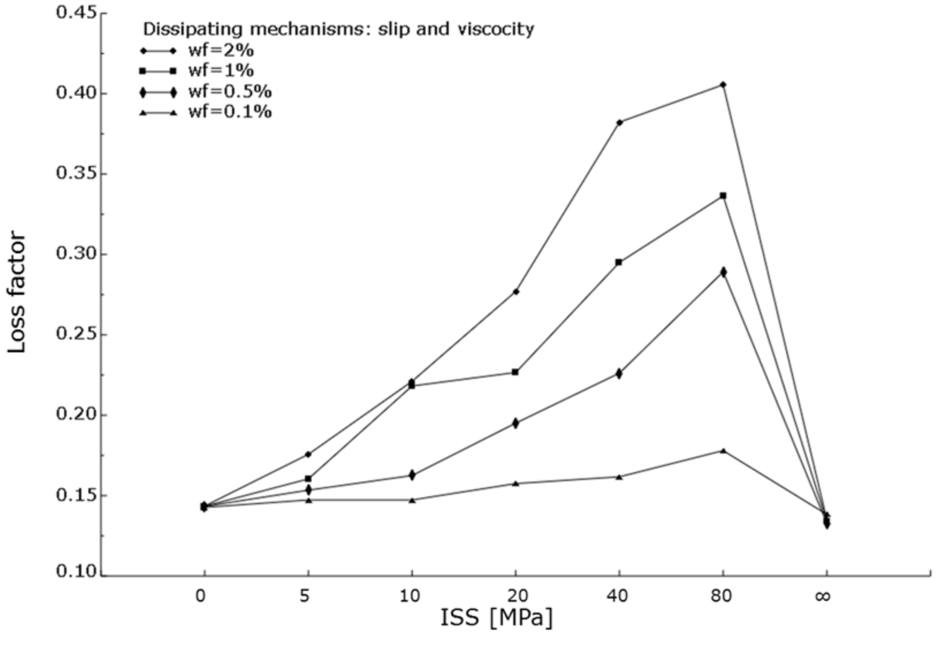

Figure 4.20: Loss factor vs ISS of CNT-RC material derived from cyclic tests of RVE models with wf$\simeq$2, 1, 0.5, 0.1% at $\nu = 1$ Hz

4.1.5.2 RVEs with wavy CNTs

In order to evaluate the effect of random CNT waviness on the mechanical and damping properties of CNT-RC material, stochastic analysis is performed based on Monte Carlo simulation. For this purpose, CNTs with random geometry are generated using Eq. (4.8). The CNTs are then embedded in the polymer matrix in order to construct the random RVE models. Only RVE models with wf$\simeq$2% and ISS = 40 MPa are studied in this section. These RVE models are subjected on cyclic loads at frequency $\nu = 1$ Hz. Dirichlet boundary conditions are applied on the FE models, which result in strain amplitudes of ±5%.

In Fig. 4.21 a cloud of stress-strain curves is plotted. These curves have been derived from the Monte Carlo simulation of 50 RVE models with random wavy CNTs. The average of these curves is also plotted in the figure, together with the corresponding curve of the RVE model with a straight CNT. It is pointed that, all the RVE models contain CNTs with the same length, so that the observed differences in the stress-strain curves are attributed solely to the stochastic waviness of the CNTs. The loss factor of the CNT-RC material is calculated from both the average curve which corresponds to wavy CNTs and the stress-strain curve which corresponds to straight CNTs. These values are recorded in Table 4.4. A 15% reduction in the loss factor of the material is observed for the case of random wavy CNTs with respect to straight CNTs. From these results, the role of straightening of CNTs in producing CNT-RC materials with enhanced damping properties is highlighted.

	Straight CNT	Wavy CNTs
Loss factor	0.3744	0.3182

Table 4.4: Loss factor values for straight and wavy CNTs.

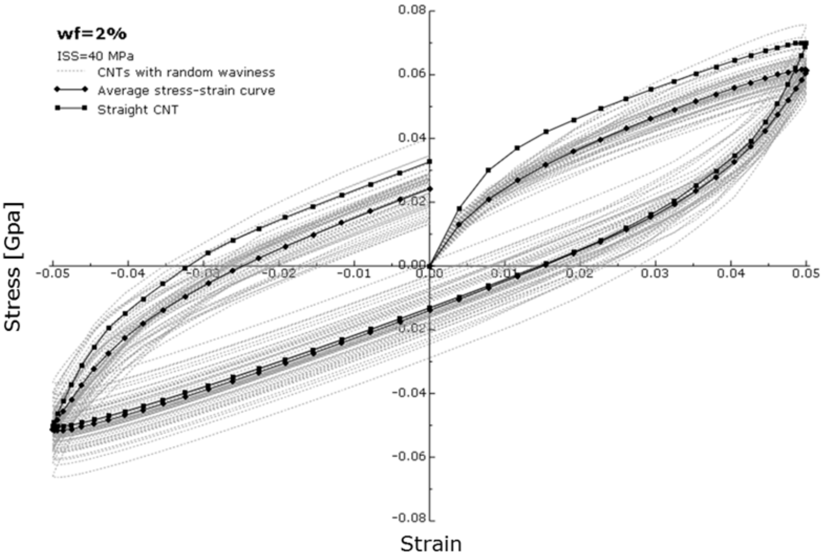

Figure 4.21: Stress-strain curves of: 50 RVEs with random wavy CNTs, average curve, RVE with a straight CNT (wf = 2% and ISS = 40 MPa)

4.2 Homogenization of CNT-RC material

In this section, a nonlinear multiscale homogenization method is proposed for CNT-RC material characterization. Specifically, the homogenized mechanical and damping properties of the CNT-RC material are obtained from the finite element analysis of RVE models. The novelty of the proposed multiscale approach is that it combines different modeling strategies in order to accurately pass information between scales. This hierarchical approach is demonstrated in Fig. 4.1, where the modeling steps from nano to micro to macro scale are illustrated. Short length CNTs are modeled at the nano scale as space frame structures using the MSM approach of Section 2.2.1. In this method the C-C covalent bonds of the CNT lattice are substituted by circular beam elements. Since CNTs form "ropes" in the order of micrometers, the aforementioned MSM model is projected into a linear EBE, which is then used as the basic building element for the discretization of long straight CNTs at microscale. Next, the RVE models are constructed by embedding these EBEs into a polymer matrix (see Section 4.1.3). The load transfer mechanism at the interface between the lateral surface of the CNT and the surrounding polymer is modeled with the nonlinear bond-slip friction-type model of Section 4.1.4. This bond-slip model is particularly suitable for modeling the stick-slip behavior of functionalized CNTs, where a chemical treatment is applied onto their lateral surface in order to form covalent bonds with the hyperbranched molecules of the surrounding polymer. In this way, functionalization results in a significant increase of the CNT/polymer interfacial shear strength verified by Frankland et al [22] and Barber et al [3].

The nonlinear homogenization method is applied to the microstructured RVEs, so as the effective properties of the homogeneous CNT-RC material to be defined. Microstructural analysis is performed by applying Dirichlet boundary conditions on the FE models of the RVEs. These displacement-type boundary conditions result in prescribed macrostrain tensors on the homogeneous FE models. Macrostress tensors are calculated as volume averages, using the results obtained from the FE analysis of the microstructured RVE models. In the context of hierarchical homogenization method, a phenomenological constitutive law, based on Hill's anisotropic plasticity and Maxwell-Wiechert viscoelasticity, is proposed for the homogeneous CNT-RC material. These combined constitutive models constitute a novel viscoplastic model, which is able to capture both the anisotropic stiffness and the anisotropic energy dissipation of the CNT-RC material. This anisotropy of the material is specifically due to the directionality of the CNTs inside the polymer matrix. The proposed viscoplastic model is capable to predict stress-strain curves under cyclic loads. Validation of the homogenization method is performed through sensitivity analysis on RVEs with various wf and ISS values. The effective mechanical and damping properties of the homogeneous CNT-RC material are assessed and compared with direct calculations on detailed fine scale models.

4.2.1 Homogenization method

A hierarchical computational homogenization method is adopted in the thesis in order to homogenize the nonlinear behavior of the CNT-RC material. In this class of methods, the microscopic behavior of the heterogeneous medium is projected to an equivalent homogeneous model at an upper scale. Thus, a specific constitutive behavior of the material has to be identified from the microstructure through FE analysis of the heterogeneous models. As stated by Hashin [28], the fundamental assumption in all homogenization problems is the statistical homogeneity of the heterogeneous medium. This means that all statistical properties of the state variables are the same at any material point and thus a representative volume element (RVE) can be recognized. The concept of the RVE requires complete separation of scales to be valid. Figure 4.22 graphically illustrates the homogenization method applied to the CNT-RC material.

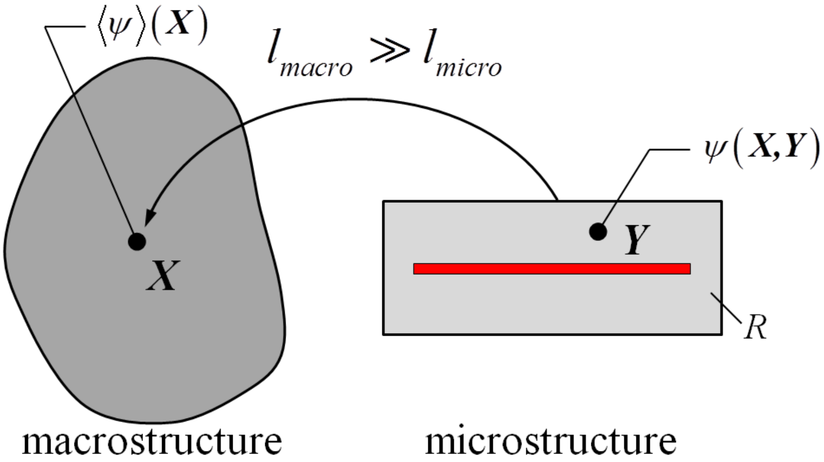

Figure 4.22: Homogenization method applied to the CNT-RC material

According to Miehe and Koch [57], the first step in the homogenization procedure is to define the relations between the microscopic and macroscopic state variables, which are known as ”micro-macro relations”. By imposing appropriate boundary conditions on the FE model of RVE, these relations are extracted and then are used in order to determine the effective material properties of the homogeneous constitutive model. Macroscopic quantities are formulated as volume averages of the corresponding microscopic state variables. According to the deterministic theories of Hill [31] and Maugin [55] the total macroscopic stress and strain tensors at some point $\boldsymbol{X}$ of the macroscopic body are computed by

$$\Sigma_{ij}(\boldsymbol{X}) = \langle\sigma_{ij}\rangle(\boldsymbol{X}), \quad E_{ij}(\boldsymbol{X}) = \langle\varepsilon_{ij}\rangle(\boldsymbol{X}) \tag{4.24}$$

where the average of a microstructure quantity ψ is defined as its integral over the volume V of the RVE as

$$\langle\psi\rangle(\boldsymbol{X}) = \frac{1}{V}\int_R \psi(\boldsymbol{X},\boldsymbol{Y})\,\mathrm{d}\boldsymbol{Y} \quad \text{with} \quad V = \int_R \mathrm{d}\boldsymbol{Y} \tag{4.25}$$

where $\boldsymbol{Y}$ denotes the spatial coordinates of a point in the microstructure (see Fig. 4.22). The averaging theorem requires the strain energy of the the microstructured RVE to be equal to that of the homogeneous medium. This equivalence, which is known as the Hill's energy condition, is formulated as follows:

$$\boldsymbol{\Sigma} : \boldsymbol{E} = \frac{1}{|V|}\int_R \boldsymbol{\sigma} : \boldsymbol{\varepsilon}\,\mathrm{d}\boldsymbol{Y} \tag{4.26}$$

4.2.2 Viscoplastic model

The viscoplastic model is intended for modeling materials in which significant time-dependent behavior as well as plasticity is observed, which for metals typically occurs at elevated temperatures. Here, the microstructural behavior of the CNT-RC material is captured at macroscale by a continuum viscoplastic model. This model is able to simulate the viscosity induced to the CNT-RC material by the polymer matrix and the anisotropic plasticity induced to the CNT-RC material by the anisotropic CNT reinforcement and slip. The nonlinear behavior of the CNT-RC material is broken down into three parts: elastic, plastic, and viscous. Figure 4.23 shows a one-dimensional idealization of the proposed viscoplastic model, with the elastic-plastic and the elastic-viscous networks in parallel. For the elastic-plastic network, an anisotropic plasticity model proposed by Hill [30] is implemented in order to define anisotropic yield due to CNT slippage. Note that, the elastic-plastic network does not take into account rate-dependent yield; hence, any specification of strain rate dependence for the plasticity model is not allowed. On the other hand, strain rate dependent behavior of CNT-RC material is taken into account by the elastic-viscous network. For this network, the Maxwell-Wiechert viscoelasticity model of Section 3.2.3 is implemented.

The elastic response of the viscoplastic model depends on the rate of the applied loads. For the one-dimensional representation of the model shown in

Fig. 4.23, its time dependent relaxation modulus can be expressed as:

$$E_c(t) = E_{cnt} + E_{m_\infty} + \sum_{j=1}^{N} E_{m_j} e^{-\frac{t}{\tau_j}} \tag{4.27}$$

If the loads are applied on the model instantly thus $t \to 0$, then the elastic response of the composite is obtained from its instantaneous elastic modulus

$$E_{c_0} = \lim_{t\to 0} E_c(t) = E_{cnt} + E_{m_\infty} + \sum_{j=1}^{N} E_{m_j} \tag{4.28}$$

If the loads are applied on the model very slowly thus $t \to \infty$, then the elastic response of the composite is obtained from its long term elastic modulus

$$E_{c_\infty} = \lim_{t\to \infty} E(t) = E_{cnt} + E_{m_\infty} \tag{4.29}$$

The plasticity parameters τ_{cr} and H_{slip} correspond to the initial yield stress and to the kinematic hardening of the CNT-RC material, respectively. The shear stress developed at the CNT/polymer interface at the moment of slip initiation is regarded as the initial yield stress. Hill's plasticity can account for an anisotropic yield surface, which can efficiently predict slip of CNTs in various directions. After the initiation of slip, the kinematic hardening of the model defines the nonlinear behavior of the composite, which is due to the evolution of slip. On the other hand, the nonlinear behavior of the composite, which is due to the viscosity of the PEEK matrix, is captured by the elastic-viscous network of the viscoplastic model.

4.2.2.1 Hill's orthotropic plasticity model

In this section, the basic equations of Hill's orthotropic plasticity model, which is assigned to the elastic-plastic network of the viscoplastic model of Section 4.2.2, are presented. The proposed model can capture the orthotropic elasto-plastic behavior of the CNT-RC material, which is due to reinforcement of its polymer matrix by straight and one-direction oriented CNTs. All the equations are expressed in the reference coordinate system of Fig. 4.24, which remains constant during the plastic deformation of the material. The stress tensor components σ_{ij}

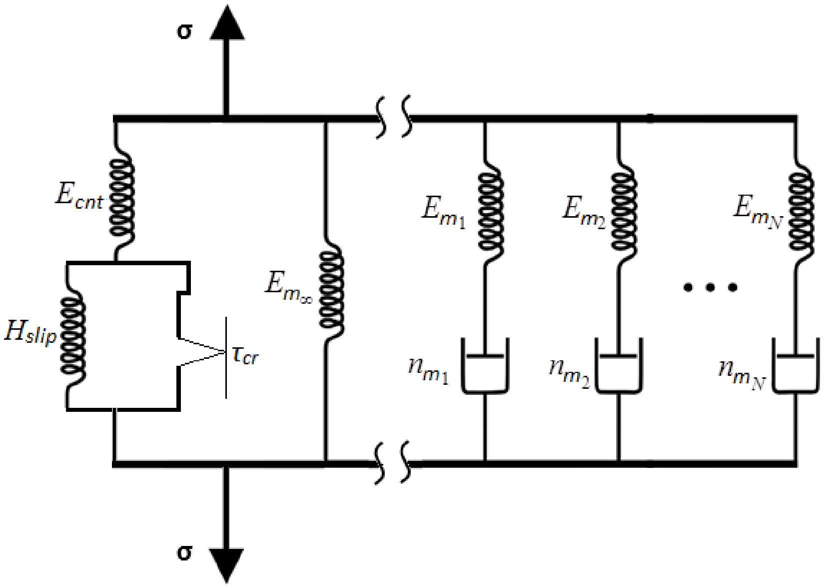

Figure 4.23: One-dimensional viscoplastic model for CNT-RC material

can then be expressed on the orthonormal basis $\{e_1, e_2, e_3\}$, where the normal vectors coincide with the principal axes of plastic orthotropy.

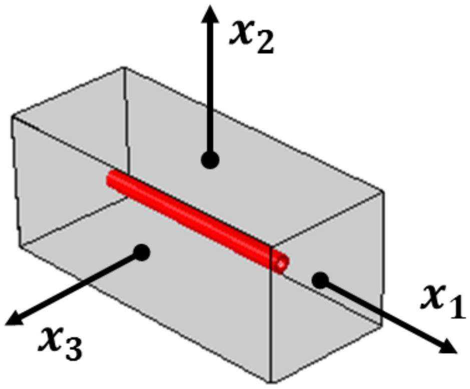

Figure 4.24: Reference coordinate system for CNT-RC orthotropic material

The yield function associated with Hill's model can be written in the form:

$$\Phi(\boldsymbol{\sigma},\bar{\sigma}) = F(\sigma_{22}-\sigma_{33})^2+G(\sigma_{33}-\sigma_{11})^2+H(\sigma_{11}-\sigma_{22})^2+2L\sigma_{23}^2+2M\sigma_{13}^2+2N\sigma_{12}^2-\bar{\sigma}^2 \tag{4.30}$$

where F, G, H, L, M and N are constants. These are obtained by testing the material in all principal directions and can be expressed as:

$$\begin{aligned}
F &= \tfrac{\sigma_0^2}{2}\left(\tfrac{1}{\bar{\sigma}_{22}^2}+\tfrac{1}{\bar{\sigma}_{33}^2}-\tfrac{1}{\bar{\sigma}_{11}^2}\right) = \tfrac{1}{2}\left(\tfrac{1}{R_{22}^2}+\tfrac{1}{R_{33}^2}-\tfrac{1}{R_{11}^2}\right),\\
G &= \tfrac{\sigma_0^2}{2}\left(\tfrac{1}{\bar{\sigma}_{33}^2}+\tfrac{1}{\bar{\sigma}_{11}^2}-\tfrac{1}{\bar{\sigma}_{22}^2}\right) = \tfrac{1}{2}\left(\tfrac{1}{R_{33}^2}+\tfrac{1}{R_{11}^2}-\tfrac{1}{R_{22}^2}\right),\\
H &= \tfrac{\sigma_0^2}{2}\left(\tfrac{1}{\bar{\sigma}_{11}^2}+\tfrac{1}{\bar{\sigma}_{22}^2}-\tfrac{1}{\bar{\sigma}_{33}^2}\right) = \tfrac{1}{2}\left(\tfrac{1}{R_{11}^2}+\tfrac{1}{R_{22}^2}-\tfrac{1}{R_{33}^2}\right),\\
L &= \tfrac{3}{2}\left(\tfrac{\tau_0}{\bar{\sigma}_{23}}\right)^2 = \tfrac{3}{2R_{23}^2},\\
M &= \tfrac{3}{2}\left(\tfrac{\tau_0}{\bar{\sigma}_{13}}\right)^2 = \tfrac{3}{2R_{13}^2},\\
N &= \tfrac{3}{2}\left(\tfrac{\tau_0}{\bar{\sigma}_{12}}\right)^2 = \tfrac{3}{2R_{12}^2},
\end{aligned} \tag{4.31}$$

where each $\bar{\sigma}_{ij}$ is the measured yield stress value when σ_{ij} is applied as the only nonzero stress component; σ_0 is the reference yield stress which defines the initial size of the yield surface and τ_0 is the reference shear yield stress defined as $\tau_0 = \sigma_0/\sqrt{3}$. The six yield stress ratios $R_{11} = \bar{\sigma}_{11}/\sigma_0$, $R_{22} = \bar{\sigma}_{22}/\sigma_0$, $R_{33} = \bar{\sigma}_{33}/\sigma_0$, $R_{12} = \bar{\sigma}_{12}/\tau_0$, $R_{13} = \bar{\sigma}_{13}/\tau_0$ and $R_{23} = \bar{\sigma}_{23}/\tau_0$ determine the shape of the anisotropic yield surface, which is a truly 6-dimensional hypersurface in the space of stress components. Using matrix notation, the yield condition in Eq. (4.30) can be rewritten in the form:

$$\Phi(\boldsymbol{\sigma},\bar{\sigma},\boldsymbol{\alpha}) = \frac{1}{2}(\boldsymbol{\sigma}-\boldsymbol{\alpha})^T\boldsymbol{P}(\boldsymbol{\sigma}-\boldsymbol{\alpha})-\bar{\sigma}^2 = \frac{1}{2}\boldsymbol{n}^T\boldsymbol{P}\boldsymbol{n}-\bar{\sigma}^2 = \boldsymbol{0} \tag{4.32}$$

where matrix $\boldsymbol{P}$ is defined as:

$$\boldsymbol{P} = \begin{bmatrix} H+G & -H & -G & 0 & 0 & 0 \\ -F & F+H & -H & 0 & 0 & 0 \\ -G & -F & G+F & 0 & 0 & 0 \\ 0 & 0 & 0 & 2N & 0 & 0 \\ 0 & 0 & 0 & 0 & 2M & 0 \\ 0 & 0 & 0 & 0 & 0 & 2L \end{bmatrix} \tag{4.33}$$

and $\boldsymbol{n} = \boldsymbol{\sigma} - \boldsymbol{\alpha}$ is the relative stress tensor written in vector notation and defined as the difference between the stress tensor $\boldsymbol{\sigma}$ and the back stress tensor $\boldsymbol{\alpha}$. Hill's rate-independent plasticity model postulates an associative plastic flow rule which is expressed as:

$$\dot{\boldsymbol{\varepsilon}}^p = \dot{\gamma}\frac{\partial \Phi}{\partial \boldsymbol{\sigma}} = \dot{\gamma}\boldsymbol{N} = \dot{\gamma}\boldsymbol{P}\boldsymbol{n} \tag{4.34}$$

where $\boldsymbol{N} = \boldsymbol{P}\boldsymbol{n}$ is the flow vector and γ is the plastic multiplier. The rate of the accumulated plastic strain can be expressed as:

$$\dot{\bar{\varepsilon}}^p = \sqrt{\frac{2}{3}\left(\dot{\boldsymbol{\varepsilon}}^p\right)^T \boldsymbol{Z}\left(\dot{\boldsymbol{\varepsilon}}^p\right)} = \dot{\gamma}\sqrt{\frac{2}{3}\left(\boldsymbol{P}\boldsymbol{n}\right)^T \boldsymbol{Z}\left(\boldsymbol{P}\boldsymbol{n}\right)} \tag{4.35}$$

where matrix $\boldsymbol{Z}$ is a compatibility matrix used to equate the tensorial contraction to matrix-vectors multiplications. The rate of change of the back stress tensor is supposed to follow Prager's nonlinear kinematic hardening rule:

$$\dot{\boldsymbol{\alpha}} = \frac{2}{3}C\left(\bar{\varepsilon}^p\right)\dot{\boldsymbol{\varepsilon}}^p = \dot{\gamma}C\left(\bar{\varepsilon}^p\right)\boldsymbol{P}\boldsymbol{n} \tag{4.36}$$

where $C\left(\bar{\varepsilon}^p\right) = d\bar{\alpha}/d\bar{\varepsilon}^p$ is the kinematic hardening modulus defined by the scalar function $\bar{\alpha}\left(\bar{\varepsilon}^p\right)$ of the accumulated plastic strain. Notice in Eqs. (4.30) and (5.10) that, $\bar{\sigma}$ is the relative yield stress, which in case of isotropic hardening is a function of $\bar{\varepsilon}^p$ and defines the size of the yield surface according to the isotropic hardening curve $H\left(\bar{\varepsilon}^p\right) = d\bar{\sigma}/d\bar{\varepsilon}^p$. For materials with only kinematic hardening behavior, $H = 0$ and $\bar{\sigma} \equiv \sigma_0$ is constant. This means that, the yield surface preserves its shape and size but translates in the stress space as a rigid body according to the kinematic hardening law. Kinematic hardening data can be obtained from simple uniaxial tests. A detailed description of Hill's plasticity model, along with the state update procedure and computation of the associated consistent tangent modulus of the elastoplastic material can be found in Kojić et al [42] and Souza [84]. These numerical procedures are necessary for the implicit finite element solution of small strain plasticity problems. Also, a review for the finite element implementation of Hill's plasticity equations can be found in Appendix B.

4.2.2.2 Calibration of viscoplastic model

Calibration of the proposed viscoplastic model for the CNT-RC material involves the definition of all its elastic, plastic and viscous parameters. This is performed numerically through FE analysis of the microstructured RVEs. Assuming that, the viscous behavior of the CNT-RC material is only due to the viscoelastic nature of PEEK matrix, its viscosity parameters are derived from the calibration procedure of the Maxwell-Wiechert model presented in Section 3.2.6. The effective elastic properties of the homogeneous CNT-RC material need also to be computed. The elastic stress-strain relation for the homogeneous model of an RVE with straight and oriented nanotubes can be expressed in the reference coordinate system of Fig. 4.24 in the form:

$$\begin{bmatrix} \Sigma_{11} \\ \Sigma_{22} \\ \Sigma_{33} \\ \Sigma_{12} \\ \Sigma_{13} \\ \Sigma_{23} \end{bmatrix} = \begin{bmatrix} \mathbb{C}_{1111} & \mathbb{C}_{1122} & \mathbb{C}_{1133} & 0 & 0 & 0 \\ & \mathbb{C}_{2222} & \mathbb{C}_{2233} & 0 & 0 & 0 \\ & & \mathbb{C}_{3333} & 0 & 0 & 0 \\ & & & \mathbb{C}_{1212} & 0 & 0 \\ & sym. & & & \mathbb{C}_{1313} & 0 \\ & & & & & \mathbb{C}_{2323} \end{bmatrix} \begin{bmatrix} E_{11} \\ E_{22} \\ E_{33} \\ E_{12} \\ E_{13} \\ E_{23} \end{bmatrix} \tag{4.37}$$

where $\mathbb{C}$ is a transversely orthotropic elasticity matrix, which involves nine unknown components. These unknowns are related with Young's moduli E_1, E_2, E_3, which are associated with the orthotropic directions 1, 2, and 3 respectively, the shear moduli G_{12}, G_{13}, G_{23}, which are associated with orthotropic planes 12, 13 and 23 respectively ($G_{ij} = G_{ji}$), and finally the three Poisson's ratios ν_{12}, ν_{13} and ν_{23}. Four independent Dirichlet boundary conditions have to be applied on the FE model of the RVE in order to determine all the unknowns in matrix $\mathbb{C}$. These are derived from the following set of predefined macrostrains:

$$\boldsymbol{E} = \left\{ \begin{bmatrix} E_{11} \\ 0 \\ 0 \\ 0 \\ 0 \\ 0 \end{bmatrix}, \begin{bmatrix} 0 \\ E_{22} \\ 0 \\ 0 \\ 0 \\ 0 \end{bmatrix}, \begin{bmatrix} 0 \\ 0 \\ E_{33} \\ 0 \\ 0 \\ 0 \end{bmatrix}, \begin{bmatrix} 0 \\ 0 \\ 0 \\ E_{12} \\ E_{13} \\ E_{23} \end{bmatrix} \right\} \tag{4.38}$$

which correspond to point $\boldsymbol{X}$ of the homogeneous material where the RVE model is assigned (see Fig. 4.22). Thus, the displacement type boundary conditions are derived from:

$$\boldsymbol{u}_q = \mathbb{D}_q^T \, \boldsymbol{E} \tag{4.39}$$

$\boldsymbol{u}_q$ contains the displacements of each boundary node q on the FE mesh of the RVE model. $\mathbb{D}_q$ is a geometric matrix defined for node q in the form:

$$\mathbb{D}_q^T = \begin{bmatrix} x_1 & 0 & 0 & \frac{1}{2}x_2 & 0 & \frac{1}{2}x_3 \\ 0 & x_2 & 0 & \frac{1}{2}x_1 & \frac{1}{2}x_3 & 0 \\ 0 & 0 & x_3 & 0 & \frac{1}{2}x_2 & \frac{1}{2}x_1 \end{bmatrix} \tag{4.40}$$

where (x_1, x_2, x_3) are the spatial coordinates of the specific node in the microstructure. For example, substituting the first macrostrain $\boldsymbol{E} = [E_{11} \;\; 0 \;\; 0 \;\; 0 \;\; 0 \;\; 0]^T$ in Eq. (4.37), the components $\mathbb{C}_{1111} = \Sigma_{11}/E_{11}$, $\mathbb{C}_{2211} = \Sigma_{22}/E_{11}$ and $\mathbb{C}_{3311} = \Sigma_{33}/E_{11}$ can be directly obtained. After the FE analysis of the RVE model the macrostress $\boldsymbol{\Sigma}$ is derived from the reaction forces $\boldsymbol{f_q}$ calculated on the boundary nodes q of the FE model in an average form as:

$$\boldsymbol{\Sigma} = \frac{1}{|V|} \sum_{q=1}^{n_q} \mathbb{D}_{\boldsymbol{q}} \boldsymbol{f_q} \tag{4.41}$$

where n_q is the number of the boundary nodes q and V is the volume of the RVE. The other unknown components of the elasticity matrix $\mathbb{C}$ are computed in a similar way by applying the remaining predefined macrostrains of Eq. (4.38). Note that, the response of the RVE is considered linear elastic as far as the shear stresses developed at the CNT/polymer interface do not exceed the ISS of the composite material. Thus, in order to calibrate the elastic parameters of the macro constitutive model, the amplitude of the imposed macrostrain have to be lower than the limit point at which CNT slippage is initiated. This means that the total strains in the viscoplasticity model are regarded elastic, $\boldsymbol{E} = \boldsymbol{E}^e$, and thus no permanent deformation occurs. Note also that, these calibration tests have been performed in high strain rates, thus the computed effective elastic properties corresponds to the instantaneous elastic response of the material.

On the other hand, calibration of the plasticity parameters is performed at the long term response of the material where the steady-state behavior of PEEK matrix is attained. Specifically, calibration of Hill's plasticity parameters involves the determination of the constants F, G, H, L, M and N of Eq. (4.31), which define the yield surface of the model, and the extraction of its kinematic hardening data. For the elastic-plastic network of the viscoplastic model, material nonlinearity is attributed solely to CNT slippage at the CNT/polymer interface. Due to the fact that CNTs are oriented and aligned along the longitudinal direction of the RVE (Fig. 4.24), the boundary conditions imposed by the uniaxial strain $\boldsymbol{E} = [E_{11}\ \ 0\ \ 0\ \ 0\ \ 0\ \ 0]^T$ are sufficient for the determination of the yield parameters of Eq. (4.31). Since the aforementioned imposed strains result in multiaxial stress conditions, the yield stress value $\bar{\sigma}_{11}$ of Eq. (4.31) is obtained as the equivalent von Mises stress in the form:

$$\bar{\Sigma}_y = \sqrt{\frac{3}{2}\Sigma^d_{ij}\Sigma^d_{ij}} \tag{4.42}$$

where Σ^d_{ij} are the deviatoric components of the effective stress tensor defined by:

$$\Sigma^d_{ij} = \Sigma_{ij} - \frac{1}{3}\left(tr\boldsymbol{\Sigma}\right)\delta_{ij} \tag{4.43}$$

The equivalent stress value $\bar{\Sigma}_y$ is calculated by the multiaxial stress states developed in the microstructure at the exact time of slip initiation. This value corresponds to the initial effective yield stress in the direction of CNT reinforcement. The nonlinear kinematic hardening data are derived by calculating the equivalent yield stresses $\bar{\Sigma}$ as a function of the accumulated plastic strains $\bar{E}^p$ obtained by:

$$\bar{E}^p = \sqrt{\frac{2}{3} E_{ij}^p E_{ij}^p} \tag{4.44}$$

where $\boldsymbol{E}^p$ is the plastic strain. This is defined from the decomposition of the total strain $\boldsymbol{E}$, into the sum of an elastic (or reversible) component, $\boldsymbol{E}^e$, and a plastic (or permanent) component, $\boldsymbol{E}^p$. So it can be expressed in vector notation as:

$$\boldsymbol{E}^p = \boldsymbol{E} - \boldsymbol{E}^e = \boldsymbol{E} - \mathbb{C}^{-1}\boldsymbol{\Sigma} \tag{4.45}$$

Large values are assigned to the other plasticity parameters of Eq. (4.31), which correspond to the initial yield stresses in the transverse material directions. Thus, the stresses of the material developed at these directions remain inside the elastic domain delimited by the Hill's yield surface. This is due to the fact that at the microsccale, interfacial slippage occurs only in the direction of the CNT reinforcement and thus plastic flow does not occur in other directions.

4.2.3 Numerical results on homogenization

The validity of the proposed nonlinear hierarchical multiscale homogenization method is tested in this section. This is performed by comparing the results obtained from FE simulations of the heterogeneous medium with these of the homogeneous medium. The results for the heterogeneous medium are obtained through detailed FE discretization of the corresponding microstructure and thus serve as a reference solution. Two test cases are considered. The first corresponds to cyclic tests on microstructured RVEs which contain a single straight and oriented CNT and the second corresponds to tensile tests on a CNT-RC specimen reinforced by four CNTs. In both cases, validation of the proposed homogenization method is performed through sensitivity analysis on RVEs with respect to various weight fractions of CNTs and ISS values.

4.2.3.1 Test case 1: Cyclic tests on CNT-RC RVEs

In this example, the proposed homogenization method is tested through cyclic tests on CNT-RC material. Initially, calibration of the viscoplastic model of Section 4.2.2 is performed through FE analysis of microstructured RVE models. The computed effective properties are then used to simulate the behavior of the homogenized material. Geometry, materials and mesh characteristics of the RVE models used in this test case have been described in Section 4.1.5.1. A cyclic uniaxial macrostrain $\boldsymbol{E} = [E_{11} \;\; 0 \;\; 0 \;\; 0 \;\; 0 \;\; 0]^T$ is applied on the RVE models with

$$E_{11} = E_0 \sin(2\pi\nu t) \tag{4.46}$$

where E_0 is the strain amplitude, t is the current analysis time and ν is the imposed circular frequency. According to the homogenization method, the macrostrain $\boldsymbol{E}$ is applied on the RVE models through Dirichlet boundary conditions with the nodal displacements derived from Eq. (4.39). After the FE analysis of the RVE models the macrostress $\boldsymbol{\Sigma}$ is calculated from Eq. (4.41) using the obtained microstructural results.

Figures 4.25, 4.26 and 4.27 present the stress-strain curves obtained from the FE analysis of both the heterogeneous and the homogeneous models of the CNT-RC material with wf=0.5, 1 and 2% of CNTs, respectively. The plots (a), (b) and (c) in each figure correspond to ISS=40, 80 and 160 MPa, respectively. The results of the heterogeneous models are obtained from the multiscale analysis of the microstructured RVE models and thus can be considered as the reference solutions. Note that, instantaneous elastic response of PEEK is assumed in all simulations. This means that, a high, practically infinity, strain rate is imposed to the models, with $\nu \rightarrow \infty$ in Eq. (4.46). The strain amplitude in all cyclic simulations is ±5%. Identical stress-strain curves for the heterogeneous and the homogeneous models are obtained. The Bauschinger effect, which is attributed to the stick-slip mechanism at the CNT/polymer interface, is accurately captured by the homogeneous model through appropriate kinematic hardening data of Hill's orthotropic plasticity model. Small discrepancy of the results may be attributed to calibration errors. These errors are mainly due to the inaccurate prediction of the initial yield stress of the plasticity model, which has to be defined at the exact time when CNT slippage in the RVE initiates.

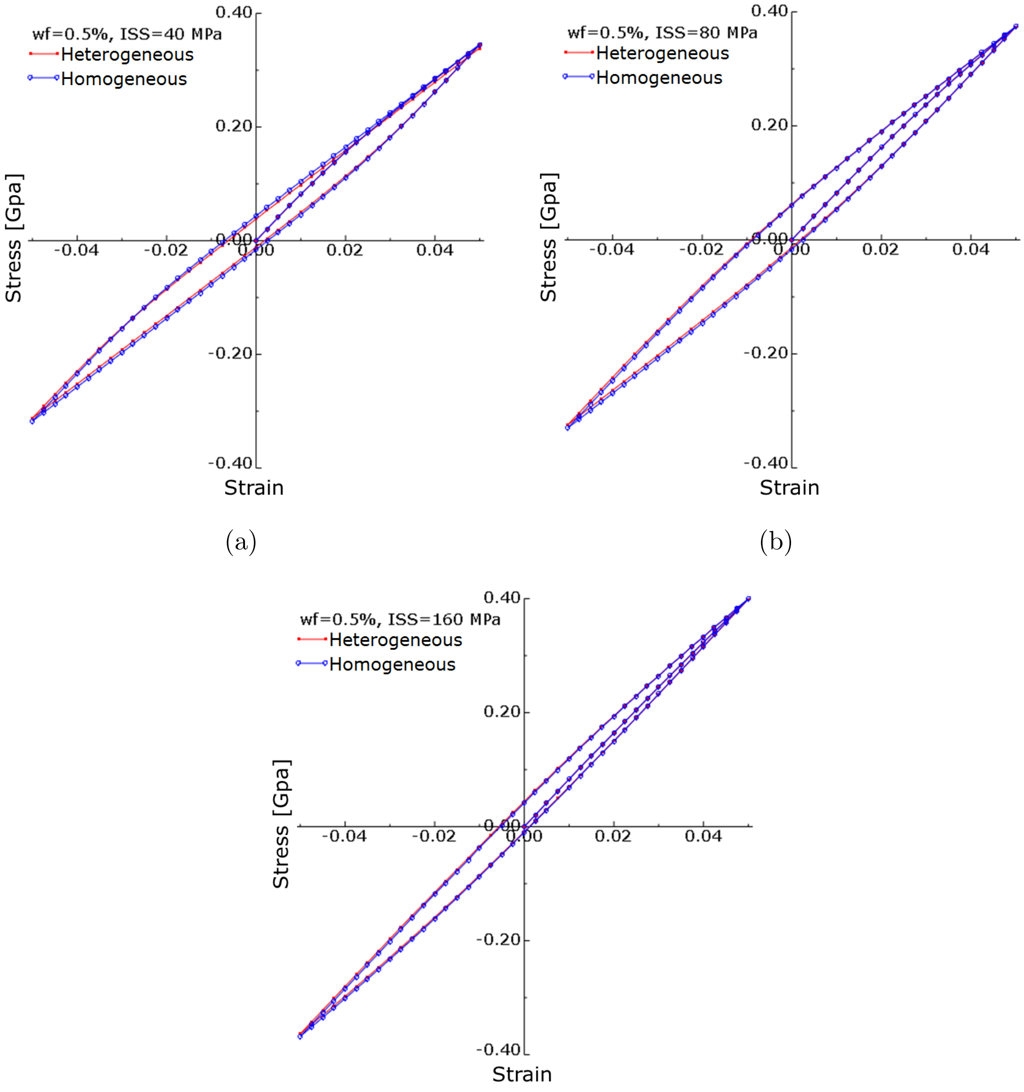

(a)

(b)

(c)

Figure 4.25: Stress-strain curves of heterogeneous and homogeneous CNT-RC material from cyclic tests at $\nu \to \infty$; wf=0.5% and ISS=40, 80 and 160 MPa

The loss factor of the CNT-RC material is calculated by Eq. (4.23) from the stress-strain curves of both the heterogeneous and the homogeneous models. The results are plotted in Fig. 4.28(a) with respect to the wf values and in Fig. 4.28(b) with respect to ISS values. The loss factor values of the homogeneous material

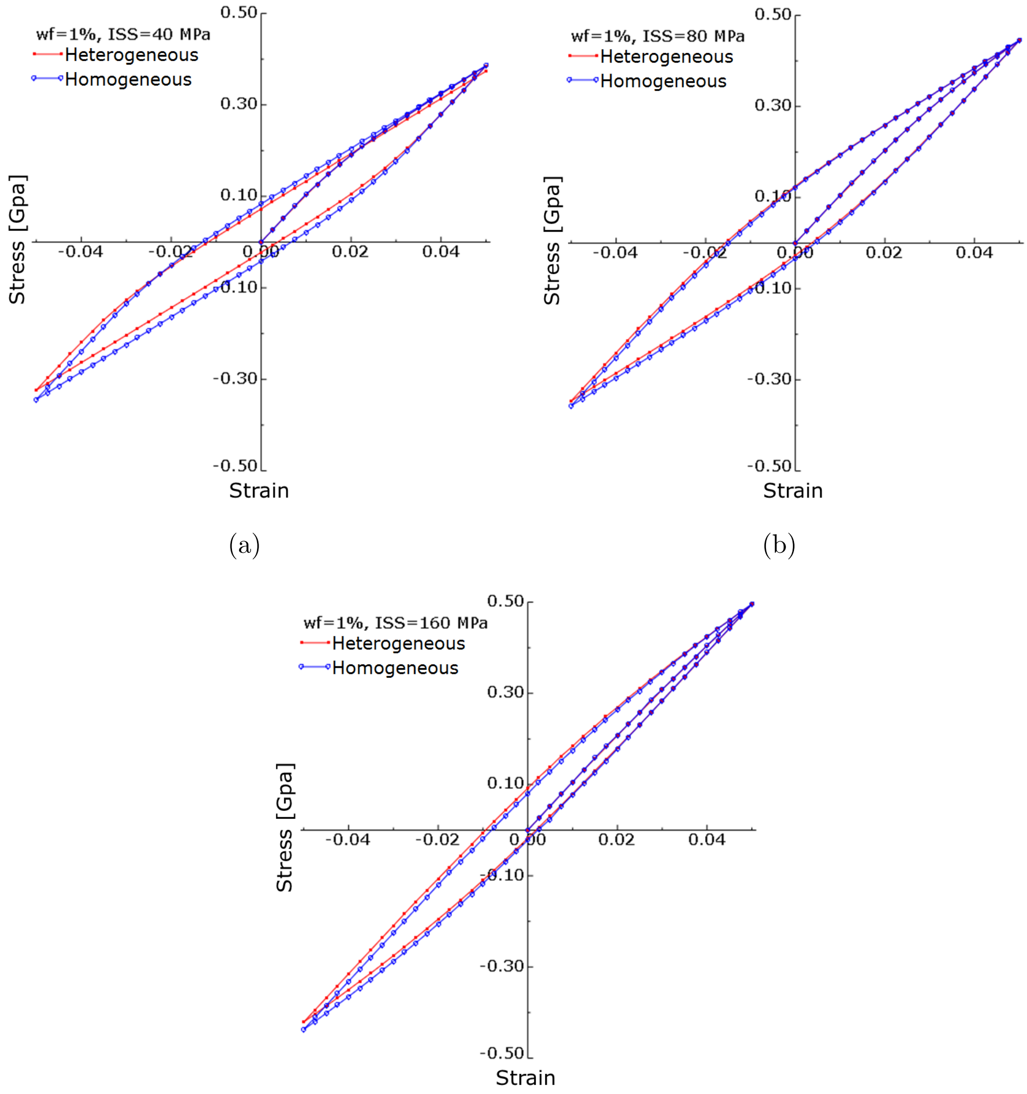

(a) (b)

(c)

Figure 4.26: Stress-strain curves of heterogeneous and homogeneous CNT-RC material from cyclic tests at $\nu \to \infty$; wf=1% and ISS=40, 80 and 160 MPa

seem to be close enough to these of the heterogeneous, with the best correlation occurring for ISS=80 MPa in all wf cases. Notice that, since strain rate effects are not considered in these simulations, the behavior of the CNT-RC material during the cyclic loading remains linear elastic and thus the energy dissipation of the RVE is attributed solely to CNT slippage. Also, some qualitative remarks

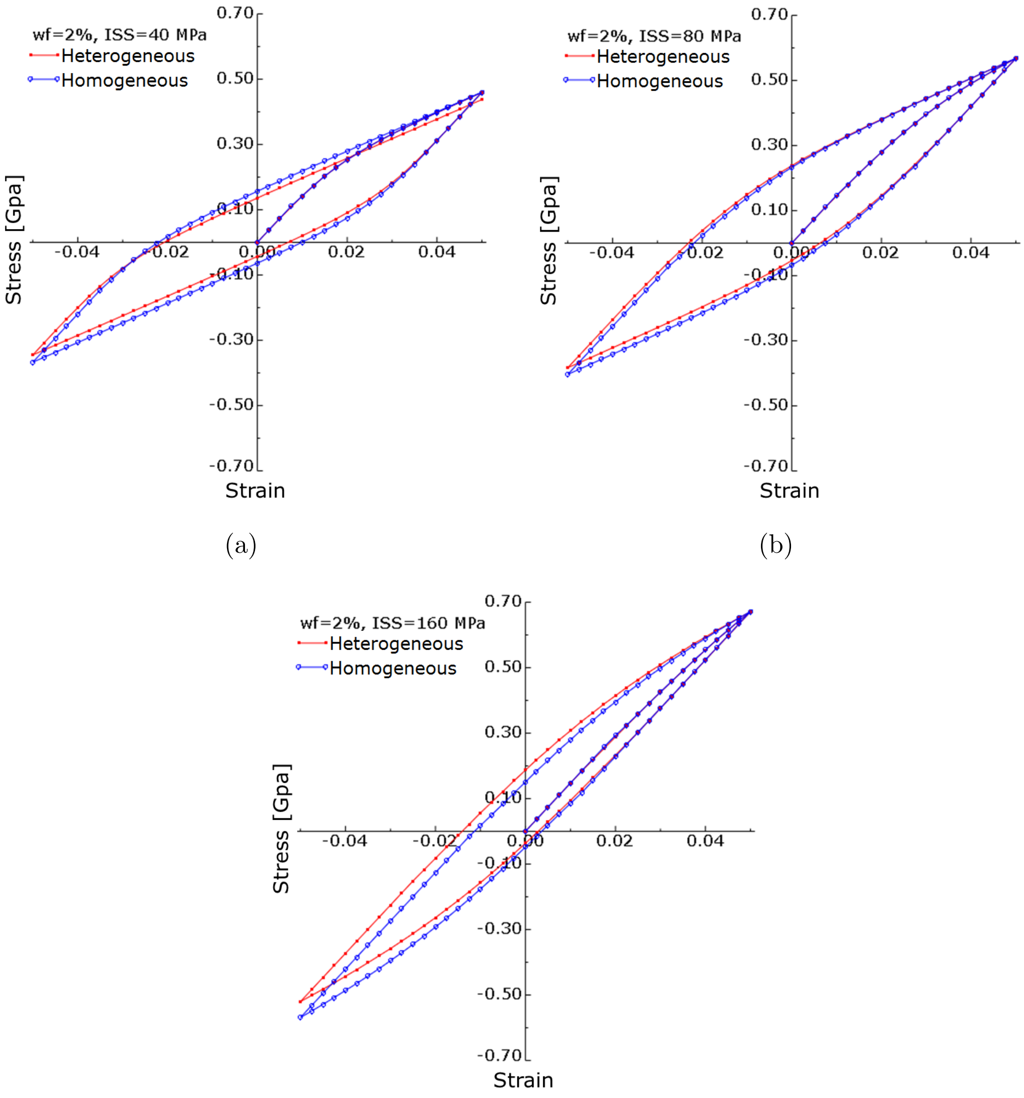

(a) (b)

(c)

Figure 4.27: Stress-strain curves of heterogeneous and homogeneous CNT-RC material from cyclic tests at $\nu \to \infty$; wf=2% and ISS=40, 80 and 160 MPa

for the damping behavior of the composite can be deduced from these figures. Specifically, an increase of the loss factor with the increase of the wf value and a peak point of the loss factor for ISS values between 80 and 160 MPa for all wf cases, are observed. If the ISS limit point is exceeded, then the loss factor is decreased. This means that as the full-bond condition is reached, slippage of CNTs is hardly initiated and thus no energy dissipation mechanism in the material exists.

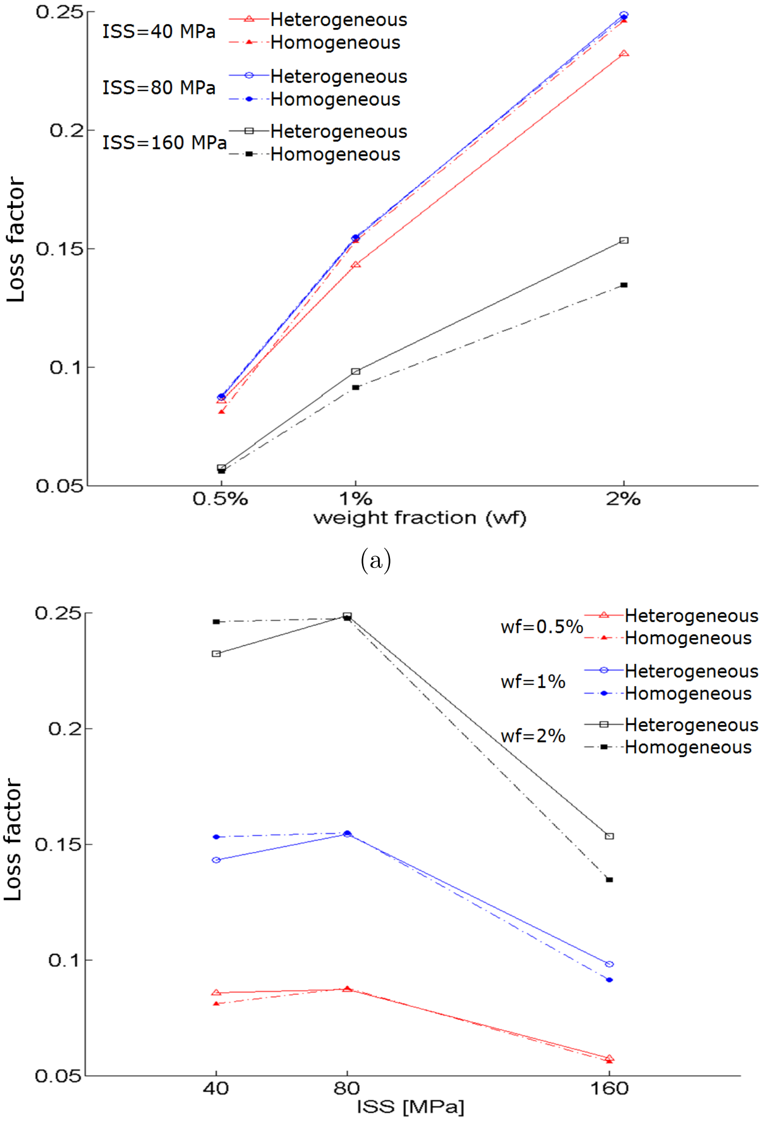

(a)

(b)

Figure 4.28: Loss factor of the heterogeneous and homogeneous CNT-RC material vs (a) wf and (b) ISS

Figure 4.29 plots the stress-strain curves of both the heterogeneous and homogeneous CNT-RC material obtained from cyclic tests at frequency $\nu = 1$ Hz. The results correspond to CNT-RC models with wf=2% and ISS=40, 80 and 160

MPa. In these simulations, PEEK matrix exhibits viscoelastic response, thus the energy dissipation mechanism of the composite material is due to viscosity and slip. For this case, the observed differences in the results may be attributed to insufficient homogenization of the strain rate effects in the material. As mentioned in Section 4.2.2.2, effective plasticity parameters are calibrated in the long term response of the viscoelastic matrix. A more realistic approach would occur, if these effective properties were obtained in various strain rates. However, the results are still very close to each other and thus the validity of the proposed homogenization method is also verified in this case.

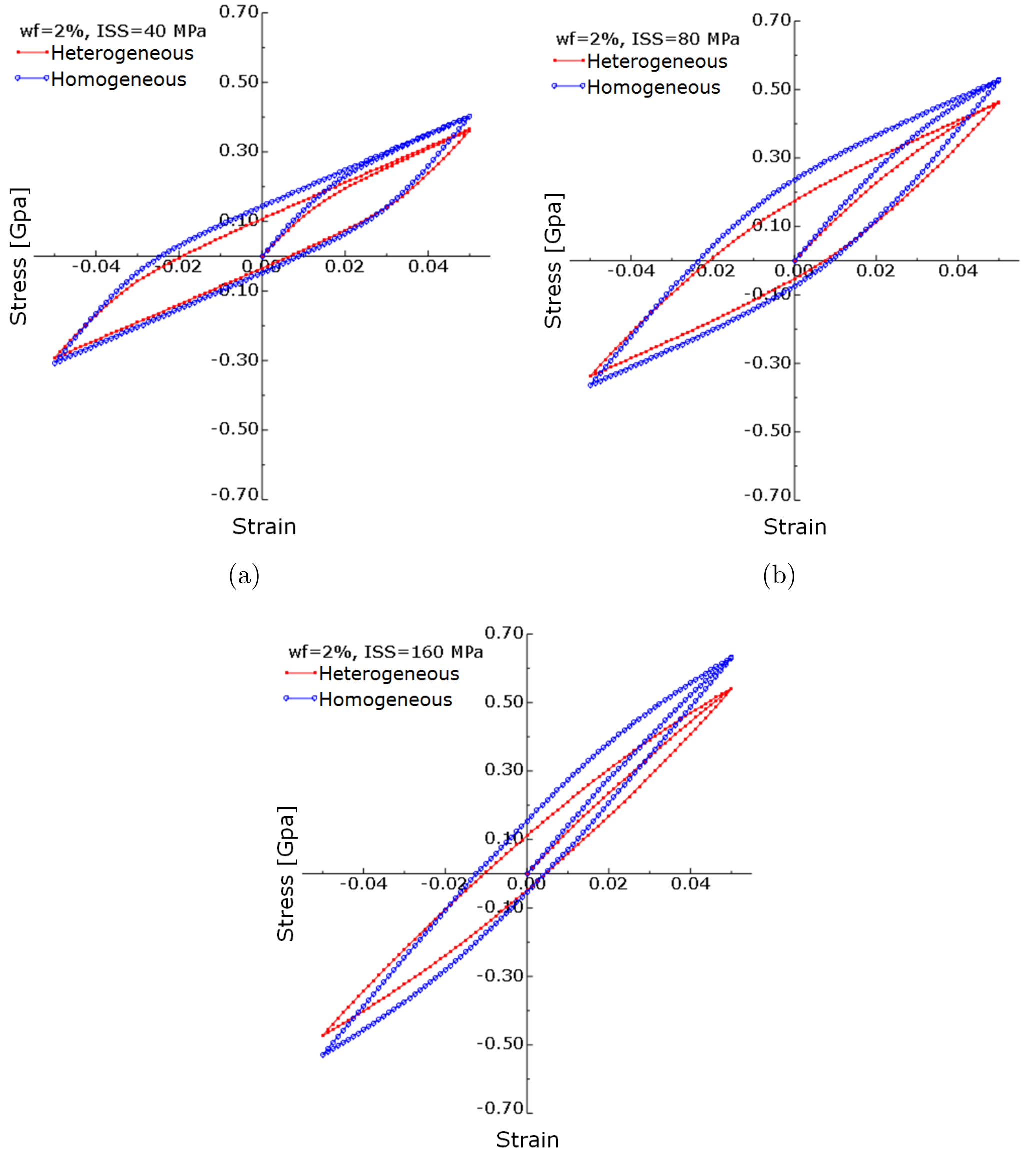

(a)

(b)

(c)

Figure 4.29: Stress-strain curves of heterogeneous and homogeneous CNT-RC material from cyclic tests at $\nu = 1$ Hz; wf=2% and ISS=40, 80 and 160 MPa

4.2.3.2 Test case 2: Tensile tests on CNT-RC specimens

In this example, tensile tests on CNT-RC specimens are simulated. These specimens are consisted of a rectangular PEEK matrix reinforced by four straight

CNTs. Distribution of CNTs inside the matrix follows a square pattern. The efficiency of the proposed homogenization method is evaluated by comparing the stress-strain curves of the heterogeneous and the homogeneous models. Finite element meshes of both models are illustrated in Fig. 4.30. Particularly, the matrix of the composite in both models is discretized by 4100 solid elements, while each CNT in the heterogeneous model is discretized by 37 Bernoulli beam elements. The wf of the CNT-RC material of the specimen is 2%, while ISS=40, 80 and 160 MPa. As shown in Fig. 4.31, the microstructure of the heterogeneous model can be constructed by merging four RVE models with wf=2%. The specific RVEs were previously analyzed in test case 1 of Section 4.2.3.1. Calibrated parameters for the viscoplastic model of Section 4.2.2 have been calculated from these RVE models. In this test case, these calculated effective parameters are assigned to the homogeneous CNT-RC material of the specimens.

A monotonic axial tensile load is applied on these specimens through Eq. (4.39) with $\boldsymbol{E} = [E_{11}\ \ 0\ \ 0\ \ 0\ \ 0\ \ 0]^T$ and $E_{11} = 5\%$. Figures 4.32(a), 4.32(b) and 4.32(c) plot the stress-strain curves of both the heterogeneous and the homogeneous models for wf=2% and ISS=40, 80 and 160 MPa, respectively. These results have been obtained without considering strain rate effects of the material. Thus in these simulations PEEK matrix exhibits instantaneous elastic response. The stress-strain curves of the homogeneous models are well fitted to these of the heterogeneous models. The efficiency of the proposed homogenization method is therefore asserted. Figures 4.33(a), 4.33(b) and 4.33(c) plot the stress-strain curves of the aforementioned models, but this time viscoelastic response of PEEK matrix is considered. The imposed strain rates correspond to a loading frequency of 1 Hz. Small discrepancy of the results may be again attributed to calibration errors. However, the results are expected to fit each other if larger RVEs with random distribution of CNTs are considered. In this case, the effect of the local strain rates in the microstructure can be smoothed away and thus microstructural behavior can be better captured by the homogeneous models.

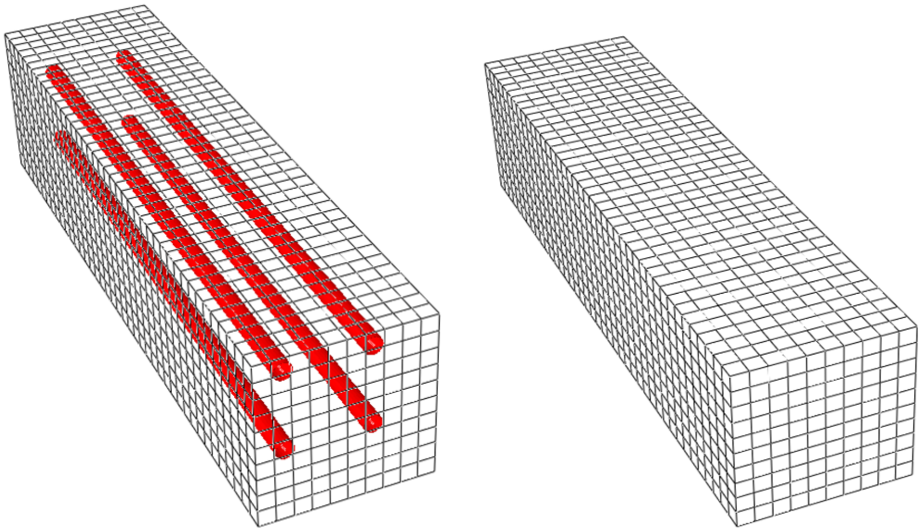
(a) (b)

Figure 4.30: FE mesh of (a) heterogeneous, (b) homogeneous CNT-RC specimen

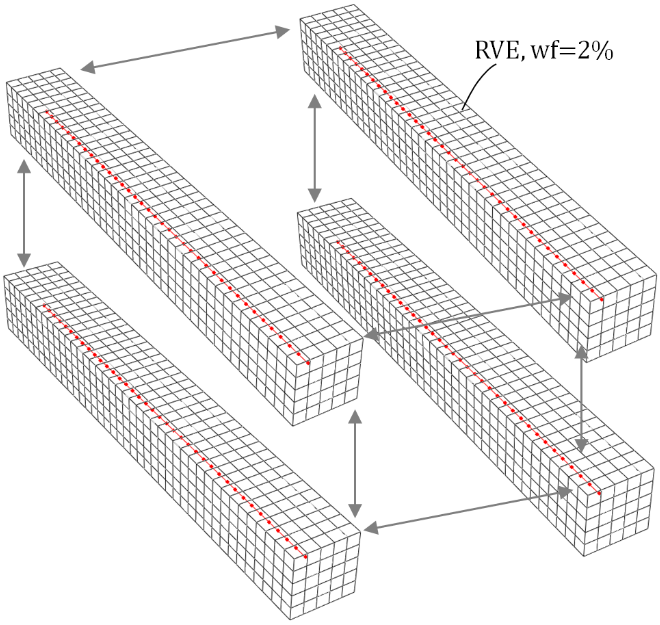

Figure 4.31: Construction of heterogeneous model of CNT-RC specimen by merging four RVEs with wf=2%

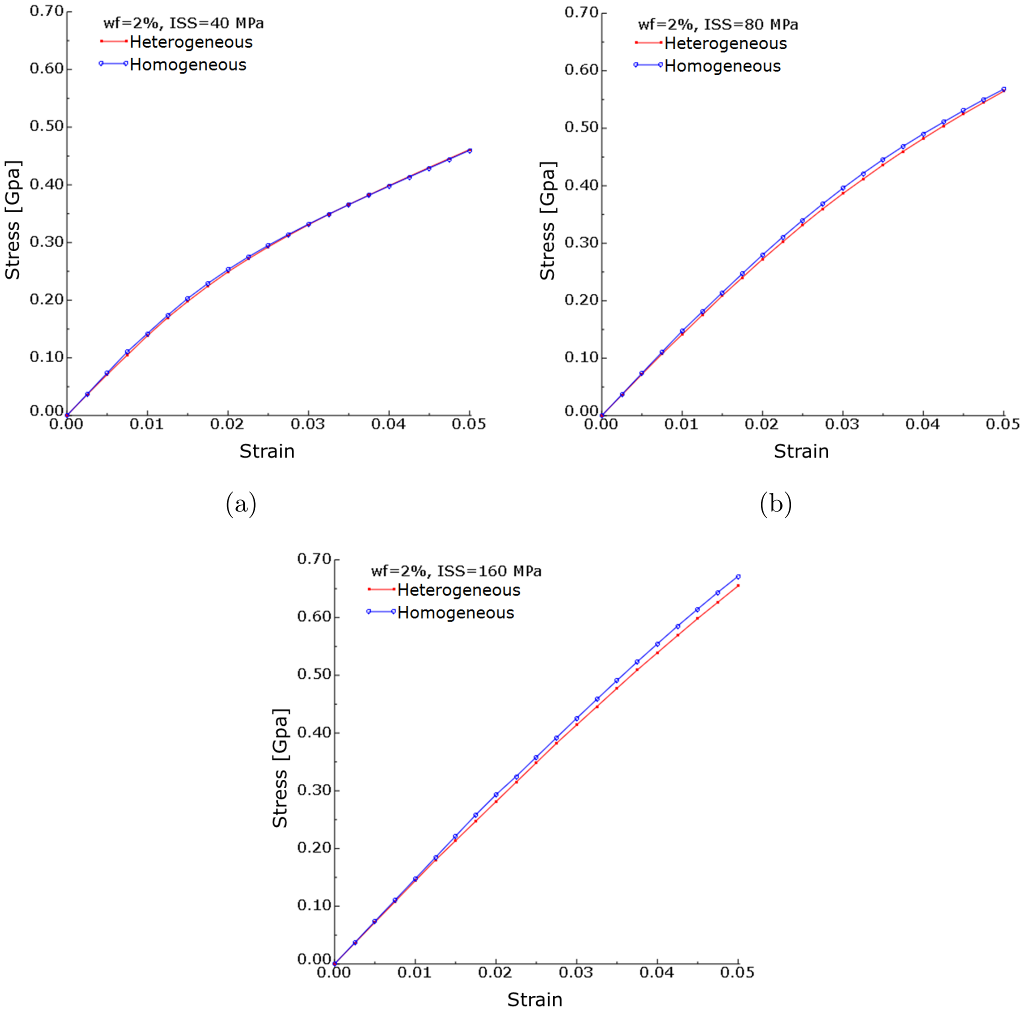

(a)

(b)

(c)

Figure 4.32: Stress-strain curves of heterogeneous and homogeneous models of CNT-RC specimen without considering strain rates; wf=2% and ISS=40, 80 and 160 MPa

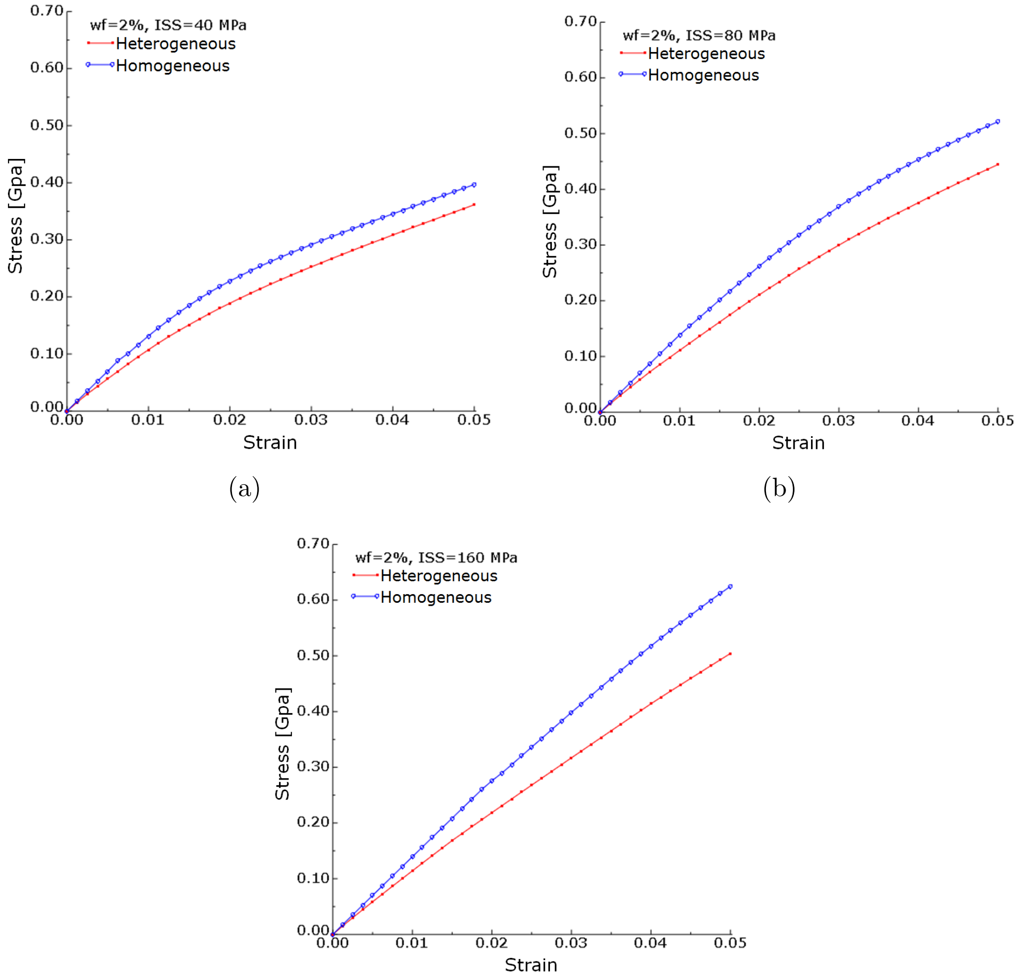

(a)

(b)

(c)

Figure 4.33: Stress-strain curves of heterogeneous and homogeneous models of CNT-RC specimen considering strain rates ($\nu = 1$ Hz); wf=2% and ISS=40, 80 and 160 MPa

Chapter 5

Graphene nanoplatelet-reinforced composites

Graphene nanoplatelets (GnPs) are unique carbon materials with multifunctional properties. They are considered as two-dimensional nanoparticles consisting of small stacks of graphene sheets that are 1-15 nm thick and 1-100 μm wide. These stacked layers are bonded to each other by van der Waals forces with an inter-layer distance of 0.34 nm and exhibit a specific surface area of 2630-2965 m^2/g [66, 11]. The geometrical characteristics of GnPs can be tuned by a variety of techniques, such as intercalation, oxidation, heat treatment, microwave irradiation and ultrasonic treatment [99]. Scanning electron microscope (SEM) images provided in Fig. 5.1 illustrate the bulk morphology of exfoliated GnPs. Since GnPs are composed of the same material as carbon nanotubes, they share many of their electrochemical characteristics, which lead to their supreme mechanical and physical properties. Specifically, GnPs exhibit tensile modulus ∼1 TPa, tensile strength 10-20 GPa, thermal conductivity ∼3000 W/(m·K), electrical resistivity $\sim 5 \times 10^{-5} \Omega\cdot\text{cm}$, with only a bulk density of 0.03-0.15 g/cm^3 [39, 41, 37].

Incorporation of GNPs into a polymer matrix has significant advantages over CNTs. For example, GNPs do not require disentanglement that is one of the most difficult parts in processing CNTs. The platelet shape offers GnP boundary edges that are easier to be modified through functionalization, leading to enhanced interfacial adhesion between GnP and polymer. Also, GNPs are produced from the very affordable and abundant natural graphite, and thus can be used as a cost-effective alternative, replacing the expensive CNTs. These advantages along with the high aspect ratio and the large surface area make GnP a promising candidate for enhancing the mechanical and physical properties of polymer composites.

This chapter deals with the homogenization of random GnP-RCs containing arbitrarily shaped platelets. Homogenization is performed numerically in the framework of extended finite element method (XFEM) coupled with Monte Carlo simulation (MCS). In particular, the influence of the platelet shape on the effective properties of the GnP-reinforced composites is highlighted. The platelet inclusions are randomly distributed and oriented within the polymer and their shape is implicitly modeled by the iso-zero of an analytically defined random level set function, which also serves as the enrichment function in the framework of XFEM. The analytical function used is a random ”rough” circle defined by a set of independent identically distributed (i.i.d.) random variables and deterministic constants governing the roughness of the shape [86]. Homogenization is performed based on Hill’s energy condition and MCS [57]. The homogenization involves the generation of a large number of random realizations of the microstructure geometry based on a given volume fraction of the inclusions and other parameters (shape, spatial distribution and orientation). Although the proposed homogenization method aims to derive effective properties for GnP-RCs, its usage can be generalized in every heterogeneous medium containing arbitrarily shaped inclusions. For this reason, the applicability of the method is tested for various stiffness ratio values, which correspond to both stiff and compliant inclusions (see the numerical results of Section 5.3).

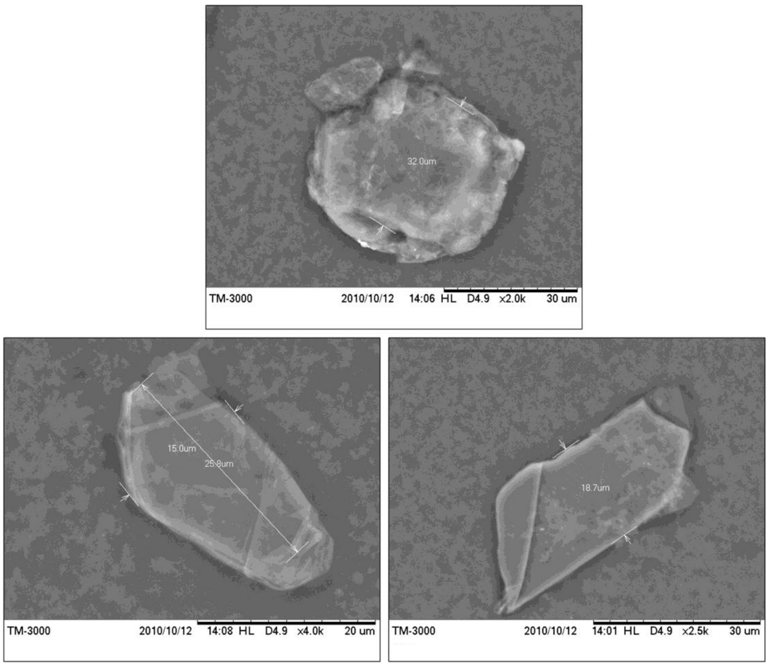

Figure 5.1: Scanning electron microscope images of exfoliated GnPs showing bulk morphology and average platelet diameter (Source: Duguay [21])

5.1 Modeling RVEs of GnP-reinforced composites with XFEM

Classical finite element (FE) methods are commonly used to analyze complex microstructures. In this case, the mesh conforms to the internal material interface boundaries that cause the strong or weak discontinuities in the displacement solution field. While fast meshing algorithms are available to discretize a domain with such internal features, this step still involves a significant computational effort. This is especially true when large number of simulations are to be performed to quantify the probability distributions involved, with reasonable confidence. In Zohdi and Wriggers [115], the homogenization of random heterogeneous media is performed using the standard FE method with material discontinuities within the elements, following a microstructure-nonconforming approach. Micro-geometrical idealizations for the irregular shapes of the inclusions are used, where a generalized diameter is defined for the smallest sphere that can enclose a single particle, which can be considered of arbitrary shape. The development of the extended finite element method (XFEM) by Moës et al [60] offers the possibility to use a regular mesh which does not have to be adapted to the internal details (cracks or material interfaces) of each random realization of the microstructure. Extended finite element method is therefore particularly suitable to model the local heterogeneous material structure in a representative volume element (RVE) for the application of homogenization techniques.

The extended finite element method uses nodal enrichment functions within the framework of the partition of unity method to augment the FE approximations over a structured mesh [56]. These enrichment functions act as additional bases to model strong or weak discontinuities that occur along the interface boundaries. The method was initially developed to model strong discontinuities in the primary field variables as they occur at a crack [60]. It has also been applied to the modeling of material interfaces which represent weak discontinuities in the mechanical boundary value problem [4, 88, 61, 23]. In Yvonnet et al [110], an XFEM/level set approach is implemented in order to model interface effects and to compute the size-dependent effective properties of composites containing nanopores. Nowadays XFEM is used in many other applications. Zhao et al [112] used a smoothed extended finite element method (SmXFEM) to study the morphological transformation of precipitates in phase-separated alloys. In Lang et al [47], an extended stochastic FEM (X-SFEM) is applied in order to predict heat transfer in composite materials with uncertain inclusion geometry. An open source XFEM library which can handle a wide variety of problems with discontinuities, has been developed by Bordas et al [7]. Talebi et al [91] developed an open-source software framework called PERMIX for multiscale modeling and simulation of fracture in solids. A comprehensive review of the method and its application to material modeling can be found in [6].

5.1.1 Problem formulation

Consider a medium which occupies a domain $\Omega \subset \mathbb{R}^2$ whose boundary is represented by Γ. Let prescribed traction $\bar{t}$ applied on surface $\Gamma_t \subset \Gamma$ (natural boundary conditions) and prescribed displacements $\bar{u}$ applied on $\Gamma_u \subset \Gamma$ (essential boundary conditions). The medium contains an inclusion which occupies the domain Ω^+ and is surrounded by the internal surface $\Gamma_{incl} \subset \Gamma$ such that $\Omega = \Omega^+ \cup \Omega^-$ and $\Gamma = \Gamma_t \cup \Gamma_u \cup \Gamma_{incl}$ (Fig. 5.2). The governing equilibrium and kinematic equations for the elastostatic problem of the medium ignoring the body forces is:

$$\begin{aligned} \mathrm{div}\boldsymbol{\sigma} &= 0 && \text{in } \Omega && (5.1a)\\ u &= \bar{u} && \text{in } \Gamma_u && (5.1b)\\ \boldsymbol{\sigma} \cdot n &= \bar{t} && \text{in } \Gamma_t && (5.1c)\\ [\![\boldsymbol{\sigma} \cdot n_{incl}]\!] &= 0 && \text{in } \Gamma_{incl} && (5.1d) \end{aligned}$$

where n and n_{incl} are the unit normals to Γ_t and Γ_{incl}, respectively. Note that Eq. (5.1d) implies traction continuity along the material interface Γ_{incl}.

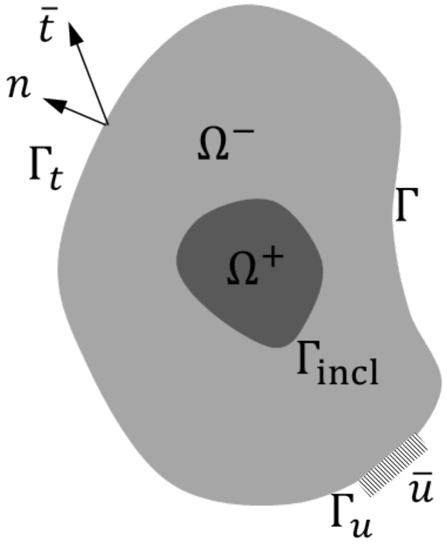

Figure 5.2: Schematic of a medium which occupies a domain $\Omega = \Omega^+ \cup \Omega^-$, contains an inclusion (Ω^+) and is subjected to essential and natural boundary conditions on surfaces Γ_u and Γ_t respectively

5.1.2 XFEM weak form

The differential Eq. (5.1a) represents the strong form of the elastostatic boundary value problem. In order to find a numerical solution u of the problem, the differential equation is transformed into a suitable variational form by first multiplying it with a test function v and then integrating over the domain Ω. So, a trial solution u is seeked, which satisfies the weak form and the essential boundary conditions of the problem in a functional space U defined as:

$$U := \left\{ u \in H^1\left(\Omega\right) : u = \bar{u} \ \text{ on } \ \Gamma_u \right\} \tag{5.2}$$

The test function v belongs to the functional space V, which contains any set of kinematically admissible test functions (virtual displacements) and is defined as:

$$V := \left\{ v \in H^1\left(\Omega\right) : u = 0 \ \text{ on } \ \Gamma_u \right\} \tag{5.3}$$

where $H^1\left(\Omega\right)$ is the Sobolev space of functions with square-integrable first derivatives in Ω. The weak formulation of the static problem can now be stated as:

$$\text{find } u \in U \text{ such that } \forall v \in V, \quad a\left(u, v\right) = l\left(v\right) \tag{5.4}$$

where the bilinear form $a\left(\cdot,\cdot\right)$ and the linear form $l\left(\cdot\right)$ are defined as:

$$\begin{aligned} a\left(u, v\right) &:= \int_{\Omega} \boldsymbol{\sigma}\left(u\right) : \nabla v \, \mathrm{d}\Omega \\ l\left(v\right) &:= \int_{\Gamma_t} v \cdot \bar{t} \, \mathrm{d}\Gamma \end{aligned} \tag{5.5}$$

5.1.3 XFEM discrete system

Considering the Bubnov-Galerkin method for the extended finite element (XFE) elastostatic problem, the trial function u as well as the test function v are represented as a linear combination of the same interpolation functions. The weak form of the discrete problem can be stated as:

$$\begin{aligned}
&\text{find } u^h \in U^h \subset U \text{ such that } \forall v^h \in V^h \subset V, \\
&a\left(u^h, v^h\right) = l\left(v^h\right)
\end{aligned} \tag{5.6}$$

where h stands for the characteristic size of the elements in the mesh. Note that to accurately capture a non-smooth solution resulting from material interfaces, the traditional FE method requires a mesh that conforms to the inclusion geometry. On the contrary, the XFEM eliminates the requirement of a conforming mesh by enriching the traditional FE approximation with a suitably constructed enrichment function. The XFEM displacement approximation for the trial and test functions can be decomposed into the standard FE part and the enriched part as follows:

$$\begin{aligned}
&u^h(\mathbf{x}) = u^h_{fem}(\mathbf{x}) + u^h_{enr}(\mathbf{x}) = \\
&\sum_{i\in I} N_i(\mathbf{x})\, u_i + \sum_{j\in J} N_j(\mathbf{x})\, \psi(\mathbf{x})\, \alpha_j \\
&v^h(\mathbf{x}) = v^h_{fem}(\mathbf{x}) + v^h_{enr}(\mathbf{x}) = \\
&\sum_{i\in I} N_i(\mathbf{x})\, v_i + \sum_{j\in J} N_j(\mathbf{x})\, \psi(\mathbf{x})\, \beta_j
\end{aligned} \tag{5.7}$$

where I is the set of all nodes in the mesh and J is the set of nodes that are enriched with the enrichment function ψ that satisfies the local character of the displacement field. A detailed description of the stochastic enrichment function that has been developed for arbitrarily shaped inclusions is provided in Section 5.1.4. To satisfy partition of unity, the enrichment function is enveloped by the original shape functions N_j and additional to the standard nodal variables u_i or v_i, enriched nodal variables α_j or β_j are introduced in the approximation equations for u^h or v^h, respectively.

In case of microstructures containing high volume fraction of inclusions or very nearby inclusions, the use of XFEM/level set method induces numerical artefacts that degrade the accuracy and convergence of the solution. To avoid these problems, the approach proposed by Tran et al [95] and Hiriyur et al [32] has been adopted in this study. In this approach, a node whose support is cut by multiple inclusions n_0 is enriched by different enrichment functions ψ_k corresponding to each inclusion k. The enriched nodal variables α_{jk} or β_{jk} of Eq. (5.8) correspond to node j whose support is cut by the k-th inclusion. The approximation displacement field can then be written as:

$$\begin{aligned} u^h(\mathbf{x}) &= \sum_{i\in I} N_i(\mathbf{x})\, u_i + \sum_{j\in J} N_j(\mathbf{x}) \left(\sum_{k=1}^{n_0} \psi_k(\mathbf{x})\, \alpha_{jk} \right) \\ v^h(\mathbf{x}) &= \sum_{i\in I} N_i(\mathbf{x})\, v_i + \sum_{j\in J} N_j(\mathbf{x}) \left(\sum_{k=1}^{n_0} \psi_k(\mathbf{x})\, \beta_{jk} \right) \end{aligned} \tag{5.8}$$

Substituting Eq. (5.8) into the weak form of Eq. (5.6), a discrete system of algebraic equations is obtained:

$$\begin{bmatrix} K_{uu} & K_{u\alpha} \\ K_{\alpha u} & K_{\alpha\alpha} \end{bmatrix} \begin{bmatrix} u \\ \alpha \end{bmatrix} = \begin{bmatrix} F_u \\ F_\alpha \end{bmatrix} \tag{5.9}$$

where $[K_{uu}]_{ij} = a(N_i, N_j)$, $[K_{\alpha\alpha}]_{ij} = a\left(N_i \sum_{k=1}^{n_0} \psi_k, N_j \sum_{k=1}^{n_0} \psi_k\right)$ and $[K_{u\alpha}]_{ij} = [K_{\alpha u}]_{ji} = a\left(N_i, N_j \sum_{k=1}^{n_0} \psi_k\right)$ are the stiffness matrices associated with the standard FE approximation, the enriched approximation and the coupling between them, respectively. The forces are expressed as $[F_u]_i = l(N_i)$ and $[F_\alpha]_j = l\left(N_j \sum_{k=1}^{n_0} \psi_k\right)$. From the solution of the system, the nodal displacements u and enriched variables α are finally obtained. It is worth noting that, although the algebraic system of Eq. (5.9) is of larger dimension than that before the enrichment, XFEM has the benefits of using a coarser mesh compared with FEM and thus solving a smaller global system of equations.

5.1.4 Enrichment function

Inclusions into a medium introduce a weak discontinuity in the displacement field (due to change in material properties), which shows a kink at the interface and a discontinuous first derivative. For modeling such fields in the framework of XFEM, usually a ramp function in the form of absolute distance function is used to enrich the approximation field [44]. XFEM is typically combined with the level set approach where a level set function ϕ is used to implicitly describe random inclusion geometry [83, 47]. While the level set method is often used to track moving interfaces on a fixed mesh [81], it is used herein to define the location of the inclusion interface and its stochastic variation. The location of the interface $\Gamma_{incl}(\theta)$ is implicitly defined by the iso-zero of the following random level set function representing a "rough" circle, which is taken as the signed radial distance function to the curve:

$$\phi(\mathbf{x}, \theta) = \|\mathbf{x} - \mathbf{c}\| - R(\alpha(\mathbf{x}), \theta) \tag{5.10}$$

where $\mathbf{x}$ is the spatial location of a point in the meshed domain, $\mathbf{c}$ is the center of the rough circle, $R(\alpha(\mathbf{x}), \theta)$ is a random field representing the radius of the rough circle, $\alpha(\mathbf{x}) \in [0, 2\pi]$ is the polar angle at position $\mathbf{x}$ and θ denotes the randomness of a quantity (Fig. 5.3).

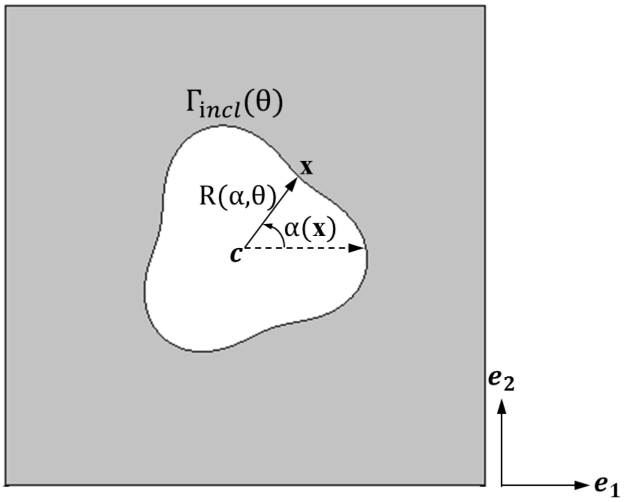

Figure 5.3: Schematic representation of a rough circle

In this study, the following equation is used for the random radius [86]:

$$R\left(\alpha,\theta\right)=0.2+0.03Y_1(\theta)+0.015\{Y_2(\theta)cos(k_1\alpha)+ \\ Y_3(\theta)sin(k_1\alpha)+Y_4(\theta)cos(k_2\alpha)+Y_5(\theta)sin(k_2\alpha)\} \tag{5.11}$$

where the i.i.d. uniform random variables $Y_i(\theta)\in U\left(-\sqrt{3},\sqrt{3}\right)$, $i=1,...,5$. Note that the first random variable controls the "mean" reference radius while the other four control its amplitude. k_1, k_2 are deterministic constants which define the period of oscillations of the random rough circle around the shape of the reference (perfect) circle. An example of the level set function ϕ for a random rough circle inclusion with $k_1=0$ and $k_2=3$ is shown in Fig. 5.4. The iso-zero contour level of ϕ displayed in Fig. 5.4(b) defines the boundary $\Gamma_{incl}(\theta)$ which describes the shape of the inclusion.

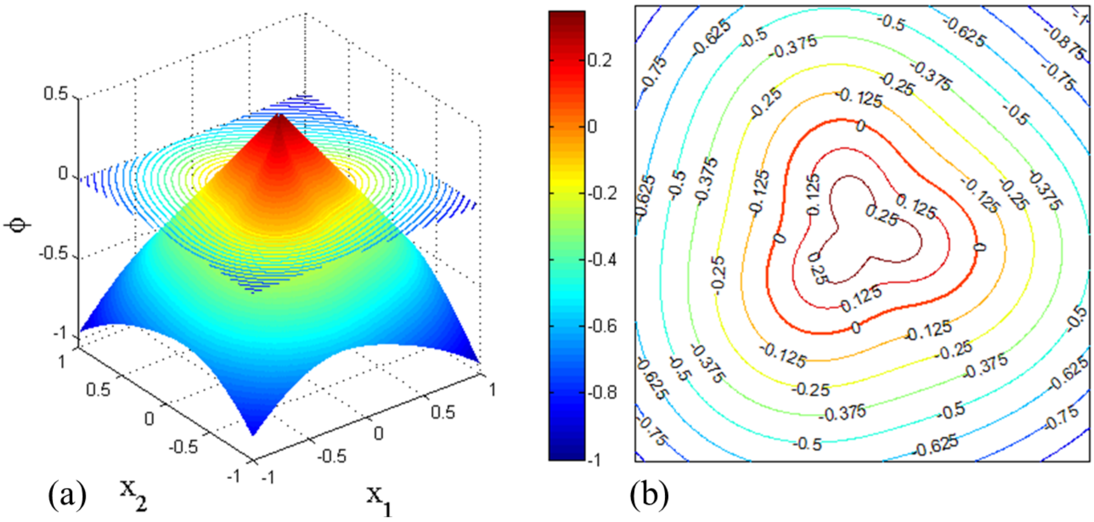

Figure 5.4: a) Signed level set function and b) contour levels of ϕ for a random rough circle inclusion with $k_1=0$ and $k_2=3$

An appropriate enrichment function which captures discontinuous first derivatives in the approximation fields was proposed by Sukumar et al [88]. This is a ramp function defined as the absolute value of the random level set function discretized according to the FE mesh of the spatial domain as follows:

$$\psi_k(\mathbf{x}) = \left| \sum_{i \in I} N_i(\mathbf{x}) \phi_i^k \right| \tag{5.12}$$

where ϕ_i^k is the value of the level set function of Eq. (5.10) at node i for the k-th inclusion and $N_i(\mathbf{x})$ are the FE nodal basis functions. In order for the XFE approximations to retain the Kronecker-δ property of the standard FE approximations so that at node j, $u^h(\mathbf{x}_j) = u_j$, a shifted enrichment function $S_k(\mathbf{x}) = \psi_k(\mathbf{x}) - \psi_k(\mathbf{x}_j)$ was first suggested by Belytschko et al [4]. By this shifting operator, the enrichment terms vanish at all nodes $j \in J$ and thus smoothing of the discontinuous solution is achieved on the problematic blending elements leading to improved convergence.

Another choice for the enrichment function was introduced by Moës et al [61]. This is a ridge function centered on the interface, having zero value on the elements which are not crossed by the interface and defined as follows:

$$\psi_k(\mathbf{x}) = \sum_{i \in I} N_i(\mathbf{x}) \left|\phi_i^k\right| - \left| \sum_{i \in I} N_i(\mathbf{x}) \phi_i^k \right| \tag{5.13}$$

This enrichment function avoids spurious numerical results on blending elements and thus improves the accuracy and convergence of the XFEM solution, as shown in the next section.

5.1.5 Convergence study of XFEM solution for single inclusion

In this section, three RVE models containing a single centered inclusion with different geometry are simulated with both XFEM and standard FEM. Equations (5.10) and (5.11) are used for the construction of the inclusions, where parameters (k_1, k_2) are chosen as $(0, 0)$, $(0, 3)$ and $(0, 6)$. All RVEs have a unit cell geometry with dimensions 10 × 10 mm and a volume fraction (vf) of inclusions 30%. This is achieved by scaling the inclusion geometry as explained in Section 5.2.1. In the case of XFEM, a structured mesh of bilinear quadrilateral elements is used. The same type of elements is used for FEM but in this case, the mesh must conform to the boundaries of the inclusions (see Figs. 5.7-5.9). The RVEs with the boundary conditions and loads shown in Fig. 5.5 are subjected to pure tension. The magnitude of the traction q along the right edge is 1 GPa. The matrix and the GnP inclusions are modeled using linear elastic isotropic materials with Young's moduli $E_m = 1$ and $E_{incl} = 1000$ GPa, respectively. The Poisson ratio for both materials is set equal to 0.3.

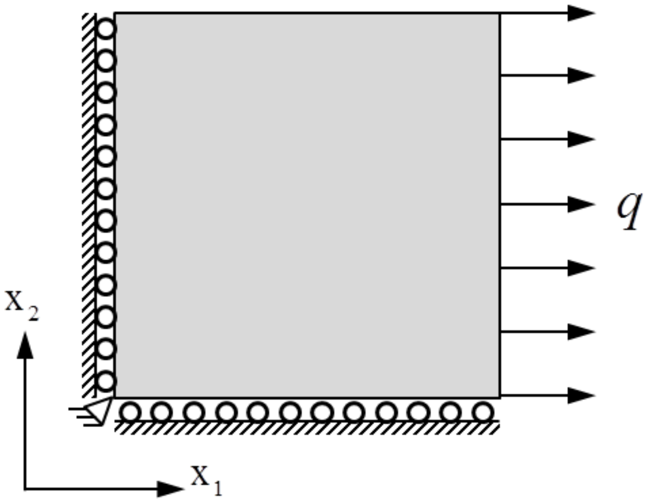

Figure 5.5: Schematic of boundary conditions and loading of the RVE models used in Section 5.1.5

A convergence study with regard to XFE size is carried out for the aforementioned RVE models using equispaced rectangular $L_h \times L_h$ meshes, where $L_h = 10, 20, 40, 80$. Since no analytical solution exists for an RVE containing a single inclusion of arbitrary shape, the results obtained with a fine mesh FEM model are considered as the reference solution. The convergence study is based both on the L_2 norm and the energy norm, which are defined as:

$$e_{L_2} = \frac{\| u^{fem} - u^{xfem} \|_2}{\| u^{fem} \|_2} \tag{5.14}$$

$$e_E = \frac{\| u^{fem} - u^{xfem} \|_E}{\| u^{fem} \|_E} = \frac{| \Pi^{fem} - \Pi^{xfem} |}{| \Pi^{fem} |} \tag{5.15}$$

where $\Pi = \frac{1}{2}u^T K u$ is the strain energy of the model.

The results of the convergence study are presented in Fig. 5.6. It is verified that the enrichment function of Eq. (5.13) leads to improved accuracy and convergence compared to the enrichment function of Eq. (5.12). As shown in Fig. 5.6, the relative error in both L_2 and energy norms when the enrichment function of Eq. (5.13) is used, is at most 0.48% for an XFEM mesh of 40×40. This mesh size can be considered sufficiently fine for an accurate representation of the interface geometry details. Therefore, all the subsequent simulations in this chapter are conducted using this specific mesh size and the enrichment function of Eq. (5.13). Figs. 5.7-5.9 display the selected XFE mesh and the fine FE mesh for each RVE along with the corresponding displacement fields (U_{x_1}), which agree very well to each other. Details about the XFE and FE meshes for the RVE model depicted in Fig. 5.9 are provided in Table 5.1.

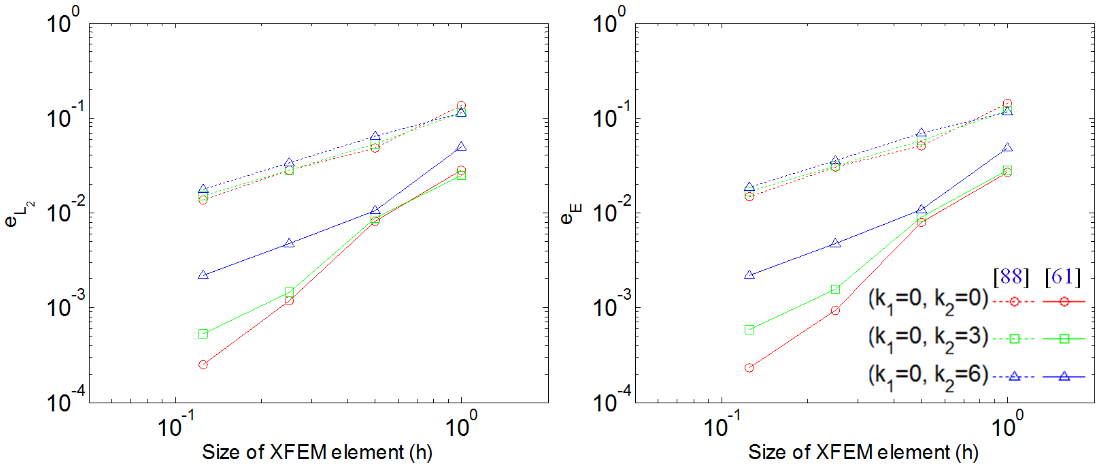

Figure 5.6: Convergence of XFEM to FEM results with regard to four element sizes corresponding to XFEM mesh density $L_h \times L_h$ ($L_h = 10, 20, 40, 80$) using the enrichment functions of Sukumar et al [88] and Moës et al [61]

A convergence study with respect to the matrix-inclusion stiffness ratio is also conducted for the RVE models described previously. Both stiff ($E_{incl} > E_m$) and compliant ($E_m > E_{incl}$) inclusions are considered for stiffness ratio values (E_{incl}/E_m or E_m/E_{incl}) ranging from 5 to 10^4. In Fig. 5.10, the relative error in L_2 and energy norm is plotted against the corresponding ratio of elastic moduli.

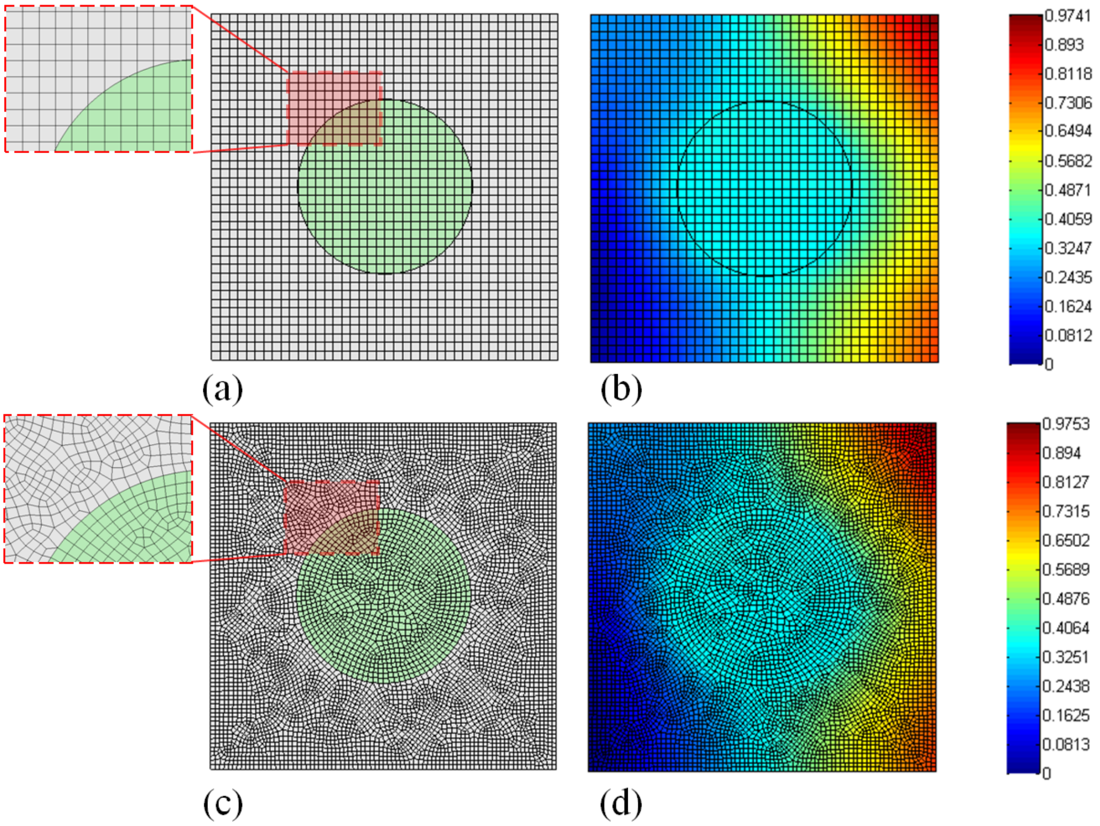

(a) (b) (c) (d)

Figure 5.7: Comparison of displacement fields U_{x_1} obtained from XFEM and FEM for RVE with inclusion $(k_1 = 0, k_2 = 0)$: a) XFEM mesh, b) XFEM displacements, c) FEM mesh and d) FEM displacements

		XFEM			
	FEM	10×10	20×20	40×40	80×80
nodes	8281	121	441	1681	6561
elements	8120	100	400	1600	6400
dofs	16562	318	1074	3746	13890

Table 5.1: Mesh details of RVE with a single inclusion of arbitrary shape $(k_1 = 0, k_2 = 6)$

In the case of stiff inclusions, the relative error seems to increase as the stiffness ratio increases whereas for compliant inclusions the relative error seems to reach a plateau for stiffness ratio greater than 10^2. For the elastic moduli ratio 10^3

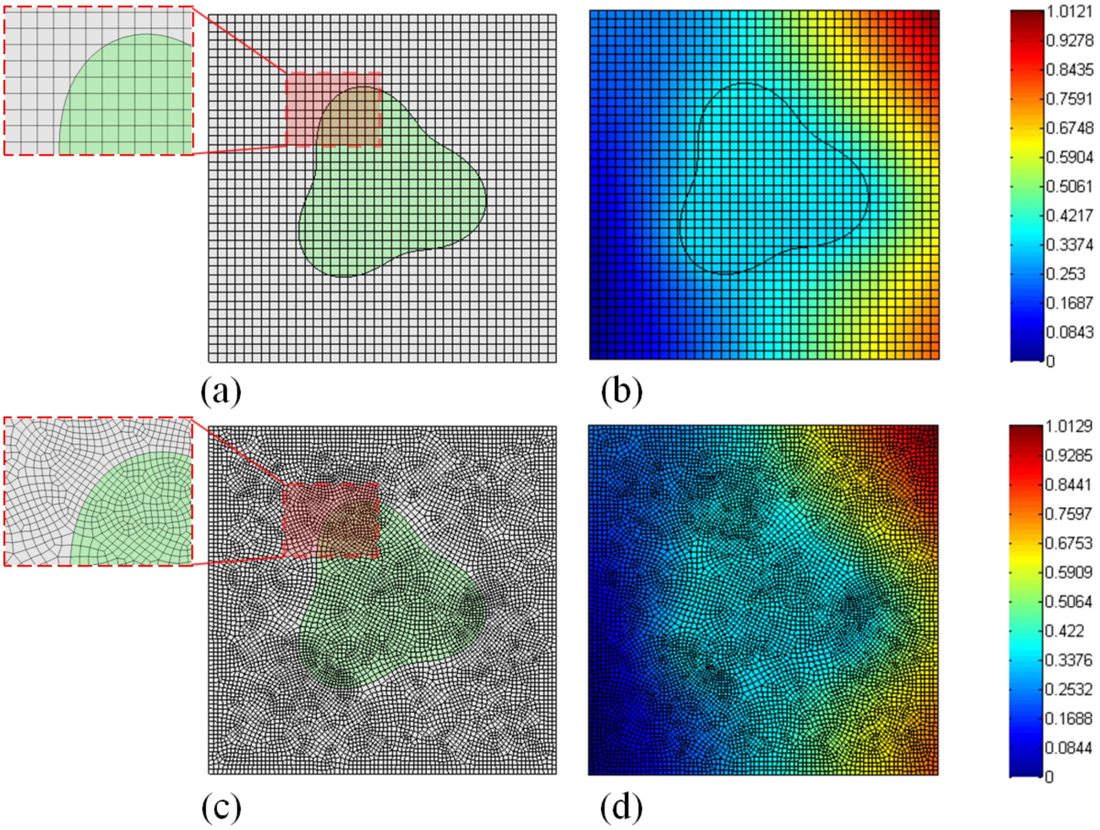

Figure 5.8: Comparison of displacement fields U_{x_1} obtained from XFEM and FEM for RVE with inclusion $(k_1 = 0, k_2 = 3)$: a) XFEM mesh, b) XFEM displacements, c) FEM mesh and d) FEM displacements

used in the numerical examples (Section 5.3), the differences between XFEM and reference FEM solutions are at most 0.48%.

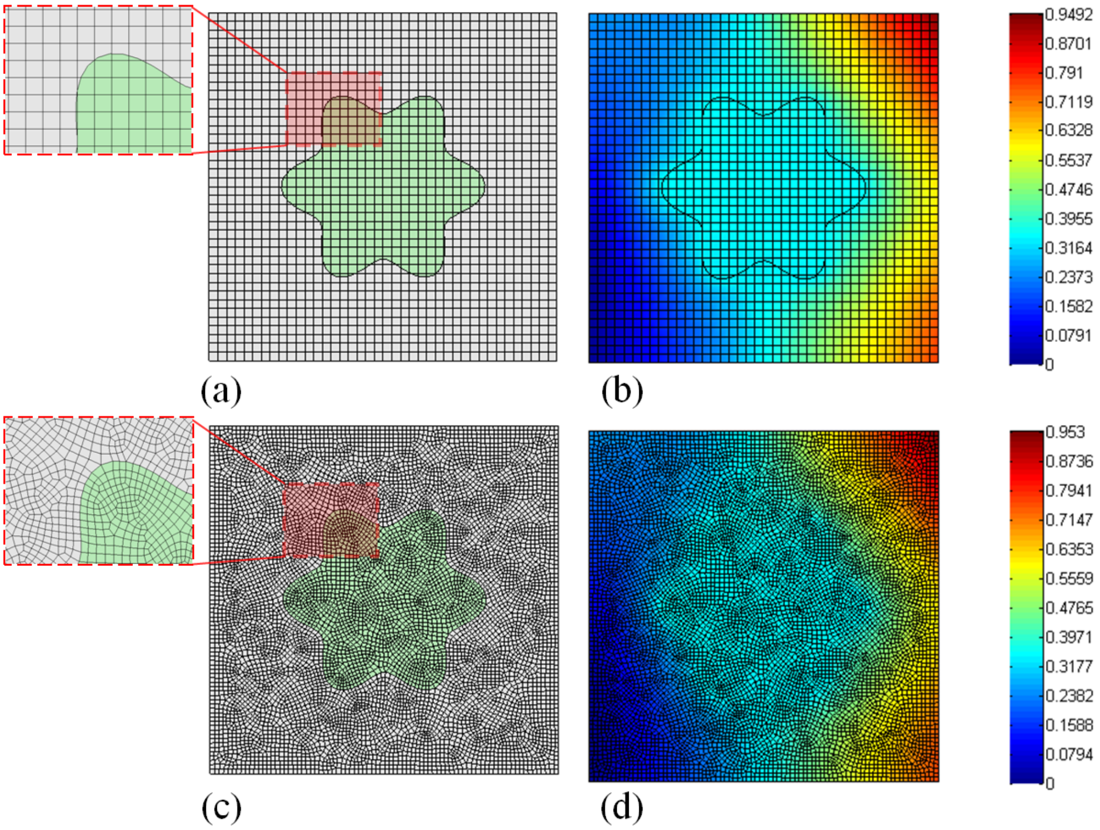

Figure 5.9: Comparison of displacement fields U_{x_1} obtained from XFEM and FEM for RVE with inclusion $(k_1 = 0, k_2 = 6)$: a) XFEM mesh, b) XFEM displacements, c) FEM mesh and d) FEM displacements

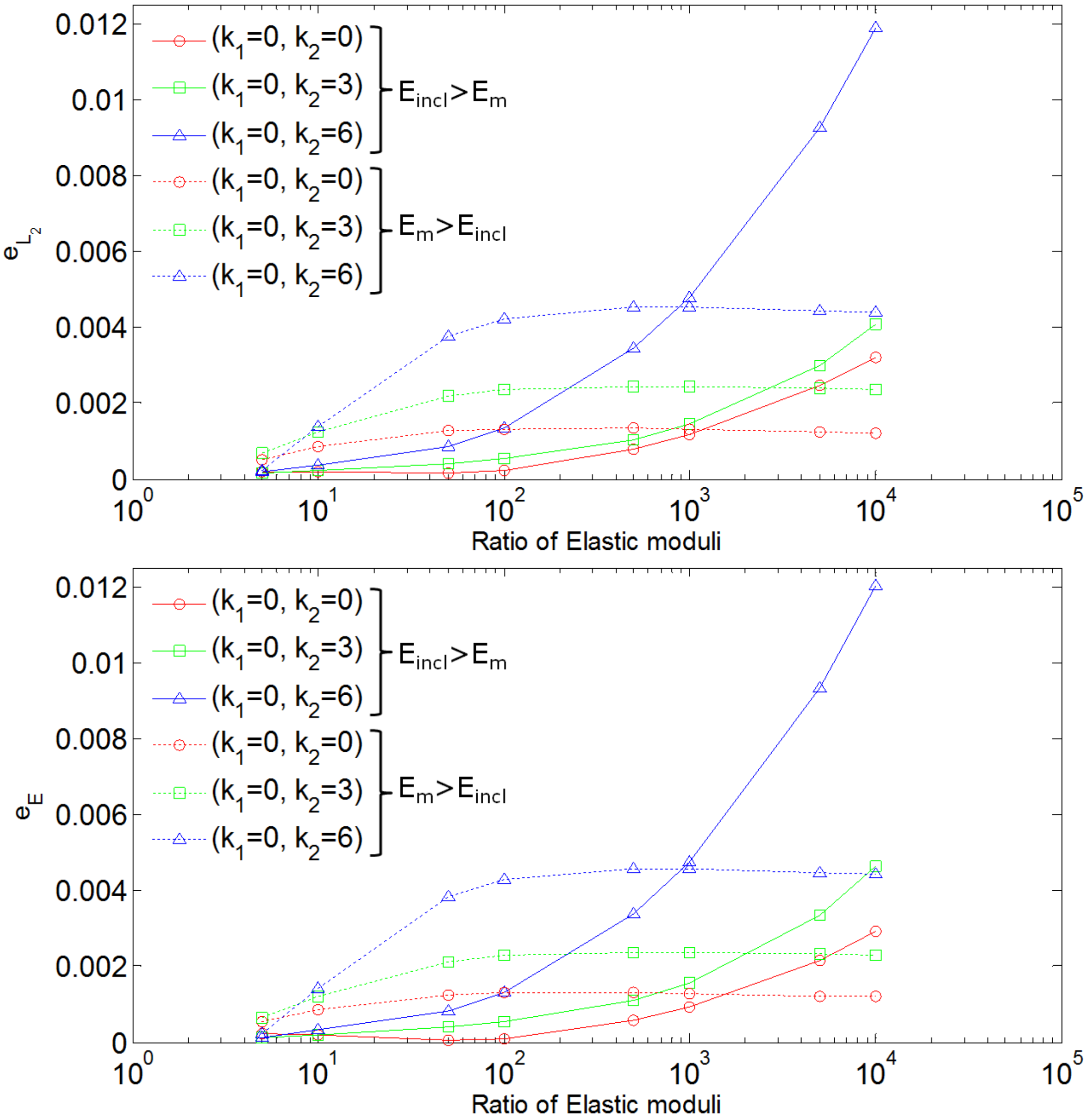

Figure 5.10: Effect of elastic moduli ratio on the accuracy of the XFEM solution in terms of L_2 and energy norm

5.2 Homogenization

5.2.1 Generation of random microstructures

In order to proceed to the stochastic homogenization procedure in the framework of MCS (Section 5.2.2), the first step is to generate a large number of random realizations of the microstructure geometry of the GnP-RC RVEs. For this purpose an efficient algorithm was used in Hiriyur et al [32], the basic steps of which are described in Table 5.2. This algorithm has been appropriately modified here to account for arbitrarily shaped inclusions. A specific volume fraction (vf) and number of inclusions n_{incl} is assigned to each RVE with dimensions $X_1 \times X_2$. For the generation of arbitrarily shaped inclusions, Equations (5.10) and (5.11) are used with specific deterministic constants k_1, k_2 and random variables $Y_i(\theta)$ produced according to a prescribed uniform probability density function (PDF) f_{Y_i}. The random boundary curve $\Gamma_{incl}(\theta)$ of an inclusion is constructed using N discrete points as follows:

$$\Gamma_{incl}(\theta) : \{\mathbf{x} = \mathbf{c} + R\left(\alpha, \theta\right)\left(cos\alpha \cdot \mathbf{e_1} + sin\alpha \cdot \mathbf{e_2}\right)\} \tag{5.16}$$

where $\mathbf{e_1}$, $\mathbf{e_2}$ are the unit vectors of the Cartesian coordinate system (Fig. 5.3). Figure 5.11 presents the different inclusion shapes considered in this study. For each inclusion, a set of random coordinates representing the center of the rough circle and its random orientation angle are also generated according to prescribed uniform distributions f_c and f_β.

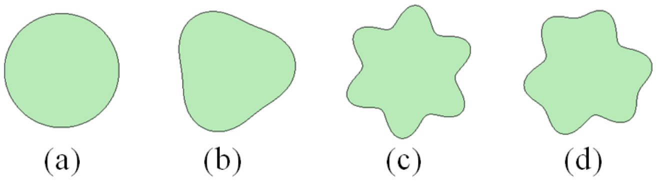
(a) (b) (c) (d)

Figure 5.11: Shapes of GnP inclusions constructed by: a)$k_1 = 0$, $k_2 = 0$, b) $k_1 = 0$, $k_2 = 3$, c) $k_1 = 0$, $k_2 = 6$ and d) $k_1 = 3$, $k_2 = 6$

After the generation of n_{incl} inclusions, their size needs to be scaled in order to achieve the desired vf for the RVE. For this purpose, the cumulative area of all the randomly generated inclusions is calculated first and an appropriate scaling factor is determined which is then applied to the random radius of the rough circle for all N discrete points. To eliminate the chance of overlap of a particular inclusion with the others that are spatially distributed in the RVE, the inclusions are sorted in decreasing order of area size. Starting with the inclusion with the largest area, the algorithm proceeds to the spatial distribution of the remaining inclusions in decreasing order of size, checking simultaneously for overlapping. The level set function corresponding to a specific inclusion is evaluated on the N discretization points belonging to all previously positioned inclusions. If all the values of the level set function of the specific inclusion are positive, then no overlapping occurs and the algorithm proceeds to position the next smaller inclusion according to its area. If any inclusion placed and oriented according to the generated random position variables is found to overlap with any previously located inclusion, then new center coordinates and orientation angle are generated until no overlap is observed. In Fig. 5.12, a set of RVE realizations generated using the algorithm of Table 5.2 are shown. These RVEs have a volume fraction vf=30% and contain different number of inclusions with parameters $k_1 = 0$ and $k_2 = 3$.

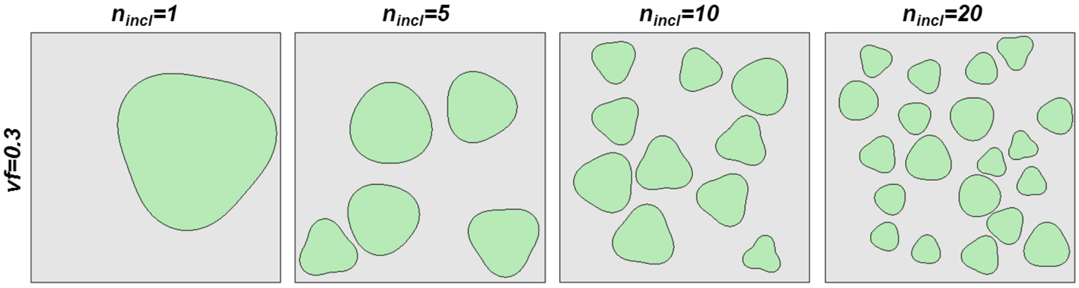

Figure 5.12: Sample realizations of generated random microstructures with vf=30% and parameters $k_1 = 0$ and $k_2 = 3$

Table 5.2: Algorithm for the generation of random microstructure geometry of RVEs

---

- INPUT
  - X_1, X_2: Size of RVE
  - vf: Inclusion volume fraction in RVE
  - n_{incl}: Total number of inclusions in RVE
  - f_{Y_i}: Independent probability distributions for the random variables $Y_i(\theta) \in U\left(-\sqrt{3}, \sqrt{3}\right)$, $i = 1, ..., 5$ in Eq. (5.11)
  - f_c, f_β: Independent probability distributions for the center coordinates and orientation angle
  - k_1, k_2: Deterministic constants which define the period of oscillations of the random rough circle boundary curve
- GENERATE / SCALE / SORT INCLUSIONS
  - Generate n_{incl} random inclusions
  - Calculate numerically by trapezoidal rule the cumulative area of all inclusions as $\hat{A}_{incl} = \sum_{k=1}^{n_{incl}} \left\{ \sum_{n=1}^{N} \left[\left(x^k_{1,n+1} - x^k_{1,n}\right) \cdot \left(\frac{x^k_{2,n} + x^k_{2,n+1}}{2} \right) \right] \right\}$ $n = 1, ..., N$: number of discretization points on the boundary curve of the random rough circle, $\left(x^k_{1,n}, x^k_{2,n}\right) \in \Gamma^k_{incl}(\theta)$
  - Scale rough circle radii: $R_n = \hat{R}_n \sqrt{\text{vf} \frac{X_1 X_2}{\hat{A}_{incl}}}$
  - Sort inclusions in decreasing order of area
- SPATIALLY DISTRIBUTE INCLUSIONS IN RVE
  - Loop over inclusions $k = 1$ to n_{incl}
    - Generate random numbers $\left(x^k_1, x^k_2\right)$ uniform in $[0, X_1]$ and $[0, X_2]$, respectively and β^k uniform in $[0, 2\pi]$ to represent rough circle center and orientation
    - Check overlap with previously positioned inclusions 1 to $k - 1$
      - If TRUE, repeat step for inclusion k with new random values for coordinates $\left(x^k_1, x^k_2\right)$ and orientation β^k
      - If FALSE, proceed to next smaller inclusion

5.2.2 Homogenization in the framework of MCS

The homogenization scheme adopted in this study is based on the fundamental assumption of statistical homogeneity of the heterogeneous medium [28], which means that all statistical properties of the state variables are the same at any material point and thus a representative volume element (RVE) can be identified. Effective homogeneous material properties, corresponding to the random microstructures generated by the algorithm in Section 5.2.1, are obtained by MCS. For this purpose, a sufficiently large number of elastic analyses are conducted where the RVEs are subjected to displacement boundary conditions [57]. Although there is a constant homogenized material property within the RVE, this property changes from realization to realization making it a random variable. Assuming that the resulting homogeneous material will remain linear and isotropic, the effective Young's modulus E_{eff} and Poisson ratio ν_{eff} are the only parameters to be defined through the stochastic homogenization procedure. It should be mentioned that a more general orthotropic material model could more accurately simulate the behavior of the homogenized medium. However, such model would increase significantly the computational cost and therefore it is not used in this study. Note also that the isotropy assumption can be considered valid in an average sense.

Homogenization is based on Hill's energy averaging theorem, which postulates that the strain energy of the homogenized macro-continuum has to be equal to that of the microstructured RVE in an average sense:

$$\bar{\boldsymbol{\sigma}} : \bar{\boldsymbol{\varepsilon}} = \frac{1}{|V|} \int_{\Omega} \boldsymbol{\sigma} : \boldsymbol{\varepsilon} \, \mathrm{d}\boldsymbol{Y} \tag{5.17}$$

where $\boldsymbol{Y}$ denotes the coordinate system in the microstructured RVE. The macroscopic quantities are related to the corresponding state variables at microscale through established micro to macro relations. According to the deterministic theories of Hill [31], the total macroscopic stress and strain tensors at some point $\boldsymbol{X}$ of the continuum are computed by

$$\bar{\boldsymbol{\sigma}}(\boldsymbol{X}) = \langle \boldsymbol{\sigma} \rangle (\boldsymbol{X}) \text{ and } \bar{\boldsymbol{\varepsilon}}(\boldsymbol{X}) = \langle \boldsymbol{\varepsilon} \rangle (\boldsymbol{X}) \tag{5.18}$$

where the average of a quantity $\boldsymbol{\zeta}$ at the microstructure is defined as its integral over the corresponding RVE volume V as

$$\begin{aligned} \bar{\boldsymbol{\zeta}}(\boldsymbol{X}) &= \langle \boldsymbol{\zeta} \rangle (\boldsymbol{X}) = \frac{1}{V} \int_{\Omega} \boldsymbol{\zeta}(\boldsymbol{X}, \boldsymbol{Y}) \, \mathrm{d}\boldsymbol{Y} \\ \text{with } V &= \int_{\Omega} \mathrm{d}\boldsymbol{Y} \end{aligned} \tag{5.19}$$

Miehe and Koch [57] proposed a computational procedure to exclusively define the overall macroscopic stresses and tangent moduli of a typical microstructure from the discrete forces and stiffness properties on the boundary nodes of the meshed RVE model. Following this procedure, a prescribed strain tensor $\bar{\boldsymbol{\varepsilon}}$ is applied on the boundary of the microstructure models through displacement boundary conditions in the form:

$$\boldsymbol{u}_q = \mathbb{D}_q^T \bar{\boldsymbol{\varepsilon}} \tag{5.20}$$

where $\mathbb{D}_q$ is a geometric matrix that depends on the coordinates of the nodal point q which lies on the boundary of the model, defined by

$$\mathbb{D}_q = \frac{1}{2} \begin{bmatrix} 2x_1 & 0 \\ 0 & 2x_2 \\ x_2 & x_1 \end{bmatrix} \tag{5.21}$$

where $(x_1, x_2) \in \boldsymbol{Y}$. The overall macroscopic stress $\bar{\boldsymbol{\sigma}}$ is then calculated in an average manner from the nodal reaction forces $\boldsymbol{f}_q$ obtained by XFEM analysis as

$$\bar{\boldsymbol{\sigma}} = \frac{1}{|V|} \sum_{q=1}^{M} \mathbb{D}_q \boldsymbol{f}_q \tag{5.22}$$

where M is the number of boundary nodes q. As mentioned previously, the macroscopic stress is related to the imposed macroscopic strain by a linear isotropic elastic constitutive matrix in the form

$$\begin{bmatrix}\bar{\sigma}_{11}\\ \bar{\sigma}_{22}\\ \bar{\sigma}_{12}\end{bmatrix} = \begin{bmatrix}C_{eff} & D_{eff} & 0\\ D_{eff} & C_{eff} & 0\\ 0 & 0 & G_{eff}\end{bmatrix}\begin{bmatrix}\bar{\varepsilon}_{11}\\ \bar{\varepsilon}_{22}\\ \bar{\varepsilon}_{12}\end{bmatrix} \tag{5.23}$$

where

$$C_{eff} = \begin{cases}\dfrac{E_{eff}}{1-\nu_{eff}^2} & \text{plane stress}\\ \dfrac{(1-\nu_{eff})\,E_{eff}}{(1+\nu_{eff})\,(1-2\nu_{eff})} & \text{plane strain}\end{cases} \tag{5.24}$$

$$D_{eff} = \begin{cases}\dfrac{\nu_{eff}E_{eff}}{1-\nu_{eff}^2} & \text{plane stress}\\ \dfrac{\nu_{eff}E_{eff}}{(1+\nu_{eff})\,(1-2\nu_{eff})} & \text{plane strain}\end{cases} \tag{5.25}$$

$$\text{and } G_{eff} = \frac{E_{eff}}{2\,(1+\nu_{eff})} \tag{5.26}$$

The computation of the effective Young's modulus and Poisson ratio is accomplished by imposing the macrostrain vector $\bar{\boldsymbol{\varepsilon}} = [\bar{\varepsilon}_{11}\ \ 0\ \ 0]^T$ in form of displacements (see Eq. (5.20)). Thus $C_{eff} = \bar{\sigma}_{11}/\bar{\varepsilon}_{11}$ and $D_{eff} = \bar{\sigma}_{22}/\bar{\varepsilon}_{11}$ can be calculated from which E_{eff} and ν_{eff} are derived for each Monte Carlo sample.

5.2.3 Solution strategy

The XFE elastostatic problem of RVEs with random inclusions requires the solution of the linear system of Eq. (5.9). The local stiffness matrices of the regular and enriched elements are calculated numerically by the trapezoidal integration method with 4 quadrature points in an equispaced 2×2 grid and with 64 quadrature points in an equispaced 8×8 grid, respectively. The global stiffness matrix comprises K_{uu} which corresponds to the regular dofs u, $K_{\alpha\alpha}$ which corresponds to the enriched dofs α and $K_{u\alpha}$=$K_{\alpha u}$ which derive from the coupling between u and α. As the bandwith of this matrix is quite large, the Reverse Cuthill-McKee algorithm for symmetric sparse matrix reordering is used to reduce the bandwidth and accelerate the solution of the linear system. Figure 5.13 illustrates the stiffness matrix K of a discretized RVE model with inclusions of shape type $(k_1 = 0, k_2 = 6)$, before and after implementation of the reordering algorithm. The solution is finally obtained by factorizing the reordered narrower bandwidth stiffness matrix, using the Cholesky decomposition.

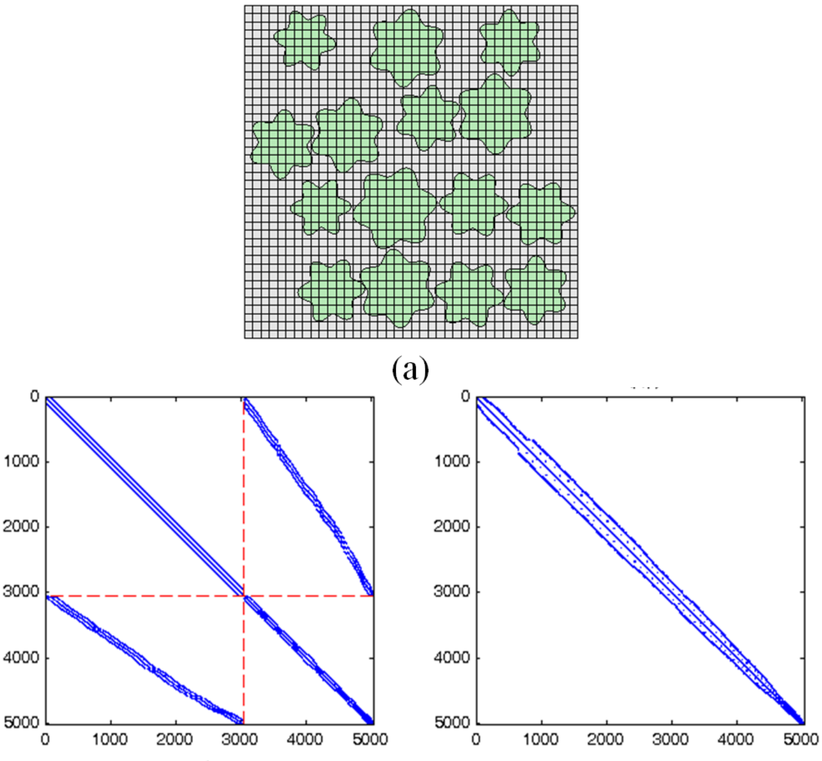

(a)

(b)

(c)

Figure 5.13: RVE model with inclusions $(k_1, k_2) = (0, 6)$: a) Mesh, b) Stiffness matrix K without reordering and c) Stiffness matrix K reordered by Reverse Cuthill-McKee algorithm

5.3 Numerical examples

The probability distribution of the effective elastic modulus and Poisson ratio for a plane-stress medium containing inclusions of arbitrary shape is obtained using the approach described in sections 5.1 and 5.2. As already stated, a linear isotropic material model is considered for both matrix and inclusions with the same Poisson ratio $\nu_m = \nu_{incl} = 0.3$. Moreover, examples with different Poisson ratios $\nu_m = 0.49$ (nearly incompressible matrix) and $\nu_{incl} = 0.3$ are presented. E_{eff}, ν_{eff} are computed through the coupled XFEM-MCS homogenization approach of Section 5.2.

A unit cell of size 10×10 mm subjected to displacement boundary conditions, is used in the analyses. A total of 1000 Monte Carlo simulations are performed for each volume fraction of inclusions considered ranging from 0.2 to 0.4. The number of inclusions in each MC sample is fixed to 15. Parametric investigations with respect to the stiffness ratio E_{incl}/E_m are conducted to highlight its effect on the results. It is noted that the computed E_{eff} is in all cases within the upper and lower bounds defined by the Voigt and Reuss models, respectively.

Figure 5.14 shows the histograms of E_{eff}, ν_{eff} along with the statistical convergence of their mean and coefficient of variation (COV) for stiffness ratio $E_{incl}/E_m = 10$, vf =0.4 and four different cases of inclusion shape roughness $(k_1 = 0, k_2 = 0)$, $(k_1 = 0, k_2 = 3)$, $(k_1 = 0, k_2 = 6)$ and $(k_1 = 3, k_2 = 6)$, (see Fig. 5.11). The same results are displayed in Fig. 5.15 for the case of compliant inclusions ($E_m/E_{incl} = 10$). It can be seen that the effect of the inclusion shape is negligible in both cases as the difference in the mean value of the effective elastic modulus between $(k_1 = 0, k_2 = 0)$ (perfect circle) and $(k_1 = 0, k_2 = 6)$ (arbitrary shape) is less than 3.5%.

The effect of the inclusion shape on E_{eff}, ν_{eff} becomes more pronounced in the case of large stiffness ratios. Figures 5.16-5.19 display the histograms of E_{eff}, ν_{eff} and the statistical convergence of their mean and COV for stiffness ratio $E_{incl}/E_m = 1000$, which is typical in case of GnP-RC RVEs, three values of vf and four cases of inclusion shape roughness. The differences in the mean value of the effective elastic coefficient E_{eff} for the various inclusion shapes and volume fractions are given in Table 5.3. An increase of about 16% in E_{eff} can be observed in the case of vf =0.4 between $(k_1 = 0, k_2 = 0)$ and $(k_1 = 0, k_2 = 6)$. The shape of the histograms is significantly affected by the volume fraction and shape of the inclusions, in contrast to the case of a small stiffness ratio (see Fig. 5.14). The computed COV is also much larger in this case for both E_{eff} and ν_{eff}.

As shown in Fig. 5.20, a reduction of the effective elastic modulus occurs with the increase of shape roughness in the case of compliant inclusions ($E_m/E_{incl} =$

1000). The effect of volume fraction and inclusion shape on the histograms of E_{eff}, ν_{eff} is less pronounced than in the case of stiff inclusions. The differences in the mean value of E_{eff} are still significant (Table 5.4). A decrease of about 12% in E_{eff} can be noticed in the case of vf =0.4 between ($k_1 = 0, k_2 = 0$) and ($k_1 = 0, k_2 = 6$) . Statistical convergence of mean and COV is achieved within the same number of MC simulations (Figs. 5.22-5.23).

Figures 5.24 and 5.25 present the results obtained with different Poisson ratios for the matrix and inclusions, respectively. The stiffness ratio is $E_{incl}/E_m = 1000$ in case of stiff inclusions and $E_m/E_{incl} = 1000$ in case of compliant inclusions. The results corresponding to the cases with the largest differences in E_{eff} are shown (RVEs with vf=0.4 and inclusions of shape type ($k_1 = 0, k_2 = 0$) and ($k_1 = 0, k_2 = 6$)). The differences in E_{eff} are 18% for stiff and 11.6% for compliant inclusions. Note that, for the case of GnP-reinforced composites where $E_{incl}/E_m \simeq 1000$, increase of the platelet shape roughness results in higher composite stiffness. Although in this study, full bond condition is assumed at the GnP/polymer interface, theoretically the increased roughness of the platelets can also achieve better adhesion to matrix. From the above mentioned issues the significance of platelet shape in studying GnP-reinforced polymers is highlighted.

vf	$(0,0)-(0,3)$	$(0,0)-(0,6)$	$(0,3)-(0,6)$	$(0,0)-(3,6)$
0.2	2.55	5.31	2.69	2.89
0.3	3.22	9.77	6.34	4.22
0.4	4.11	16.13	11.55	6.15

Table 5.3: Effect (% increase) of shape roughness (k_1, k_2) on mean(E_{eff}) for stiff inclusions ($E_{incl}/E_m = 1000$)

vf	$(0,0)-(0,3)$	$(0,0)-(0,6)$	$(0,3)-(0,6)$	$(0,0)-(3,6)$
0.2	2.29	2.81	0.50	-0.28
0.3	4.14	6.28	2.06	1.49
0.4	5.24	11.85	6.28	4.22

Table 5.4: Effect (% decrease) of shape roughness (k_1, k_2) on mean(E_{eff}) for compliant inclusions ($E_m/E_{incl} = 1000$)

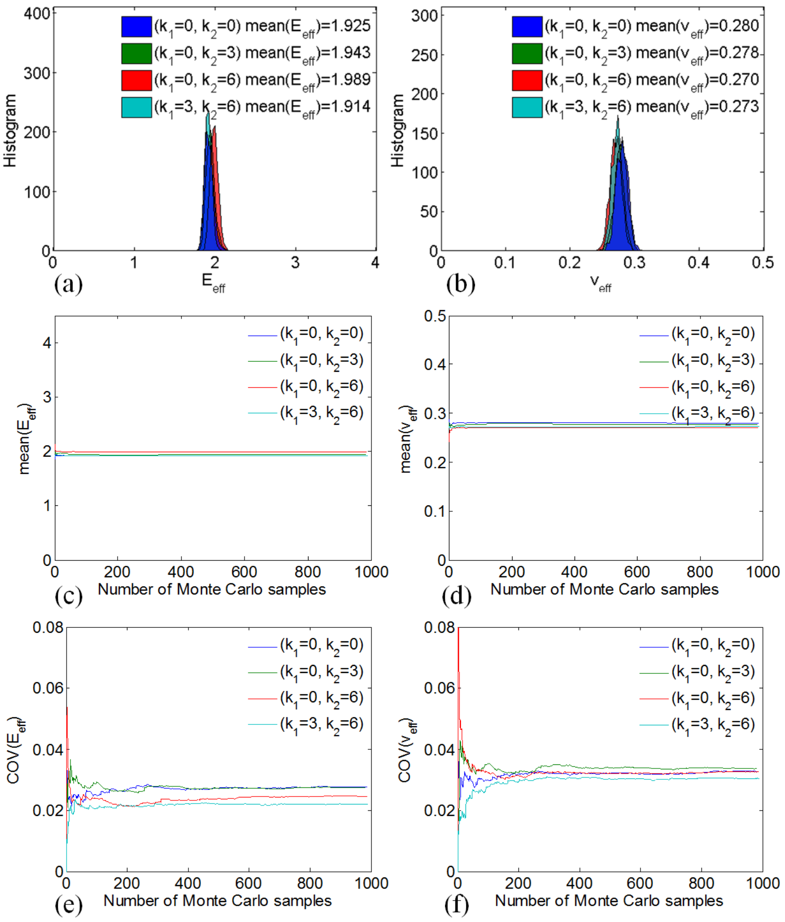

Figure 5.14: Stiff inclusions ($E_{incl}/E_m = 10$): a-b) Histograms, c-d) mean values and e-f) COVs of E_{eff} and ν_{eff} respectively for RVEs with vf=0.4 and inclusions with $(k_1, k_2) = [(0,0),(0,3),(0,6),(3,6)]$

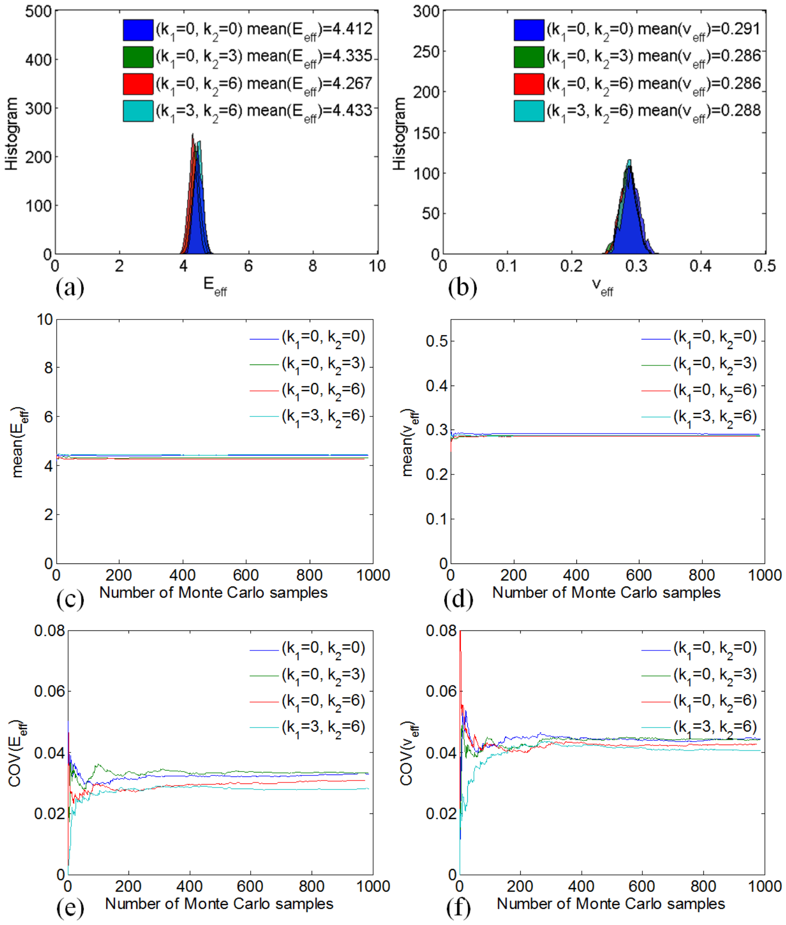

Figure 5.15: Compliant inclusions ($E_m/E_{incl} = 10$): a-b) Histograms, c-d) mean values and e-f) COVs of E_{eff} and ν_{eff} respectively for RVEs with vf=0.4 and inclusions with $(k_1, k_2) = [(0, 0), (0, 3), (0, 6), (3, 6)]$

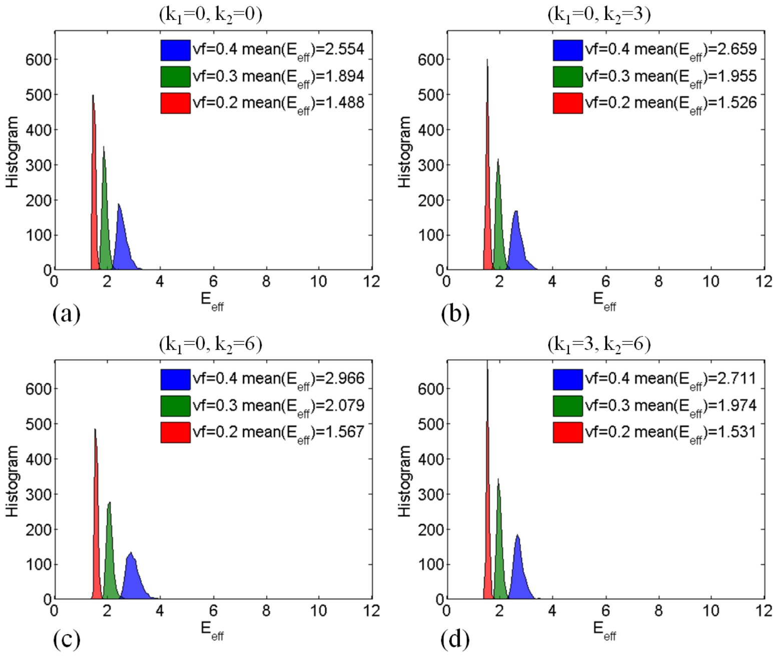

Figure 5.16: Stiff inclusions ($E_{incl}/E_m = 1000$) Histograms of E_{eff}: a) ($k_1 = 0, k_2 = 0$), b) ($k_1 = 0, k_2 = 3$), c) ($k_1 = 0, k_2 = 6$) and d) ($k_1 = 3, k_2 = 6$) for vf=[0.2, 0.3, 0.4]

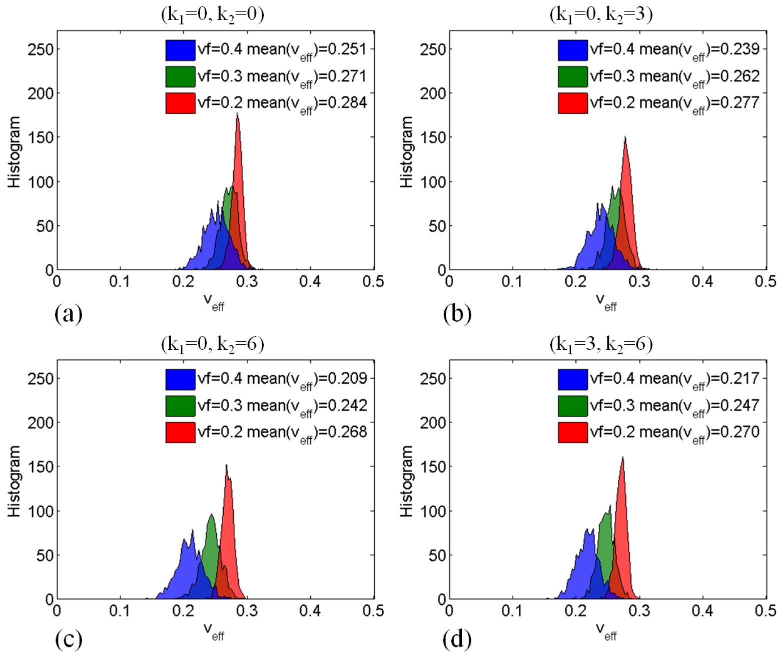

(a) (b) (c) (d)

Figure 5.17: Stiff inclusions ($E_{incl}/E_m = 1000$) Histograms of ν_{eff}: a) ($k_1 = 0, k_2 = 0$), b) ($k_1 = 0, k_2 = 3$), c) ($k_1 = 0, k_2 = 6$) and d) ($k_1 = 3, k_2 = 6$) for vf=[0.2, 0.3, 0.4]

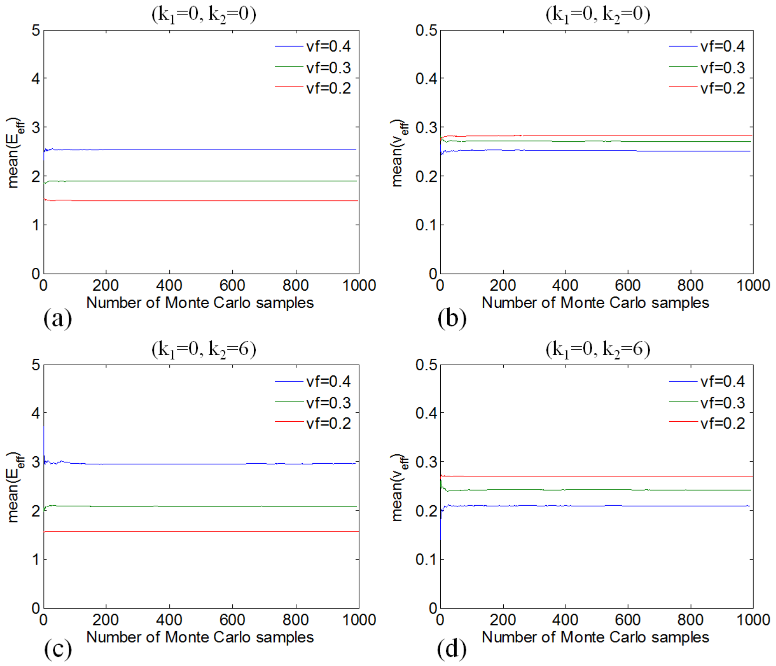

Figure 5.18: Stiff inclusions ($E_{incl}/E_m = 1000$): a-b) mean(E_{eff}), mean(ν_{eff}) for inclusions with ($k_1 = 0, k_2 = 0$) and c-d) mean(E_{eff}), mean(ν_{eff}) for inclusions with ($k_1 = 0, k_2 = 6$), respectively for vf=[0.2, 0.3, 0.4]

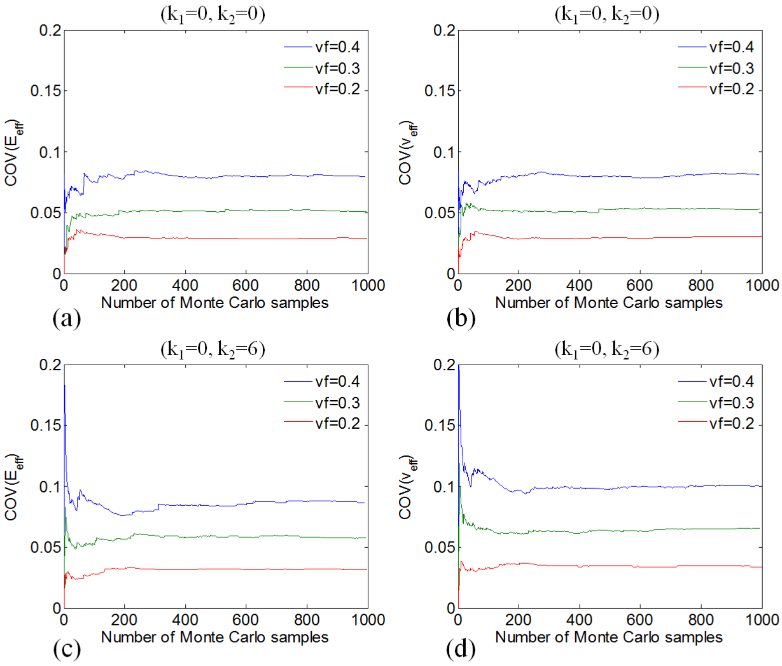

Figure 5.19: Stiff inclusions ($E_{incl}/E_m = 1000$): a-b) COV(E_{eff}), COV(ν_{eff}) for inclusions with ($k_1 = 0, k_2 = 0$) and c-d) COV(E_{eff}), COV(ν_{eff}) for inclusions with ($k_1 = 0, k_2 = 6$), respectively for vf=[0.2, 0.3, 0.4]

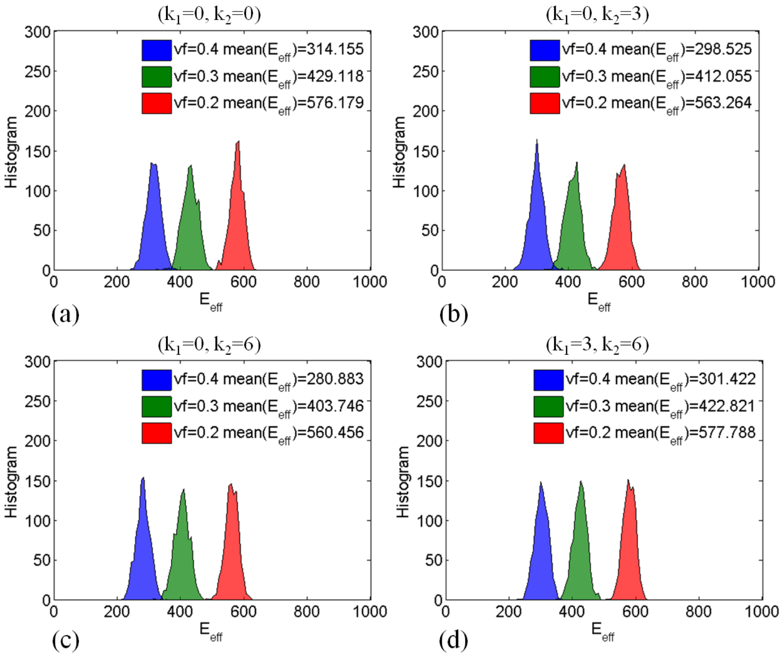

Figure 5.20: Compliant inclusions ($E_m/E_{incl} = 1000$) Histograms of E_{eff}: a) ($k_1 = 0, k_2 = 0$), b) ($k_1 = 0, k_2 = 3$), c) ($k_1 = 0, k_2 = 6$) and d) ($k_1 = 3, k_2 = 6$) for vf=[0.2, 0.3, 0.4]

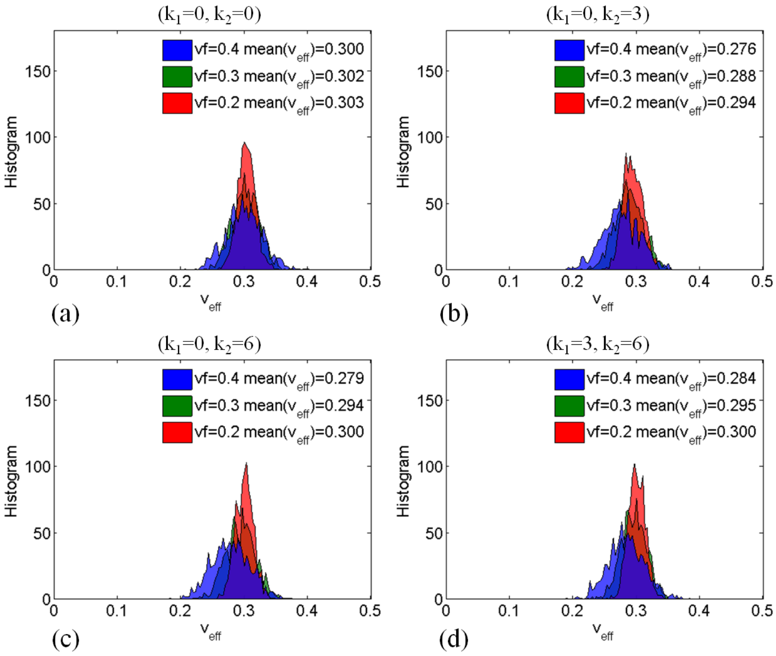

Figure 5.21: Compliant inclusions ($E_m/E_{incl} = 1000$) Histograms of ν_{eff}: a) ($k_1 = 0, k_2 = 0$), b) ($k_1 = 0, k_2 = 3$), c) ($k_1 = 0, k_2 = 6$) and d) ($k_1 = 3, k_2 = 6$) for vf=[0.2, 0.3, 0.4]

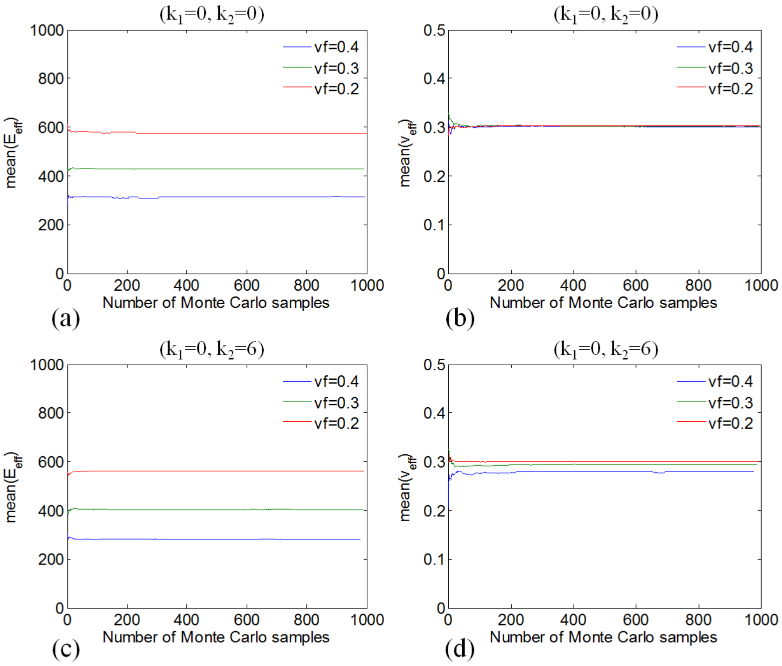

Figure 5.22: Compliant inclusions ($E_m/E_{incl} = 1000$): a-b) mean(E_{eff}), mean(ν_{eff}) for inclusions with ($k_1 = 0, k_2 = 0$) and c-d) mean(E_{eff}), mean(ν_{eff}) for inclusions with ($k_1 = 0, k_2 = 6$), respectively for vf=[0.2, 0.3, 0.4]

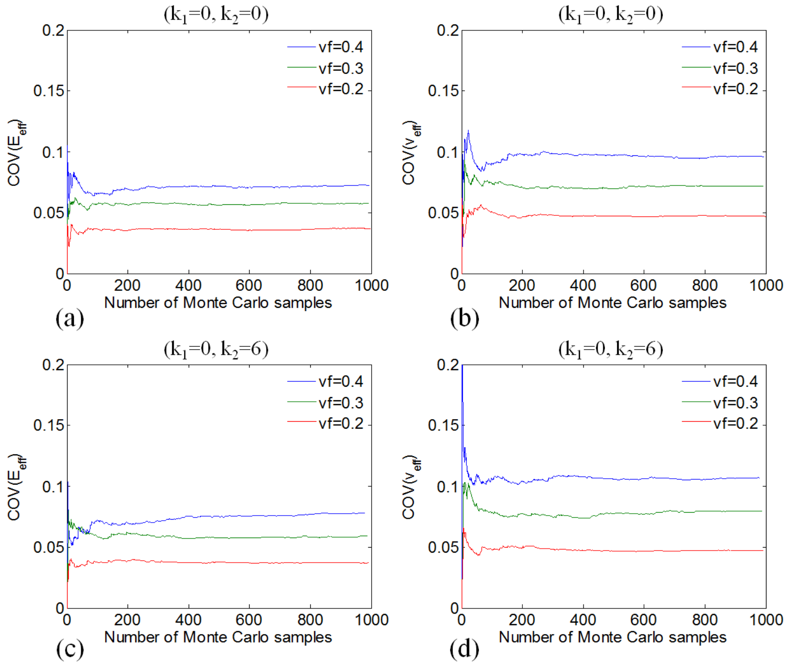

(a) (b) (c) (d)

Figure 5.23: Compliant inclusions ($E_m/E_{incl} = 1000$): a-b) COV(E_{eff}), COV(ν_{eff}) for inclusions with ($k_1 = 0, k_2 = 0$) and c-d) COV(E_{eff}), COV(ν_{eff}) for inclusions with ($k_1 = 0, k_2 = 6$), respectively for vf=[0.2, 0.3, 0.4]

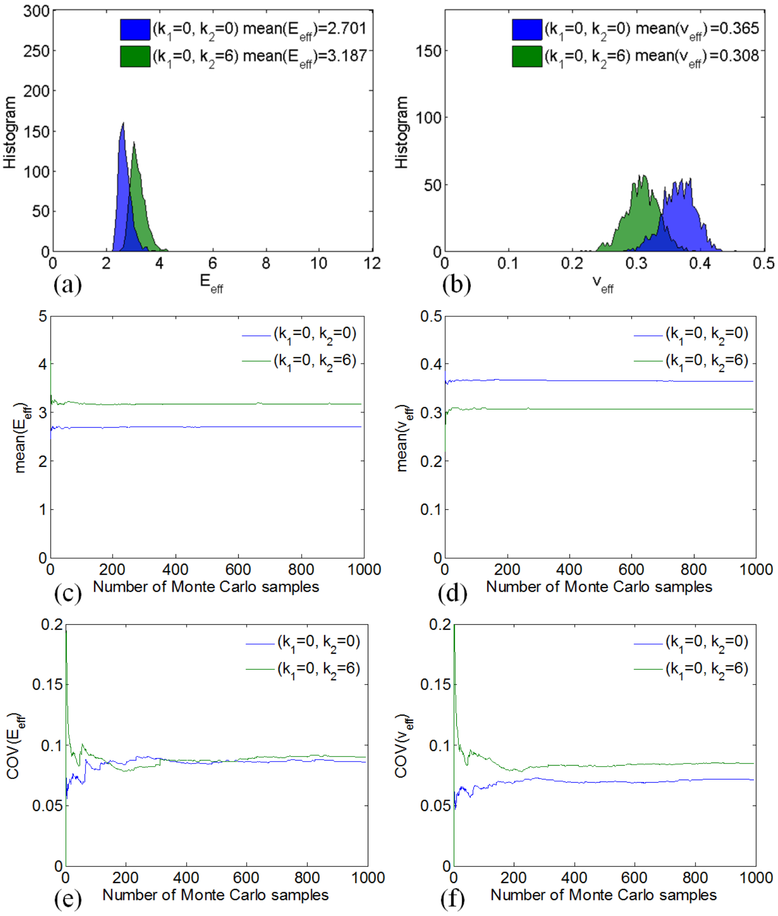

Figure 5.24: Case of different Poisson ratios ($\nu_m = 0.49$, $\nu_{incl} = 0.3$) for stiff inclusions ($E_{incl}/E_m = 1000$): a-b) Histograms, c-d) mean values and e-f) COVs of E_{eff} and ν_{eff} respectively for RVEs with vf=0.4 and shape types $(k_1 = 0, k_2 = 0)$, $(k_1 = 0, k_2 = 6)$

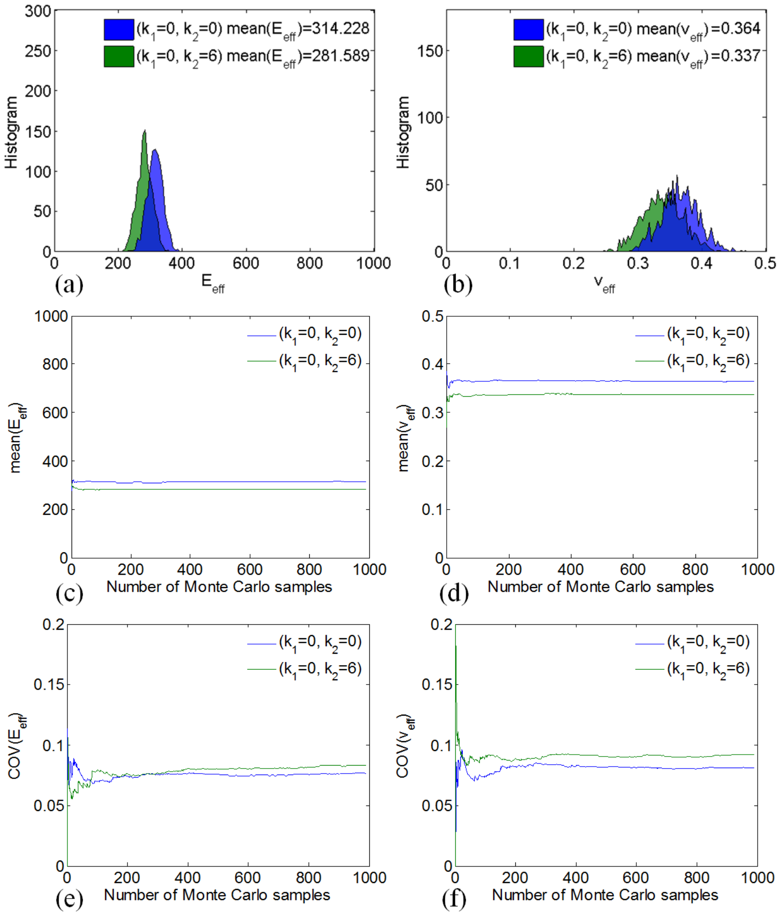

Figure 5.25: Case of different Poisson ratios ($\nu_m = 0.49$, $\nu_{incl} = 0.3$) for compliant inclusions ($E_m/E_{incl} = 1000$): a-b) Histograms, c-d) mean values and e-f) COVs of E_{eff} and ν_{eff} respectively for RVEs with vf=0.4 and shape types $(k_1 = 0, k_2 = 0)$, $(k_1 = 0, k_2 = 6)$

Chapter 6

Conclusions

6.1 Conclusions

In this PhD thesis, different multiscale modeling techniques were utilized and new constitutive models were developed for the simulation of CNT and GnP reinforced composite materials within reasonable computational time and accuracy. Various stochastic parameters have been considered by the proposed multiscale analysis of the nanocomposite RVEs, so that the real microstructural geometry and interfacial phenomena of such heterogeneous materials were properly simulated. In the context of CNT-RCs, the coupled atomistic-continuum MSM approach was adopted for modeling the lattice structure of CNTs where the atomic C-C covalent bond was substituted by a structural beam element. Then, at the nanoscale the resulting space frame FE model of the nanotube was replaced by an equivalent beam, which was used as the basic element for the construction of full length CNTs at the microscale. Random waviness of CNTs geometry was considered in the multiscale analysis through a novel stochastic approach, where the spectral representation method was used with evolutionary power spectra derived from real SEM images of CNT-RCs. The viscoelastic constitutive model of Maxwell-Wiechert was implemented for accurate predictions of the nonlinear strain rate dependent response of polymers, which exhibit multiple relaxation times. Calibration procedure of that model was performed for the case of PEEK material, which was then assigned to the polymer matrix. The embedded element technique was also adopted so as the RVE FE models were disretized by two independent meshes: a structured one with solid elements for the matrix and a series of embedded beams for the full length CNTs inside the matrix. The interfacial load transfer mechanism between the lateral surface of the CNT and the surrounding matrix was taken into account with the incorporation of a nonlinear bond-slip friction-type model in the FE code.

The mechanical and damping properties of the CNT-RCs were assessed on the basis of sensitivity analyses with respect to various weight fraction content in CNTs and different interfacial shear stress values at the CNT/polymer interface. In case of random CNT waviness stochastic average properties were derived with Monte Carlo simulation. The presented numerical results have demonstrated the significant effect of the ISS as well as the influence of CNT waviness on the mechanical and damping behavior of CNT-RCs. Specifically, it was shown that the loss factor increases with increasing ISS and reaches a peak value for ISS values equal or greater than the shear strength of the polymer. This fact implies that, a successful functionalization process on CNTs which results in increased interfacial shear strength is crucial for achieving optimum damping characteristics of CNT-RCs. In addition, it was shown that CNT waviness results in a reduction of the loss factor. Thus, the significance of straightening the CNTs before the nanocomposite fabrication is highlighted in order to produce materials with enhanced mechanical and damping properties.

Analysis of CNT-RCs was then upscaled from micro to macro scale through a nonlinear multiscale homogenization approach. The novelty of the proposed sequential homogenization method is that it has been efficiently applied for the characterization of the mechanical and damping properties of CNT-RCs considering slippage at CNT/polymer interface. This was performed through the development of a novel viscoplastic constitutive model which was then assigned to the homogeneous composite material. Based on Hill's anisotropic plasticity model combined with the viscoelastic Maxwell-Wiechert model, both the anisotropic stiffness reinforcement of the bulk polymer and the anisotropic adhesive behavior at the CNT/polymer interface caused by the randomly dispersed CNTs inside the viscoelastic matrix are adequately described. The presented numerical results verify the efficiency of the proposed homogenization method in solving large mechanical problems where finer scale phenomena are considered in a continuum manner.

In the context of multiscale analysis of GnP-RCs, a homogenization strategy was proposed where effective material parameters for polymer matrices reinforced with arbitrarily shaped graphene platelet inclusions were calculated using XFEM, coupled with Monte Carlo simulation. In particular, the influence of the inclusion shape on the effective properties of such random media was studied. The inclusions were randomly distributed and oriented within the medium and their shape was implicitly modeled by the iso-zero of an analytically defined random level set function (”rough” circle), which also served as the enrichment function. The formulation which exploits the characteristic features of XFEM avoiding the regeneration of a new finite element mesh at each Monte Carlo simulation have led to accelerated computations. Parametric investigations with respect to the inclusion/matrix stiffness ratio and the inclusion volume fraction were conducted. The numerical results have shown that the statistical characteristics of the effective properties can be significantly affected by the shape of the inclusions. This is more obvious for RVEs with large volume fraction and high stiffness ratio which are typical in GnP-reinforced composites.

6.2 Recommendations for future work

The multiscale analysis of CNT and GnP-reinforced composites, as this proposed in this thesis, constitutes a powerful numerical tool for predicting the mechanical and damping properties of these types of materials. However, further research is needed in the following topics:

1. Derivation of the nonlinear EBE which can capture nonlinear phenomena in CNTs such as buckling or defected C-C bonds.
2. Calibration of the proposed viscoplastic constitutive model in various strain rates for more accurate predictions of the homogeneous material behavior when viscoelasticity of the polymer matrix is considered.
3. Investigation of the effect of random CNT orientation and waviness on the nonlinear effective properties of the CNT-RCs in larger RVEs which contain

many numbers of CNTs.

4. Computational homogenization of CNT and GnP-RCs RVEs with evolving micro-cracks.
5. Robust optimum design of CNT-RCs and GnP-RCs for stiffness and strength with regard to topology and geometry of the nanofillers.
6. Study hybrid nanocomposites containing both CNTs and GnPs.

Appendix A

Viscoelasticity

Source: Abaqus Theory Manual, Version 6.8.

The basic hereditary integral formulation for linear isotropic viscoelasticity is

$$\boldsymbol{\sigma}(t) = \int_0^t 2G\left(\tau - \tau'\right) \dot{\mathrm{e}}\; dt' + \boldsymbol{I} \int_0^t K\left(\tau - \tau'\right) \dot{\phi}\; dt' \tag{A.1}$$

Here e and ϕ are the mechanical deviatoric and volumetric strains; K is the bulk modulus and G is the shear modulus, which are functions of the reduced time τ; and $\dot{}$ denotes differentiation with respect to t'.

The reduced time is related to the actual time through the integral differential equation

$$\tau = \int_0^t \frac{dt'}{A_\theta\left(\theta\left(t'\right)\right)}, \quad \frac{d\tau}{dt} = \frac{1}{A_\theta\left(\theta\left(t\right)\right)} \tag{A.2}$$

where θ is the temperature and A_θ is the shift function. (Hence, if $A_\theta = 1$, $\tau = t$.) A commonly used shift function is the Williams-Landell-Ferry (WLF) equation, which has the following form:

$$-\log A_\theta = h\left(\theta\right) = \frac{C_1^g\left(\theta - \theta_g\right)}{C_2^g + \left(\theta - \theta_g\right)} \tag{A.3}$$

where C_1^g and C_2^g are constants and θ_g is the "glass" transition temperature. This is the temperature at which, in principle, the behavior of the material changes from glassy to rubbery. If $\theta \leq \theta_g - C_2^g$, deformation changes will be elastic. C_1^g and C_2^g were once thought to be "universal" constants whose values were obtained at θ_g, but these constants have been shown to vary slightly from polymer to polymer.

The WLF equation can be used with any convenient temperature, other than the glass transition temperature, as the reference temperature. The form of the equation remains the same, but the constants are different. Namely,

$$-\log A_\theta = h\left(\theta\right) = \frac{C_1\left(\theta - \theta_0\right)}{C_2 + \left(\theta - \theta_0\right)} \tag{A.4}$$

where θ_0 is the reference temperature at which the relaxation data are given, and C_1 and C_2 are the calibration constants at the reference temperature. The "universal" constants C_1^g and C_2^g are related to C_1 and C_2 as follows:

$$\begin{aligned} C_1 &= \frac{C_1^g}{1 + \left(\theta_0 - \theta_g\right)/C_2^g}, \\ C_2 &= C_2^g + \theta_0 - \theta_g \end{aligned} \tag{A.5}$$

Other forms of $h\left(\theta\right)$ are also used, such as a power series in $\theta - \theta_0$.

The relaxation functions $K(t)$ and $G(t)$ can be defined individually in terms of a series of exponentials known as the Prony series:

$$K(t) = K_\infty + \sum_{i=1}^{n_K} K_i e^{-\tau/\tau_i^K}, \quad G(t) = G_\infty + \sum_{i=1}^{n_G} G_i e^{-\tau/\tau_i^G} \tag{A.6}$$

where K_∞ and G_∞ represent the long-term bulk and shear moduli. In general, the relaxation times τ_i^K and τ_i^G need not equal each other; however, we can assume that $\tau_i = \tau_i^K = \tau_i^G$. On the other hand, the number of terms in bulk and shear, n_K and n_G, need not equal each other. In fact, in many practical cases it can be assumed that $n_K = 0$. Hence, we now concentrate on the deviatoric behavior. The equations for the volumetric terms can be derived in an analogous way.

The deviatoric integral equation is

$$\begin{aligned}\boldsymbol{S} &= \int_0^t 2\left(G_\infty + \sum_{i=1}^{n_G} G_i e^{(\tau'-\tau)/\tau_i}\right)\dot{\mathrm{e}}\ dt' \\ &= \int_0^\tau 2\left(G_\infty + \sum_{i=1}^{n_G} G_i e^{(\tau'-\tau)/\tau_i}\right)\frac{d\mathrm{e}}{d\tau'}\ d\tau'.\end{aligned} \tag{A.7}$$

We rewrite this equation in the form

$$\boldsymbol{S} = 2G_0\left(\mathrm{e} - \sum_{i=1}^{n} \alpha_i \mathrm{e}_i\right), \tag{A.8}$$

where $G_0 = G_\infty + \sum_{i=1}^n G_i$ is the instantaneous shear modulus, $\alpha_i = G_i/G_0$ is the relative modulus of term i, and

$$\mathrm{e}_i = \int_0^\tau \left(1 - e^{(\tau'-\tau)/\tau_i}\right)\frac{d\mathrm{e}}{d\tau'}\ d\tau' \tag{A.9}$$

is the viscous (creep) strain in each term of the series. For finite element analysis this equation must be integrated over a finite increment of time. To perform this integration, we will assume that during the increment e varies linearly with τ; hence, $d\mathrm{e}/d\tau' = \Delta\mathrm{e}/\Delta\tau$. To use this relation, we break up Eq. (A.9) into two parts:

$$\begin{aligned}\mathrm{e}_i^{n+1} = &\int_0^{\tau^n} \left(1 - e^{(\tau'-\tau^{n+1})/\tau_i}\right)\frac{d\mathrm{e}}{d\tau'}\ d\tau' \\ &+ \int_{\tau^n}^{\tau^{n+1}} \left(1 - e^{(\tau'-\tau^{n+1})/\tau_i}\right)\frac{d\mathrm{e}}{d\tau'}\ d\tau'.\end{aligned} \tag{A.10}$$

Now observe that

$$1 - e^{(\tau'-\tau^{n+1})/\tau_i} = 1 - e^{-\Delta\tau/\tau_i} + e^{-\Delta\tau/\tau_i}\left(1 - e^{(\tau'-\tau^n)/\tau_i}\right). \tag{A.11}$$

Use of this expression and the approximation for $d\mathrm{e}/d\tau'$ during the increment yields

$$\begin{aligned}\mathrm{e}_i^{n+1} &= \left(1 - e^{-\Delta\tau/\tau_i}\right) \int_0^{\tau^n} \frac{d\mathrm{e}}{d\tau'}\, d\tau' \\ &+ e^{-\Delta\tau/\tau_i} \int_0^{\tau^n} \left(1 - e^{(\tau'-\tau^n)/\tau_i}\right) \frac{d\mathrm{e}}{d\tau'}\, d\tau' \\ &+ \frac{\Delta\mathrm{e}}{\Delta\tau} \int_{\tau^n}^{\tau^{n+1}} \left(1 - e^{(\tau'-\tau^{n+1})/\tau_i}\right) d\tau'.\end{aligned} \tag{A.12}$$

The first and last integrals in this expression are readily evaluated, whereas from Eq. (A.9) follows that the second integral represents the viscous strain in the i^{th} term at the beginning of the increment. Hence, the change in the i^{th} viscous strain is

$$\begin{aligned}\Delta\mathrm{e}_i &= \left(1 - e^{-\Delta\tau/\tau_i}\right) \mathrm{e}^n + \left(e^{-\Delta\tau/\tau_i} - 1\right) \mathrm{e}_i^n + \left(\Delta\tau - \tau_i\left(1 - e^{-\Delta\tau/\tau_i}\right)\right) \frac{\Delta\mathrm{e}}{\Delta\tau} \\ &= \frac{\tau_i}{\Delta\tau} \left(\frac{\Delta\tau}{\tau_i} + e^{-\Delta\tau/\tau_i} - 1\right) \Delta\mathrm{e} + \left(1 - e^{-\Delta\tau/\tau_i}\right) \left(\mathrm{e}^n - \mathrm{e}_i^n\right).\end{aligned} \tag{A.13}$$

If $\Delta\tau/\tau_i$ approaches zero, this expression can be approximated by

$$\Delta\mathrm{e}_i = \frac{\Delta\tau}{\tau_i} \left(\frac{1}{2}\Delta\mathrm{e} + \mathrm{e}^n - \mathrm{e}_i^n\right). \tag{A.14}$$

The last form is used in the computations if $\Delta\tau/\tau_i < 10^{-7}$.

Hence, in an increment, Eq. (A.13) or Eq. (A.14) is used to calculate the new value of the viscous strains. Eq. (A.8) is then used subsequently to obtain the new value of the stresses.

The tangent modulus is readily derived from these equations by differentiating the deviatoric stress increment, which is

$$\Delta\boldsymbol{S} = 2G_0 \left(\Delta\mathrm{e} - \sum_{i=1}^{n_G} \alpha_i \left(\mathrm{e}_i^{n+1} - \mathrm{e}_i^n\right)\right) \tag{A.15}$$

with respect to the deviatoric strain increment $\Delta \mathrm{e}$. Since the equations are linear, the modulus depends only on the reduced time step:

$$G^T = \begin{cases} G_0 \left[1 - \sum_{i=1}^{n} \alpha_i \frac{\tau_i}{\Delta\tau} \left(\frac{\Delta\tau}{\tau_i} + e^{-\Delta\tau/\tau_i} - 1 \right)\right] & \text{if } \Delta\tau/\tau_i > 10^{-7} \\ G_0 \left[1 - \sum_{i=1}^{n} \frac{1}{2}\alpha_i \frac{\Delta\tau}{\tau_i}\right] & \text{if } \Delta\tau/\tau_i < 10^{-7} \end{cases} \tag{A.16}$$

The energy dissipation follows from

$$\begin{aligned} P_D &= \frac{1}{2}\left(\boldsymbol{S}^{n+1} + \boldsymbol{S}^{n}\right) : \sum_{i=1}^{n_G} \alpha_i \Delta \mathrm{e}_i \\ &= \frac{1}{2}\left(\boldsymbol{S}^{n+1} + \boldsymbol{S}^{n}\right) : \left(\Delta \mathrm{e} - \frac{1}{2G_0}\left(\boldsymbol{S}^{n+1} + \boldsymbol{S}^{n}\right)\right) \\ &= P - P_E \end{aligned} \tag{A.17}$$

with the total work

$$P = \frac{1}{2}\left(\boldsymbol{S}^{n+1} + \boldsymbol{S}^{n}\right) : \Delta \mathrm{e} \tag{A.18}$$

and the elastic energy increase

$$P_E = \frac{1}{4G_0}\left(\boldsymbol{S}^{n+1} : \boldsymbol{S}^{n+1} - \boldsymbol{S}^{n} : \boldsymbol{S}^{n}\right). \tag{A.19}$$

Finally, one needs a relation between the reduced time increment, $\Delta\tau$, and the actual time increment, Δt. To do this, we observe that A_θ varies very nonlinearly with temperature; hence, any direct approximation of A_θ is likely to lead to large errors. On the other hand, $h(\theta)$ will generally be a smoothly varying function of temperature that is well approximated by a linear function of temperature over an increment. If we further assume that incrementally the temperature θ is a linear function of time t, one finds the relation

$$h(\theta) = -\log A_\theta(\theta(t)) = \alpha + bt \tag{A.20}$$

or

$$A_\theta^{-1}\left(\theta\left(t\right)\right) = e^{\alpha+bt} \tag{A.21}$$

with

$$\begin{aligned} \alpha &= \frac{1}{\Delta t}\left[t^{n+1}h(\theta^n) - t^n h(\theta^{n+1})\right] \\ b &= \frac{1}{\Delta t}\left[h(\theta^{n+1}) - h(\theta^n)\right]. \end{aligned} \tag{A.22}$$

This yields the relation

$$\Delta\tau = \int_{t^n}^{t^{n+1}} e^{\alpha+bt}\, dt = \frac{1}{b}\left(e^{\alpha+bt^{n+1}} - e^{\alpha+bt^n}\right). \tag{A.23}$$

This expression can also be written as

$$\Delta\tau = \frac{A_\theta^{-1}\left(\theta^{n+1}\right) - A_\theta^{-1}\left(\theta^n\right)}{h\left(\theta^{n+1}\right) - h\left(\theta^n\right)}\Delta t. \tag{A.24}$$

Reduced states of stress

So far, we have discussed full triaxial stress states. If the stress state is reduced (i.e., plane stress or uniaxial stress), the equations derived here cannot be used directly because only the total stress state is reduced, not the individual terms in the series. Therefore, we use the following procedure.

For plane stress let the third component be the zero stress component. At the beginning of the increment we presumably know the volumetric elastic strain ϕ_e^n, the volumetric viscous strain ϕ_c^n, and the volumetric viscous strains ϕ_i^n associated with the Prony series. The total volumetric strain can be obtained by adding together the elastic volumetric strain and the volumetric viscous strain

$$\phi^n = \phi_e^n + \phi_c^n. \tag{A.25}$$

The deviatoric strain in the 3-direction follows from the relation $\phi = \varepsilon_1 + \varepsilon_2 + \varepsilon_3$, which yields:

$$e_3^n = \varepsilon_3^n - \frac{1}{3}\phi^n = \frac{2}{3}\phi^n - \varepsilon_1^n - \varepsilon_2^n. \tag{A.26}$$

The out-of-plane deviatoric stress at the end of the increment is

$$s_3^{n+1} = 2G_0 \left(e_3^{n+1} - \sum_{i=1}^{n_G} \alpha_i^G e_{3i}^{n+1} \right). \tag{A.27}$$

Substituting Eq. (A.13) for e_{3i}^{n+1}, letting $e_3^{n+1} = e_3^n + \Delta e_3$, and collecting terms gives

$$\begin{aligned} s_3^{n+1} = 2G^T \Delta e_3 + 2G_0 e_3^n &\left[1 - \sum_{i=1}^{n_G} \alpha_i^G \left(1 - e^{-\Delta\tau/\tau_i} \right) \right] \\ - 2G_0 &\sum_{i=1}^{n_G} \alpha_i^G e^{-\Delta\tau/\tau_i} e_{3i}^n. \end{aligned} \tag{A.28}$$

The hydrostatic stress is derived similarly as

$$\begin{aligned} -p^{n+1} = K^T \Delta\phi + K_0 \phi^n &\left[1 - \sum_{i=1}^{n_K} \alpha_i^K \left(1 - e^{-\Delta\tau/\tau_i} \right) \right] \\ - K_0 &\sum_{i=1}^{n_K} \alpha_i^K e^{-\Delta\tau/\tau_i} \phi_i^n. \end{aligned} \tag{A.29}$$

We can write these equations in the form

$$\begin{aligned} s_3^{n+1} &= 2G^T \Delta e_3 + \bar{s}_3 \\ -p^{n+1} &= K^T \Delta\phi - \bar{p}. \end{aligned} \tag{A.30}$$

In the third direction the deviatoric stress minus the hydrostatic pressure is zero; hence,

$$2G^T \Delta e_3 + K^T \Delta\phi + \bar{s}_3 - \bar{p} = 0. \tag{A.31}$$

Since $\Delta e_3 = \frac{2}{3}\Delta\phi - \Delta\varepsilon_1 - \Delta\varepsilon_2$, it follows that

$$\left(K^T + \frac{4}{3}G^T\right)\Delta\phi = 2G^T\left(\Delta\varepsilon_1 + \Delta\varepsilon_2\right) - \bar{s}_3 + \bar{p}, \tag{A.32}$$

from which $\Delta\phi$ can be solved. One can then also calculate Δe_1 and Δe_2, and with Eq. (A.13) or Eq. (A.14) one can update the deviatoric viscous strains e_i^{n+1}. The volumetric strains ϕ_i^{n+1} are obtained with a relation similar to Eq. (A.13).

For uniaxial stress states a similar procedure is used. As before, ϕ^n follows from Eq. (A.25) and e_3^n and e_2^n follow from $\varepsilon_1 + 2\varepsilon_3 = \phi$:

$$e_3^n = e_2^n = \varepsilon_3^n - \frac{1}{3}\phi^n = \frac{1}{6}\phi^n - \frac{1}{2}\varepsilon_1^n. \tag{A.33}$$

Equations (A.28) and (A.29) can be used to calculate $\bar{s}_3$ and $\bar{p}$, which again leads to Eq. (A.31). Applying Eq. (A.33) for Δe_3,

$$\left(K^T + \frac{1}{3}G^T\right)\Delta\phi = G^T\Delta\varepsilon_1 - \bar{s}_3 + \bar{p}. \tag{A.34}$$

After this, one can follow the same procedure as for plane stress.

Appendix B

Hill's plasticity

Yield function:

$$\Phi\left(\boldsymbol{\sigma},\bar{\sigma},\boldsymbol{\alpha}\right)=\frac{1}{2}\left(\boldsymbol{\sigma}-\boldsymbol{\alpha}\right)^{T}\boldsymbol{P}\left(\boldsymbol{\sigma}-\boldsymbol{\alpha}\right)-\bar{\sigma}^{2}=\frac{1}{2}\boldsymbol{n}^{T}\boldsymbol{P}\boldsymbol{n}-\bar{\sigma}^{2}=\mathbf{0} \tag{B.1}$$

where $\boldsymbol{n}=\boldsymbol{\sigma}-\boldsymbol{\alpha}$ is the relative stress tensor.

Flow rule:

$$\dot{\boldsymbol{\varepsilon}}^{p}=\dot{\gamma}\frac{\partial\Phi}{\partial\boldsymbol{\sigma}}=\dot{\gamma}\boldsymbol{N}=\dot{\gamma}\boldsymbol{P}\boldsymbol{n} \tag{B.2}$$

Accumulated plastic strain:

$$\dot{\bar{\varepsilon}}^{p}=\sqrt{\frac{2}{3}\dot{\boldsymbol{\varepsilon}}^{p}:\dot{\boldsymbol{\varepsilon}}^{p}}=\dot{\gamma}\sqrt{\frac{2}{3}\left(\boldsymbol{P}\boldsymbol{n}\right)^{T}Z\left(\boldsymbol{P}\boldsymbol{n}\right)} \tag{B.3}$$

Prager's nonlinear kinematic hardening rule:

$$\dot{\boldsymbol{\alpha}}=\frac{2}{3}C\left(\bar{\varepsilon}^{p}\right)\dot{\boldsymbol{\varepsilon}}^{p}=\dot{\gamma}C\left(\bar{\varepsilon}^{p}\right)\boldsymbol{P}\boldsymbol{n} \tag{B.4}$$

The incremental elastoplastic constitutive problem. Given the values $\boldsymbol{\varepsilon}_{n}^{e}$ and $\boldsymbol{\alpha}_{n}$, of the elastic strain and internal variables set at the beginning of the pseudo-time interval $[t_{n},t_{n+1}]$, and given the prescribed incremental strain $\Delta\boldsymbol{\varepsilon}$ for this interval, solve the following system of algebraic equations

$$\begin{aligned}
\boldsymbol{\varepsilon}^e_{n+1} &= \boldsymbol{\varepsilon}^e_n + \Delta\boldsymbol{\varepsilon} - \Delta\gamma P\boldsymbol{n}_{n+1} \\
\boldsymbol{\alpha}_{n+1} &= \boldsymbol{\alpha}_n + \Delta\gamma\tfrac{2}{3}C\left(\bar{\varepsilon}^p_{n+1}\right)P\boldsymbol{n}_{n+1} \\
\bar{\varepsilon}^p_{n+1} &= \bar{\varepsilon}^p_n + \Delta\gamma\sqrt{\tfrac{2}{3}\left(\boldsymbol{P}\boldsymbol{n}_{n+1}\right)^T Z\left(\boldsymbol{P}\boldsymbol{n}_{n+1}\right)}
\end{aligned} \tag{B.5}$$

for the unknowns $\boldsymbol{\varepsilon}^e_{n+1}, \boldsymbol{\alpha}_{n+1}$ and $\Delta\gamma$, subjected to the constraints

$$\Delta\gamma \geq 0, \;\; \Phi\left(\boldsymbol{\sigma}_{n+1}, \bar{\sigma}, \boldsymbol{\alpha}_{n+1}\right) \leq 0, \;\; \Delta\gamma\ \Phi\left(\boldsymbol{\sigma}_{n+1}, \bar{\sigma}, \boldsymbol{\alpha}_{n+1}\right) = 0 \tag{B.6}$$

where

$$\boldsymbol{\sigma}_{n+1} = \boldsymbol{D}^e \varepsilon^e_{n+1}, \;\; C\left(\bar{\varepsilon}^p\right) = \frac{\Delta\bar{\alpha}}{\Delta\bar{\varepsilon}^p} \tag{B.7}$$

with $\boldsymbol{D}^e$ the orthotropic elasticity matrix and $\bar{\alpha}$ the equivalent back stresses which depend on equivalent plastic strains $\bar{\varepsilon}^p$ and are known from the kinematic hardening law. The incremental equations in the system (B.5) have been derived from the differential equations (B.2) and (B.4) using the backward Euler approximation scheme. In the above, the notation $\Delta(\cdot) \equiv (\cdot)_{n+1} - (\cdot)_n$ has been adopted, with $(\cdot)_n$ and $(\cdot)_{n+1}$ denoting the value of $(\cdot)$ at t_n and t_{n+1}, respectively. The increment $\Delta\gamma$ is called the incremental plastic multiplier. Note that once the solution $\boldsymbol{\varepsilon}^e_{n+1}$ has been obtained, the plastic strain at t_{n+1} can be calculated as

$$\boldsymbol{\varepsilon}^p_{n+1} = \boldsymbol{\varepsilon}^p_n + \Delta\boldsymbol{\varepsilon} - \Delta\boldsymbol{\varepsilon}^e \tag{B.8}$$

so that all variables of the model are known at the end of the interval $[t_n, t_{n+1}]$.

The fully implicit elastic predictor/return-mapping algorithm for numerical integration of Hill's elastoplastic constitutive equations can be formulated as:

i. Elastic predictor. Given $\Delta\boldsymbol{\varepsilon}$ and the state variables at t_n, evaluate the elastic trial state

$$\begin{aligned}
&\boldsymbol{\varepsilon}^{e\ \text{trial}}_{n+1} = \boldsymbol{\varepsilon}^{e}_{n} + \Delta\boldsymbol{\varepsilon},\\
&\bar{\varepsilon}^{p\ \text{trial}}_{n+1} = \bar{\varepsilon}^{p}_{n},\ \ \boldsymbol{\alpha}^{\text{trial}}_{n+1} = \boldsymbol{\alpha}_{n},\ \ \boldsymbol{\sigma}^{\text{trial}}_{n+1} = \boldsymbol{D}^{e}\ \varepsilon^{e\ \text{trial}}_{n+1}
\end{aligned}$$

ii. Check plastic admissibility

$$\begin{aligned}
&\text{IF}\ \Phi\left(\boldsymbol{\sigma}^{\text{trial}}_{n+1}, \bar{\sigma}, \boldsymbol{\alpha}^{\text{trial}}_{n+1}\right) \leq 0\\
&\text{THEN set}\ (\cdot)_{n+1} = (\cdot)^{\text{trial}}_{n+1}\ \text{and EXIT}
\end{aligned}$$

iii. Return mapping. Solve the system

$$\left\{\begin{matrix}
\boldsymbol{\varepsilon}^{e}_{n+1} - \boldsymbol{\varepsilon}^{e\ \text{trial}}_{n+1} + \Delta\gamma P\boldsymbol{n}_{n+1}\\
\boldsymbol{\alpha}_{n+1} - \boldsymbol{\alpha}^{\text{trial}}_{n+1} - \Delta\gamma\frac{2}{3}C\left(\bar{\varepsilon}^{p}_{n+1}\right)P\boldsymbol{n}_{n+1}\\
\bar{\varepsilon}^{p}_{n+1} - \bar{\varepsilon}^{p\ \text{trial}}_{n+1} - \Delta\gamma\sqrt{\frac{2}{3}\left(\boldsymbol{P}\boldsymbol{n}_{n+1}\right)^{T} Z\left(\boldsymbol{P}\boldsymbol{n}_{n+1}\right)}\\
\Phi\left(\boldsymbol{\sigma}_{n+1}, \bar{\sigma}, \boldsymbol{\alpha}_{n+1}\right)
\end{matrix}\right\} = \left\{\begin{matrix}0\\0\\0\\0\end{matrix}\right\}$$

for $\boldsymbol{\varepsilon}^{e}_{n+1}$, $\boldsymbol{\alpha}_{n+1}$ and $\Delta\gamma$, with $\boldsymbol{\sigma}_{n+1} = \boldsymbol{D}^{e}\varepsilon^{e}_{n+1}$

iv. EXIT

Single-equation return mapping

For the return mapping algorithm the system of the incremental plasticity equations is solved, based on the governing parameter method [42]. In this context, the stress integration is practically achieved by solving one nonlinear equation with respect to the governing scalar parameter. For the return mapping algorithm, the above system can be reduced to the solution of a single scalar equation for the plastic multiplier $\Delta\gamma$

Newton-Raphson iterative scheme:

$$\begin{aligned}
&\Delta\gamma^{(k)} = \Delta\gamma^{(k-1)} + \delta\Delta\gamma^{(k)}\\
&\text{with}\ \delta\Delta\gamma^{(k)} = -\left.\frac{\tilde{\Phi}\left(\Delta\gamma\right)}{d\tilde{\Phi}\left(\Delta\gamma\right)/d\Delta\gamma}\right|^{(k-1)}
\end{aligned}$$

The yield function is written in terms of $\Delta\gamma$ as

$$\tilde{\Phi}(\Delta\gamma) = \frac{1}{2}\left[\boldsymbol{n}(\Delta\gamma)\right]^T \boldsymbol{P}\left[\boldsymbol{n}(\Delta\gamma)\right] - \left[\bar{\sigma}\left(\bar{\varepsilon}^p(\Delta\gamma)\right)\right]^2 = \boldsymbol{0}$$

and its derivative with respect to $\Delta\gamma$ is

$$\frac{d\tilde{\Phi}(\Delta\gamma)}{d\Delta\gamma} = \left[\boldsymbol{P}\boldsymbol{n}(\Delta\gamma)\right]^T \frac{d\boldsymbol{n}(\Delta\gamma)}{d\Delta\gamma} - 2\bar{\sigma}H^i\frac{d\bar{\varepsilon}^p(\Delta\gamma)}{d\Delta\gamma}$$

where $H^i = d\bar{\sigma}/d\bar{\varepsilon}^p$ is the isotropic hardening. After some manipulations the following variables are expressed in terms of the governing parameter

$$\boldsymbol{n}(\Delta\gamma) \equiv \boldsymbol{n}_{n+1} = \left[\boldsymbol{I} + \left(\Delta\gamma\boldsymbol{D}^e + \frac{2}{3q_n}\left(\bar{\alpha}_{n+1} - \bar{\alpha}_n\right)\boldsymbol{I}\right)\boldsymbol{P}\right]^{-1}\boldsymbol{n}^{\text{trial}}$$

$$\frac{d\boldsymbol{n}(\Delta\gamma)}{d\Delta\gamma} = -\left[\boldsymbol{I} + \left(\Delta\gamma\boldsymbol{D}^e + \frac{2}{3q_n}\left(\bar{\alpha}_{n+1} - \bar{\alpha}_n\right)\boldsymbol{I}\right)\boldsymbol{P}\right]^{-1}\left[\boldsymbol{D}^e + \frac{2}{3q_n}H^k\frac{d\bar{\varepsilon}^p}{d\Delta\gamma}\boldsymbol{I}\right]\boldsymbol{P}\boldsymbol{n}_{n+1}$$

where $H^k = C(\bar{\varepsilon}^p) = d\bar{\alpha}/d\bar{\varepsilon}^p$ is the kinematic hardening and $q_n = \sqrt{\frac{2}{3}\left(\boldsymbol{P}\boldsymbol{n}_n\right)^T\boldsymbol{Z}\left(\boldsymbol{P}\boldsymbol{n}_n\right)}$ is an equivalent stress measure. The equivalent plastic strain is expressed as:

$$\bar{\varepsilon}^p(\Delta\gamma) \equiv \bar{\varepsilon}^p_{n+1} = \bar{\varepsilon}^p_n + \Delta\gamma\; q_{n+1}$$

and its derivative is:

$$\frac{d\bar{\varepsilon}^p(\Delta\gamma)}{d\Delta\gamma} = q_{n+1} + \Delta\gamma\frac{2}{3q_{n+1}}\left(\boldsymbol{P}\boldsymbol{n}_{n+1}\right)^T\boldsymbol{Z}\boldsymbol{P}\frac{d\boldsymbol{n}(\Delta\gamma)}{d\Delta\gamma}$$

The elastoplastic consistent tangent

By differentiating the system of the incremental nonlinear equations, the following linearized system is obtained:

$$\begin{bmatrix} \boldsymbol{D}^e + \Delta\gamma \boldsymbol{P} & 0 & \boldsymbol{N} & -\Delta\gamma \boldsymbol{P} \\ -\Delta\gamma \dfrac{2}{3q_{n+1}} \boldsymbol{N}^T \boldsymbol{Z} \boldsymbol{P} & 1 & -q_{n+1} & \Delta\gamma \dfrac{2}{3q_{n+1}} \boldsymbol{N}^T \boldsymbol{Z} \boldsymbol{P} \\ \boldsymbol{N}^T & -2\bar{\sigma} H^i & 0 & -\boldsymbol{N}^T \\ -\dfrac{2}{3q_n} \left(\bar{\alpha}_{n+1} - \bar{\alpha}_n\right) \boldsymbol{P} & -\dfrac{2}{3q_n} H^k \boldsymbol{N} & 0 & \boldsymbol{I} + \dfrac{2}{3q_n} \left(\bar{\alpha}_{n+1} - \bar{\alpha}_n\right) \boldsymbol{P} \end{bmatrix} \begin{bmatrix} d\sigma_{n+1} \\ d\bar{\varepsilon}^p_{n+1} \\ d\Delta\gamma \\ d\alpha_{n+1} \end{bmatrix} = \begin{bmatrix} d\boldsymbol{\varepsilon}^{e\ \text{trial}} \\ 0 \\ 0 \\ 0 \end{bmatrix}$$

After some manipulations the elastoplastic consistent tangent is obtained as:

$$\boldsymbol{D}^{ep} = \frac{d\boldsymbol{\sigma}_{n+1}}{d\boldsymbol{\varepsilon}^{e\ \text{trial}}} = \left[\boldsymbol{D}^{e\ -1} + \Delta\gamma \boldsymbol{P} + \boldsymbol{N}\boldsymbol{B}\left(\boldsymbol{I} - \boldsymbol{D}^{-1}\boldsymbol{C}^{-1}\boldsymbol{E}\right) - \Delta\gamma \boldsymbol{P}\boldsymbol{D}^{-1}\boldsymbol{C}^{-1}\boldsymbol{E}\right]^{-1}$$

where

$$\begin{aligned} \boldsymbol{B} &= \left[-\Delta\gamma \frac{2}{3q_{n+1}^2} \boldsymbol{N}^T \boldsymbol{Z} \boldsymbol{P} + \frac{1}{2q_{n+1}\bar{\sigma} H^i} \boldsymbol{N}^T\right] \\ \boldsymbol{C} &= \boldsymbol{I} + \frac{2}{3q_n} \left(\bar{\alpha}_{n+1} - \bar{\alpha}_n\right) \boldsymbol{P} \\ \boldsymbol{D} &= \boldsymbol{I} + \boldsymbol{C}^{-1} \frac{2}{3q_n} H^k \frac{1}{2\bar{\sigma} H^i} \boldsymbol{N}\boldsymbol{N}^T \\ \boldsymbol{E} &= \frac{2}{3q_n} \left(\bar{\alpha}_{n+1} - \bar{\alpha}_n\right) \boldsymbol{P} + \frac{2}{3q_n} H^k \frac{1}{2\bar{\sigma} H^i} \boldsymbol{N}\boldsymbol{N}^T \end{aligned}$$

References

[1] Ahuja T, Kumar D, et al (2009) Recent progress in the development of nano-structured conducting polymers/nanocomposites for sensor applications. Sensors and Actuators B: Chemical 136(1):275–286

[2] Arash B, Wang Q (2014) A review on the application of nonlocal elastic models in modeling of carbon nanotubes and graphenes. In: Modeling of Carbon Nanotubes, Graphene and their Composites, Springer Series in Materials Science, vol 188, Springer International Publishing, pp 57–82

[3] Barber AH, Cohen SR, Wagner HD (2003) Measurement of carbon nanotube–polymer interfacial strength. Applied Physics Letters 82(23):4140–4142

[4] Belytschko T, Moës N, Usui S, Parimi C (2001) Arbitrary discontinuities in finite elements. International Journal for Numerical Methods in Engineering 50(4):993–1013

[5] Belytschko T, Xiao S, Schatz G, Ruoff R (2002) Atomistic simulations of nanotube fracture. Physical Review B 65(23):235,430

[6] Belytschko T, Gracie R, Ventura G (2009) A review of extended/generalized finite element methods for material modeling. Modelling and Simulation in Materials Science and Engineering 17(4):1–24

[7] Bordas S, Nguyen PV, Dunant C, Guidoum A, Nguyen-Dang H (2007) An extended finite element library. International Journal for Numerical Methods in Engineering 71(6):703–732

[8] Brenner DW (1990) Empirical potential for hydrocarbons for use in simulating the chemical vapor deposition of diamond films. Physical Review B 42(15):9458

[9] Broggi M, Schuëller G (2011) Efficient modeling of imperfections for buckling analysis of composite cylindrical shells. Engineering Structures 33(5):1796–1806

[10] Byrne MT, Gun'ko YK (2010) Recent advances in research on carbon nanotube–polymer composites. Advanced Materials 22(15):1672–1688

[11] Chae HK, Siberio-Pérez DY, Kim J, Go Y, Eddaoudi M, Matzger AJ, O'Keeffe M, Yaghi OM (2004) A route to high surface area, porosity and inclusion of large molecules in crystals. Nature 427(6974):523–527

[12] Chang T (2010) A molecular based anisotropic shell model for single-walled carbon nanotubes. Journal of the Mechanics and Physics of Solids 58(9):1422–1433

[13] Chen X, Liu Y (2004) Square representative volume elements for evaluating the effective material properties of carbon nanotube-based composites. Computational Materials Science 29(1):1–11

[14] Cohen L (1995) Time-frequency analysis, vol 778. Prentice Hall PTR Englewood Cliffs, New Jersey

[15] Coleman JN, Khan U, Blau WJ, Gun"ko YK (2006) Small but strong: a review of the mechanical properties of carbon nanotube–polymer composites. Carbon 44(9):1624–1652

[16] Cornell WD, Cieplak P, Bayly CI, Gould IR, Merz KM, Ferguson DM, Spellmeyer DC, Fox T, Caldwell JW, Kollman PA (1995) A second generation force field for the simulation of proteins, nucleic acids, and organic molecules. Journal of the American Chemical Society 117(19):5179–5197

[17] Cornwell C, Wille L (1997) Elastic properties of single-walled carbon nanotubes in compression. Solid State Communications 101(8):555–558

[18] Corr SA, Rakovich YP, Gun"ko YK (2008) Multifunctional magnetic-fluorescent nanocomposites for biomedical applications. Nanoscale Research Letters 3(3):87–104

[19] Curtin WA, Miller RE (2003) Atomistic/continuum coupling in computational materials science. Modelling and simulation in materials science and engineering 11(3):R33

[20] Dresselhaus M, Dresselhaus G, Saito R (1995) Physics of carbon nanotubes. Carbon 33(7):883–891

[21] Duguay A (2011) Exfoliated graphite nanoplatelet-filled impact modified polypropylene nanocomposites. Electronic Theses and Dissertations, Paper 1574

[22] Frankland S, Caglar A, Brenner D, Griebel M (2002) Molecular simulation of the influence of chemical cross-links on the shear strength of carbon nanotube-polymer interfaces. The Journal of Physical Chemistry B 106(12):3046–3048

[23] Fries TP (2008) A corrected XFEM approximation without problems in blending elements. International Journal for Numerical Methods in Engineering 75(5):503–532

[24] Ganesan Y, Peng C, Lu Y, Loya PE, Moloney P, Barrera E, Yakobson BI, Tour JM, Ballarini R, Lou J, et al (2011) Interface toughness of carbon nanotube reinforced epoxy composites. ACS applied materials & interfaces 3(2):129

[25] Gelin RB (1994) Molecular Modeling of Polymer Structures and Properties. Hanser Gardner Publications

[26] Gojny FH, Wichmann MH, Fiedler B, Kinloch IA, Bauhofer W, Windle AH, Schulte K (2006) Evaluation and identification of electrical and thermal conduction mechanisms in carbon nanotube/epoxy composites. Polymer 47(6):2036–2045

[27] Gou J, Minaie B, Wang B, Liang Z, Zhang C (2004) Computational and experimental study of interfacial bonding of single-walled nanotube reinforced composites. Computational Materials Science 31(3):225–236

[28] Hashin Z (1983) Analysis of composite materials. Journal of applied Mechanics 50(2):481–505

[29] Hernandez E, Goze C, Bernier P, Rubio A (1998) Elastic properties of C and $B_xC_yN_z$ composite nanotubes. Physical Review Letters 80(20):4502

[30] Hill R (1950) The Mathematical Theory of Plasticity. London: Oxford University Press

[31] Hill R (1963) Elastic properties of reinforced solids: Some theoretical principles. Journal of the Mechanics and Physics of Solids 11(5):357 – 372

[32] Hiriyur B, Waisman H, Deodatis G (2011) Uncertainty quantification in homogenization of heterogeneous microstructures modeled by XFEM. International Journal for Numerical Methods in Engineering 88(3):257–278

[33] Hussain F, Hojjati M, Okamoto M, Gorga RE (2006) Review article: polymer-matrix nanocomposites, processing, manufacturing, and application: an overview. Journal of composite materials 40(17):1511–1575

[34] Iijima S (1991) Helical microtubules of graphitic carbon. nature 354(6348):56–58

[35] Iijima S, Brabec C, Maiti A, Bernholc J (1996) Structural flexibility of carbon nanotubes. The Journal of chemical physics 104(5):2089–2092

[36] Jendele L, Červenka J (2009) On the solution of multi-point constraints–application to FE analysis of reinforced concrete structures. Computers & Structures 87(15):970–980

[37] Jiang X, Drzal LT (2010) Multifunctional high density polyethylene nanocomposites produced by incorporation of exfoliated graphite nanoplatelets 1: Morphology and mechanical properties. Polymer Composites 31(6):1091–1098

[38] Jin Y, Yuan F (2003) Simulation of elastic properties of single-walled carbon nanotubes. Composites Science and Technology 63(11):1507 – 1515

[39] Kalaitzidou K, Fukushima H, Drzal LT (2007) Mechanical properties and morphological characterization of exfoliated graphite–polypropylene nanocomposites. Composites Part A: Applied science and manufacturing 38(7):1675–1682

[40] Kim BC, Park SW, Lee DG (2008) Fracture toughness of the nano-particle reinforced epoxy composite. Composite Structures 86(1):69–77

[41] Kim H, Abdala AA, Macosko CW (2010) Graphene/polymer nanocomposites. Macromolecules 43(16):6515–6530

[42] Kojić M, Grujović N, Slavković R, Živković M (1996) A General Orthotropic von Mises Plasticity Material Model With Mixed Hardening: Model Definition and Implicit Stress Integration Procedure. Journal of Applied Mechanics 63:376

[43] Kouznetsova V, Geers M, Brekelmans W (2004) Multi-scale second-order computational homogenization of multi-phase materials: a nested finite element solution strategy. Computer Methods in Applied Mechanics and Engineering 193(48):5525–5550

[44] Krongauz Y, Belytschko T (1998) EFG approximation with discontinuous derivatives. International Journal for Numerical Methods in Engineering 41(7):1215–1233

[45] Kudin KN, Scuseria GE, Yakobson BI (2001) C_ {2} f, bn, and c nanoshell elasticity from ab initio computations. Physical Review B 64(23):235,406

[46] Kuilla T, Bhadra S, Yao D, Kim NH, Bose S, Lee JH (2010) Recent advances in graphene based polymer composites. Progress in Polymer Science 35(11):1350–1375

[47] Lang C, Doostan A, Maute K (2013) Extended stochastic FEM for diffusion problems with uncertain material interfaces. Computational Mechanics 51:1031–1049

[48] Leach AR (2001) Molecular modelling: principles and applications. Pearson Education

[49] Li B, Zhong WH (2011) Review on polymer/graphite nanoplatelet nanocomposites. Journal of materials science 46(17):5595–5614

[50] Li C, Chou TW (2003) A structural mechanics approach for the analysis of carbon nanotubes. International Journal of Solids and Structures 40(10):2487–2499

[51] Lordi V, Yao N (2000) Molecular mechanics of binding in carbon-nanotube–polymer composites. Journal of Materials Research 15(12):2770–2779

[52] Lu JP (1997) Elastic properties of carbon nanotubes and nanoropes. Physical Review Letters 79(7):1297–1300

[53] Mallat S (1999) A wavelet tour of signal processing. Academic press

[54] Markou G, Papadrakakis M (2012) An efficient generation method of embedded reinforcement in hexahedral elements for reinforced concrete simulations. Advances in Engineering Software 45(1):175–187

[55] Maugin G (1992) The thermomechanics of plasticity and fracture, vol 7. Cambridge University Press

[56] Melenk JM, Babuška I (1996) The partition of unity finite element method: basic theory and applications. Computer Methods in Applied Mechanics and Engineering 139(1):289–314

[57] Miehe C, Koch A (2002) Computational micro-to-macro transitions of discretized microstructures undergoing small strains. Archive of Applied Mechanics 72(4-5):300–317

[58] Miller RE, Tadmor EB (2002) The quasicontinuum method: Overview, applications and current directions. Journal of Computer-Aided Materials Design 9(3):203–239

[59] Mittal G, Dhand V, Rhee KY, Park SJ, Lee WR (2014) A review on carbon nanotubes and graphene as fillers in reinforced polymer nanocomposites. Journal of Industrial and Engineering Chemistry

[60] Moës N, Dolbow J, Belytschko T (1999) A finite element method for crack growth without remeshing. International Journal for Numerical Methods in Engineering 46:131–150

[61] Moës N, Cloirec M, Cartraud P, Remacle JF (2003) A computational approach to handle complex microstructure geometries. Computer Methods in Applied Mechanics and Engineering 192(28):3163–3177

[62] Nasdala L, Ernst G (2005) Development of a 4-node finite element for the computation of nano-structured materials. Computational materials science 33(4):443–458

[63] Newland DE (1994) Wavelet analysis of vibration. I: Theory. Journal of vibration and acoustics 116(4):409–416

[64] Odegard GM, Gates TS, Nicholson LM, Wise KE (2002) Equivalent-continuum modeling of nano-structured materials. Composites Science and Technology 62(14):1869–1880

[65] Pantano A, M Parks D, Boyce MC (2004) Mechanics of deformation of single-and multi-wall carbon nanotubes. Journal of the Mechanics and Physics of Solids 52(4):789–821

[66] Peigney A, Laurent C, Flahaut E, Bacsa R, Rousset A (2001) Specific surface area of carbon nanotubes and bundles of carbon nanotubes. Carbon 39(4):507–514

[67] Peng J, Wu J, Hwang K, Song J, Huang Y (2008) Can a single-wall carbon nanotube be modeled as a thin shell? Journal of the Mechanics and Physics of Solids 56(6):2213–2224

[68] Qian D, Dickey EC, Andrews R, Rantell T (2000) Load transfer and deformation mechanisms in carbon nanotube-polystyrene composites. Applied Physics Letters 76(20):2868 –2870

[69] Qian H, Greenhalgh ES, Shaffer MS, Bismarck A (2010) Carbon nanotube-based hierarchical composites: a review. Journal of Materials Chemistry 20(23):4751–4762

[70] Ramanathan T, Liu H, Brinson LC (2005) Functionalized SWNT/polymer nanocomposites for dramatic property improvement. Journal of Polymer Science Part B: Polymer Physics 43(17):2269–2279

[71] Rappé AK, Casewit CJ, Colwell K, Goddard Iii W, Skiff W (1992) UFF, a full periodic table force field for molecular mechanics and molecular dynamics simulations. Journal of the American Chemical Society 114(25):10,024–10,035

[72] Salehi-Khojin A, Jana S, Zhong WH (2007) Thermal-mechanical properties of a graphitic-nanofibers reinforced epoxy. Journal of nanoscience and nanotechnology 7(3):898–906

[73] Sánchez-Portal D, Artacho E, Soler JM, Rubio A, Ordejón P (1999) Ab initio structural, elastic, and vibrational properties of carbon nanotubes. Physical Review B 59(19):12,678

[74] Savvas D, Papadopoulos V (2014a) Nonlinear multiscale homogenization of carbon nanotube reinforced composites with interfacial slippage. International Journal for Multiscale Computational Engineering 12(4):271–289

[75] Savvas D, Papadopoulos V, Papadrakakis M (2012) The effect of interfacial shear strength on damping behavior of carbon nanotube reinforced composites. International Journal of Solids and Structures 49(26):3823–3837

[76] Savvas D, Stefanou G, Papadrakakis M, Deodatis G (2014b) Homogenization of random heterogeneous media with inclusions of arbitrary shape modeled by XFEM. Computational Mechanics 54(5):1221–1235

[77] Schadler LS, Giannaris SC, Ajayan PM (1998) Load transfer in carbon nanotube epoxy composites. Applied Physics Letters 73(26):3842 –3844

[78] Schillinger D, Papadopoulos V (2010) Accurate estimation of evolutionary power spectra for strongly narrow-band random fields. Computer Methods in Applied Mechanics and Engineering 199(17):947–960

[79] Schillinger D, Papadopoulos V, Bischoff M, Papadrakakis M (2010) Buckling analysis of imperfect i-section beam-columns with stochastic shell finite elements. Computational Mechanics 46(3):495–510

[80] Schwarzl F, Staverman A (1952) Time-temperature dependence of linear viscoelastic behavior. Journal of Applied Physics 23(8):838–843

[81] Sethian JA (1999) Level Set Methods and Fast Marching Methods, Evolving Interfaces in Computational Geometry, Fluid Mechanics, Computer Vision, and Materials Science. Cambridge university press

[82] Van der Sluis O, Schreurs P, Meijer H (1999) Effective properties of a viscoplastic constitutive model obtained by homogenisation. Mechanics of Materials 31(11):743–759

[83] Sonon B, Francois B, Massart T (2012) A unified level set based methodology for fast generation of complex microstructural multi-phase RVEs. Computer Methods in Applied Mechanics and Engineering 223-224:103–122

[84] Souza EN (2008) Computational methods for plasticity: Theory and applications. John Wiley and Sons, Ltd, Publication

[85] Spanos PD, Tezcan J, Tratskas P (2005) Stochastic processes evolutionary spectrum estimation via harmonic wavelets. Computer Methods in Applied Mechanics and Engineering 194(12):1367–1383

[86] Stefanou G, Nouy A, Clément A (2009) Identification of random shapes from images through polynomial chaos expansion of random level set functions. International Journal for Numerical Methods in Engineering 79(2):127–155

[87] Suhr J, Koratkar NA (2008) Energy dissipation in carbon nanotube composites: a review. Journal of Materials Science 43(13):4370–4382

[88] Sukumar N, Chopp DL, Moës N, Belytschko T (2001) Modeling holes and inclusions by level sets in the extended finite-element method. Computer Methods in Applied Mechanics and Engineering 190(46):6183–6200

[89] Sun X, Zhao W (2005) Prediction of stiffness and strength of single-walled carbon nanotubes by molecular-mechanics based finite element approach. Materials Science and Engineering: A 390(1):366–371

[90] Tadmor E, Phillips R, Ortiz M (1996) Mixed atomistic and continuum models of deformation in solids. Langmuir 12(19):4529–4534

[91] Talebi H, Silani M, Bordas SP, Kerfriden P, Rabczuk T (2014) A computational library for multiscale modeling of material failure. Computational Mechanics 53(5):1047–1071

[92] Tanaka T, Montanari G, Mulhaupt R (2004) Polymer nanocomposites as dielectrics and electrical insulation-perspectives for processing technologies, material characterization and future applications. Dielectrics and Electrical Insulation, IEEE Transactions on 11(5):763–784

[93] Thostenson ET, Ren Z, Chou TW (2001) Advances in the science and technology of carbon nanotubes and their composites: a review. Composites science and technology 61(13):1899–1912

[94] Thostenson ET, Li C, Chou TW (2005) Nanocomposites in context. Composites Science and Technology 65(3):491–516

[95] Tran A, Yvonnet J, He QC, Toulemonde C, Sanahuja J (2011) A multiple level set approach to prevent numerical artefacts in complex microstructures with nearby inclusions within XFEM. International Journal for Numerical Methods in Engineering 85(11):1436–1459

[96] Tserpes K, Papanikos P, Tsirkas S (2006) A progressive fracture model for carbon nanotubes. Composites Part B: Engineering 37(7):662–669

[97] Tu Zc, Ou-Yang Zc (2002) Single-walled and multiwalled carbon nanotubes viewed as elastic tubes with the effective young"s moduli dependent on layer number. Physical Review B 65(23):233,407

[98] Velasco-Santos C, Martínez-Hernández AL, Fisher FT, Ruoff R, Castano VM (2003) Improvement of thermal and mechanical properties of carbon nanotube composites through chemical functionalization. Chemistry of Materials 15(23):4470–4475

[99] Viculis LM, Mack JJ, Mayer OM, Hahn HT, Kaner RB (2005) Intercalation and exfoliation routes to graphite nanoplatelets. Journal of Materials Chemistry 15(9):974–978

[100] Wang C, Ru C, Mioduchowski A (2004) Applicability and limitations of simplified elastic shell equations for carbon nanotubes. Journal of applied mechanics 71(5):622–631

[101] Wernik J, Meguid SA (2009) Coupling atomistics and continuum in solids: status, prospects, and challenges. International Journal of Mechanics and Materials in Design 5(1):79–110

[102] Williams ML, Landel RF, Ferry JD (1955) The temperature dependence of relaxation mechanisms in amorphous polymers and other glass-forming liquids. Journal of the American Chemical Society 77(14):3701–3707

[103] Xiao J, Gama B, Gillespie Jr J (2005) An analytical molecular structural mechanics model for the mechanical properties of carbon nanotubes. International Journal of Solids and Structures 42(11):3075–3092

[104] Xin Z, Jianjun Z, Zhong-Can OY (2000) Strain energy and young's modulus of single-wall carbon nanotubes calculated from electronic energy-band theory. Physical Review B 62:13,692–13,696

[105] Yakobson B, Brabec C, Bernholc J (1996) Structural mechanics of carbon nanotubes: From continuum elasticity to atomistic fracture. Journal of Computer-Aided Materials Design 3(1-3):173–182

[106] Yang S, Yu S, Kyoung W, Han DS, Cho M (2012) Multiscale modeling of size-dependent elastic properties of carbon nanotube/polymer nanocomposites with interfacial imperfections. Polymer 53(2):623–633

[107] Yao N, Lordi V (1998) Young"s modulus of single-walled carbon nanotubes. Journal of Applied Physics 84(4):1939–1943

[108] Yu A, Ramesh P, Itkis ME, Bekyarova E, Haddon RC (2007) Graphite nanoplatelet-epoxy composite thermal interface materials. The Journal of Physical Chemistry C 111(21):7565–7569

[109] Yu MF, Lourie O, Dyer MJ, Moloni K, Kelly TF, Ruoff RS (2000) Strength and breaking mechanism of multiwalled carbon nanotubes under tensile load. Science 287(5453):637–640

[110] Yvonnet J, Quang HL, He QC (2008) An XFEM/level set approach to modelling surface/interface effects and to computing the size-dependent effective properties of nanocomposites. Computational Mechanics 42(1):119–131

[111] Zhai L, Ling G, Wang Y (2008) Effect of nano-Al_2O_3 on adhesion strength of epoxy adhesive and steel. International Journal of Adhesion and Adhesives 28(1):23–28

[112] Zhao X, Duddu R, Bordas SP, Qu J (2013) Effects of elastic strain energy and interfacial stress on the equilibrium morphology of misfit particles in heterogeneous solids. Journal of the Mechanics and Physics of Solids 61(6):1433–1445

[113] Zheng Q, Xia D, Xue Q, Yan K, Gao X, Li Q (2009) Computational analysis of effect of modification on the interfacial characteristics of a carbon nanotube–polyethylene composite system. Applied Surface Science 255(6):3534–3543

[114] Zhu J, Kim J, Peng H, Margrave JL, Khabashesku VN, Barrera EV (2003) Improving the dispersion and integration of single-walled carbon nanotubes in epoxy composites through functionalization. Nano Letters 3(8):1107–1113

[115] Zohdi TI, Wriggers P (2008) An Introduction to Computational Micromechanics, 2nd Edition, Lecture Notes in Applied and Computational Mechanics, vol 20. Springer, Heidelberg